

The Magnet Project Technical Design Report

Acquistapace G.¹, André J.¹, Bovard M.H.¹, Calvo A.¹, Campi D.^{1*}, Curé B.¹, Delikaris D.¹, Desirelli A.¹, Fabbricatore P.⁴, Farinon S.⁴, Feyzi F.⁷, Gélébart J.C.², Gerwig H.¹, Girod J.P.¹, Grillet J.P.¹, Greenler L.⁷, Gregerson G.M.⁷, Hervé A.¹, Horvath I.L.⁵, Huhtinen M.¹, Kaftanov V.⁶, Le Coroller A.², Lesmond C.², Levesy B.², Lottin J.C.², Lottin J.P.², Loveless R.⁷, Lyraud C.², Mason W.P.⁷, Maugain J.M.¹, Musenich R.⁴, Passardi G.¹, Pes C.², Petiot P.¹, Pintus R.¹, Pippin J.⁷, Pogorelko O.⁶, Priano C.⁴, Rey J.M.², Rondeaux F.², Roussé J.Y.², Rykaczewski H.⁵, Smith R.³, de Visser T.¹, Veillet L.¹, Wands B.³, Waurick G.¹

* Main Editor

1- *CERN, European Laboratory for Particle Physics, Geneva, Switzerland*

2- *DSM/DAPNIA, CEA/Saclay, Gif-sur-Yvette, France*

3- *Fermi National Accelerator Laboratory, Batavia, USA*

4- *Università di Genova e Sezione dell'INFN di Genova, Italy*

5- *Institut für Teilchenphysik, Eidgenössische Technische Hochschule, Zürich, Switzerland*

6- *Institute for Theoretical and Experimental Physics, Moscow, Russia*

7- *University of Wisconsin, Madison, USA*

The list of the Institutes participating to the CMS Collaboration can be found on page x

Contact persons

CMS Spokesperson	CMS Technical Coordinator	CMS Magnet Project Manager
M. Della Negra ¹	E. Radermacher ¹	A. Hervé ¹
michel.della.negra@cern.ch	ernst.radermacher@cern.ch	alain.herve@cern.ch

Acknowledgement

The CMS Magnet Project would like to particularly thank the following experts for their continuous support and advise without which the project would not have been possible :

Baynham E.¹¹, Desportes H.², Evans D.¹¹, Hartwig T.¹², Lazeyras P.¹, Maurer W.⁸, Schneider-Müntau H.⁹, Wittgenstein F.⁵, Yamamoto A.¹⁰

The Magnet Group wants also to acknowledge important technical contributions made to this Technical Design Report by:

Bénichou J.L.¹, Blondel J.¹, Bacher J.P.¹, Baldy J.L¹, Bertinelli F.¹, Bonal P.¹, Bos J.¹, Carocci D.¹, Coin A.¹, Duthion G.¹, Faber G.⁵, Férigoule C.¹, Fernqvist G.¹, Ingenito P.⁵, Mazzone V.¹, Merlino A.¹, Meyer T.¹, Michaud J.F.¹, More D.¹, Kershaw K.¹, Kuipers J.¹, Pabot Y.², B.Pirollet¹, Pothier J.¹, Potter K.¹, Rabany M.¹, Rau G.¹, J.Roche¹, Schönbacher H.¹, Saudemont JC.², Scola L.², Sgobba S.¹, Stevenson G.¹, Watson T.¹, Wikberg T.¹

The group is also indebted to the invaluable help given for the publishing by :

Madeleine Catin¹, Anne Lissajoux¹, Guy Martin¹ and Madeleine Nazard²

and would also like to thank Mirka Seneira¹ and Francine Vermeille¹ for providing a continuous secretarial support from the start of the project.

Institutes

CERN, European Laboratory for Particle Physics, Geneva, Switzerland

DSM/DAPNIA, CEA/Saclay, Gif-sur-Yvette, France

Fermi National Accelerator Laboratory, Batavia, USA

Università di Genova e Sezione dell'INFN di Genova, Italy

Institut für Teilchenphysik, Eidgenössische Technische Hochschule, Zürich, Switzerland

Institute for Theoretical and Experimental Physics, Moscow, Russia

University of Wisconsin, Madison, USA

Forschungszentrum Karlsruhe, Karlsruhe, Germany

NHMFL, National High Magnetic Field Laboratory, Tallahassee , USA

KEK, Tsukuba , Japan

RAL, Rutherford Appleton Laboratory, Oxford, United Kingdom

Texas University , USA

CMS Collaboration

Armenia

Yerevan Physics Institute, Yerevan

Austria

Institut fur Hochenergiephysik der OeAW, Wien

Belarus

Byelorussian State University, Minsk
Institute of Nuclear Problems, Minsk
National Scientific and Educational Centre, Minsk
Research Institute of Applied Physical Problems, Minsk

Belgium

Universite Libre de Bruxelles, Brussels
Vrije Universiteit Brussel, Brussels
Universite Catholique de Louvain, Louvain-la-Neuve
Universite de Mons-Hainaut, Mons
Universitaire Instelling Antwerpen, Wilrijk

Bulgaria

Institute for Nuclear Research and Nuclear Energy, Sofia
University of Sofia, Sofia

China, PR

Institute of High Energy Physics, Beijing
Beijing University, Beijing
University for Science and Technology of China, Hefei

Croatia

Technical University of Split, Split
University of Split, Split

Cyprus

University of Cyprus, Nicosia

Czech Republic

Institute of Scientific Instruments, Brno
Czech Technical University, Praha

Charles University, Praha
Institute of Computing Machines, Praha,
Nuclear Research Institute, Rez

Estonia

Institute of Chemical Physics and Biophysics, Tallinn

Finland

HIP, Helsinki University of Technology, Espoo
HIP, University of Helsinki, Helsinki,
Department of Physics, University of Helsinki, Helsinki
University of Jyvaskyla, Jyvaskyla
Dept. of Physics & Microelectronics Instrumentation Lab., University of Oulu, Oulu,
Tampere University of Technology, Tampere

France

Laboratoire d'Annecy-le-Vieux de Physique des Particules, IN2P3-CNRS, Annecy-le-Vieux
DSM/DAPNIA, CEA/Saclay, Gif-sur-Yvette
Laboratoire de Physique Nucleaire des Hautes Energies, Ecole Polytechnique, IN2P3-CNRS, Palaiseau
Institut de Recherches Subatomiques, IN2P3-CNRS – ULP, UHA, Strasbourg
Institut de Physique Nucleaire de Lyon, IN2P3-CNRS, Univ. Lyon I, Villeurbanne

Georgia

High Energy Physics Institute, Tbilisi
Institute of Physics, Tbilisi

Germany

RWTH, I. Physikalisches Institut, Aachen
RWTH, III. Physikalisches Institut A, Aachen
RWTH, III. Physikalisches Institut B, Aachen
Humboldt-Universitat zu Berlin, Berlin,
Institut fur Experimentelle Kernphysik, Karlsruhe

Greece

University of Athens, Athens
Institute of Nuclear Physics Demokritos, Attiki
University of Ioannina, Ioannina

Hungary

KFKI Research Institute for Particle and Nuclear Physics, Budapest
Kossuth Lajos University, Debrecen

India

Bhubaneswar Institute of Physics, Bhubaneswar
Panjab University, Chandigarh
Nuclear Physics Division, Bhabha Atomic Research Centre, Mumbai
Tata Institute of Fundamental Research - EHEP, Mumbai
Tata Institute of Fundamental Research - HECR, Mumbai
University of Delhi South Campus, New Delhi

Italy

Universita di Bari e Sezione dell' INFN, Bari
Universita di Bologna e Sezione dell' INFN, Bologna
Universita di Catania e Sezione dell' INFN, Catania
Universita di Firenze e Sezione dell' INFN, Firenze
Universita di Genova e Sezione dell' INFN, Genova
Universita de L'Aquila e Sezione dell' INFN, L'Aquila
Universita di Padova e Sezione dell' INFN, Padova
Universita di Pavia e Sezione dell' INFN, Pavia
Universita di Perugia e Sezione dell' INFN, Perugia
Universita di Pisa e Sezione dell' INFN, Pisa
Universita di Roma e Sezione dell' INFN, Roma
Dip. di Fisica Sperimentale & INFN, Torino

Latvia

Institute of Electronics and Computer Science, Riga - Salaspils

Pakistan

Quaid-I-Azam University, Islamabad

Poland

Institute of Experimental Physics, Warsaw
Soltan Institute for Nuclear Studies, Warsaw

Portugal

Laboratorio de Instrumentacao e Fisica Experimental de Particulas, Lisboa

Russia

Joint Institute for Nuclear Research, Dubna
Petersburg Nuclear Physics Institute, Gatchina (St Petersburg)
Institute for Nuclear Research, Moscow
Institute for Theoretical and Experimental Physics, Moscow
Moscow State University, Moscow
P.N. Lebedev Physical Institute, Moscow
Budker Institute for Nuclear Physics, Novosibirsk
Institute for High Energy Physics, Protvino

Slovak Republic

Institute of Computing Machines, Zilina

Spain

Centro de Investigaciones Energeticas Medioambientales y Tecnologicas, Madrid
Universidad Autonoma de Madrid, Madrid
Universidad de Cantabria, Santander

Switzerland

Universitat Basel, Basel
CERN, European Laboratory for Particle Physics, Geneva
Ecole Polytechnique Federale Lausanne, Lausanne
Paul Scherrer Institut, Villigen
Institut fur Teilchenphysik, Eidgenossische Technische Hochschule, Zurich
Universitat Zurich, Zurich

Turkey

Cukurova University, Adana,
Middle East Technical University, Physics Department, Ankara

Ukraine

Institute of Single Crystals of National Academy of Science, Kharkov
Kharkov State University, Kharkov
National Scientific Center Kharkov Institute of Physics and Technology, Kharkov

United Kingdom

University of Bristol, Bristol
Rutherford Appleton Laboratory, Didcot
Imperial College, University of London, London
Brunel University, Uxbridge

USA

Iowa State University, Ames
Johns Hopkins University, Baltimore
Fermi National Accelerator Laboratory, Batavia
Virginia Polytechnic Institute and State University, Blacksburg
Boston University, Boston
Northeastern University, Boston
Massachusetts Institute of Technology, Cambridge
University of Illinois at Chicago (UIC), Chicago
University of Maryland, College Park
The Ohio State University, Columbus
University of California at Davis, Davis
Northwestern University, Evanston

Fairfield University, Fairfield
University of Florida, Gainesville
Rice University, Houston
The University of Iowa, Iowa City
University of California San Diego, La Jolla
University of Nebraska-Lincoln, Lincoln
Lawrence Livermore National Laboratory, Livermore
Los Alamos National Laboratory, Los Alamos
University of California at Los Angeles, Los Angeles
Texas Tech University, Lubbock
University of Wisconsin, Madison
University of Minnesota, Minneapolis
University of Notre Dame, Notre Dame
California Institute of Technology, Pasadena
Carnegie Mellon University, Pittsburgh
Princeton University, Princeton
University of Texas at Dallas, Richardson
University of California, Riverside
University of Rochester, Rochester
State University of New York, Stony Brook
Florida State University - HEPG, Tallahassee
Florida State University - SCRI, Tallahassee
University of Alabama, Tuscaloosa
University of Mississippi, Oxford
Brookhaven National Laboratory, Upton
Purdue University - Task D, West Lafayette
Purdue University - Task G, West Lafayette

Uzbekistan

Institute of Nuclear Physics of the Uzbekistan Academy of Sciences, Ulugbek, Tashkent

Table of Contents

- 1. INTRODUCTION**
- 2. Requirements for Physics**
 - 2.1 INTRODUCTION
 - 2.2 THE CHOICE OF THE FIELD CONFIGURATION AND PARAMETERS
 - 2.3 THE BENEFITS OF A MAGNETIC FIELD OF 4T
 - 2.3.1 Muon momentum resolution and trigger
 - 2.3.2 Inner tracking and momentum resolution
 - 2.3.3 Electromagnetic calorimetry
 - 2.4 CONCLUSIONS
- 3. The CMS Magnet Project**
 - 3.1 INTRODUCTION
 - 3.2 THE MAGNETIC YOKE
 - 3.3 THE BARREL YOKE
 - 3.4 THE END CAP YOKE
 - 3.5 VACUUM TANK
 - 3.6 SUPERCONDUCTING COIL SYSTEM
 - 3.6.1 The superconducting Coil
 - 3.6.2 The Superconducting Conductor
 - 3.6.3 Ancillaries for the Superconducting Coil
 - 3.6.4 The external cryogenics
 - 3.6.5 Power Supply
 - 3.6.6 Process Control
 - 3.7 EXPERIMENTAL AREA
 - 3.7.1 Surface buildings
 - 3.7.2 Underground area
- 4. Interface with other detectors**
 - 4.1 INTRODUCTION
 - 4.2 INTEGRATION OF SUB-DETECTORS
 - 4.2.1 Magnet
 - 4.2.2 Muon System
 - 4.2.3 Hadron Calorimeter
 - 4.2.4 Electromagnetic Calorimeter
 - 4.2.5 Tracker and Beam Pipe
 - 4.2.6 Forward Calorimeter
 - 4.3. CABLING AND SERVICES
 - 4.4. ACCESS AND MAINTENANCE OF SUB-DETECTORS
- 5. Parameters**
 - 5.1 INTRODUCTION
 - 5.2 ACCESS TO PARAMETER BOOK

6. MAGNETIC ANALYSIS

- 6.1. Geometry of the iron yoke
- 6.2. Magnetic model and inputs
- 6.3. Field map and forces generated
- 6.4. Field at the detectors and field mapping strategy
- 6.5. Field at the winding and forces exerted
- 6.6. Stray field
- 6.7. 3D-Finite Element calculations

7. The Barrel Yoke

7.1 STRUCTURAL ANALYSIS OF BARREL YOKE

- 7.1.1 Dimensions and loads
- 7.1.2 Material properties and allowable stresses
- 7.1.3 FEA model for central barrel
- 7.1.4 FEA Results for the central barrel
- 7.1.5 FEA Results for the outer barrels
- 7.1.6 Barrel Materials
- 7.1.7 Axial forces on barrel rings

7.2 FERRIS WHEEL

- 7.2.1 Assembly principle
- 7.2.2 Doweling and machining of z-stop surfaces

7.3 SUMMARY

8. End-Cap Yoke

8.1 STRUCTURAL ANALYSIS

- 8.1.1 Purpose
- 8.1.2 The Model
- 8.1.3 Model Results

8.2 ENDCAP YOKE CONSTRUCTION

- 8.2.1 Design Criteria
- 8.2.2 Endcap Yoke Components
- 8.2.3 Overall Disk Tolerances
- 8.2.4 Design Options
- 8.2.5 Mechanically Joined Option
- 8.2.6 Joint Alternatives
- 8.2.7 Joint Preload
- 8.2.8 Center Ring Connection
- 8.2.9 Center Ring Loading
- 8.2.10 Center Ring Stress Analysis
- 8.2.11 Pin Stress Analysis
- 8.2.12 Sector Connection
- 8.2.13 Tie Rods
- 8.2.14 Disk Material
- 8.2.15 Fabrication
- 8.2.16 Assembly
- 8.2.17 Endcap Calorimeter Connection

8.3 SUPPORT SYSTEM

- 8.3.1 Stability
- 8.3.2 Cart Design
- 8.3.3 Operation

9. Vacuum Tank

9.1 STRUCTURAL ANALYSIS OF THE VACUUM TANK

- 9.1.1 Introduction
- 9.1.2 Material properties and allowable stresses
- 9.1.3 Dimensions and loads
- 9.1.4 FEA Models and Results

9.2 CONSTRUCTION CONCEPT

- 9.2.1 Transportable components
- 9.2.2 Manufacture of the outer shell
- 9.2.3 Manufacture of the outer shell end-sections
- 9.2.4 Manufacture of the inner shell
- 9.2.5 Trial Assembly
- 9.2.6 Transport

9.3 FINAL ASSEMBLY

- 9.3.1 Reconstruction of the shells on the CERN Site
- 9.3.2 Closing of the Vacuum Tank

10. Pre-industrialisation and test for the yoke construction

- 10.1 HIGH PRESSURE AIR PAD MOVING SYSTEM
- 10.2 DRILLING OF DOWEL HOLES
- 10.3 ASSEMBLY TECHNIQUES

11. Design concept of the cold mass

- 11.1 DESIGN CONSIDERATIONS
- 11.2 COLD MASS DESCRIPTION
- 11.3 THE CURRENT AND THE CURRENT DENSITY
- 11.4 SELF SUPPORTING WINDING STRUCTURE
- 11.5 NUMBER OF LAYERS
- 11.6 PURE ALUMINIUM BEHAVIOUR
 - 11.6.1 Structural function
 - 11.6.2 Electrical effect of the cyclic plastic strain

12. Conductor

- 12.1 INTRODUCTION
- 12.2 THE CMS CONDUCTOR
 - 12.2.1 Conductor overall characteristics
- 12.3 MECHANICAL CONSIDERATION
- 12.4 CONDUCTOR COMPONENTS
 - 12.4.1 SC Wire
 - 12.4.2 Rutherford type cable
 - 12.4.3 Insert
 - 12.4.4 Mechanical Reinforcement
 - 12.4.5 Conductor joints
- 12.5 RECENT PROGRESS IN ALUMINIUM STABILISED CONDUCTOR PRODUCTION

13. Insulation

- 13.1 INTRODUCTION
- 13.2 TECHNICAL REQUIREMENTS
- 13.3 INSULATION PROCESS
- 13.4 DRAWBACKS OF ALTERNATIVE METHODS
 - 13.4.1 Alternative impregnation processes
 - 13.4.2 Alternative Curing processes
- 13.5 MATERIAL SELECTION
- 13.6 QUALIFICATION OF THE PROCESS

14. Coil Mechanical Analysis

- 14.1 MAGNETIC FEA
 - 14.1.1 The magnetic FE model
 - 14.1.2 Magnetic FEA results
- 14.2 STRESS FEA
 - 14.2.1 Material properties
 - 14.2.2 The mechanical FE model
 - 14.2.3 Stress FEA results
- 14.3 CONCLUSIONS

15. Stability and thermal analysis

- 15.1 INTRODUCTORY CONSIDERATIONS
- 15.2 ENTHALPY MARGIN
- 15.3 TRANSIENT ANALYSIS. LOCALISED DISTURBANCES
- 15.4 POSSIBLE DISTURBANCE SOURCES
- 15.5 COMPARISON WITH LARGE RUNNING COILS
- 15.6 CONCLUSIONS

16. Quench analysis

- 16.1 INTRODUCTION
- 16.2 QUENCH BACK PROTECTION
 - 16.2.1 Quench back typical results
 - 16.2.2 Comparison of the methods
 - 16.2.3 Quench back process
 - 16.2.4 Influence of parameters
- 16.3 PROTECTION SYSTEM FAILURE
 - 16.3.1 Quench propagation typical results
 - 16.3.2 Influence of parameters
- 16.4 INDUCED FORCES DURING DISCHARGES

17. Coil cooling and insulation

- 17.1 INTRODUCTION
- 17.2 CRYOGENIC LOADS
 - 17.2.1 Radiation heat flux
 - 17.2.2 Cryogenic coil Supports
- 17.3 CRYOGENIC LOAD AT LIQUID HELIUM TEMPERATURE
 - 17.3.1 Thermal shield cryogenic load
- 17.4 INTERNAL COOLING CIRCUITS

- 17.4.1 Thermal shield system
- 17.4.2 Thermosiphon circuit

17.5 COIL TEMPERATURE DISTRIBUTION

17.6 CRYOGENIC SEQUENCES

18. Support system

- 18.1 INTRODUCTION
- 18.2 DESCRIPTION
- 18.3 LOADS AND DEFORMATIONS
 - 18.3.1 Mechanical loads
 - 18.3.2 Coil Shrinking and deformation under field
- 18.4 REQUIREMENTS
- 18.5 LONGITUDINAL TIE RODS
- 18.6 RADIAL BELTS
- 18.7 INDUCED STRESSES ON THE COIL
- 18.8 ADJUSTMENT PROCEDURE

19. coil manufacturing and assembly

- 19.1 INTRODUCTION
- 19.2. DESCRIPTION OF THE WINDING MACHINE
 - 19.2.1 Winding Machine principle
 - 19.2.2 Winding Mandrel
 - 19.2.3 Applying the winding tension on the conductor
 - 19.2.4 Positioning the conductor
 - 19.2.5 Controlling the filling factor
 - 19.2.6 Insulating the conductor
- 19.3. DESCRIPTION OF THE WINDING PROCESS
 - 19.3.1 Winding of the layers
 - 19.3.2 Applying the inter-layer insulation
 - 19.3.3 Curing of a layer
 - 19.3.4 Making the layer to layer junctions
 - 19.3.5 Making lead ends and locking the winding
 - 19.3.6 Laying down the longitudinal thermal drains
 - 19.3.7 Winding of the quench-back cylinder
 - 19.3.8 Adding the radial belts and cooling circuits
 - 19.3.9 Final curing of the whole coil
- 19.4 COMPLETION OF THE COLD MASS
 - 19.4.1 Wrapping the pure aluminium film
 - 19.4.2 Mounting the solenoid equipment and the thermal shields
 - 19.4.3 Swivelling the coil to the horizontal position
- 19.5 COMPLETION OF THE SOLENOID
 - 19.5.1 Wrapping of the superinsulation around the thermal shield
 - 19.5.2 Insertion of the solenoid inside the vacuum vessel
 - 19.5.3 Completion of the ground insulation
 - 19.5.4 Re-constructing the inner vacuum vessel
 - 19.5.5 Mounting the thermal shield and the superinsulation
 - 19.5.6 Completing the vacuum vessel

19.5.7 Completing the cold mass and closing the vacuum vessel

20. Electrical circuit and Power supply

20.1 INTRODUCTION

20.1.1 General description

20.1.2 Protection concept

20.2 ELECTRICAL COMPONENTS

20.2.1 DC Power Supply

20.2.2 Breakers CP

20.2.3 Dump resistor and breakers CR

20.2.4 Grounding circuit

20.2.5 Electrical lines

20.2.6 Current leads

20.3 DISCHARGE MODES

20.4 SAFETY VS FAULTS

20.4.1 Fault interlocks

20.4.2 Fault repertory

20.5 SURFACE MAGNET TESTS

21. Cryogenic Plant

21.1 REFRIGERATION PLANT

21.1.1 Compressors, helium gas and liquid nitrogen storage

21.1.2 Cold Box, transfer lines and 5000 l liquid helium cryostat

21.2 CRYOGENIC FLOW-SHEET AND PROCESS

21.2.1 Cooling-down phase from 300 K to 100 K

21.2.2 Final cooling-down phase from 100 K to 4.5 K

21.2.3 Normal operation at 4.5 K

21.2.4 Operation at 4.5 K..

21.2.5 Fast energy dump

21.2.6 Warming-up of the magnet

21.3 VACUUM INSULATION OF THE MAGNET

21.4 CRYOGENIC PLANT FOR THE SURFACE TEST OF THE MAGNET

21.5 INSTALLATION

21.6 TIMETABLE FOR THE CRYOGENIC EQUIPMENT

22. Process control and protection

22.1 PRINCIPLES

22.2 INSTRUMENTATION

22.3 CONTROL SYSTEM

22.3.1 The PLC's

22.3.2 The fieldbus

22.3.3 The supervisor network

22.4 MAGNET PROTECTION (MSS)

22.4.1 Principles

22.4.2 Protection actions

22.4.3 Safety system reliability

22.4.4 Magnet Safety Interlocks

22.5 INTERFACES

23. Conductor characterization and pre-industrialization

23.1 INTRODUCTION

23.2 MANUFACTURING SAMPLES

23.3 TESTS AND MEASUREMENTS TO ENSURE CONDUCTOR QUALITY

23.3.1 SC strands

23.3.2 Rutherford type cable

23.3.3 Mechanical bonding at the SC cable/Al interface

23.3.4 Bending tests

23.3.5 Macro and micro photography, electrons micro probe analysis

23.3.6 Ultrasonic testing

23.3.7 Measurement of the residual resistivity ratio (RRR)

23.3.8 Ic measurements on single strands after extrusion

23.3.9 Ic and MQE measurements on the full conductor

23.3.10 Final conductor characterisation in the SULTAN test facility

23.3.11 Further facilities for conductor characterisation in NHMFL

23.4 RUNNING AND PLANNED R&D ACTIVITIES FOR CONTROL METHODS

23.4.1 RRR measurements under cyclic strain

23.4.2 Ultrasonic Testing of Aluminium Stabilised High-Current Superconducting Cables

23.4.3 Eddy current testing

23.5 DEVELOPMENTS FOR FIXING THE REINFORCEMENT

23.5.1 EB welding

23.5.2 Continuous soft soldering of aluminium

23.6 JOINTS

23.6.1 Joining the insert

23.6.2 Joining the reinforced conductor

23.7 PRE-INDUSTRIALISATION

24. PRE-INDUSTRIALISATION OF THE WINDING AND POLYMERISATION TECHNIQUES

24.1. Introduction

24.2. Main activities

24.3. Bending

24.4. Characterisation of the insulation

24.5. Quench Back cylinder winding and welding tests

24.6. Full diameter short winding model

24.7. Solenoid winding PROTOTYPE

25. Experimental Area

25.1 INTRODUCTION

25.2 SURFACE BUILDINGS

25.2.1 Building Dimensions

25.2.2 Environmental Impact

25.3 UNDERGROUND AREAS

25.3.1 General Considerations

25.3.2 Layout of the Underground Caverns

25.3.3 Main Cavern Infrastructure

- 25.3.4 Auxiliary Cavern
- 25.4 CONSTRUCTION PLANNING
- 25.5 SAFETY
- 25.6 OTHER SURFACE FACILITIES
- 25.7 CONCLUSIONS
- 26. General Assembly and Planning**
 - 26.1 EXPERIMENTAL AREA REQUIREMENTS
 - 26.1.1 Requirement for Surface Buildings
 - 26.1.2 Requirement for Underground Area
 - 26.2 ASSEMBLY ON THE SURFACE
 - 26.3 PLANNING
- 27. Quality assurance**
 - 27.1 INTRODUCTION
 - 27.2 THE QUALITY ASSURANCE PLAN (QAP)
 - 27.3 LEVEL A - INTRODUCTORY INFORMATION
 - 27.4 LEVEL B - QUALITY ASSURANCE MANAGEMENT
 - 27.4.1 Breakdown structures
 - 27.4.2 Configuration Management and Change Control
 - 27.5 LEVEL C - QUALITY DURING PROCESSES
 - 27.6 LEVEL D - QUALITY RESULT MANUAL
 - 27.7 QUALITY CONTROL
- 28. Safety OF THE MAGNET**
 - 28.1 GENERAL PRINCIPLES
 - 28.2 DESIGN PROBLEMS RELATED TO SAFETY
 - 28.3 MECHANICAL SAFETY AND DESIGN STANDARDS
 - 28.4 SAFETY SYSTEM FOR EXPLOITATION
- 29. RADIATION ENVIRONMENT AND SHIELDING**
 - 29.1 RADIATION AND SHIELDING IN THE UNDERGROUND AREA
 - 29.2 THE MAIN SHIELDING PLUG ON TOP OF PX 56
- 30. MANAGEMENT OF THE PROJECT**
 - 30.1 INTRODUCTION
 - 30.2 ORGANISATION
 - 30.2.1 The Magnet Technical Board
 - 30.2.2 Technical Working Group
 - 30.2.3 Co-operation Protocol with CEA Saclay
 - 30.3 PARTICIPATING LABORATORIES
 - 30.3.1 Collaboration with the University of Wisconsin
 - 30.3.2 Collaboration with ITEP Moscow
 - 30.3.3 Collaboration with Fermi National Accelerator Laboratory (FNAL)
 - 30.3.4 Collaboration with ETH Zürich and EMPA
 - 30.3.5 Collaboration with INFN Genoa
 - 30.3.6 Collaboration with NHMFL
 - 31. Cost estimate and Procurements

31.1 COST ESTIMATE

31.2 PROCUREMENT

 31.2.1 Procedures

 31.2.2 Initial Large Procurements

32. References

1. INTRODUCTION

1.1 STRUCTURE OF THE TDR BOOKLET

This Technical Design Report booklet, which is organised in four sections, covers the complete magnet project – yoke, coil, and ancillaries – and also comprises chapters presenting the magnet project in its relation to the CMS experiment, including the experimental area.

The first section, Chap. 1 to 6, contains introductory and general chapters, commencing with this chapter and followed by physics requirements in Chap. 2, general introduction to the project in Chap. 3, interface with the subdetectors in Chap. 4, parameter book in Chap. 5, and the magnetic analysis in Chap. 6.

The second section, Chap. 7 to 10, covers the yoke and the vacuum tank (which in CMS is a structural element closely related to the barrel yoke). The barrel yoke is described in Chap. 7, the endcap yokes in Chap. 8, the vacuum tank in Chap. 9, and the pre-industrialisation for the yoke in Chap. 10.

The third section, Chap. 11 to 24, describes the coil and ancillaries, the first part covering the coil proper from Chap. 11 to 19, the second part coil ancillaries, and the third part the pre-industrialisation plans for the conductor and winding process in Chap. 23 and 24.

The final section, Chap. 25 to 32, covers the experimental area, assembly and planning, quality assurance and safety. Project management and costing are also discussed, and all references are collected in chapter 32.

Perhaps less convenient for the reader, all coloured pictures have been regrouped at the end of the booklet to reduce printing costs. Each figure is not only referred to by its number, in the form of Fig. xx, but also by the page of the colour section on which it appears, in the form of p. C-xx.

1.2 STATUS OF THE MAGNET PROJECT

The design of the coil has evolved since the reference design, prepared by the Saclay team, was presented in the CMS Technical Proposal [1-1].

The two main features which have changed are:

- the choice of winding the full length coil on site, instead of winding it in four parts,
- the assembly of the composite conductor by electron beam welding, starting from an extruded insert.

The design was presented on 7 and 8 October 1996 to a Preliminary Design Review Committee, which regrouped a number of experts from outside the CMS magnet team, to review the state of advancement of the studies, and to give advice where appropriate.

The Committee recognised that [1-2]:

- the coil in a single module, as is currently proposed, has a simpler structure, and probably poses fewer compatibility and matching problems as compared to the previous four module reference design,
- the use of a reinforced conductor eliminating the necessity of a support cylinder also appears to be a good choice,

and it approved the idea to wind “on site”, now that the coil is to be wound as a single item.

Nevertheless, the Committee addressed a list of questions on subjects needing further clarification such as:

- winding pack configuration (number of layers and turns),
- conductor geometry,
- insulation,

and requested to have a clear definition of the maximum operating field.

Following the PDR, the design team initiated an extensive review of the project in the light of the remarks and suggestions made by the Committee. Most of the technical choices have been confirmed. However, the mechanical structure of the winding has been improved, and, as the conductor *is* the mechanical structure, this implied also a change in the conductor geometry, leading to the “block” design. The new conductor geometry has the added advantage of being particularly well adapted to the use of electron beam welding, which has been retained as the base technique for fixing the reinforcement.

A brief summary of the present project situation, highlighting answers to points of concern raised by the Committee, is given below.

1.2.1 Coil

One important feature of the project is the high nominal field of 4 T. This parameter, which is central to the design, comes from physics requirements (Chap. 2), and the CMS Collaboration governing bodies have recently reconfirmed that to reach 4 T was a desirable goal to maximise the physics performance of CMS.

All safety factors and parameters are computed accordingly for 4 T, however, the limited radial space given to the coil has imposed, from the beginning, a ‘leading edge’ design in which some parameters are beyond what can be considered today as state of the art. In particular, the hoop strain reaches the high value of 0.15%. Although great care has been taken in the design to make sure that this strain does not induce large shear stresses in the insulation, possible effects, on the stability for example, may limit the operational field to a value slightly below 4 T. This fact has been fully recognised and accepted by the CMS Collaboration (Chap. 2).

Indeed, the basic design of the CMS coil has been oriented from the very beginning to maximise the chances of reaching 4 T (Chap. 11). The main innovative feature is to connect the conductor directly to the reinforcement, thus resisting the force where it is created. This allows suppression of the thick external cylinder and all mechanical analyses show that the induced shear stresses are very small. In fact, the shear stress distribution in the insulation is practically driven by the cool down differential contraction, and is essentially independent of the field (Chap. 14). Thus the CMS coil stability level at 4 T should be very similar to the level of stability of the ALEPH and DELPHI coils (Chap. 15).

It is considered vital that the pure aluminium, which will undergo cycles in the plastic range, be supported constantly by nearby elastic components. This is achieved in the “block” conductor design whereby two reinforcement sections are welded, by electron beam, on a conventional insert obtained by the co-extrusion process (Chap. 12 and 23). These two reinforcement sections act, at the same time, as hoop and axial elastic components for the winding structure.

Another important element for the final quality of the coil, apart from the conductor itself, is the quality of the winding and impregnation process. The choice of four layers as the

optimum winding configuration has been confirmed. The present design, which calls for a monolithic four layer coil to be wound “on site” at CERN (Chap. 19 and 24), appears well adapted to a magnet of this size. It does not need any large mechanical structures (flanges, containment cylinder, etc.) as normally used in existing aluminium stabilised thin solenoids. In this way, mechanical coupling problems are avoided whilst minimising the shear stress in the insulation.

The finished coil is a 220-tonne monolithic object and clearly the associated risks must be analysed and minimised. These risks are well identified as they are mainly associated with electrical insulation and joints, and the pre-industrialisation programmes must fully take this fact into account. Nevertheless, other solutions, such as co-winding or the building of the coil in sections, have been or are still being looked at, to ascertain that the present choice is the correct one.

The selected insulation technique makes full use, as a starting point, of the developments carried out at RAL for the DELPHI and H1 coils (Chap. 13). Alternative insulation materials with improved mechanical properties (e.g. glass/polyimide composite as developed recently at KEK) are actively being considered, and the final choice will be a part of the pre-industrialisation programme for the winding.

Ancillaries such as cryogenics, power supply, process control, etc., are now well defined and detailed specification work can proceed.

In conclusion, the design of the coil has now reached a state of complete coherence, including manufacture, assembly and ancillaries, which allows well defined full pre-industrialisation programs to start as initial actions of the construction phase.

1.2.2 Yoke

The design of the barrel yoke, including assembly tools, is complete (Chap. 7). The recent market survey, and related visits to firms, has confirmed that this project is within the possibilities of industry, and the order could be placed towards the end of 1997.

The high magnetic field has a direct impact in terms of forces on the two endcap yokes and this call for 600 mm thick plates for the first and second disks. Assembly by electroslag welding was envisaged initially but has since been abandoned. The present design, which now uses a fully mechanical fixation, allows a precise trial assembly at the factory. Design is being finalised to allow a call for tenders before the end of 1997 (Chap. 8). The design of the supporting cart system for the endcap disks is also near completion.

Assembly and maintenance of CMS calls for a simple and reliable displacement system in both the surface hall and the underground area, to allow displacement of large and heavy sections of the magnet. High pressure air pads have been chosen for both the barrel and the two endcap yokes (Chap. 10), and this will greatly simplify logistics problems.

All the basic choices pertaining to the magnet have been made, allowing the completion of the experimental area design within timescale (Chap. 25), and allowing to proceed with the civil engineering call for tender.

[1-2] Report on the CMS Magnet Review held at CERN on October 7th-8th 1996,
Preliminary Design Review Committee. Chairman, T. Taylor, CERN. Members: E. Baynham,
Rutherford Appleton Laboratory, L. Bottura, CERN, H. Desportes, CEA-Saclay, M. Huguet,
ITER, P. Komarek, Forchungszentrum, Karlsruhe, D. Leroy, CERN, W. Maurer,
Forchungszentrum, Karlsruhe, R Parodi, INFN-Genova, H. Schneider-Muntau, National High
Magnetic Field Laboratory, Tallahassee, H. ten Kate, CERN, B. Turk, CEA-Cadarache, A.
Yamamoto, KEK.

2. REQUIREMENTS FOR PHYSICS

2.1 INTRODUCTION

The primary aim of the Compact Muon Solenoid Collaboration is to discover new physics underlying the breakdown of electroweak symmetry. Several theoretical possibilities exist though the Higgs mechanism in the context of Supersymmetry is the favoured one. Many diverse experimental signatures from the new physics are possible involving high transverse energy muons, electrons, photons and jets. In order to cleanly detect these signatures the identification and precise energy measurement of muons, electrons, photons and jets over a large energy range and at high luminosities is essential.

CMS is a general purpose proton-proton detector designed to run at the highest luminosity ($L > 10^{34} \text{ cm}^{-2} \text{ s}^{-1}$) at the LHC. The design has been optimised for the search of the Standard Model Higgs boson over a mass range 80 GeV - 1 TeV but it will also allow the detection of a wide range of possible signatures from alternative electro-weak symmetry breaking mechanisms. Although high luminosity is essential to cover the entire range of mechanisms of electro-weak symmetry breaking the LHC machine will start at significantly lower luminosities ($L \leq 10^{33} \text{ cm}^{-2} \text{ s}^{-1}$) for which the CMS detector is also well adapted. Such studies of importance are CP violation in the B system and top quark studies. Another goal of CMS is to carry out specific studies of quark-gluon plasma (QGP) formation. One of the cleanest signatures of QGP formation will be the observation of anomalies in the production rates of heavy quark bound states J/ψ , ψ' , and within the Υ family.

The main design goals of CMS are:

- i) a highly performant muon system,
- ii) the best possible electromagnetic calorimeter consistent with (i),
- iii) a high quality central tracking to achieve (i) and (ii),
- iv) a hadron calorimetry with sufficient energy resolution and good hermiticity,
- v) a detector costing less than 475 MCHF.

These goals are fulfilled by the CMS detector (see Fig. 1.1, p. C-1) whose distinctive features include a high solenoidal magnetic field (4 T) coupled with a multilayer muon system, a fully active scintillating crystal electromagnetic calorimeter and a powerful inner tracking system based on fine-grained microstrip and pixel detectors. These features allow a very good measurement of the energies of muons, electrons, other charged particles and photons, typically with a precision of about 1% at 100 GeV. Such a high precision leads to excellent mass resolution for states such as intermediate mass Higgs bosons, Z' , B mesons in proton-proton collisions or Υ states in heavy ion collisions. CMS is a compact and powerful spectrometer that is well matched to the physics potential of the LHC ranging from the elucidation of the electroweak symmetry breaking (search for the Higgs boson and supersymmetry), the study of CP violation, search for the signatures of the onset of quark-gluon plasma etc. Furthermore the use of a crystal calorimeter and pixel detectors considerably enhances the potential for discovery in CMS at the initially lower luminosities.

2.2 THE CHOICE OF THE FIELD CONFIGURATION AND PARAMETERS

The single most important aspect of the overall detector design is the configuration and parameters of the magnetic field for the measurement of muon momenta. The requirement for a good momentum resolution, without making stringent demands on the spatial resolution and the alignment of muon chambers, and keeping a compact spectrometer, leads naturally to

the choice of a high magnetic field.

We have considered both toroidal and solenoidal fields. A solenoid is preferred for the following reasons:

- a) with the field parallel to the beams, the bending of the muon track is in the transverse plane (see Fig. 2.2, p. C-2). In this plane the small transverse dimensions of the beams determines the transverse position of the vertex to an accuracy of better than 20 mm. The strong bending in the transverse plane facilitates the task of triggers based on tracks pointing back to the vertex.
- b) momentum measurement in a solenoid starts at $r = 0$, while for a toroid it starts after the absorber, typically at $r > 4$ m. For a similar bending power the overall size of a solenoidal system is smaller than that for a toroid.

A long superconducting solenoid ($L = 13$ m) has been chosen with a free inner diameter of 5.9 m and a uniform magnetic field of 4 T. The favourable dimensional ratio (length/radius) of the solenoid and the high field allow efficient muon detection and measurement up to a pseudorapidity (η) of 2.4 (see Fig. 2.3, p. C-3). The muon spectrometer then consists of a single magnet allowing for a simpler architecture for the detector. The inner coil radius is large enough to accommodate the inner tracker and the calorimeters. The magnetic flux is returned via a 1.5 m thick saturated iron yoke instrumented with four stations of muon chambers. The yoke is thick enough to allow safe identification and powerful trigger on muons.

2.3 THE BENEFITS OF A MAGNETIC FIELD OF 4T

A high magnetic field is mandatory for a compact detector based on a single and long solenoid detector. A field of 4 T brings substantial benefits not only for the muon tracking and inner tracking but also for electromagnetic calorimetry. To illustrate this we shall compare the performances between two field choices, 4 T and 3 T.

2.3.1 Muon momentum resolution and trigger

One of the main arguments in favour of a strong magnetic field is to enable an efficient first level trigger.

Efficient triggering on muons is a difficult task in hadron colliders. So far all hadron collider experiments triggering on muons have had to make substantial improvements after initial data taking. From the outset the CMS philosophy has been to optimise a design which assures a powerful trigger without compromising the performance of other parts of the detector. The goal is to achieve sharp trigger thresholds in order to keep first level trigger rate low and hence avoid a hardwired 2nd level trigger. At a muon p_t threshold of 20 GeV the muon trigger rate almost doubles going up from 6 kHz to about 10 kHz when the magnetic field goes down from 4 T to 3 T (see Fig. 2.1).

The robustness of the CMS muon trigger relies on two independent measurements. The first and the more precise one relies on the measurement of the direction of the muon in the first muon station in the transverse plane. Lowering the field would require a corresponding improvement in the spatial accuracy in the muon chambers. The second one uses the measurements in all four muon stations. This takes on great significance when the first muon station is spoiled which happens for about a quarter of the muons. The magnetic flux generated by a 4 T central field is sufficient to saturate 1.50 m of iron in the return yoke. For

a 3 T field, the bending power is reduced by 25% and only around 1.1 m of iron can be saturated. Four muon stations are required for a muon system that is robust, redundant and provides full geometric acceptance. Installation of four muon stations in a reduced thickness of 1.1 m is not optimal. At 3 T these factors lead to a system that is too marginal to be acceptable in light of the difficulties encountered by all the hadron collider experiments so far.

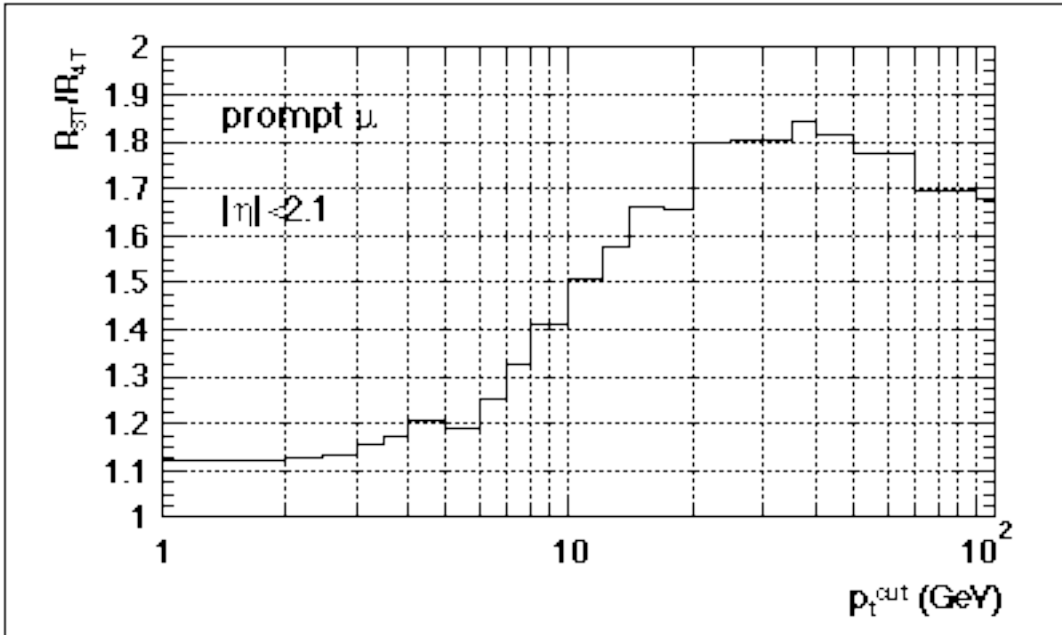


Fig. 2.1: The ratio of trigger rates for single muons for fields of 3T and 4T.

2.3.2 Inner tracking and momentum resolution

Reducing the field from 4 to 3 T will lead to a corresponding deterioration of the momentum resolution. The mass resolutions for multi charged particle states are given in Table 2.1. For a signal of a given significance, involving such states, the percentage additional running time required increase by one third when the field is lowered to 3 T from 4 T.

Table 2.1
Mass Resolution for various states at 4 and 3 T.

State	Mass Resolution at 4 T	Mass Resolution at 3 T
H _{SUSY} (300 GeV) ® ZZ ® 4m	2.1 GeV	2.8 GeV
H _{SM} (150 GeV) ® ZZ* ® 4m	0.8 GeV	1.1 GeV
B _d ⁰ ® p p	27 MeV	36 MeV
Y ® mm	36 MeV	48 MeV

When changing from 4 T to 3 T the occupancy increases in the inner tracker by about 40% in the outermost regions of the barrel region and by about 25% in the outer parts of the forward disks. In contrast, it decreases by about 20% in the innermost areas like the Si barrel.

The outer regions play an essential role for muon track reconstruction in heavy ion running. The difference is expected to be even larger in heavy ion running as the mean p_t is expected to be smaller and hence more tracks are expected not to reach the outer regions for a field of 4 T. This considerably improves the pattern recognition capability and the muon track reconstruction efficiency. In fact the strip length of the MSGCs has recently been reduced from 25 cm to 12.5 cm precisely to halve the occupancy to enable good muon track reconstruction efficiency for heavy ion running.

2.3.3 Electromagnetic calorimetry

Maximum benefit from a crystal electromagnetic calorimeter can only be derived if it can be calibrated to an accuracy of a fraction of a percent. This is possible by using copiously produced isolated electrons from the production of Ws, Zs and b-quarks. The energy of electrons measured in the calorimeter can be compared with their momenta measured in the tracker. The number of electrons required is proportional to the square of the standard deviation of the quantity energy/momenta. Optimally both the inner tracking momentum and the electromagnetic calorimeter energy resolutions should be comparable in the relevant range of the energy of electrons. At present this indeed is the case and the two resolutions are evenly matched. Lowering the field to 3 T will make the inner tracking resolution the limiting one and the number of electrons required for a given accuracy of calibration will increase by up to 50%. The period for a calibration with sufficient precision will typically be of the order of a month at the lower luminosity of $L \sim 10^{33} \text{ cm}^{-2} \text{ s}^{-1}$.

One of the features of the large magnetic field is the trapping of charged particles inside the tracking cavity. The flux of charged particles reaching the ECAL is therefore reduced. The charged particle transverse energy density for different values of field and pseudorapidity are given in Table 2.2. The reduction with increasing field is significant.

Table 2.2

Charged particle energy density/minimum bias event/ m^2 in the electromagnetic calorimeter.

Magnetic Field	Mean Transverse Energy Density (GeV/m^2)		
	Barrel		Endcap
	$ h = 0$	$ h = 1.5$	$ h = 2.4$
0 T	0.5	0.55	1.3
2 T	0.3	0.25	0.7
4 T	0.15	0.1	0.4

2.4 CONCLUSIONS

Lowering the magnetic field in CMS to 3 T or below would result in a permanent reduction of the physics performance. Safety margins in the inner tracking, for the overall momentum resolution, effective mass resolution, calorimeter energy pileup and especially for the muon trigger are eroded. There is an overwhelming consensus in the Collaboration that a field substantially higher than 3 T is central to the concept of CMS. In designing a coil of 4 T it is understood that a field of at least 3.5 T will be guaranteed.

3. THE CMS MAGNET PROJECT

3.1 INTRODUCTION

This chapter gives a general overview of the project and provides familiarity with the current naming of major items and activities, and, for the benefit of those who don't require much technical detail, summarises the following chapters.

The magnet for the CMS detector is the major element of the CMS experiment in terms of size, weight and structural rigidity; for this reason it is used as the principal support structure for all the other detectors.

The magnetic yoke contains the muon chambers while the barrel part of the hadron calorimeter, HB, of the electromagnetic calorimeter EB, and the Tracker are situated inside, and supported from, the inner shell of the vacuum tank, (Chapt. 4).

The infrastructure project of the experimental cavern is largely influenced by the role of the CMS magnet's support structure. By the heading "Magnet Project" we refer to all the activities related to the design, construction and commissioning of the:

- magnet Yoke (Barrel + End Cap) and Vacuum Tank,
- superconducting Coil (cold mass),
- ancillaries (Cryogenics, Power supply, Process control etc.),
- installation of the magnet and definition of the conventional magnet infrastructure.

The Main Parameters of the CMS Magnet which are related to the physics requirement (see Chapt. 2) are the following:

- field: 4 Tesla,
- yoke diameter: 14 m on flats,
- axial yoke length including endcaps: 21.6 m,
- total weight including the coil: approximately 10800 tonnes.

The CMS Magnet Project is a common project of the CMS Collaboration, and as such, is financed by all participating institutes on a prorata basis with respect to their participation in CMS, through ad-hoc procedures, as explained in Chapt. 31.

A CERN based team has been formed, as part of the CMS Collaboration, to organise and co-ordinate all the activities for the Magnet Project. Teams from different institutes are also participating in defining and designing items for the project, as explained in Chapt. 30.

The master planning for the CMS detector and the experimental area construction is largely determined by the activities of the Magnet Project. The magnet will be tested at full current in the surface building SX5, around September 2003, before being lowered into the experimental cavern UXC5. This will enable CMS to be ready for LHC by July 2005, (Chapt. 26 and Fig. 26.17, p. C-67).

An open section of the CMS magnet, with the major project item names is shown in Fig. 3.1.

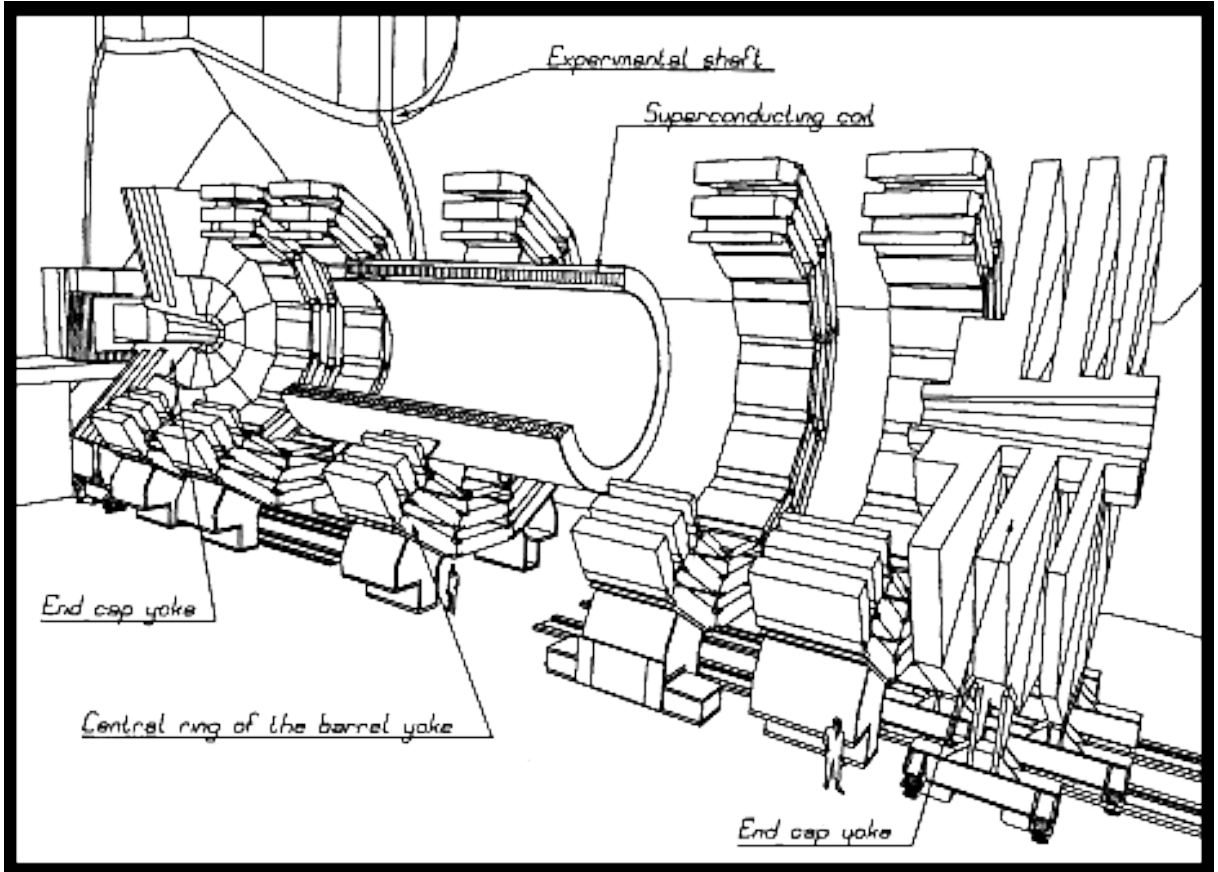


Fig. 3.1: Open view of the CMS Magnet with the major project item names.

3.2 THE MAGNETIC YOKE

The magnetic flux generated by the superconducting coil is returned via a 1.5 m thick saturated iron yoke. This yoke is designed as a 12-sided structure. A balance has been achieved between the outer diameter of the yoke and the size of the muon stations, while trying to maximise the acceptance in azimuth of the interlayer muon chambers that are interleaved between the iron plates of the yoke.

The yoke is divided into two main components:

- the barrel yoke: the cylinder surrounding the superconducting coil,
- the endcap yoke: the disks that magnetically close the barrel yoke.

The magnetic configuration is analysed in Chapt. 6.

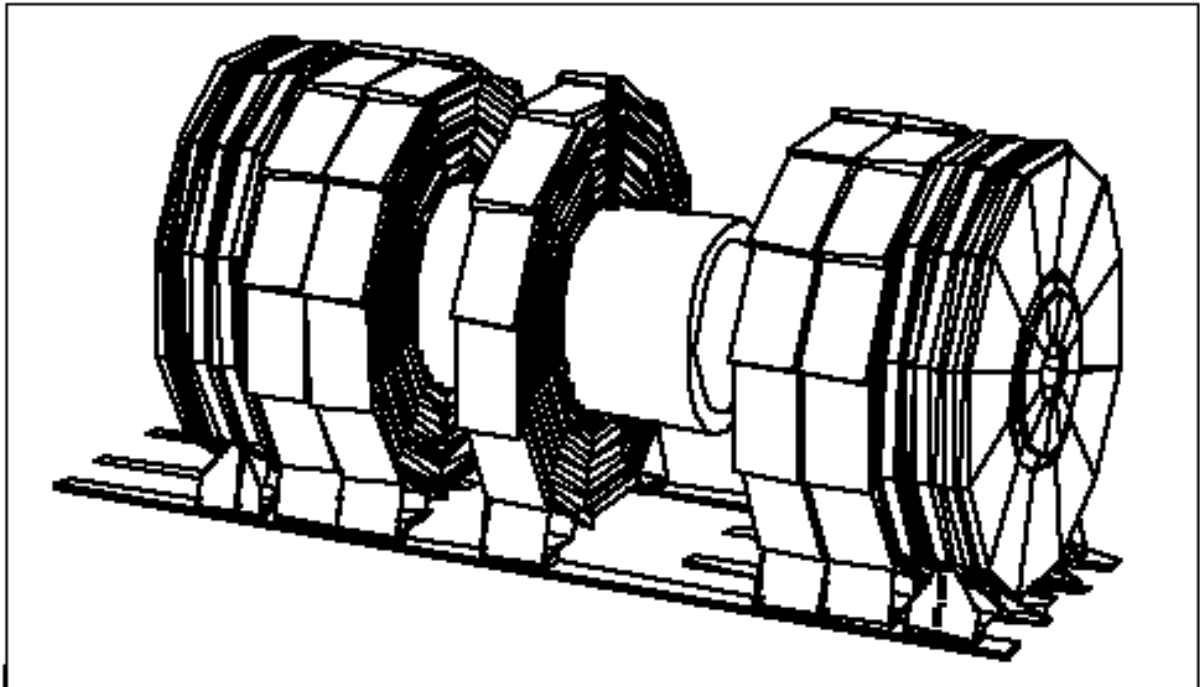


Fig. 3.2 shows an overview of the five Barrel Rings, and the two End Caps.

3.3 THE BARREL YOKE

The barrel yoke is a 12-sided structure designed at CERN. It is 11 m long, giving a total iron weight for the barrel of about 6000 tonnes, (see Chapt. 7).

The barrel yoke is subdivided along the beam axis into five rings approximately 2.5 m long. The central barrel ring, centred on the interaction point, supports the superconducting coil.

Each barrel ring is made up of three iron layers. The thickness of the inner layer is 295 mm, the middle layer and the outer layers are 630 mm. Connecting brackets join together the steel plates forming the three layers and provide the required structural rigidity.

The central barrel ring is the only stationary part around the interaction point and it is used to support the vacuum tank and the superconducting coil. The other four barrel rings and the endcap disks slide on common floor rails, running in the beam direction, to allow insertion and maintenance of the muon stations, Fig. 3.2.

From the beginning strong technical ties have been developed with ITEP/Moscow as potentially interesting manufacturing possibilities do exist in Russia. Nevertheless a world wide tender is in preparation for the procurement and trial assembly of the barrel rings.

3.4 THE END CAP YOKE

The endcap yoke is being designed at the University of Wisconsin at Madison, in connection with PSL. Wisconsin is also in charge of the integration of the forward muon chambers, these forward muon chambers being a US project inside CMS.

Each endcap is built from three independent disks which can be separated to provide access to the forward muon stations, Fig. 3.3.

Due to the axial magnetic field the two inner disks must withstand an attraction force of about 85 MN and resist the large bending moments induced. Therefore these two disks are 600 mm thick whereas the outer disk is only 250 mm thick. Each endcap weighs 2300 tonnes, (see Chapt. 8).

A world wide tender, to be managed by the Wisconsin group, is in preparation for the procurement of the end-cap disks.

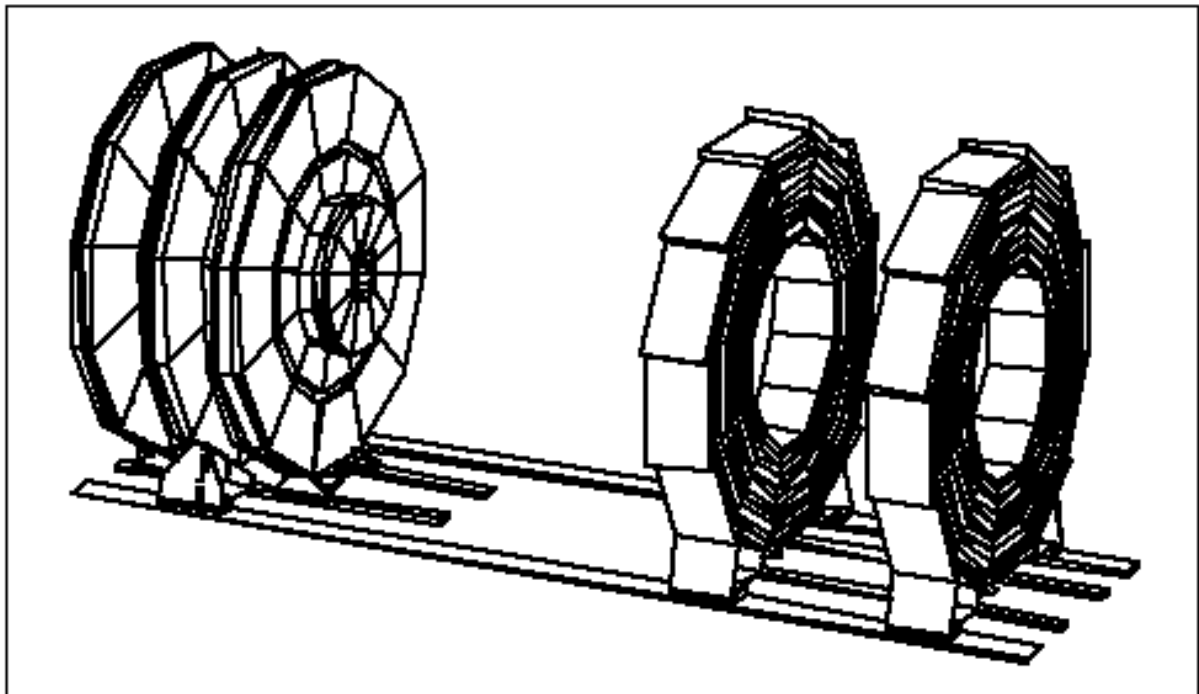


Fig. 3.3 gives a partial view of the open magnet showing three separated End Cap disks and two outer Barrel Yoke Rings.

3.5 VACUUM TANK

The vacuum tank is made of stainless steel and houses the superconducting coil.

The outer shell of the vacuum tank is attached to the inner part of the central barrel ring and the coil is symmetrically supported from it.

All the barrel sub-detectors, HB, EB and Tracker are supported by the inner shell of the vacuum tank via a system of horizontal welded rails, (see Chapt. 9).

3.6 SUPERCONDUCTING COIL SYSTEM

The superconducting coil system is defined as the coil and the ancillary subsystems required for its operation. This is the main subject of Chapt. 11 to 24.

In the following paragraph a short description will be given of the main items of the cold mass and some of the major sub-components.

3.6.1 The superconducting Coil

The conceptual design of the CMS superconducting coil is based on experience gained

by CEA/Saclay over the past fifteen years with superconducting magnets for high energy physics, in particular from the ALEPH design. This experience has been incorporated into the design together with several new features, (see Chapt. 11).

The reinforced conductor cable of the 4 layer CMS coil is capable of sustaining by itself all the induced magnetic forces.

A collaboration agreement between CERN and CEA-Saclay for the engineering of the superconducting coil up to the time of the commissioning has been agreed upon.

The engineering of the superconducting coil includes the detailed definition of the internal cryogenics, the protection system and the definition of the technical requirements for the ancillary subsystems.

Figure 3.4 shows an open view of the superconducting coil inside its vacuum tank with some of its sub-systems attached.

These items will be discussed in the following paragraphs; Table 3.1 resumes the most important parameters of the cold mass.

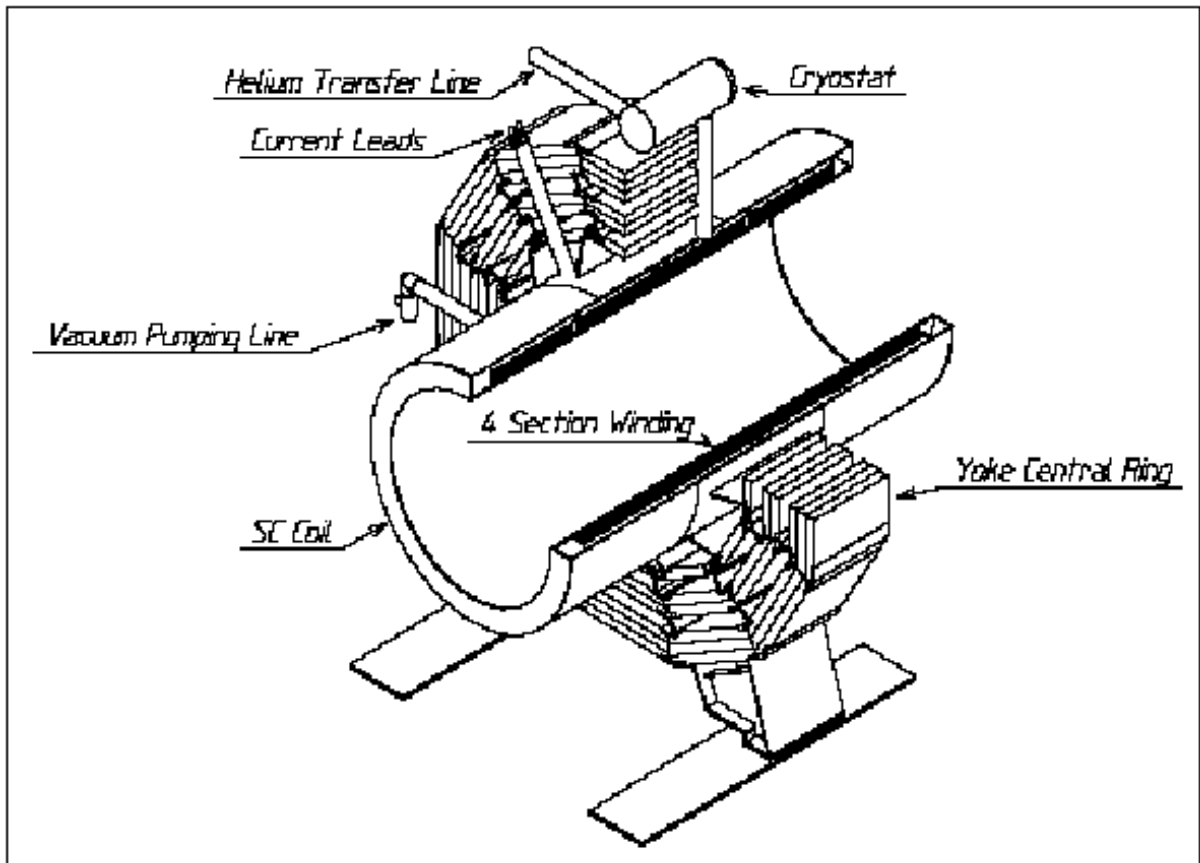


Fig. 3.4: Open view of the cold mass.

Table 3.1
Main parameters of the cold mass.

Magnetic induction at interaction point	T	4.0
Peak magnetic induction on the conductor	T	4.6

Magnetic length	m	12.48
Stored energy	G J	2.52
Magnetomotive force	MAt	42.24
Magnetic radial pressure	MPa	6.47
Axial compressive force at mid plane	MN	122

3.6.2 The Superconducting Conductor

One of the major engineering challenges of the superconducting coil is its self-supporting structure, whereby magnetic forces are resisted where they are produced, rather than transferring them to an external heavy mechanical structure, causing dangerously high shear stresses in the insulation.

As the forces induced in the conductor by the magnetic and thermal loads go beyond the yield stress of the pure aluminium a metallurgically bonded mechanical reinforcement is needed. The best way is to have this reinforcement acting axially and tangentially to the coil, thus minimising the conductor construction and winding operation as shown in Fig. 3, (see Chapt. 12).

3.6.3 Ancillaries for the Superconducting Coil

This heading comprises:

- the external cryogenic system from the flanges of the outer cryostat,
- the power supply from the current breakers,
- the vacuum system from the flange on the pumping line,
- the process control and the interface to the Slow control system of the experiment.

CEA-Saclay will define the characteristics of the ancillary equipment and will write the functional part of the technical specifications.

3.6.4 The external cryogenics

The external cryogenic sub-system consists of the compressors, the cold box, the vessels containing the 200 m³ of pressurised helium gas, the 5000 l LHe container and the cryogenic lines. The cold box and LHe container will be installed near the magnet whereas the compressors and pressure vessel will be at the surface level. The complete system will be installed temporarily on the surface for refrigerator commissioning and coil tests, (see Chapt. 21).

From a cryogenic point of view, coil operation is continuous, apart from annual shutdown periods for the necessary maintenance of electrical and cryogenic components. A dedicated helium refrigerator has been dimensioned for all the operating phases. A pre-cooler, fed with 500 l/h of liquid nitrogen, provides additional refrigeration power for the cool-down which is expected to last approximately 30 days from room temperature. Re-cooling from the post-fast-discharge temperature of 50 K will last three days.

3.6.5 Power Supply

The power supply is located alongside the refrigerator cold box in the service cavern. It will deliver a coil current of up to 20 kA at a maximum ramping voltage of 16 V. Current ramping time will be five hours, (see Chapt. 20).

There are two modes for slow discharging of the coil current: in normal operation discharge will be performed by the power supply and the energy will be injected back into the mains power network, this will last 18 h. In the case of a fault in the magnet power supply, the current will be dumped into the resistor bank set at its lowest resistance value of 2 mW. This last mode will last three hours.

In case of emergency, a fast discharge in a 50 mW resistor bank can be used. The time constant of the current decay is then 280 s, (see Chapt. 16 and 20).

In case of a mains power failure electrical power could be generated for helium recovery by using some of the stored magnetic energy. A study is under way to see if a DC/AC inverter can be incorporated in the magnet circuit for this purpose.

3.6.6 Process Control

The Magnet Process Control System, which is a part of the CMS Detector Control System (DCS) is capable of working independently and includes four parts, (see Chapt. 22):

- the sensors and actuators,
- the Programmable Logic Controllers including a Test and Development Station,
- the Magnet Safety System which in case of a fault automatically secures the magnet and its auxiliary equipment using hardware protection systems.
- the Magnet Supervisor which provides the user with:
 - supervision and control facilities,
 - operator's assistance and diagnostic facilities.

The process control of the CMS Magnet will be standardised with the process controls of the other LHC experiments including the cryogenics.

3.7 EXPERIMENTAL AREA

The proposal for the construction phase of the CMS experiment has been achieved taking into account the necessity to minimise any interference between the exploitation of LEP and the construction of the CMS subdetectors while at the same time reducing time and costs, (see Chapt. 25).

For these reasons we have adopted the solution of assembling and testing the magnet in the large surface hall before lowering it into the underground experimental cavern.

This solution allows us to start working on the magnet assembly already by the end of 1999 while LEP is still in operation. The choice of using a surface hall rather than the underground area, allows us to construct the magnet and detectors in parallel and not in series as would have been the case if the assembly was done underground. It also reduces to the strict minimum the size of the underground cavern. Fig. 3.5 shows an overview of the CMS experimental area.

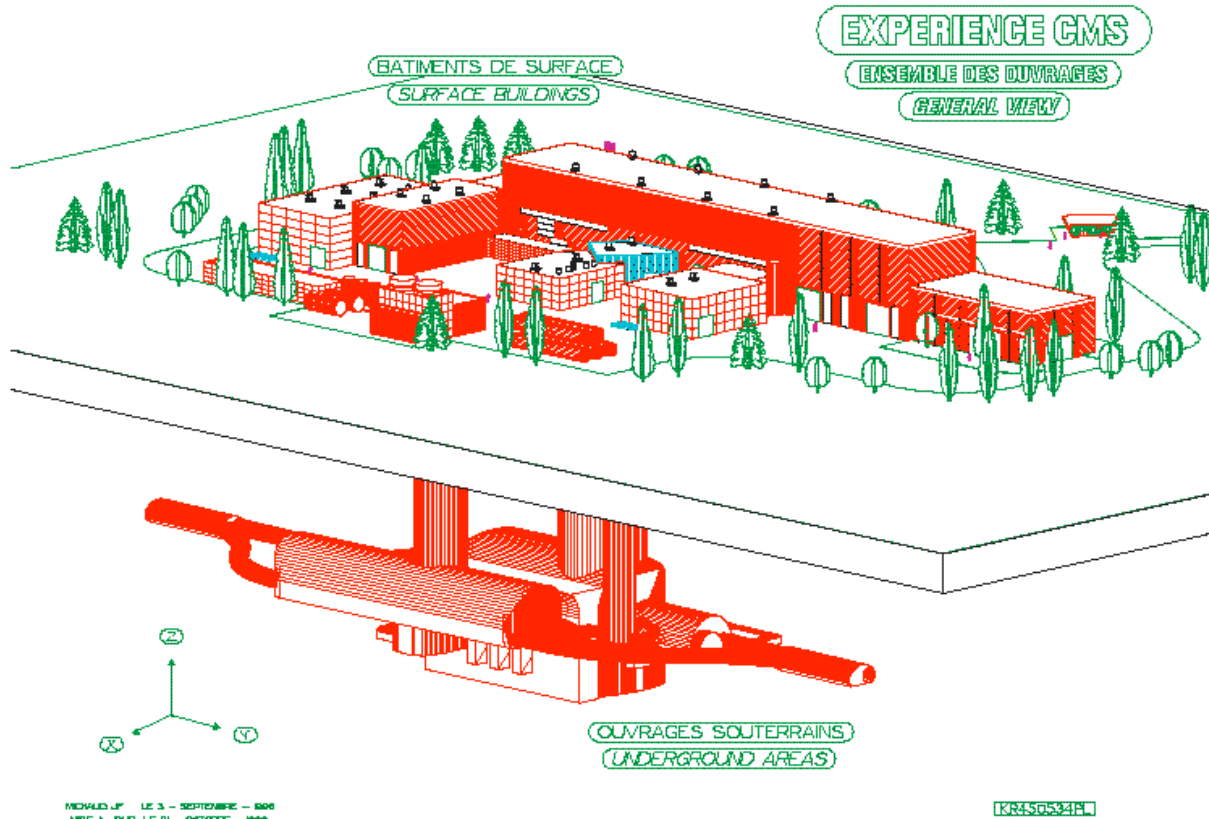


Fig. 3.5: View of the CMS Experimental Area Complex.

3.7.1 Surface buildings

The surface building complex will be located at point 5 of LHC. During the construction phase the main assembly hall will have a length of 140 m, a width and height of 23.5 m. After the magnet has been tested these dimensions will be reduced to a length of about 100 m and a height of 16 m thus having no major impact on the environment, (see Chapt. 25).

The surface assembly hall will also have two temporary alcoves which will be used as garage for the HB when moving large sections of the experiment through the hall. A third alcove will be used for testing the external cryogenics and the power supply before the surface test.

The temporary addition to the assembly hall, SXL5, is built to allow the final on-site reinforcement of the coil superconductor. Other buildings to be used for gas, primary cryogenics, ventilation etc. will be also built on the surface at point 5.

3.7.2 Underground area

The underground areas include the experimental cavern UXC5, the auxiliary cavern USC5, the access pits, PX56 and PM54, and the LHC machine bypass, (see Chapt. 25). The main access shaft PX56 is separated from UXC5 by a smaller removable metallic structure at the level of the experimental cavern ceiling.

The main cavern has a diameter of about 26.5 m and a length of 53 m. These are the minimum dimensions needed to open the CMS magnet and handle the major sub-components.

The auxiliary cavern is separated by a wall 7 m thick, (the radiation shielding requires 3 m) and will lodge the auxiliary services for the detector and the counting room.

The underground areas will be separated from the surface hall by a mobile radiation shielding situated at the top of PX56 which will also be used a support structure for the transfer of the magnet in UXC5 (see Chapt. 29).

4. INTERFACE WITH SUB-DETECTORS

4.1 INTRODUCTION

The design of the CMS detector has been driven by the requirements of modular assembly at the surface, and easy access for maintenance of the sub-detectors.

The central barrel ring is used to support the superconducting coil. The other four barrel rings and the two magnet end caps can slide on common rails along the beam direction. To keep the size of the underground area within reasonable limits, the complete magnet will be assembled inside the surface building. This also allows thorough testing of the magnet before transfer to the underground area.

While the magnet is at the surface, most of the muon chambers will be inserted in the iron yoke and each sub-detector will be prepared in large individual units, before being lowered into the underground cavern. Only final assembly, together with cabling and connection of services, will have to be carried out in the underground area.

The most difficult integration task concerns the central barrel detectors because space is at a premium within the magnetic field volume. The overall design of CMS takes this fact fully into account with the detector supporting systems using minimal radial space, nevertheless maintaining full accessibility and dismountability.

4.2 INTEGRATION OF SUB-DETECTORS

4.2.1 Magnet

Since the magnet is the main component of CMS in terms of size, weight and structural rigidity, it is used as the principal structural element to support all barrel detector components.

The central barrel ring, which is the only stationary part around the interaction point, is used to support the superconducting coil. The central section of the outer vacuum tank is attached to the inner part of the central barrel ring and the coil is symmetrically cantilevered from it. The other four barrel rings and end cap disks slide on common rails, running in the beam direction, to allow insertion and maintenance of the muon stations.

All the barrel sub-detectors, HB, EB and Tracker, are supported by the inner shell of the vacuum tank via a system of rails welded to it in the horizontal plane.

4.2.2 Muon System

Three layers of barrel muon chambers MB are interleaved inside the barrel yoke, and are thus protected when installed. The fourth layer of muon chambers, located on the outer surface of the magnet yoke, can also be installed before lowering the yoke into the cavern. Care will have to be taken to protect these chambers. The installation and testing of the completed barrel muon system will be made, as far as possible, at ground level to minimise the installation time in the cavern. This procedure allows the barrel muon system installation to remain outside the critical path of the general CMS installation planning.

Each end cap muon system consists of three vertical iron disks connected together. During installation and for maintenance of the system these iron disks can be disconnected and separated by displacing them along the rails. The end cap muon stations are mounted on the vertical disk faces and are normally inaccessible.

4.2.3 Hadron Calorimeter

The HB, which is composed of two elements, each weighing 500 tonnes, is supported only in the horizontal plane. This is achieved by rails fixed to the inner shell of the vacuum tank, and by a set of sliding pads sufficiently compliant to avoid local over-stressing of the vacuum tank wall. Maintenance access to the scintillator trays, which will be inserted during the pre-assembly at the surface, will still be possible from each end. The Tracker assembly is supported by two thin radial structures, attached directly to HB.

Each HE, which behaves as a single unit, is cantilevered from the first disk YE1 of the magnet end cap via the central shielding cone, which acts as a structural support. In addition, open straps provide added stability. This scheme leaves free space for the insertion and maintenance of the inner forward muon station ME/1/1. Maintenance access to the previously installed scintillator trays will still be possible in the radial direction.

4.2.4 Electromagnetic Calorimeter

The mechanical design of the electromagnetic calorimeter (EB) is optimised for the use of PbWO₄ crystals. Space used for the mechanical structure within the active volume of the calorimeter is reduced to a minimum, as the basket walls are designed to take only the reaction forces of the spring loaded crystals. Each super module is supported directly from the corresponding HB sector.

Each EE, which behaves as a single unit, is attached directly to the corresponding HE.

4.2.5 Tracker and Beam Pipe

At each end of the inner tracker, a 1 m long cylindrical section of beam pipe is provided for in-situ cutting and welding. The central section of the beam pipe remains an integral part of the tracker and is consequently removed with it.

The approach of installing (and removing) the central tracker as an integrated unit, containing detectors and the central section of the beam pipe, will permit independent assembly, testing and pre-alignment. In addition, this satisfies the essential requirement that the individual detectors be kept at the required temperature and gas condition during maintenance periods. Opening of the inner tracker will be carried out only in a dedicated cooled clean area situated at the surface.

4.2.6 Forward Calorimeter

To open the detector at one end, the corresponding HF must be removed. This must be done rapidly, with the HF fully cabled, to allow for optimum use of the shut-down period. For this reason, the HF is mounted on a stand supported by a structure composed of four parts, designed to support 400 tonnes. Mechanical jacks, sunk in the cavern floor, allow movement up or down in a three step operation.

A rotating shielding will provide, on both sides, the interface between the LHC machine and the CMS experiment at the level of the forward calorimeters

4.3. CABLING AND SERVICES

In contrast to the considerable amount of detector pre-assembly which can be completed at the surface, the installation of services for the various sub-detectors must be done underground. To minimise the installation time, a precise and well ordered cabling plan must

be implemented.

As a general installation principle, hardware such as manifolds, pipes, ducts and semi-rigid gas lines will be installed first, followed by the more flexible elements, i.e. electrical and optical fibre cables. Cabling will be arranged to allow maximum access to detectors and front-end electronics with a minimum of uncabling, (see Fig. 4.1).

Considering the overall assembly procedure, the logical cabling sequence requires starting from the outer muon chambers and working progressively inwards towards the central detectors. Seen in cross-section along the beam line, cable runs from the inner detectors will follow the boundary between barrel and forward detectors. Returning over the coil end flanges, the cables will then be routed along the outer cryostat wall to exit radially over the front faces of the central barrel ring. Consideration has been given to muon chamber access by alternating the cable runs over their end faces. Likewise, end cap cables will exit over the front face of each end cap. From the magnet periphery, cables and services will be channelled on a support system around the detector to flexible cable trays (cable chains) located at each side of the magnet. At the exit of the cable chains, services and cables will be separated, gas and cooling pipes being directed to the 'service' cavern, cables to the 'counting-room' cavern.

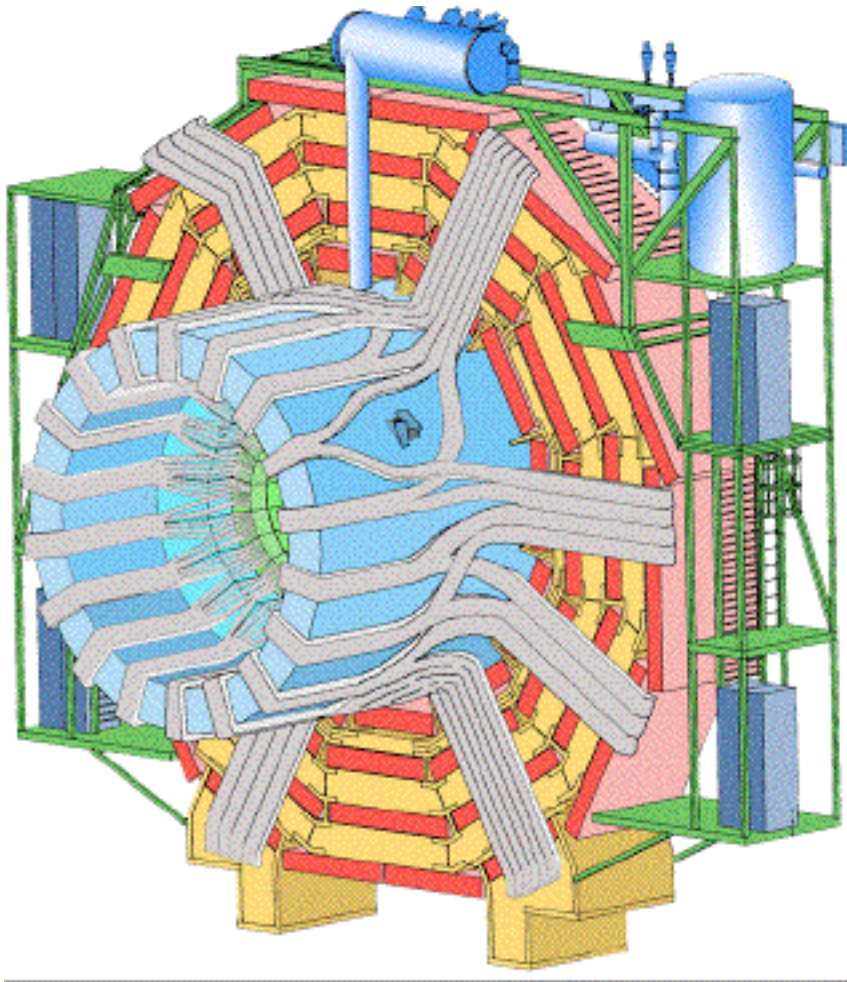


Fig. 4.1: The routing of cables and services from the inner barrel detectors over the vacuum tank, and along the barrel ring YBO

4.4 ACCESS AND MAINTENANCE OF SUB-DETECTORS

Particular attention has been given to:

- maintaining an easy access to the Tracker flanges, where most of the services for the barrel detectors are situated,
- facilitating the possibility of removing the complete Tracker to a dedicated surface laboratory during major shut-downs for maintenance or upgrade operations,
- allowing access to all sub-detectors for maintenance,
- maximising useful time during shut-downs.

Access is organised so that a minimum of uncabling (and thus recabling) of other sub-detectors is needed, and in particular to allow the electromagnetic end caps (EE) to stay fully cabled in order to maintain their calibration. Any opening of the detector at one end requires the removal of the forward calorimeter (HF) at that end. To fully use the shut down time, the HFs must be removed, and brought back to their final positions at short notice.

This also constraints the division of the experiment into end cap and barrel sections. The hadronic calorimeter end cap (HE), the electromagnetic calorimeter end cap (EE), are removed as an integral part of the corresponding magnet end cap.

The LEP experiments have been used as a model for defining safety requirements, and planning the access scenario. Thus, large scaffold arrays and hydraulic elevators for material and personnel are integrated with the gangways around the experimental hall and on the detector barrel.

Ease of access to all parts of the detector for upgrade, repair or normal maintenance has been an essential design criterion from the beginning. To obtain access from the fully closed position (see Fig. 4.2, p. XX) this will require the rotating shielding to be turned away by 90 degrees.

The forward calorimeter HF will be lowered to floor level, in three steps, by a special lifting mechanism. Each calorimeter will be stored in a shielded garage, situated at each end under the platform supporting the last machine elements, where maintenance may proceed in a radiation controlled area.

This will allow the magnet end caps to be fully retracted until the shielding cone of the magnet end cap covers the copper collimator. This gives the maximum floor space on both sides of the experiment for subsequent handling operations. In particular this position allows for the removal of the inner tracker on a special cradle.

In this position, the disks of the end cap yoke or the rings of the barrel yoke can be separated to give further access to all muon stations for maintenance (see Fig. 4.3, p. XX).

5. CMS PARAMETER BOOK

5.1 INTRODUCTION

Information and data contained in this TDR represent the best description of the project at printing time. Clearly all dimensions and parameters are not yet fixed, because the magnet project itself will evolve, but also, the magnet being the structural support for all CMS subdetectors, small changes in subdetector parameters may have an influence on the magnet project.

To make sure that information will flow correctly, the CMS collaboration has decided to maintain a **CMS Parameter Book** in electronic form which can be consulted through World Wide Web. This concerns also the magnet. The parameter book is maintained by the Working Group on Engineering and Integration (**WOGEI**). The present paper version is 2.0, issued in November 1996.

5.2 ACCESS TO PARAMETER BOOK

The most up-to-date information can be accessed through WWW at the URL:

<http://cmsdoc.cern.ch/cms.html>

which open the welcome page of the **CMS doc** (see Fig. 5.1), then selecting: **Integration**, and then the subdetector group of interest. The choice being presently between:

- people
- general parameter
- safety
- alignment and survey
- assembly
- detector machine interface
- luminosity detector
- tracker
- ecal
- preshower detector
- hcal
- muon
- rpc
- coil and ancillaries
- return yoke
- cooling & ventilation
- shielding
- experimental area
- infrastructure
- fixed cranes

This TDR will be made accessible under the heading “coil and ancillaries”.

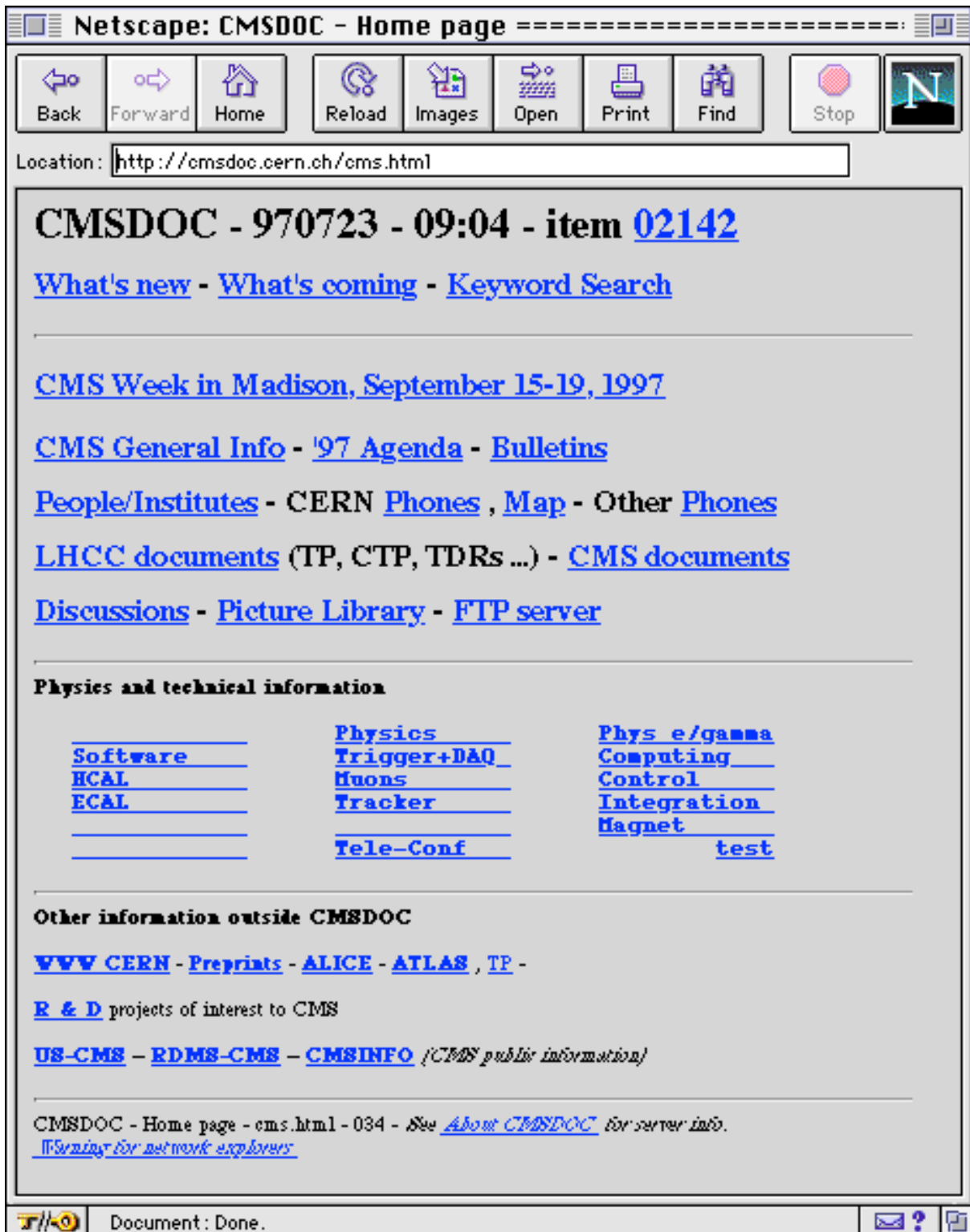


Fig. 5.1: The welcome page of CMS doc on WWW.

URL is <http://cmsdoc.cern.ch/cms.html>. Magnet can then be accessed by clicking on **Integration** then on **coil and ancillaries** or **return yoke**.

6. MAGNETIC ANALYSIS

A general description of the iron yoke, including the main dimensions, is given in Chapt. 3. Detailed constructional descriptions are given in Chapt. 7 for the barrel section, and in Chapt. 8 for the endcap sections. This chapter is only concerned with the description of the field map, including the stray field, and the forces associated with the magnetic field, both on ferromagnetic elements and on currents.

An important issue is the computation of the forces due to any asymmetry in the system, such as misalignment of the coil inside the yoke, asymmetry of the yoke itself and the coil chimney cut-outs, or an inhomogeneous magnetic permeability distribution.

6.1 GEOMETRY OF THE IRON YOKE

The following is a description of all the ferromagnetic components of the magnet yoke as it has been used for the magnetic computation (Fig. 6.1).

Some discrepancies, at the level of a few cm, may be noticed with reference to the actual CMS parameter drawings, because of recent evolution in subdetector geometries. The official and most up to date dimensions will always be accessible through WWW, as explained in Chapt. 5.

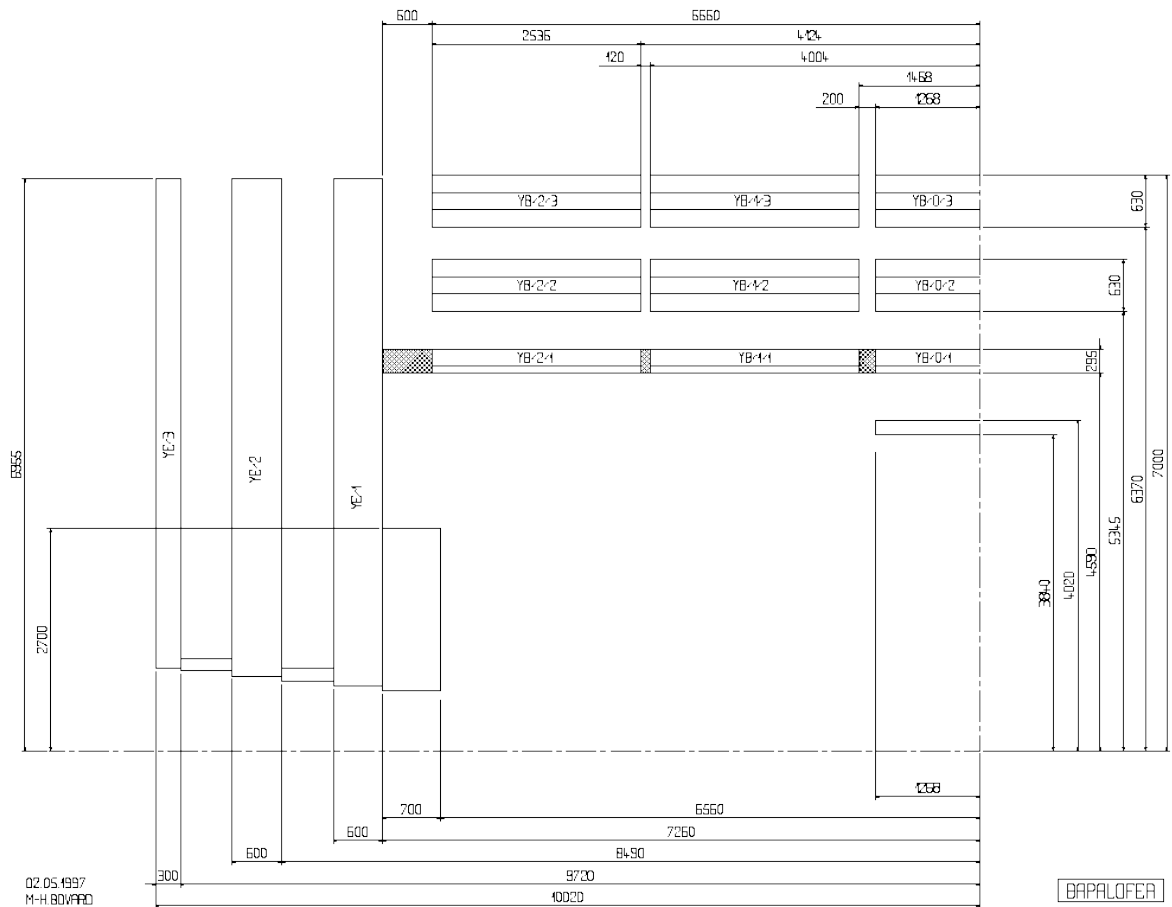


Fig. 6.1: Geometrical description of the magnet yoke used for the magnetic computations.

The innermost iron layer starts at $R = 4590$ mm on flats, and the outermost (the third

one), ends at $R = 7000$ mm (on flats).

Successive overall thickness of layers are $T_1 = 295$ mm, $T_2 = 630$ mm and $T_3 = 630$ mm.

It should be noted that the blocks of all three layers could either be made of sandwiched plates or be monoblock (rolled and/or forged).

In the former case, the inner layer blocks are composed of two plates having their matching faces fully machined while the second and third layer blocks may present, due to the tolerances of fabrication, a gap between their three constitutive plates. These plates will be machined only at the bolting points so as to be precisely assembled using calibrated washers, thus avoiding machining of large surfaces.

The fabrication tolerance of the plate thickness is required to be $+0/-10$ mm; consequently, as far as magnetic material is concerned, the real minimum thickness of the inner layer blocks could be 285 mm whereas the real minimum thickness of second and third layer blocks could be only 600 mm. This pessimistic situation has been taken into account for all the subsequent calculations.

The central ring YB0 is separated from the two adjacent ‘first outside rings’ by gaps of 200 mm, whereas the gaps separating the ‘first outside rings’ from the ‘second outside rings’ are only 120 mm.

It may be possible to reduce the two 200 mm gaps to 150 mm to increase the muon acceptance; this would also have a positive effect in reducing the stray field.

Connecting brackets, in normal construction steel, join the steel plates forming together the three layers and provide the geometry and the required structural rigidity.

Both endcap yokes are composed of three 13.9 m diameter disks (across flats). The two innermost disks are 600 mm thick and the outermost 300 mm (maybe later 250 mm). The inner disk is separated from the adjacent barrel ring by 600 mm, and all disks are equally spaced by 600 mm to accommodate the endcap muon chambers. A supplementary disk, 5 m in diameter and 250 mm thick, which serves as interface for the radiation shielding surrounding the HF calorimeter, has been added at a distance of 600 mm from the outermost large disk. Attached to the innermost disk, and facing the interaction point, is a solid iron piece 5.4 m in diameter and 700 mm thick called the nose, (YN). The total thickness of magnetic material in the nose is in fact 800 mm, as 100 mm are incorporated in the hadronic endcap calorimeter, (HE). Finally, some iron shielding rings are mounted on the inner diameter of each disk so as to rest against the preceding one when in the closed operational position. A mean radial thickness of 150 mm for these rings has been assumed for the magnetic computations.

6.2 MAGNETIC MODEL AND INPUTS

Computations have been made at CERN using the POISSON code program, at CEA Saclay using CASTEM code [6-2, 6-3], and at INFN Genova [6-4] and Wisconsin University [6-1], both using ANSYS code. All are 2-dimensional axisymmetric programs, thus needing to approximate the section of the return area from a regular 12-sided polygon to a cylinder. This may have been done in slightly different ways from one place to another but the effect is second order to negligible on the global results.

The B-H curve used for most computations have been derived from actual

measurements done on construction steel, delivered from Russia and France, for the construction of the L3 magnet (see Fig. 6.2).

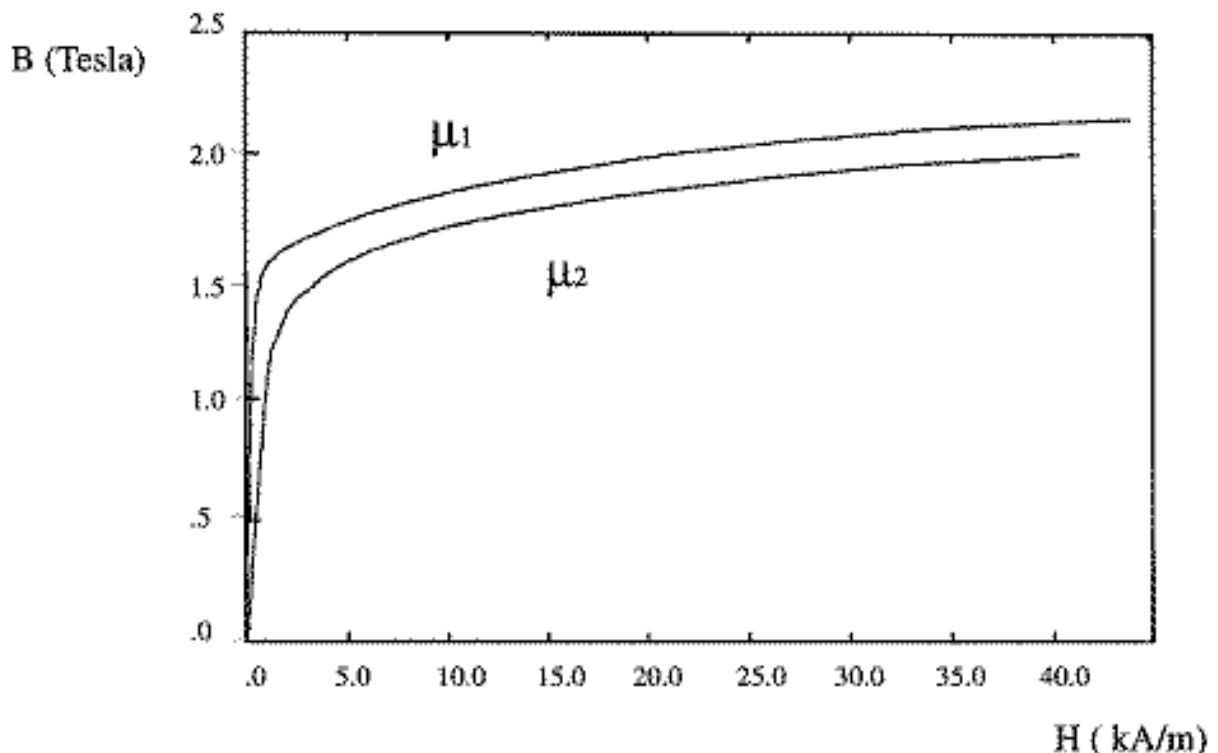


Fig. 6.2: B-H curve of a typical construction steel used for the L3 magnet, showing the maximum and minimum values used to compute forces due to inhomogeneous distribution of the magnetic permeability as explained in Chapt. 6.7.3.

The actual coil (542 turns \times 4 layers) has been input as a single turn of radial dimensions $R_i = 3.110$ m, $R_o = 3.340$ m and 12.380 m length, with a current of $nI = 42.290 \times 10^6$ A. This corresponds to an induction of 4 T at the interaction point.

6.3 FIELD MAP AND FORCES GENERATED

The magnetic forces generated in the magnet yoke are very large compared to the gravitational forces, which may be neglected.

Figure 6.3 below shows the flux distribution within a quarter of the domain RZ, taking advantage of the cylindrical symmetry around Z and the transverse symmetry in the plane $Z = 0$. This clearly shows how the favourable dimensional ratio (length/radius) of the solenoid associated to the magnet yoke allows efficient muon detection and measurement up to a pseudorapidity h of 2.4, as explained in Chapt. 2.

The total magnetic field is shown in Fig. 6.8, p. C-6; the magnetic induction is a fairly constant 4 Tesla within the coil and the innermost section of the endcap yoke, whereas the field in the barrel part of the return yoke and in the outermost disk of the endcap yoke is about 1.7 Tesla as expected. In the nose, and in the innermost section of the thick disks of the endcap, the field is changing direction and its radial component becomes quite large (see Fig. 6.9, p. C-7). The effects of the gaps between the barrel rings are clearly evident.

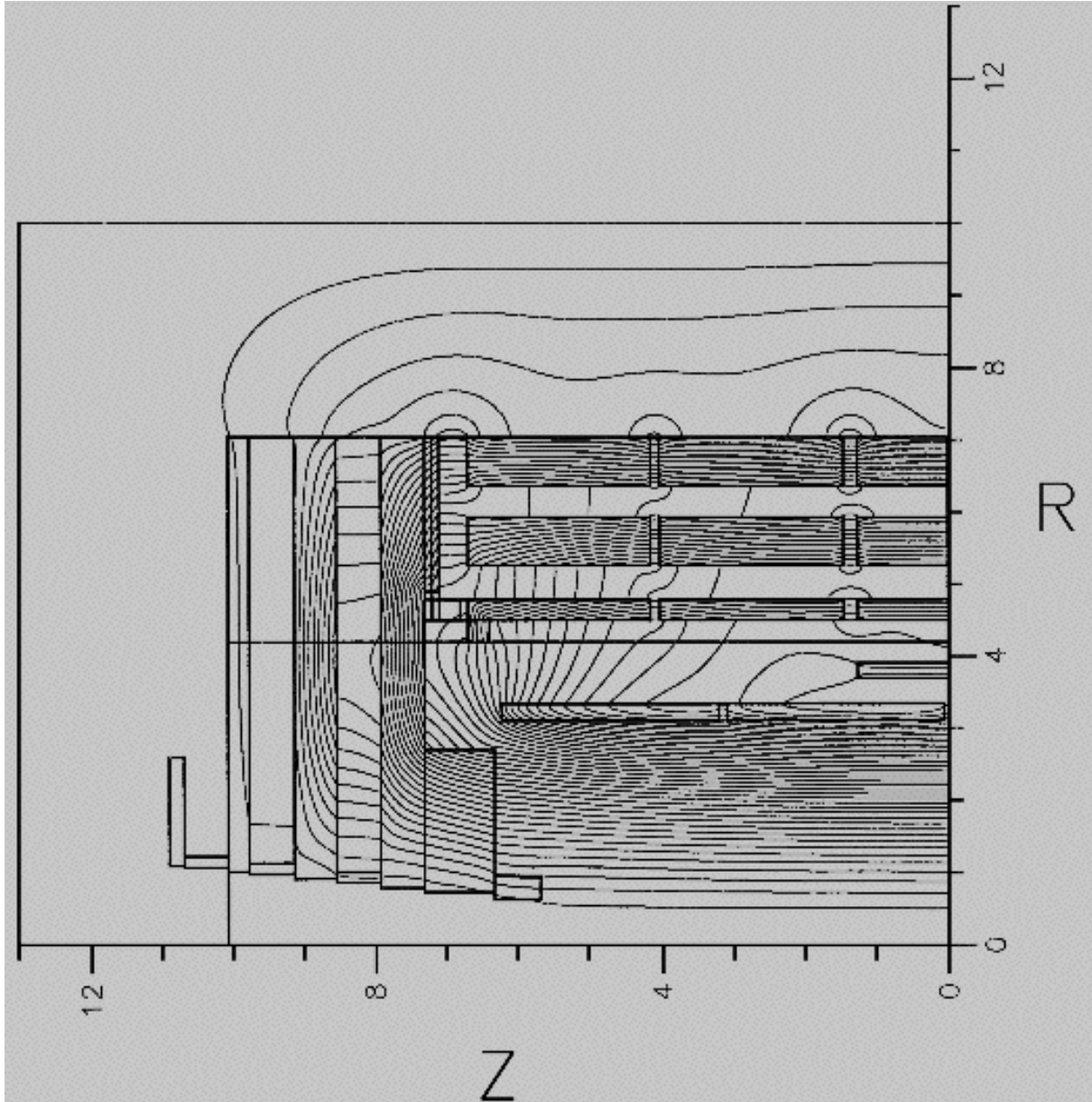


Fig. 6.3: Typical flux line distribution.

The forces generated in the barrel layers and transmitted from ring to ring are quite substantial as shown in Fig. 6.4 below, their main component being in the axial Z direction and pointing inward. They result in compressive axial forces of about 2800 tonnes in the second layer, 3000 tonnes in the third layer, and this requires attention to ensure stability of the barrel ring construction in the Z direction (see Chapt. 7.1.7).

The forces developed on the innermost endcap disk YE1 are also substantial. The vector distribution of Maxwell's equivalent surface pressure is shown in Fig. 6.5, and the resulting pressure is plotted in Fig. 8.3 and 8.4.

In general, these forces follow the flux return path, however, the ones pulling the inside edge of the disk toward the interaction point are much stronger than those pulling its outside edge out.

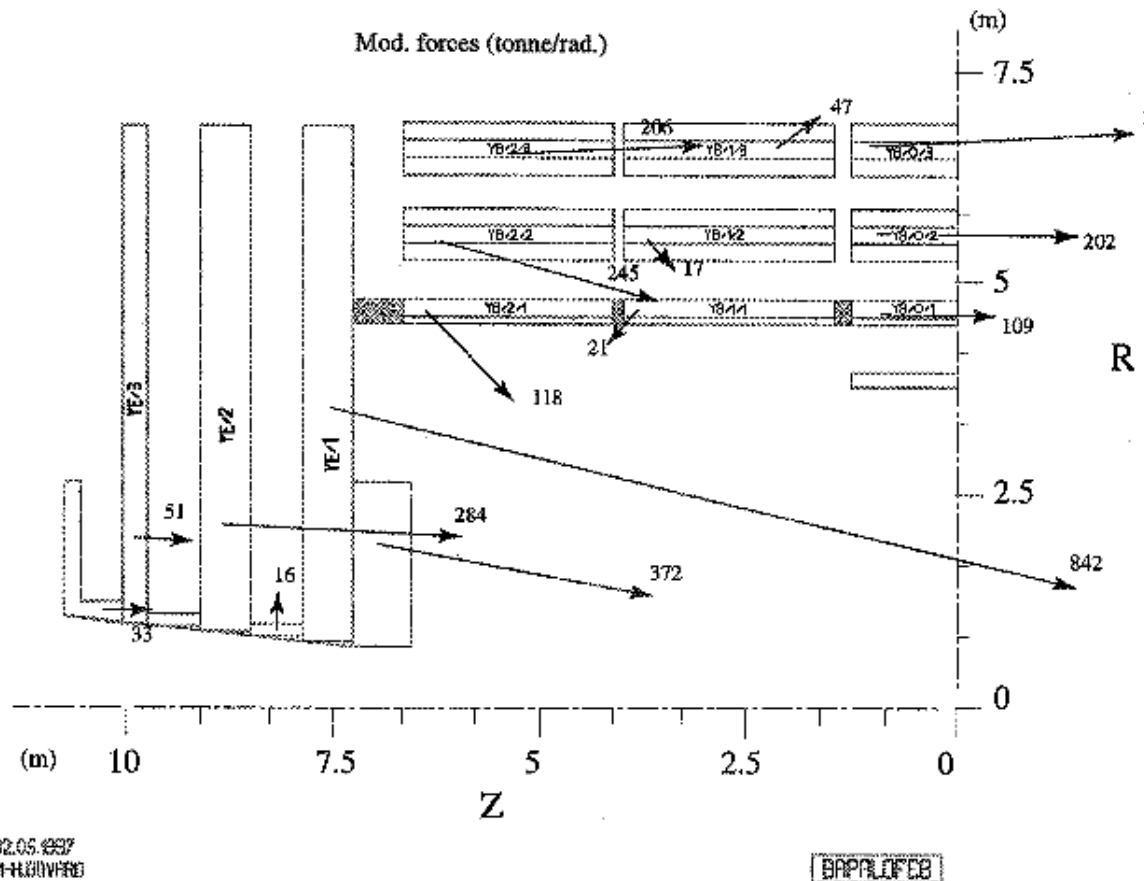


Fig. 6.4: Magnetic forces in tonne/rd acting on the individual elements of the iron yoke, given by POISSON.

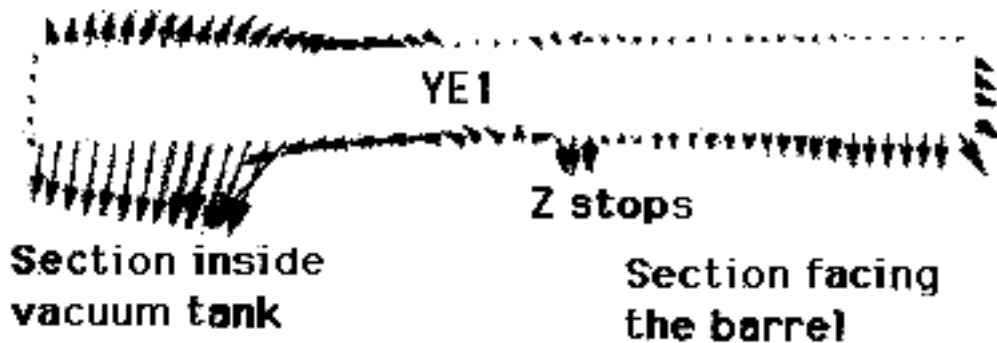


Fig. 6.5: Vector distribution of Maxwell's equivalent surface pressure on YE1.

Table 6.1 shows the total force on each disk and the nose. For both YE1 and the nose YN, this force is roughly a magnitude larger than the gravitational force. The total force of the endcap against the first layer of the barrel rings, transmitted through the Z-stops, is about 8600 tonnes, whereas the total inward pulling force, measured in the central plane, is of the order of 12000 tonnes.

Table 6.1
Magnetic effects on endcap disks.

iron element	YE1	YN	YE2	YE3	total
mass of element (tonne)	706	164	701	347	1918
magnetic force (tonne)	4915	1300	1700	153	8073

The effects of these large forces on the disk construction are fully analysed in Chapt. 8.

6.4 FIELD AT THE DETECTORS AND FIELD MAPPING STRATEGY

Since many of the muon drift chambers will stand in a large magnetic field, both the magnitude and the direction of the field are crucial in determining the correction for each chamber. Despite any possible correction, the field gradient is so important in some areas that it will reduce the expected resolution in the muon chambers (Fig. 6.8, p. C-6 and Fig. 6.9, p. C-7).

A working group has been formed to determine, starting from subdetector performances and physics requirements, the field mapping strategy. In particular the precision to which the field must be known has to be determined for every section, inside of the coil, inside the iron, inside the muon chamber volume etc.

6.5 FIELD AT THE WINDING AND FORCES EXERTED

The current-carrying elements of the superconductor experience both radial and axial forces. Fig. 6.10, p. C-8 shows the distribution of the magnetic induction within the four layers of the coil (for legibility, it should be noted that the layers have been shown separated radially).

Figure 6.6 and Fig. 6.7 given below are respectively showing the axial and radial forces exerted on the coil as a function of distance from the interaction point and/or the Z axis. In this latter case the coil has been implemented in its former four-section modular construction, and it should be noted how the radial force is discontinuous when crossing from one section to the next, thus generating higher shear stresses.

The present magnetic configuration for the monolithic case has been studied in detail and is reported in Chapt. 14.1.1, as it is used as the basis for the mechanical analysis of the coil.

6.6 STRAY FIELD

The stray field has been evaluated to a maximum distance of 50 m with ANSYS at Wisconsin. Fig. 6.11, p. C-9 which incorporates also two close-up views, A and B, for the sake of clarity, gives an idea of what the stray field could be in the UXC5 and USC5 caverns in which most of the electronics will be situated. It is worth noting that, at this stage, the present calculations extend only to 12 m in the Z direction, but they will be extended farther out.

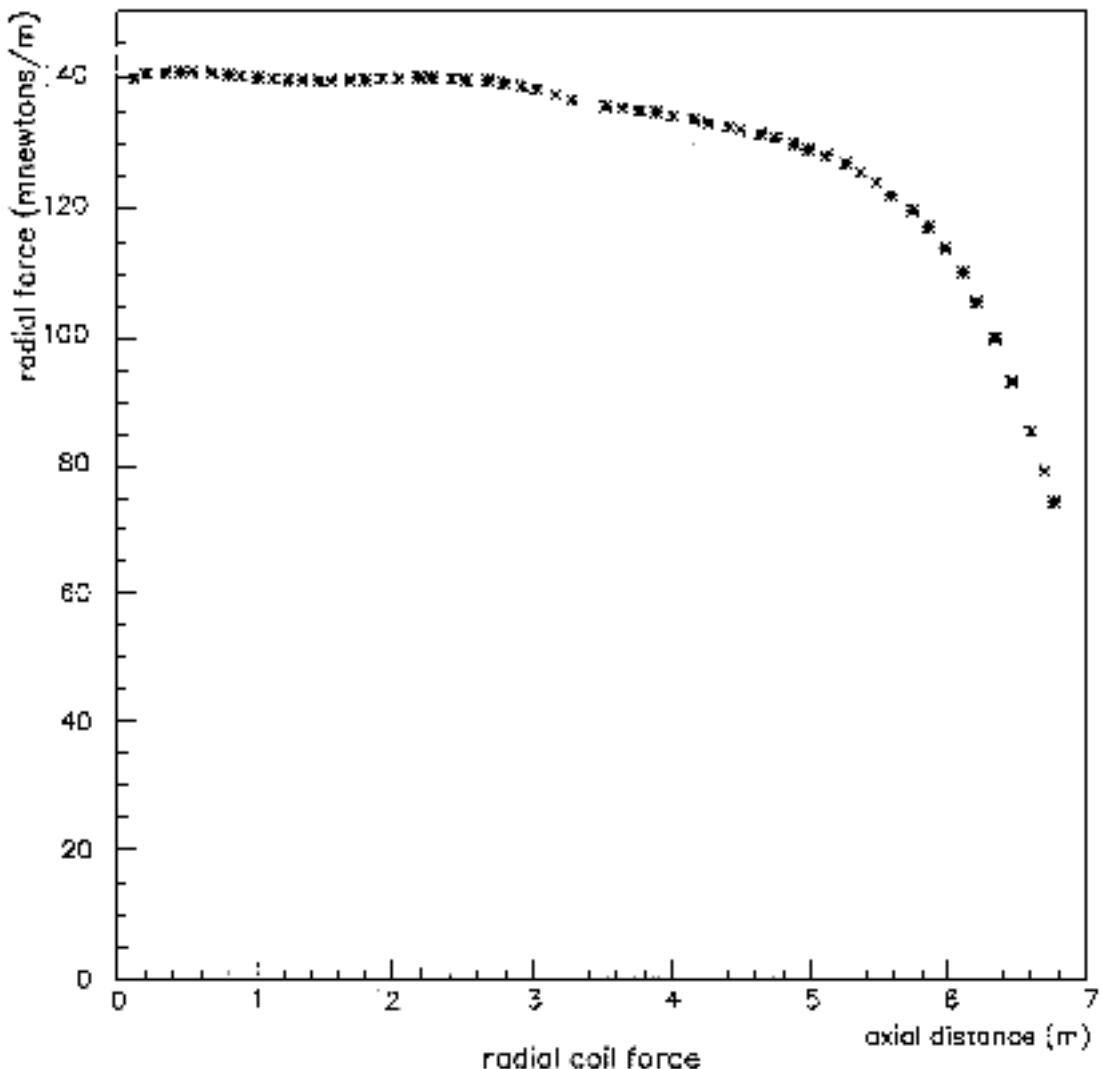


Fig. 6.6: Axial forces in MN/m exerted on the coil.

Generally speaking, the stray field has been found, in the vicinity of the barrel element separations, and at about 1 m distance from the last iron layer, to be of the order of 0.12 T.

This is the area in which some electronic racks will be installed in close proximity on balconies fixed to the magnet yoke, and the presence of this stray field must be fully taken into account from the beginning (see Fig. 26.5, p. C-55 and 26.6, p. C-56).

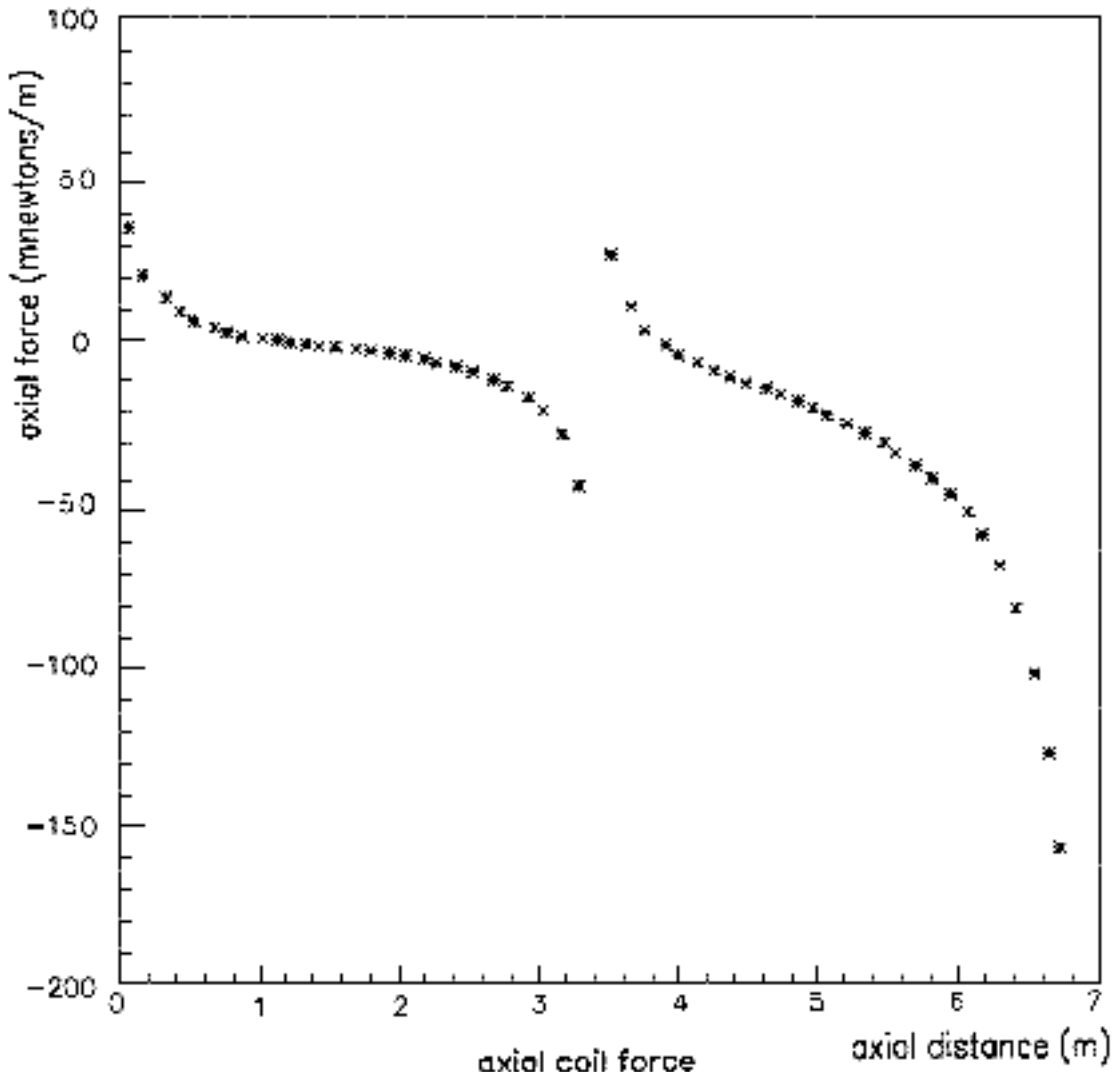


Fig. 6.7: Radial forces in MN/m exerted on the coil.

6.7 3D-FINITE ELEMENT CALCULATIONS

Three dimensional calculations have been performed at CEA Saclay, using the code CASTEM 2000, and at Wisconsin using ANSYS (see also Chapt. 8).

6.7.1 Magnetic forces on the coil due to its misalignment within the iron yoke

Out-of-symmetry displacements of the coil, both off-axis and angular, due to fabrication tolerances and to deformations induced by gravity and by the magnetic field itself may introduce forces and torques acting on the cold mass.

The iron return yoke is considered homogeneous and its non-linear behaviour corresponds to Fig. 6.2.

The resulting axial and radial forces due to axial and radial offsets of the coil of 1, 3 and 10 cm, and resulting torques due to angular tilt of the coil by the same amounts over its half-length, are summarised in Table 6.2 below.

Table 6.2

Forces and torques resulting from axial and radial offset, and from angular tilt of the coil.

axial displacement (cm)	1	3	10
axial force (kN)	840	2540	8140
radial displacement (cm)	1	3	10
radial force (kN)	380	1130	3740
angular tilt (radian / minute)	$1/620 \approx 5.5'$	$3/620 \approx 16.5'$	$10/620 \approx 55'$
torque (kN.m)	2730	8220	27240

These results indicate that the magnetic forces and torques increase linearly with the corresponding displacement, so it will be required to limit the offsets by proper constraint, the means to reduce them are explained in Chapt. 18.

6.7.2 Magnetic forces on the coil due to asymmetries in the yoke

Whilst both endcap yokes are structurally symmetrical, the barrel yoke has two substantial azimuthal cut outs, to provide passage for the cryogenic and for the electrical and pumping chimneys. The first cut out is a vertical opening traversing the three layers of barrel YB1, with a section of 540 mm x 340 mm in Z for housing a 400 mm diameter conduit. The second one, similarly in barrel YB-1 but at an angle of 30° from the vertical, has a section of 840 mm x 340 mm in Z, for housing an oval conduit 400 mm x 700 mm. The return yoke has been fully modelled in azimuth, and its magnetic behaviour has been taken as uniform. The calculation resulted in a modest force of 2 tonnes, pulling the coil toward the negative Z; the two other components being zero by nature of its symmetry.

Any other asymmetries resulting from the vertical deflection of the barrel rings due to gravity (of second order importance since this does not affect the cross-section of iron offered to the return flux) and from the geometrical tolerances accumulated in assembling the constitutive iron slabs, (expected to be minor and equally distributed in azimuth), have not been taken into consideration.

6.7.3. Magnetic forces on the coil due to inhomogeneous permeability in iron

In the second case, the return yoke is supposed fully symmetrical geometrically but constituted in two halves of different permeabilities m_1 and m_2 , as shown in Fig. 6.2.

Two calculations were then carried out: a first one in which the barrel yoke only is affected with two permeabilities; a second one in which both the barrel yoke and the endcap yoke are affected. The result is far more sensitive in the latter case: an order of magnitude larger than in the preceding one. It demonstrates that particular attention should be paid to the endcap disks in which the best homogeneity in permeability must be obtained. Thanks to their construction in sectors (see Chapt. 8), the risk of inhomogeneous permeability will be lessened - if not completely suppressed in the first order – by positioning two sectors coming from the same parent plate into two locations diametrically opposed (see Fig. 8.10) – thus averaging in practice the azimuthal permeability distribution.

The table below summarises these important results.

Table 6.3

Magnetic forces exerted on the coil due to physical asymmetries in the barrel, and to inhomogeneous permeability in the barrel alone and/or in the barrel and endcaps.

condition	Fx (tonne)	Fy (tonne)	Fz (tonne)
physical asymmetries (chimney openings in barrel)	0.	0.	2.
inhomogeneous permeability (in barrel only)	0.	0.	17.
inhomogeneous permeability (both in barrel and endcaps)	0.	0.	102.

7. THE BARREL YOKE

As explained in Chapt. 3, the CMS magnet consists mainly of three parts: a superconducting coil, a vacuum tank and the magnet yoke. The solenoid produces an axial field whereas the yoke is responsible for the return of the magnetic flux. Due to the general design of the CMS detector, the yoke is split into a cylindrical central part, the barrel, and at the extremities, two endcaps made of 600 mm thick disks. This chapter describes the barrel part of the yoke.

To understand the behaviour of the barrel a large effort has been made by modelling the barrel yoke in two and three dimensions with different finite element programs. In addition, several manufacturing schemes for the thick iron absorber plates have been considered. Not only forged monoblocks, formed from an ingot weighing roughly double that of the final product, have been considered, but also a sandwich-like build-up of the iron. This allows the use of 210 mm thick steel plates, produced by continuous casting, connected together by welding, shear pins or shear keys. Fig. 7.1, p. XX, shows the central barrel ring with the main dimensions. The most important structural elements are shown in Fig. 7.2, p. XX.

Having different design options for manufacturing the massif iron blocks of the barrel yoke increases considerably the number of potential firms able to reply to a call for tenders.

In the following sections the results for the central barrel ring analysis as well as for the outer barrel wheels are presented.

7.1 STRUCTURAL ANALYSIS OF BARREL YOKE

7.1.1 Dimensions and loads

The barrel yoke has a total length of 13320 mm. It is split into five independent rings, each one being 2536 mm long. The four gaps between the barrel rings (2×120 mm + 2×200 mm) foreseen to exit the cables and services from the central detectors, add up to 640 mm.

The central barrel ring supports the vacuum tank in which are housed the inner detectors, bringing an additional mass of 1020 tonnes. The total mass of the central barrel in running condition will thus be 3050 tonnes. Table 7.1 shows the detailed list of the mass distribution for the different rings.

The main geometric parameters used for the finite element analysis (FEA) are:

- Iron lay-up for FEA: 210/620/620 mm
- Diameter on flat: 13990 mm
- Width of each barrel ring: 2536 mm

Small disagreements between technical drawing data and the geometrical data mentioned above maybe noticed. This is due to the fact that for the finite element analysis minimum tolerances have been taken into account concerning the mechanical resistance, although the maximum tolerances have been considered to compute the dead weight. Moreover, non structural parts, serving for example only as magnetic return flux iron, have not been modelled, but their mass is taken into account elsewhere.

For the central barrel ring as well as for the outer barrels the only load is gravity. Magnetic field introduces only axial forces in the rings. To resist these forces, the 70 mm shear pins mentioned below will be tack welded and the final assembly may make use of

industrial bonding to increase the friction between the brackets and the slabs. For more details see Chapt. 7.1.6.

Having shown in the preliminary design report [7-1] that there is only a small difference between the barrel at rest, supported at the inside of the supporting foot, and the barrel supported on the outer surface during transport in the surface building, only the results for the barrel at rest are presented here.

Table 7.1
Mass distribution in central and outer barrels.

	Central Barrel	Outer Barrels
Barrel ring (slabs + brackets)	1150 tonnes	1174 tonnes
Vac Tank central part (60 mm) with connecting ribs	90 tonnes	none
Vac Tank outer shell extension cylinder (30 mm)	46 tonnes	none
Vac Tank inner shell	114 tonnes	none
End flanges of Vac Tank	14 tonnes	none
Cold mass (coil)	234 tonnes	none
Support feet	72 tonnes	66 tonnes
Tail catcher in steel	100 tonnes	none
Hadronic Barrel HB	900 tonnes	none
Elect. barrel EB. + Tracker	120 tonnes	none
Muon chambers	50 tonnes	50 tonnes
Cabling on Vac Tank and services	150 tonnes	none
Support for racks and cables	10 tonnes	10 tonnes
Total mass	3050 tonnes	1300 tonnes

7.1.2 Material properties and allowable stresses

The allowable stresses contained within a specification are to be compared with stresses determined by analysis of the effect of loading the structure. This automatically leads to the discussion of the factor of safety. This factor of safety is inherent to the allowable stresses and provides for uncertainties that are associated with typical simplifying assumptions and average calculated stresses. It is not intended that highly localised peak stresses that may occur in modern finite element analysis must be less than the stipulated allowable stresses [7-2]. Here again, exercise of engineering judgement is required.

In mechanical terms, the analysis of the barrel is a purely static problem. Due to that fact, and the very good agreement of two independent FE analysis, we will apply a factor of safety of 1.5 to yield as foreseen by the American Institute of Steel Construction Specification for the Design, Fabrication and Erection of Structural Steel for Buildings (henceforth called “AISC Code”) and the Deutsches Institut für Normung (DIN 18800 T1).

For the steel grades foreseen for the construction of the CMS yoke the allowable stresses are listed in Table 7.2. The plates to be used in the barrel being relatively thick,

between 75 and 220 mm, we have to further apply a reduction of 10 % on these values.

Table 7.2
Allowable stress for the steels foreseen for the construction.

Type of Stress	Allowable Stress Fe 310 [MPa]	Allowable Stress Fe 360 [MPa]	Allowable Stress FeE 560 [MPa]
Von Mises	120	160	290
Shear	70	95	160
Tension/ Bending	120	160	290

7.1.3 FEA model for central barrel

The CASTEM 2000 [7-3] finite element program was used to create the 2D-model of the barrel rings.

Figure. 7.3, p. XX, to Figure. 7.5, show the finite element model of the central barrel. It is made from 2-D plane stress 8-node elements. This type of element is chosen as it closely represents the stress distribution in which we are primarily interested. The brackets have at least 2 layers of these elements. This corresponds to a minimum of 5 nodes in the bending section.

The support feet for the central section are included in the model. This makes the model complete and shows also the influence of foot compliance.

The supports are fabricated by welding steel plates. As such, they cannot be truly represented by a 2-D model. The side plates, which are continuous, are modelled with real steel properties. The stiffening web plates, which are not continuous, are represented with diffuse properties. This gives correct displacement values for the support and thus for the entire yoke, but for stress related questions the foot has to be analysed separately. The entire structure is simply supported on the floor by constraining all the nodes of the floor interface in the negative vertical direction (i.e. downward) whilst upward movement is allowed. This technique represents well the stiffness of the foot. To keep the structure in place horizontally, one node has an horizontal boundary condition. No friction and no compliance of the floor have been taken into consideration.

The vacuum tank is represented by a single 60 mm thick steel cylinder which is connected at 12 points to the yoke. The weight of the inner detectors, the coil and the inner shell of the vacuum tank have been taken into account by giving an artificial density to the mesh representing the vacuum tank.

Between the slabs which are built up from three layers of iron (i.e. the middle and outer ones), 160 mm diameter shear pins are installed to keep the three layers together and provide bending stiffness. Washers which serve as spacers in between the compressing tie-rods are modelled with orthotropic elements. A standard steel modulus was used in the radial direction while only 1% of the Young's and shear moduli were used in the perpendicular direction. This is low enough to transmit quasi no shear force and large enough to avoid numerical problems.

To resist the large shear forces occurring mainly around the foot region, a pin of

120 mm diameter is installed between YB 0/3/8 and 3/9 and also between 3/11 and 3/12. In the program this is achieved by nodal coupling. Fig. 7.6, p. XX, shows the location of these pins and the numbering scheme of the blocks.

Care has been taken to model fairly accurately the highly stressed regions which are believed to be (from previous analysis) the connection brackets and their fixations.

In this model only gravity acts on the self mass of the structure. No magnetic forces and neither friction nor any other contact problem has been introduced.

All material is steel with a Young's modulus of 210000 N/mm² except the cryostat and its radial connection to the yoke. These parts are in stainless steel with a Young's modulus of 190000 N/mm².

At a first glance the yoke seems to be symmetric but it is not, because of the asymmetry in phi. Therefore the whole ring must be modelled, giving a mesh with 12138 elements and 45698 nodes.

To cross check the results, a 3-dimensional model has been made at Fermilab [7-4]. Fig. 7.7, p. XX, shows the 3-D mesh of that model including the cryostat and the support feet.

7.1.4 FEA Results for the central barrel

The colour plot in Fig. 7.8, p. XX, shows the undeformed structure in blue and the deformed in red. The amplification is 100. Due to the artificial density which was given to the cryostat, its deformed shape must not be considered. The maximum vertical displacement of the barrel ring is 10 mm. The widening of the ring in the horizontal direction is not symmetric because of the asymmetry of the structure and the boundary conditions fixing one node of the left foot in the x-direction.

In the horizontal plane of the beam axis the displacements are 6.4 mm to the left and only 4.5 mm to the right side. Horizontal and vertical displacements are shown in Fig. 7.9, p. XX, and Fig. 7.10 respectively. The deformation plots for the outer barrels are shown in Fig. 7.11, p. XX, to Fig. 7.13.

The verification of the stress distribution concentrates on the following parts of the structure: absorber slabs, brackets, shear keys between slabs, shear keys between slabs and brackets and the tie bars which are used to connect the brackets to the slabs.

Slabs and their shear pins:

The slabs are modelled as a 3 layer design. This is mechanically the most complicated way to build the magnet iron, but the fact that with such a design the maximum plate thickness needed is reduced to 210 mm, increases the number of potential firms and allows an economic use of steel plates. It is clear that if the slabs are manufactured as forged massif iron blocks there is no problem at all with the allowable stresses. To be sure that the barrel iron yoke could also be built with sandwiched iron plates we have taken this case as the reference study.

It turns out that the iron slabs with the following reference numbers, YB/0/2/08, YB/0/2/12, YB/0/3/09, YB/0/3/11, have to be reinforced in shear by adding 50000 mm² of effective shear section at the extremities:

This will be achieved by welding rectangular shear keys at the extremities of the above mentioned slabs. The weld will be 20 mm thick.

The shear stiffness is given by shrink fitting six pins between the layers. These pins have a diameter of 160 mm for the central barrel and 120 mm for the outer ones. The design of a typical absorber block is shown in Fig. 7.14, p. XX.

Brackets:

For the two brackets between the middle and outer slab at the 4 and 8 o'clock position, the maximum Von Mises stress was found to be 282 MPa, as shown in Fig. 7.15, p. XX. These are the most stressed parts of the whole structure. Due to the sharp corner, this value is certainly overestimated by the finite element analysis and in reality this corner will be rounded by the weld, but it remains nevertheless a highly stressed part and the four corresponding brackets will be manufactured in using an appropriate high grade steel or a fine grained structural steel.

The most inner and most outer brackets have maximum stresses of the order of 100 MPa and can be made of low carbon steel. The brackets from inner to middle slabs and from middle to outer slabs have mean stresses below 140 MPa except for those situated at the 4 and 8 o'clock position.

The calculation of the forces acting at the interface between the brackets and the slabs gives extremely important information. The radial contact is assured by tie-rods, 8 are presently foreseen in the central barrel (6 in the external ones), each giving a pre-load of 800 kN. This gives a total force of 6400 kN.

In the tangential direction, friction alone cannot retain the brackets. Therefore shear pins of 70 mm diameter and 800 mm length are inserted on both sides of the barrel.

The radial force values go up to 2500 kN except in the right and left support foot region where 4400 kN occurs but this is still well below the applied prestressing force.

The maximum tangential force transmitted is 7650 kN, which corresponds to a shear stress of 68 MPa for the most stressed pin.

7.1.5 FEA Results for the outer barrels

The outer barrels have only to support their own weight and the muon chambers. This totals approximately 1300 tonnes. Therefore less reinforcement is needed. The additional shear reinforcement above the support feet can be omitted and the shear pins between brackets and slabs can be reduced in length to 600 mm. Only 6 tie-bars are required, as opposed to 8 used in the central ring. Fig. 7.11, p. XX, to Fig. 7.13 show the deformation of the outer barrels.

The stresses are all in a range that allows the use of Fe 360 for all brackets and Fe 310 for the absorber blocks.

7.1.6 Barrel Materials

The following table shows the grades of steel for the different parts of the barrel.

Table 7.3

Characteristics of different grades of steel to be used for the barrel.

	Absorber steel Fe 310	Low carbon structural steel Fe 360 D	Fine grained structural steel FeE 560	Stainless steel SS 304
Yield strength	> 175 MPa	> 235 MPa	> 450 MPa	> 195 MPa
Tensile strength	> 310 MPa	> 360 MPa	> 600 MPa	> 500 MPa
Elongation after fracture	> 18 %	> 20 %	> 14 %	> 40 %
Impact value (ISO-V/20 °C)	> 18 J	> 25 J	> 14 J	> 70 J
Used for	All 180 barrel iron blocks	1440 pins +720 shear pins in blocks + 236 brackets + 10 support feet + 2 Ferris Wheels	4 highly stressed brackets in the central wheel	complete vacuum tank
Mass [t]	5200 t	1500 t	15 t	285 t
TOTAL [t]	7000 tonnes			

For the tie-bars which connect the brackets with the iron blocks we have foreseen a diameter of M36. They are made of St 50.2 and are widely used in civil engineering constructions. At a working stress of 800 MPa, they guarantee a prestress load of 800 kN per bar.

7.1.7 Axial forces on barrel rings

According to different computations made with the programs “Poisson” and “ANSYS” there are relatively strong magnetic axial forces between the different barrel rings. Integrated over the whole ring with 3 layers, the forces are of the order of 18000 to 24000 kN. Per sector there are 2000 kN to withstand. This axial force must be resisted by the construction.

The z-stops are blocking the most inner iron ring and thus the bracket connecting to the middle slabs. It is on the interface of this bracket with the middle slab where it is necessary to verify the friction and tack welded shear pins resistance against slipping. Looking at one sector only:

In the outer barrel there are 6 tie-bars, each of them prestressed to a nominal value of 800 kN. The slab is retained by 2 rows of 6 tie-bars thus 12×800 kN giving 9600 kN.

For bolted connections with measured bolt preload as it is the case here, a typical coefficient of friction value for mechanical pieces is 0.33. In other words, one third of the measured preload acts as friction. In this case $9600/3$ kN are acting as friction, thus 3200 kN.

In addition, the doweling pins which have a diameter of 70 mm will be tack welded. This gives an additional 400 kN retaining force.

In conclusion there are 3600 kN to resist 2000 kN magnetic force acting to move the barrel towards the interaction point, i.e. there is a factor of safety against slipping of 1.8.

Tests are being carried out to see the impact of a “Loctite ®” type of product being applied at the time of assembly between slabs and brackets.

7.2 FERRIS WHEEL

From the very beginning structural welding has been avoided in the barrel yoke to allow a trial assembly at the factory thus permitting verification of the geometry before delivery to CERN.

Since the publishing of the Technical Proposal, a lot of work has been done to optimise the assembly process. At the same time, the design of the experimental area and the surface buildings has been finalised, giving more input. It turned out that a rotating jig with specially designed mobile pivoting support brackets was the best compromise between accessibility to the wheel, drilling needs and insertion and fastening of the heavy barrel slabs.

The Ferris Wheel has been studied in detail to prove that the design is sound [7-5, 7-6].

7.2.1 Assembly principle

The Ferris Wheel is used twice: first for trial assembly at the factory and then at CERN for final assembly.

To maintain static equilibrium, the barrel iron slabs will be inserted in pairs. The first piece will roll on a trolley which sits on rails just under the Ferris Wheel. It then will be lifted by hydraulic jacks and brought in the exact horizontal position by sliding pads. Once in position, it will be fixed to the pivoting support brackets which are locked in position during the whole assembly.

Once this is done, the second piece will be brought by the crane and positioned on top of the wheel. After the assembly of two slabs (and thus no torque reaction on the system) a hydraulic gear will rotate the entire wheel by 30 degrees.

The same procedure is repeated with another pair of slabs. At the same time, the peripheral brackets which will form the “base” for the second layer are fastened between adjacent slabs. The second and third layer of iron slabs are assembled in the same manner.

With the barrel ring assembly complete, the support feet are attached. Hydraulic jacks provide height adjustment so that when the pivoting support brackets are released, the barrel ring stands on its support feet. The final problem is to remove the barrel ring from the Ferris Wheel structure. This is achieved by extending the central shaft of the Ferris Wheel by 5m, and removing the foot that stands in the way. The barrel ring is then put on the transporting beam and moved out with a system of high pressure air pads installed under the transporting beam, (Chapt. 10, and Fig. 10.1-A and 10.1-B).

The Barrel ring will be stored in the hall, the Ferris Wheel being ready for the subsequent assembly.

A special Ferris Wheel is foreseen for the central barrel, because the pivoting support brackets are not required. This is due to the fact that the central part of the vacuum tank outer shell acts as the support structure for slab assembly, and can be incorporated in the Ferris

Wheel (see Fig. 26.13-B, p. XX).

Figure. 26.13-A, p. XX, shows the Ferris Wheel for the outer rings. The pivoting support brackets which allow the re-use for several assemblies, as needed for the 4 outer barrels, can be seen.

7.2.2 Doweling and machining of z-stop surfaces

Due to gravity, the barrel rings deform to an ellipse. This deformation creates large forces in the circumferential direction which cannot be resisted by friction alone. Shear pins of 800 mm depth and 70 mm diameter will be needed in the central barrel to hold the ring together. In the outer barrels, the shear pin diameter of 70 mm will be retained, but the length will be reduced to 600 mm.

To drill the dowel holes is not an easy task. They have to be drilled between two plates of different steel qualities and have to be straight. Test drillings of 70 mm diameter and 800 mm depth have been performed with a special drilling head to prove the feasibility of the technique, see Chapt. 10, and Fig. 10.2-A and 10.2-B, p.XX. The holes drilled at the interface of two bolted plates had a quality of H8 and were straight within 0.2 mm [7-7].

Another important and difficult machining operation is the preparation of the z-stop seats. In the most inner corners of the 12 sided barrel we have a total of 24 z-stops transmitting the axial force of 100 MN coming from the end caps.

After assembly of the first layer of iron slabs on the Ferris Wheel, the whole unit will be taken by the crane (lifting capacity at least 400 tonnes) and positioned on the revolving table of a vertical lathe equipped with a milling head. The doweling of the first layer and the machining of the z-stop seats will be done on this lathe. This can be seen on Fig. 7.16, p. XX.

With the machining completed, the Ferris Wheel will be lifted back on its bearings, to continue the assembly of the remaining layers of iron slabs. A drilling machine, equipped with a dedicated drilling head, installed on a height adjustable platform which is attached to the support members of the Ferris Wheel will be used for the doweling of the second and third layers.

7.3 SUMMARY

The various barrel yoke rings of the CMS detector have been analysed with the finite element program CASTEM 2000.

The analysis has shown, for the central barrel ring, that the brackets between middle and outer slabs in the 4 and 8 o'clock position have a maximum Von Mises stress in the corners of the order of 280 MPa. This needs a higher grade alloy steel or fine grained structural steel.

At the same angular location but one step radially inwards, the brackets show a maximum stress of 181 MPa. These should be manufactured in fine grained structural steel.

All remaining brackets in the central barrel and all brackets in the outer barrel rings have stress values lower than 140 MPa and they will be manufactured with a low carbon structural steel such as Fe 360.

To prove the security of the barrel yoke design, an analysis has been made [7-1] with one of the most stressed brackets (4 o'clock) removed. Like spokes in a wheel, the loss of

this bracket is taken by a slight increase in stress in all other brackets but does not lead to failure. The remaining brackets show stresses still well below the yield strength. In other words the CMS barrel yoke is a fail safe structure. The maximum stress that occurs at the remaining 8 o'clock bracket is 318 MPa. General deflections increase by only 1 mm in this case.

The main assembly principles as well as the doweling and machining techniques of the most important components have been described. Visits to potential manufacturers have proven the total feasibility of the project in terms of maximum dimensions, weights and required tolerances for the machining.

8. END-CAP YOKE

This chapter describes the analysis and construction of the endcap yoke. The overall configuration of the endcap region is shown in Fig. 8.1. This chapter is concerned with the yoke portions of the endcap, namely YE1, YE2, YE3 and YN. These elements form the magnetic portion of the endcap.

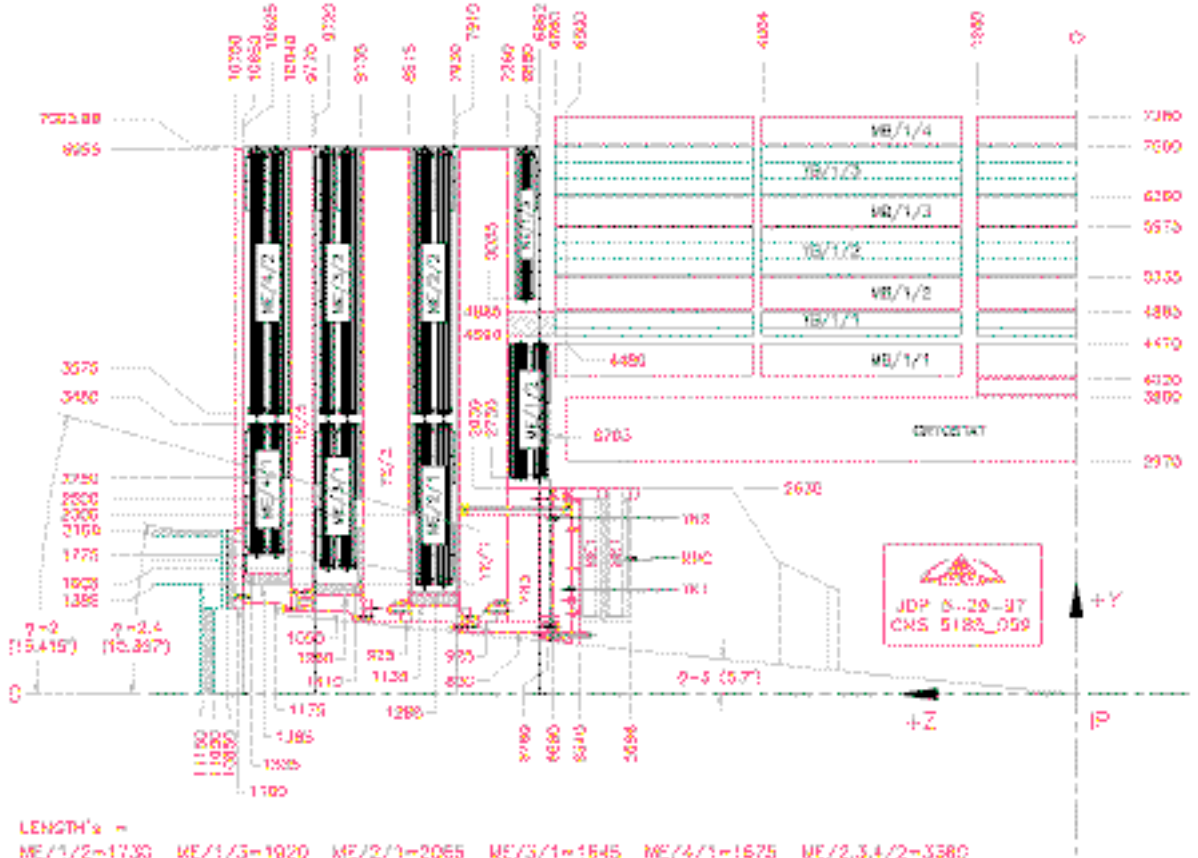


Fig. 8.1: Longitudinal view of endcap region.

8.1 STRUCTURAL ANALYSIS

An analysis has been performed on the steel structure of the endcap using the ANSYS® general purpose finite element program. The analysis is for a full 3-dimensional model of the endcap. In this model each disk is fabricated from 24 sectors. The effects of gravity and magnetic loads have been modelled.

A three dimensional analysis is required because the construction of the disks from many sectors can only be represented in a 3-D model. Also effects of gravity on a mostly round object are best analysed with a 3-D model. In this model, the endcap calorimeter and all attached objects are assumed to be 300 tonnes total. The calorimeter is assumed to have a bulk stiffness value equal to steel.

8.1.1 Purpose

The two primary areas of concern that have been addressed with this analysis are:

1. The stresses on the connections between disk segments when the disk is loaded

magnetically. The magnitude of the total magnetic load on YE1 is roughly 10 times larger than the gravitational load. This load is reacted against the ends of the barrel iron. The magnetic forces are not applied evenly over the surface of the disk but, instead, are concentrated toward the centre of the disk. The result is that the region of the disk inside, radially, of the barrel support is pulled towards the interaction point while the region outside is pivoted away (Fig. 8.26, p. XX). This deflection generates tensile forces in the segment connectors on the face closer to the IP and compressive forces in the connectors on the opposite face.

2. The stresses and deflections in the carts supporting the three disks. This investigation can focus on an examination of the cart for YE1 since the configuration of this disk is the hardest to accommodate. The nose assembly on YE1 is a large overhanging load which not only increases the total weight on the cart but also produces a large moment on the connection between YE1 and the cart. The requirements of the carts for YE2 and YE3 will be much less stringent.

8.1.2 The Model

The model assumes a disk constructed from 24 sectors. We have also analysed a disk made from one piece. The maximum deflection for a solid disk is about 7 mm under magnetic loads. This represents the lower boundary of the deflection.

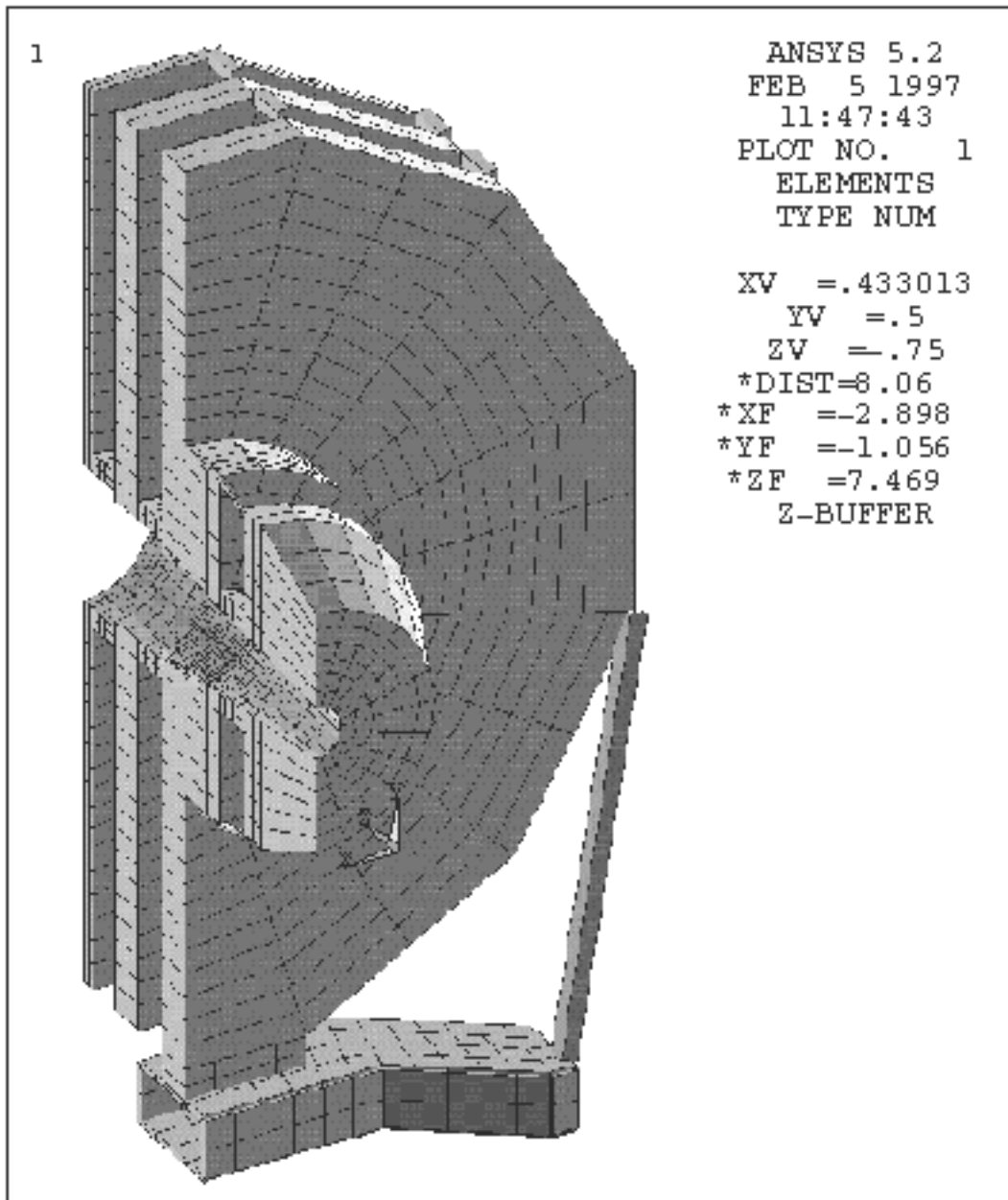


Fig. 8.2: Finite element model of endcap.

Figure 8.2 shows the 3-D finite element model of YE1 with its cart and the overhanging nose assembly. As shown, only half of the disk is modelled with a symmetry boundary condition on the cut plane replacing the missing half. The nose has been sized to match the weight and centre of mass location of the current design. Figure 8.2 also shows the model of the rest of the endcap with the carts for YE2 and YE3 replaced by simple position constraints. The support of each of the three disks is independent enough that the carts for YE2 and YE3 can be examined independently.

The two versions of the model that are of interest are:

1. YE1 and its cart with gravitational loading and the 300 tonnes cantilever load.
2. All three disks with gravitational and magnetic loads.

The disks are made from 8-node brick elements with 3 degrees of freedom at each node. The cart is made from 4-node shell elements (6 degrees of freedom at each node) since it is

anticipated that the raw material will be steel plate. The support pad between the cart and the disk is made from 8-node brick elements that have 6 degree of freedom of at each node.

All nodes that would be connected to the unmodelled half, if it were present, are given a position constraint against deflection in the x direction but allowed to move in the y and z direction. This is the above-mentioned symmetry condition that allows the modelling of only half the structure. There are position constraints against vertical motion applied to the footpads of the cart. When the entire endcap is modelled, with magnetic loads included, position constraints against motion in the z direction are applied to YE1 at the same radius at which the barrel would constrain the disk. If YE1 is modelled alone, without magnetic loads, then a single node on one of the footpads is constrained in the z direction to prevent rigid body motion in that direction.

The 1.23% slope of the floor in the hall is accounted for by applying a vertical gravitational acceleration of 9.809 m/s^2 and a horizontal gravitational acceleration of 0.121 m/s^2 . In all models the horizontal component acts in the minus z direction, the direction that adds to the moment in the cart already present from the overhanging nose.

The disks are separated by the shield rings. These rings are attached to one disk and touch the next disk. To model the shield ring between YE2 and YE3, the two coincident circles of nodes at the inner radius of the contact area between YE3 and this shield are coupled so that they have the same z displacement but are not coupled in any other way. This is based on the assumption that this region will be in compression (an assumption that is shown to be correct by inspecting the forces later). This does neglect any sliding friction between the shield and the disk.

At the other end of this shield the outer ring of nodes is anchored firmly (with constraint equations) to the face of YE2. This means that the outer ring of nodes at this end of the shield maintain their position with respect to the adjacent nodes on the surface of YE3. This shield is, therefore, fixed with respect to YE2 and slides on the surface of YE3. The same arrangement is repeated with the shield between YE2 and YE1. This ensures that the weight of each disk rests predictably on its own cart and is a reasonable model of what would actually be designed.

The construction of the disk from pie-shaped segments is imitated by the way the segments of the model are joined. On the surface of the disk farther from the IP all nodes in each sector are merged with the corresponding nodes in adjacent sectors. Since these joints connecting the sectors will be in compression this is the most realistic connection. On the opposite surface, closer to the IP, nodes are merged at the outside edge, the inside edge and four other fairly equally spaced points between. This models the case where six connectors, or ties, are used along each seam on this face (see Table 8.1). The nodes in the middle plane of the disk between the two faces are not joined as this would give an unrealistically rigid connection.

Table 8.1
Connections between sectors.

No.	Radius	Location
1	0.8 m	Inside radius of disk
2	2.013 m	An intermediate point
3	3.227 m	An intermediate point
4	4.74 m	Radius of YB1, Z support for magnetic loading
5	5.709 m	An intermediate point
6	6.955 m	Outside radius of disk

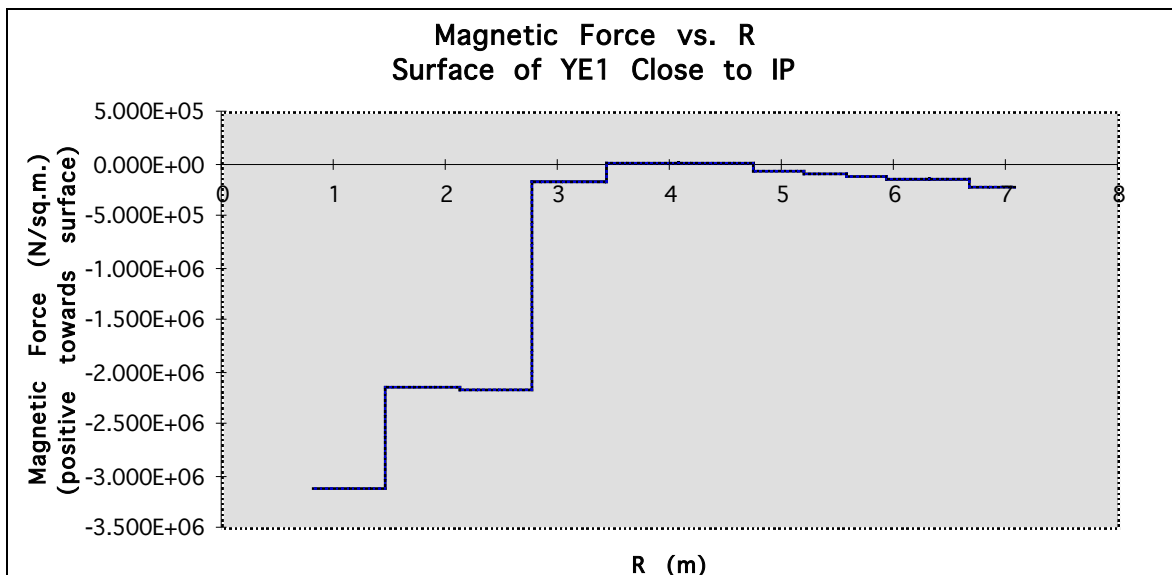


Fig. 8.3: Axial force distribution on YE1 at $Z = 7.26$ m.

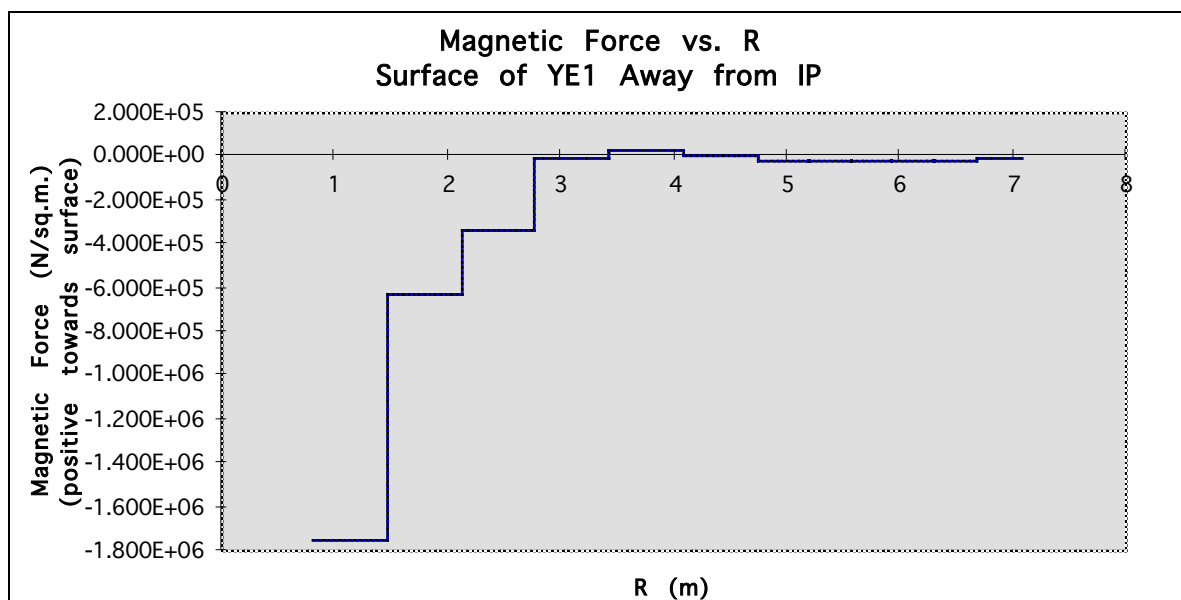


Fig. 8.4: Axial force distribution on YE1 at $Z = 7.86$ m.

The loading is derived from a 2-D, axisymmetric, magnetic analysis, also done in ANSYS, that predicts loads in the r and z direction at a number of nodes on the surface of each big disk and on the two steel disks of the nose [8-1]. On YE1 and YE2 the z forces are roughly an order of magnitude larger than the r direction forces. On disk YE3 the forces are comparable magnitude but the forces on YE3 in general are much less than on YE1 and YE2. Since, in addition, the radial forces will be less likely to distort the disks than those in the z direction, the radial components have been ignored.

The forces on each face of the 3 large disks were divided radially into 12 groups corresponding to radial rings of elements. The force in each area divided by the area of the ring yields the pressure which is applied to the elements in that area. Plots of these pressures are shown in Fig. 8.3 and Fig. 8.4 for disk YE1 at $z = 7.26$ and $z = 7.86$ respectively.

8.1.3 Model Results

Magnetic and Gravity Loading

The predicted deflection of the endcap under magnetic and gravity loading is shown in Fig. 8.26, p. XX. The nose on YE1 is pulled towards the IP about 14 mm. The outside edge of the disk is levered in the opposite direction about 8 mm. Due to the connections between the disks, YE2 and YE3 have equal deflections. This shows that the entire endcap calorimeter is predicted to move toward the IP by about 14 mm as a rigid body. Since the endcap calorimeter is made from non-magnetic materials, no additional distortions are expected in the Z-direction. Therefore, the space allocation for the endcap calorimeter must include at least 14 mm in the Z-direction as the magnetic field is energised.

Figure 8.27, p. XX, shows the deflection of the endcap in the Y-direction (vertical) due to magnetic and gravity loading. It shows that the endcap calorimeter deflects down by about 2 mm. This is almost entirely due to the gravity load on the connections of the endcap calorimeter to YE1. The endcap calorimeter is assumed to be 300 tonnes total and to have a bulk stiffness value equal to steel. This, of course, is a simplifying assumption made for the purposes of this model only. This is valid here because we are only interested in the effects of the cantilever load on the endcap. However, the structure of the endcap calorimeter is much different. It is made from copper plates with space for scintillators. It will not have a stiffness value equal to steel. Therefore, the 2 mm sag is only due to the support. The sag within the endcap calorimeter must also be added to this number. The space allocation for the endcap calorimeter must include both numbers.

Gravity Loading of YE1

The predicted Z deflection of YE1 and its cart, under gravity loading only, is shown in Fig. 8.28, p. XX. Under this condition the support is only on the cart, i.e. the detector is open and the endcap is not supported on the barrel. This figure shows a Z distortion for the endcap calorimeter of about 1 mm toward IP at the top and 2 mm away from IP at the bottom. This is due to gravity loading of the cantilevered endcap calorimeter which causes a bend in middle of the YE1. In this figure the brace is represented as a line.

The predicted Y deflection of YE1 and its cart, under gravity loading only, is shown in Fig. 8.29, p. XX. The total deflection is about 4 mm in the -Y direction. It is, again, due to gravity loading of the cantilevered endcap calorimeter. The sag of the endcap calorimeter itself, must again be added to this number as explained above.

These figures show that YE1 is not vertical by about 5 mm and the endcap calorimeter

is displaced by about 6.5 mm (vector sum of 4 mm Y and 5 mm Z deflections). To close the detector, the endcap must be made closer to vertical by lifting the front supports. This operation will make YE1 vertical on the average. However, due to its bend, it will not be vertical everywhere. As the detector closes, it is likely that the endcap will touch the supports on some but not all points. Then, when the field is turned on, then YE1 will basically “flatten” against the barrel. This is not desirable. A better approach is to make the supports with different lengths so the endcap touches all supports prior to turning on the field. This will avoid large motions. It may also be desirable to preload the supports.

Sector Connections

Figure 8.5 shows the forces on a sector schematically. The tangential forces between two sectors at $Y = 0$ for both sides of the disk are plotted in Fig. 8.6 and Fig. 8.7 for combined loading and for gravity only loading respectively. For combined loading, they are greatest at the second tie out from the inside, at a radius of about 2.01 m. The load in this tie is about 4.5 MN. The inner tie is carrying a load of about 3.2 MN. For gravity loading only, the directions switch and the forces are smaller. Therefore, the magnetic load is the main load on the ties between the sectors.

Tie Rod Forces

The nose is connected to YE1 with 24 tie rods near its outer radius. The tie rods are modelled as 80 mm diameter cylinders. These tie rods are under tension. The total tension on all tie rods is 52.4 MN. The maximum tie rod tension is 2.62 MN at the top and 1.89 MN near the bottom. The average tie rod tension is 2.18 MN. The non-uniformity is due to the moment generated by the cantilevered calorimeter.

Z Support Forces

The Z supports are spacers between the endcap and the barrel, i.e. between YE1 and YB/2/1. They occupy the radial space between the muon chambers ME/1/2 and ME/1/3. There will be 24 Z supports arranged in pairs every 30° .

The total Z support force is roughly 85 MN. This is the total magnetic load on one endcap. This force is all transmitted through the barrel rings and reacted by the equal and opposite load on the other endcap.

The Z support forces on the 24 Z supports are not equal. They vary slightly in value at different azimuths. This is due to asymmetry introduced by the cantilever load. The maximum Z support force is 3.7 MN and the minimum Z support force is 2.8 MN.

Endcap Calorimeter Connection

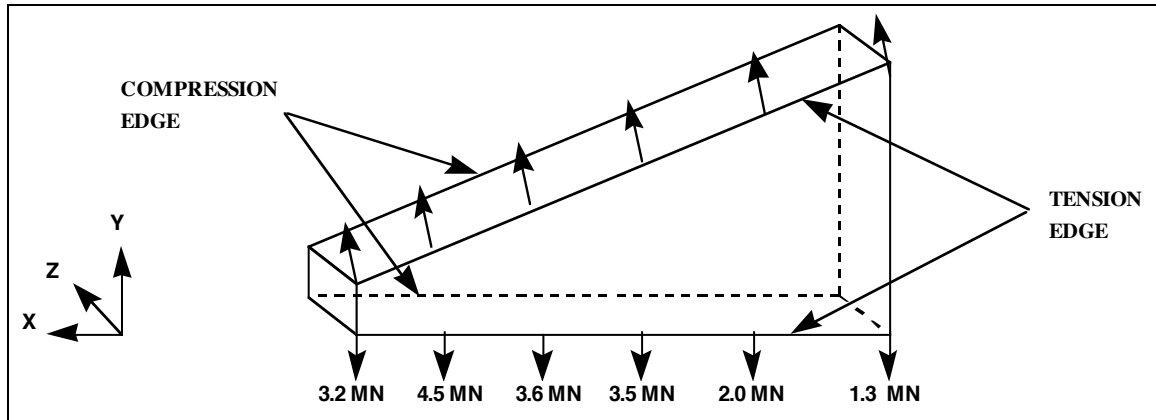


Fig. 8.5: Loads on a single sector.

The endcap calorimeter attachment to the nose is modelled with 12 tie rods near the outer radius of the nose. The tie rods are modelled as a 64 mm diameter cylinders. These tie rods are under tension. The total tension on all tie rods is 25.6 MN. The maximum tie rod tension is 4.66 MN at the top and 1.05 MN near the bottom. The average tie rod tension is 2.13 MN. The non-uniformity is due to gravity and due to the 4 struts spanning the ME1 space. (These struts are 90° apart).

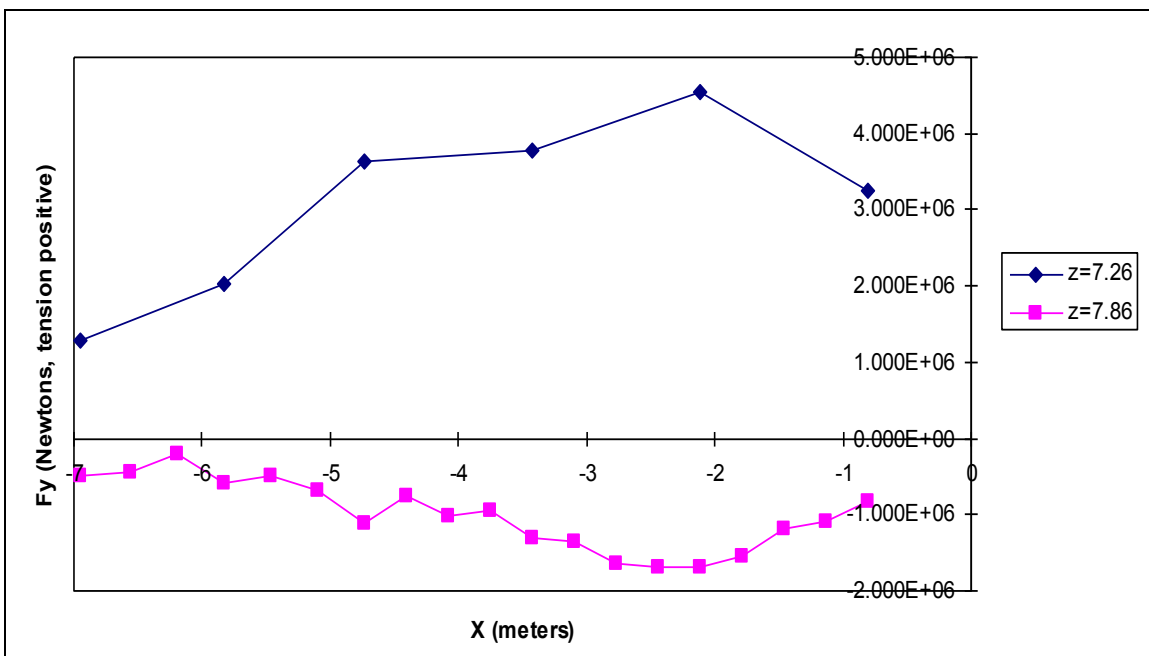


Fig. 8.6: Tangential forces at $Y = 0$ for gravity and magnetic loading.

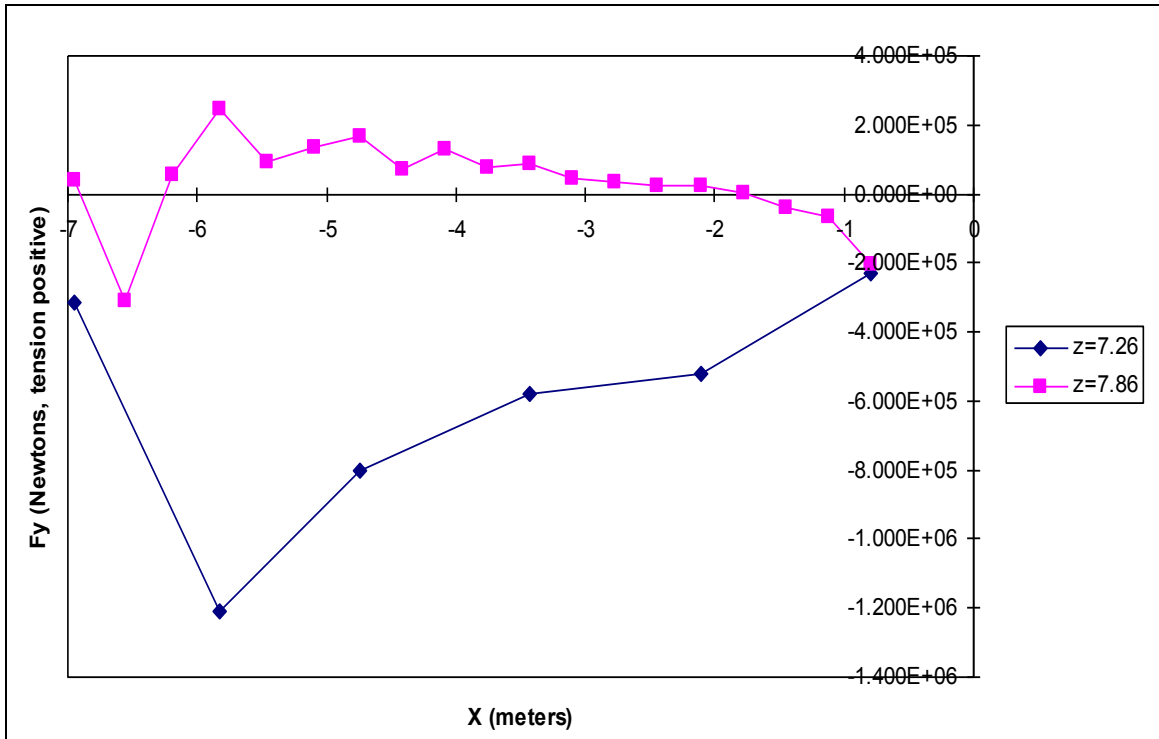


Fig. 8.7: Tangential forces at Y = 0 for gravity loading only.

8.2 ENDCAP YOKE CONSTRUCTION

8.2.1 Design Criteria

The criteria for the mechanical design of the endcap absorber are as follow:

1. Uniform steel composition and symmetrical construction to ensure proper return for magnetic flux.
2. Safety during detector operation under severe magnetic loads.
3. Safe support for endcap calorimeter and other equipment attached to the endcap. Total supported mass is about 300 tonnes for each endcap.
4. Safe support of the disks under gravity loads. Total self mass is 3800 tonnes.
5. Safe operation during access to the endcap and to interior of the detector.
6. Design that can be produced by existing technology at several steel mills and large machine shops. This is important because the requirements for the size of the endcap limit its production to a very few facilities.
7. Support of endcap muon detectors in a very rigid and stable manner.
8. On-site assembly to be compatible with conventional facilities, and with schedule.
9. Cost to be within projections.

In order to satisfy points 2-4, safe stress levels have to be chosen. As a guide we have used the American Institute of Steel Construction (AISC) Manual for Steel Construction [8-2]. This code is a thick book. It is not directly applicable to the design of large magnets of very thick section. It is mostly applicable to conventional steel construction. However, we intend to satisfy the intent of this code. We have reviewed the code and believe the following criteria to be applicable:

- Maximum stress in tension only members to be less than 60% of yield strength on gross section, and 50% of ultimate strength on net area.

- Maximum combined stress (Von Mises) in all other members to be less than 66% of yield strength.

Other design criteria are addressed in the following sections.

8.2.2 Endcap Yoke Components

The endcap yoke consists of many distinct items. Table 8.2 lists the items along with their quantity, mass and reference drawing number. It must be noted that some items, such as each of the three disks, are assemblies of many other items. For brevity, these sub-components are not listed. The drawings are on file but have not been included in this report. The CMS + and - sides are ignored for the purposes of this list, i.e. the two endcaps are assumed to be identical. The total mass for both endcap yokes is 4600 tonnes.

8.2.3 Overall Disk Tolerances

The overall disk needs to meet certain tolerances of size and form in order to satisfactorily interface with other components.

Figure 8.8 shows a schematic of a thick disk with overall tolerances.

The tolerances of form and position define the overall boundary of the disk. Several things should be noted:

1. The disk thickness varies between 590 mm and 600 mm.
2. The boundary of the centre hole is within 1 mm of its true form.
3. The 12-sided boundary of the disk is within 5 mm of its true form.
4. The entire disk is contained in a volume bounded by:
 - A 12-sided shape that is 13922 mm across,
 - by a cylinder that is 1796 in diameter and is centred on this shape,
 - and by two planes that are 600 mm apart.

Table 8.2
Endcap Yoke Top Level Parts list.

Item	Ref. Drawing	Qty (each)	Unit Mass (tonne)
YN1	5185D074	2	38
YN2	5185D062	2	23
YN3	5185D063	2	62
Inner YN1-YN2 Connection Ring	5185C064	2	2.3
Inner YE1-YN3 Sleeve	5185C066	2	5.3
YE1 IP Side ID Ring	5185C065	2	1.8
YE1 Disk Assembly	5185E123	2	721
YE1 Outside ID Ring	5185C067	2	1.9
Main Nose Tie Rod	5185E034	40	0.1
YE1 Cart Assembly		2	90
YE1-YE2 ID Spacer Ring	5185C068	2	8.5

YE2 IP Side ID Ring	5185C065	2	1.8
YE2 Disk Assembly	5185E122	2	721
YE1 Outside ID Ring	5185C069	2	2.1
YE2 Cart Assembly		2	90
YE2-YE3 ID Spacer Ring	5185C070	2	10.2
YE3 IP Side ID Ring	5185C071	2	1.5
YE3 Disk Assembly		2	299
YE3 Outside ID Ring	5185C072	2	1.4
YE2 Cart Assembly		2	90
YE2-Outside ID Spacer Ring	5185C073	2	12.1
ME/4 Shield Small Ring	5185C119	2	7.9
ME/4 Shield Large Ring	5185C120	2	108

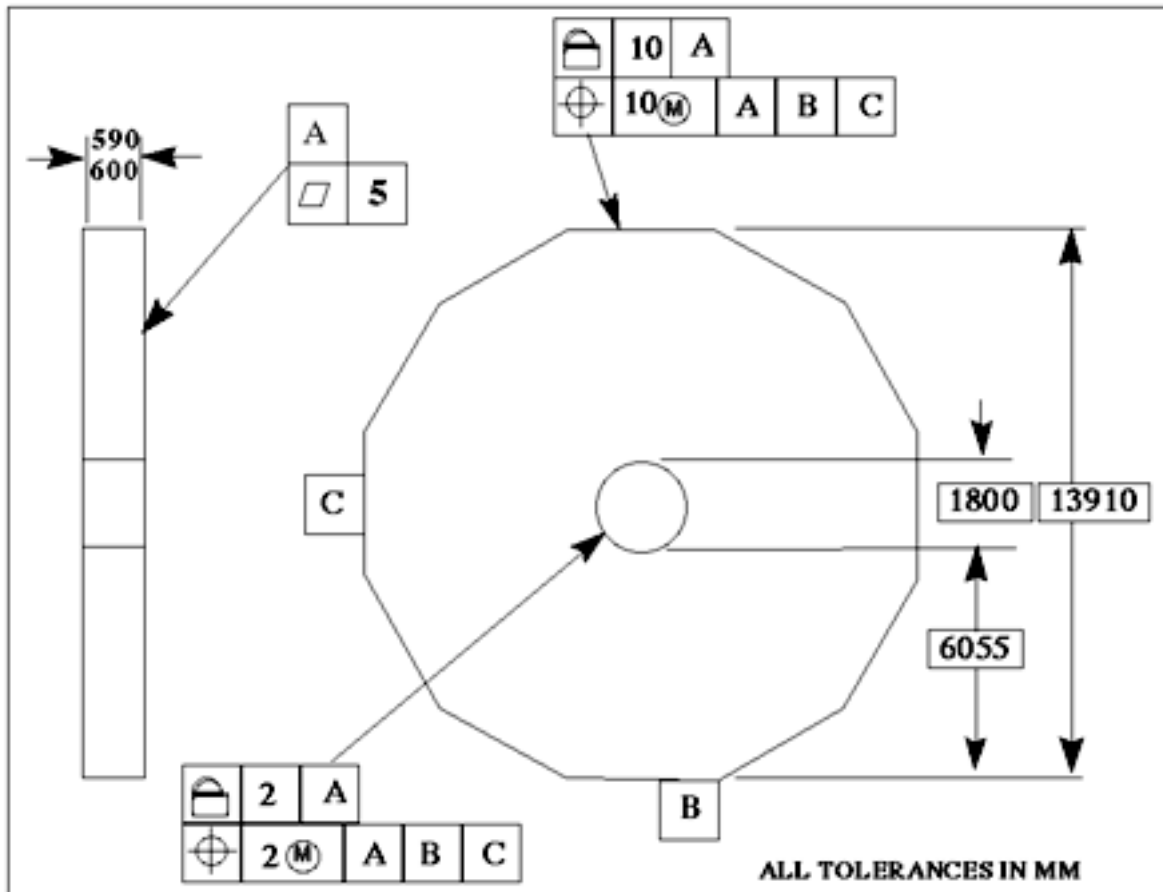


Fig. 8.8: Overall disk tolerances.

8.2.4 Design Options

Several designs have been investigated. The main criterion is that any design has to be within the capabilities of standard steel mill and large machine shop technology. The options fall into two sub-categories:

1. Mechanically joined options. Blocks are pinned and bolted, or similarly joined, to form a disk.
2. Welded options. Rectangular blocks are welded together by Electroslag (or similar) welding process to form a monolithic disk, (see Chapt. 10).

Welded options require on-site assembly as the fully welded disk is too large for transportation. Mechanically joined options can be preassembled at the factory, disassembled and then reassembled at the site. There are cost, schedule, and performance trade-off issues with either option.

Presented below is a reference design using the mechanically joined option. It is given as a reference design because many variations are possible for this option. It is our intention to present this reference design as a possible option to vendors in a request for tender. The vendor can either offer a proposal for construction based on this design, or chose a variation of it. We intend to leave options open for vendors to propose better and/or cheaper options. However, we believe it is important to have a reference design that is well analysed and has a very good chance of meeting cost and performance criteria.

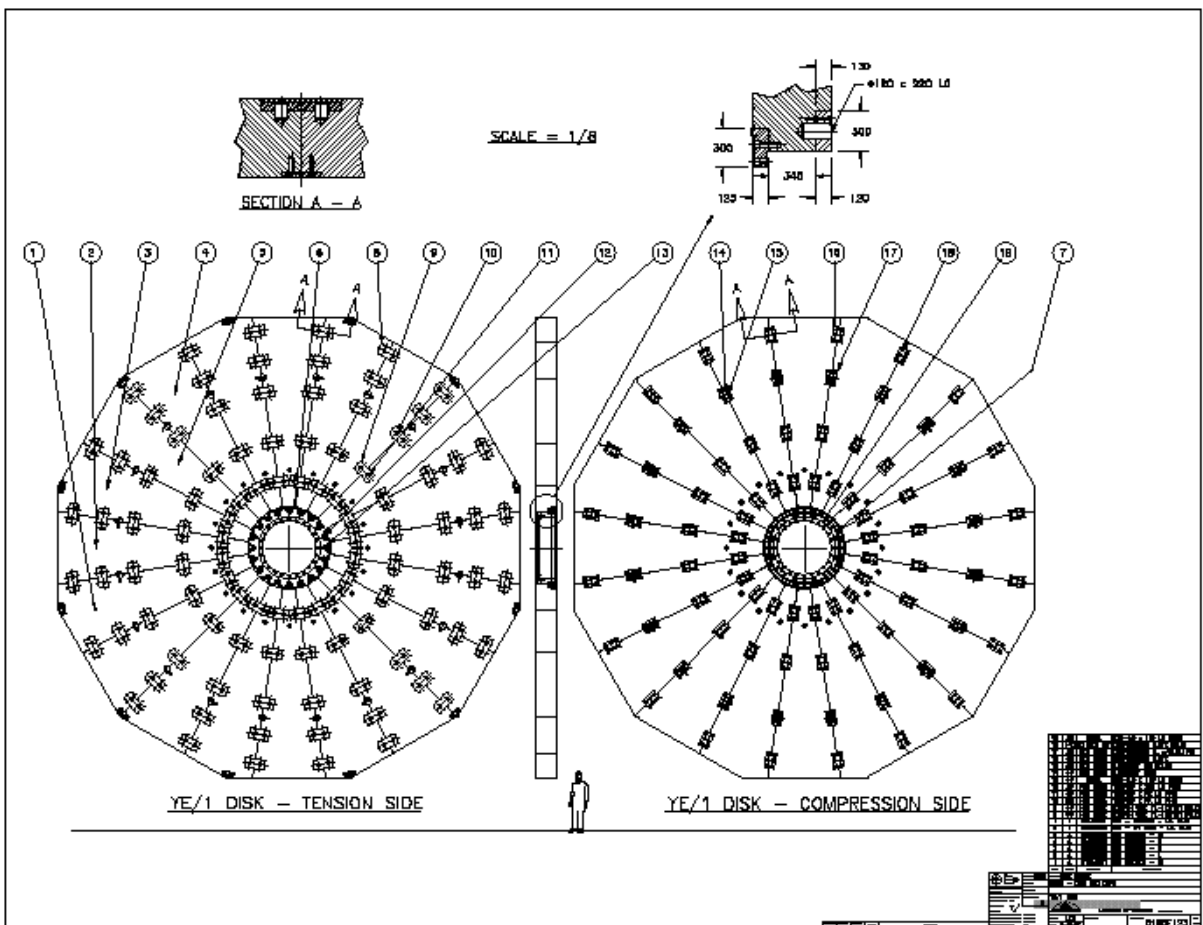


Fig. 8.9: Typical disk construction from 20 sectors.

8.2.5 Mechanically Joined Option

Figure 8.9 shows a typical disk subdivided into 20 sectors, joined by pins and fasteners. These sectors can be cut in pairs from plates of steel as shown in Fig. 8.10. The number of sectors can be more or fewer. Fewer sections are preferred as they reduce the number of joints. However, fewer sections require larger plate sizes which may not be available. From our study of steel mill capacity so far, we believe that a 20-sector construction is a possible compromise.

Figure 8.9 also shows a typical sector connection. Section A-A. On the compression side of the disk, away from IP, strap plates with bolts are used. On the tension side, toward IP, a plate and two pins are used. At the centre of the disk, a ring is fitted to the sectors. It is important to note that the pinned connections must be designed in a way that can be verified for proper fit and tolerance at the factory. However final assembly of the joints will occur once at the site.

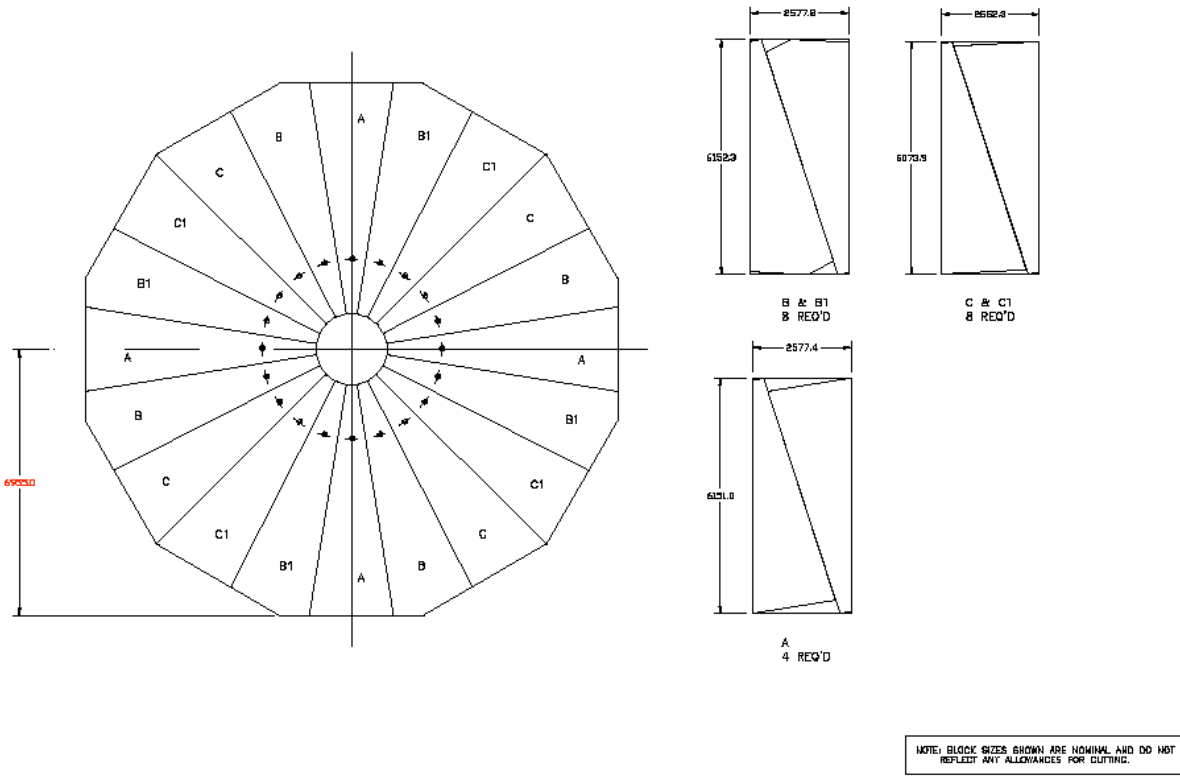


Fig. 8.10: Cutting of plates for a 20-sector construction. Note that the plate sizes are nominal and do not reflect any cutting allowance.

Figure 8.11 shows a typical machined block without tolerance. This drawing does not have any tolerances as of yet. However, it is expected that most critical dimensions will need control to about 0.5 mm. Detail A shows the features for the connection on the compression side. Detail C shows the detail for connections on the tension side. Detail B shows features for alignment pins for assembly of the sectors into the disk.

It is anticipated that to achieve proper fit between these large blocks, mating features between two blocks will have to be machined together. This can be done by stacking pairs of mating blocks and machining these features jointly.

Figure 8.12 shows the erection sequence for a typical disk. This drawing shows the use of a starting block which is attached to the support cart. This variation is most applicable for YE2, where the support cart only spans the bottom two to four sectors. The starter block may in fact be part of the cart structure.

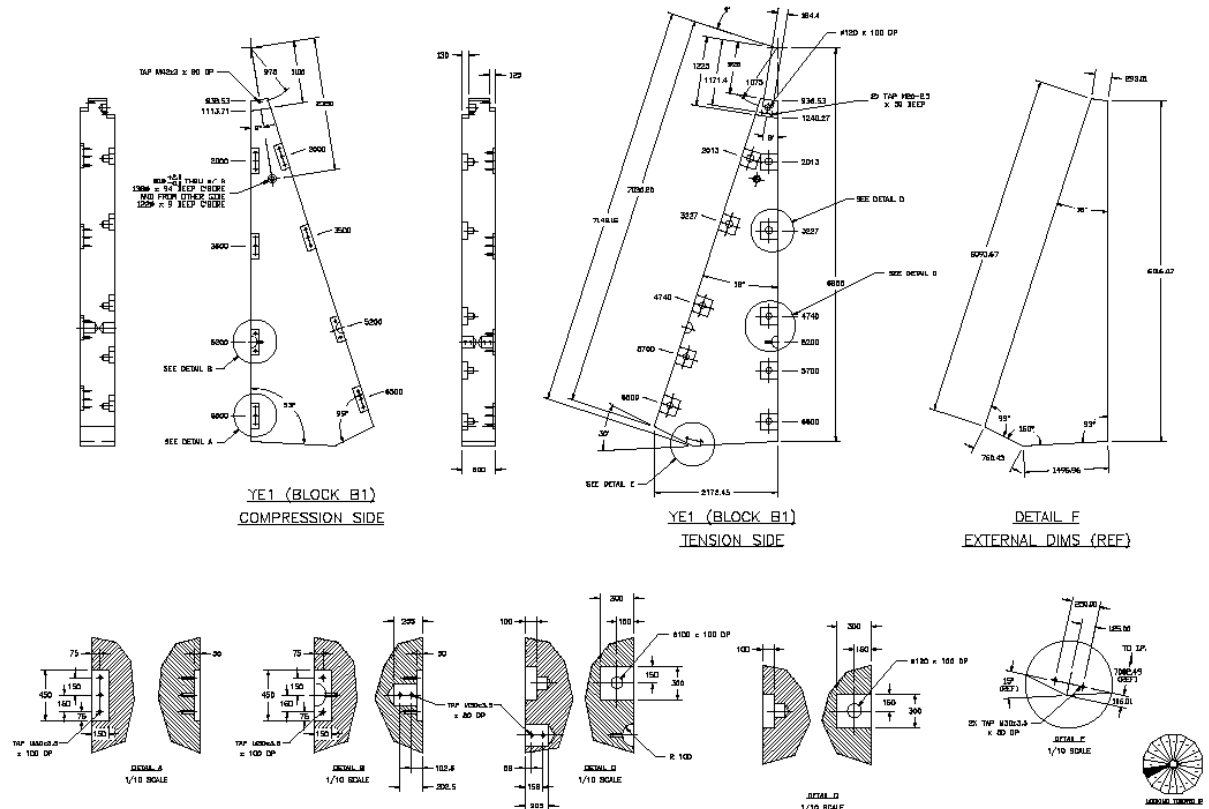


Fig. 8.11: Typical machining of a sector block showing connection features per our reference design. All dimensions are basic, no tolerances applied.

Individual block tolerances and gravity will require careful analysis of errors in this scheme. It is anticipated that the last block will have to be machined to fit. This is done by measuring the space left for the last block with respect to reference points on adjacent blocks and then determining the final shape of the last block.

8.2.6 Joint Alternatives

As mentioned earlier, there are many possible variations for a mechanical joint. The criteria for a joint are as follows:

- Ease of assembly and possible disassembly. This will allow for possible correction to a block.
 - Verification prior to final assembly at site. This will allow full erection of disk at the factory and will help minimise assembly time on site.
 - Deterministic design of load carrying parts. The joint can be analysed in detail to determine its proper operation under all loading conditions.
 - Possibility of introducing joint preload. This will allow for smaller overall distortions and will help with life expectancy of the joint.

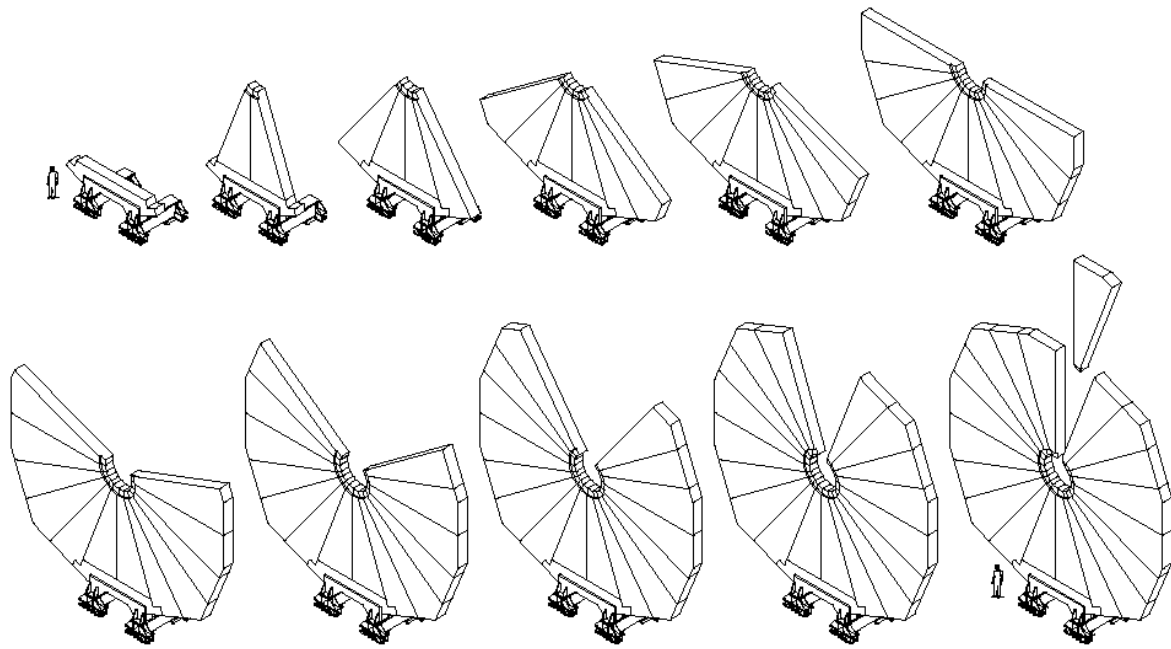


Fig. 8.12: Erection sequence. Last block machined to fit.

Many designs can satisfy these requirements. Presented below is one alternative. It must be noted that any design must minimise the amount of machining of the blocks. It must also minimise voids as they degrade magnetic performance of the disk at these locations by causing field non-uniformity. It is anticipated that this will not be a major concern unless the joint design has very large voids. The sensitivity of the magnetic performance to voids has not been studied in detail.

8.2.7 Joint Preload

In 8.1.2, a disk is modelled with 24 sectors. Each sector is attached to adjacent ones by letting them share a single common point (node) at several joint locations. In this case, regardless of the distortion field, this node remains common, i.e. the sectors are always attached at this point with zero separation. The interpretation of this is that the joint is assumed to be preloaded to a level where it never separates. If no preload is present, a small separation will occur at the joint and the overall distortion of the disk is likely to be slightly higher. This has not been modelled or calculated as of yet. It is anticipated to have a small effect on overall distortion. However, joint preload may be essential due to other factors such as aiding in assembly, and for longer life in cyclic loading.

For a large joint, application of a preload may require innovative approaches. One approach would be to use the thermal expansion of parts to introduce a preload. In the joint design shown in Fig. 8.16, no preload is assumed.

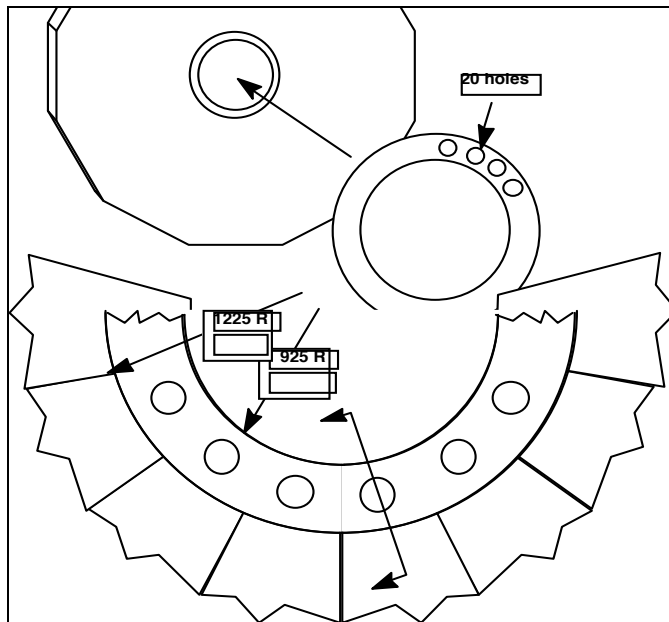


Fig. 8.13: Central ring of YE1 disk (YE2 and YE3 have similar rings).

8.2.8 Center Ring Connection

The joint at the centre of the disk is under high loads also. A central ring will be required to tie the tips of the blocks together. A ring is chosen, instead of individual plates, because the pins get very close to each other. A centre ring will also aid in the assembly process by providing a reference circle in the centre of the disk.

Figure 8.13 shows the centre ring that is fitted into the centre to resist this load.

Figure 8.15 shows the connection of the ring to the disk.

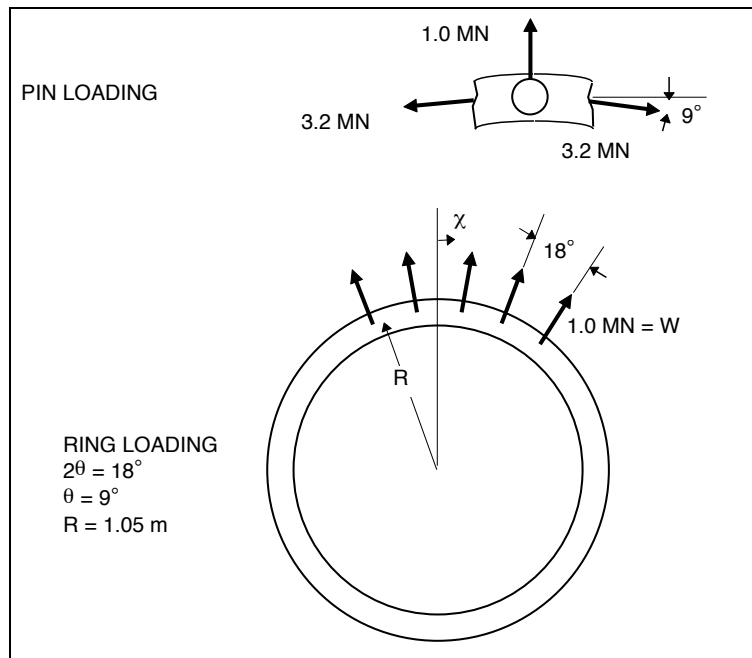


Fig. 8.14: Loading of central ring and pins.

8.2.9 Center Ring Loading

As the disk deflects toward the IP, each individual sector exerts a radial force on this ring through the pins. This load causes a combined tension and bending load on the ring cross section and a combined bending and shear on the pins.

In figure 8.5, the loads on a single sector are shown. The innermost force of 3.2 MN is resisted by the ring. This force is in a tangential direction, however, the resultant force on the ring from the pin will be in a radial direction.

In figure 8.14, the loading condition of the pin and the central ring are shown. Note that the analysis was done for a 24-sector construction. However, the plan is to build the disks from 20 sectors, so this force is applied at 20 locations on the ring. The analysis will be updated to reflect the actual number of sectors as the design progresses.

8.2.10 Center Ring Stress Analysis

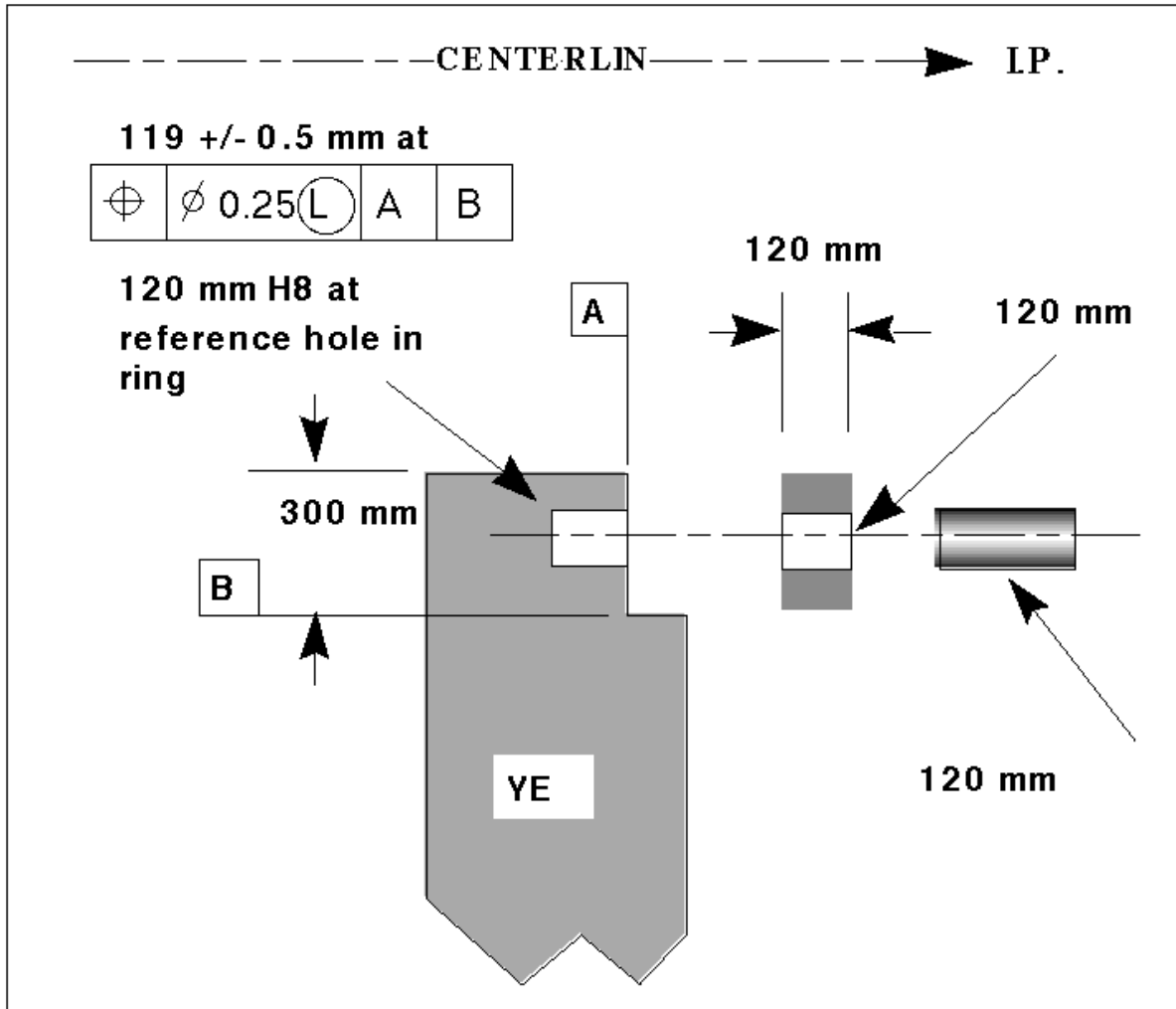


Fig. 8.15: Connection of central ring to YE.

The centre ring is under 20 equal and radial loads as shown in Fig. 8.14. These loads cause bending moment (M), tension or tangential force (T) and shear or radial force (V) as shown below [8-3]:

$$M = \frac{WR}{2} \left(\frac{\cos \chi}{\sin \theta} - \frac{1}{\theta} \right)$$

$$T = \frac{W \cos \chi}{2 \sin \theta}$$

$$V = -\frac{W \sin \chi}{2 \sin \theta}$$

The resulting values are listed in Table 8.3. The moment changes sign as a function of c . This is due to the fact that the ring is being forced from a circle into a 20-sided shape. The tension is the force between sectors and is constant. This results in a tensile stress on all cross sections. The shear force is highest at the pin holes.

Table 8.3
Loads on central ring.

Location	c (degree)	M (N-m)	T (N)	V (N)
Between pin holes	0,18,36,...	13830	3.2×10^6	0
At pin holes	9,27,45,...	-27620	3.2×10^6	0.5×10^6

Since the ring radius is large with respect to its section, one can use formulas for a straight beam to calculate stresses. The resulting error in this assumption is about $\pm 10\%$ for either the extreme fibres on the inside radius or the outside radius [8-4]. The highest stresses will be near the edge of the hole due to stress concentration. The combined bending and tensile stresses can be calculated from:

$$\sigma = \frac{T}{A} + \frac{My}{I},$$

where:

A = Net cross sectional area,

I = area moment of inertia,

y = distance from the neutral axis.

This results in a tensile stress of 152 MPa at the edge of the hole, a tensile stress of 163 MPa at the ring outside radius at the hole location and a tensile stress of 97 MPa at the ring inside radius between the hole locations.

The stress concentration factor for edge of the hole is about 2.4 [8-5] and therefore, this location is most critical for cyclic loading. The stress at this location varies between 0 and 152 MPa as the magnet is cycled because of lack of preload.

Ring material is alloy steel AISI 4340 with properties as shown in Table 8.4. The notch sensitivity factor for this material and average machined surface is about 0.9. This gives a fatigue stress concentration factor of 2.2 for near the hole. The equivalent static stress for these conditions is 772 MPa. This gives a safety factor of 1.3 for infinite life. It must be noted that infinite life is defined as more than 10^6 cycles. Therefore a safety factor of 1.3 for infinite life is appropriate as the magnet is cycled very infrequently. From a strictly static point of view, the safety factor is about 6 to yielding for the highest stress location.

Table 8.4
Material properties for centre ring.

Yield strength	1000 MPa.
Tensile strength	1140 MPa
Hardness	34 RC
Elongation	15 %
Endurance limit	570 MPa (infinite life)
Working endurance	240 MPa (machined surface, 99% reliability, 0.7 size factor)

8.2.11 Pin Stress Analysis

The pin has a bending load of 1.0 MN. Assuming all of the load is applied at the end of the pin, i.e. worst load distributions, bending moment is 120000 N-m and maximum bending stress is 707 MPa on the surface. Therefore the stress varies between 0 and 707 MPa as the magnet is cycled because of lack of preload.

Pin material is alloy steel AISI 4340 with surface properties as shown in Table 8.5.

Table 8.5
Material properties on surface of pin.

Yield strength	1570 MPa.
Tensile strength	1950 MPa
Hardness	55 RC
Elongation	10 %
Endurance limit	975 MPa (infinite life)
Working endurance	464 MPa (ground surface, 99% reliability, 0.7 size factor)

No stress risers exist on the surface. The equivalent static stress for these conditions is 1550 MPa. This gives a safety factor of about 1 for infinite life. As in the ring this is justified due to the very low cycle rate. From a static point of view, the factor of safety is 2.2 to yielding.

The pin has a shear load of 1.0 MN, which gives a maximum shear stress of 118 MPa at the centre of the pin. Therefore, the principal stresses are 118 MPa and -118 MPa at the centre.

Properties of pin material at its centre are as shown in Table 8.6. No stress risers exist at the centre. The equivalent combined static stress for these conditions is 219 MPa. This gives a safety factor of 6 for infinite life.

Table 8.6
Material properties at centre of pin.

Yield strength	1350 MPa.
Tensile strength	1500 MPa
Hardness	45 RC
Elongation	12 %
Endurance limit	750 MPa (infinite life)
Working endurance	420 MPa (99% reliability, 0.7 size factor)

8.2.12 Sector Connection

Figure 8.16 shows a typical joint between the sectors. The joint is made via 2 pins and a plate. This joint is designed to be used on the tension side of the disk. The pins transfer the tensile load in shear to the plate. The plate is then loaded in tension.

It is important that a very good fit is achieved between the plate, the sectors and the pins. For this purpose it is anticipated that the pins and the plate would be machined to final dimensions. The sectors will also be fully machined, except for the size of the pin holes. They will be machined under size at the factory and be machined to final tolerances at site with the disk fully assembled. However, if the blocks are machined to a very high level of accuracy, it may be possible to preassemble all pinned connections at the factory for verification, then disassemble and ship to site and reassemble. The required level of accuracy has not yet been determined. We will discuss this with potential vendors.

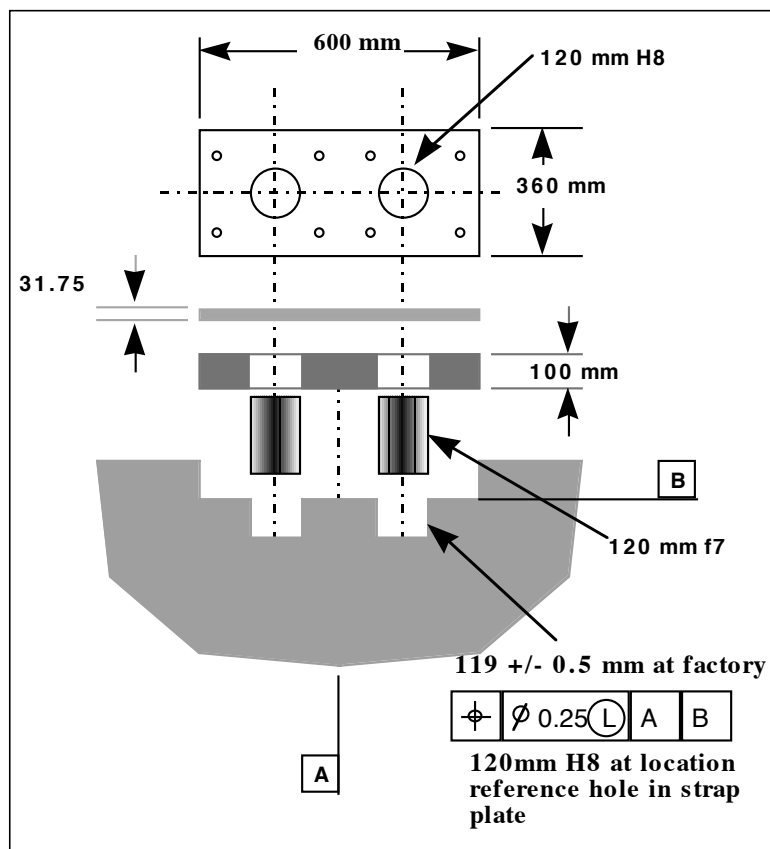
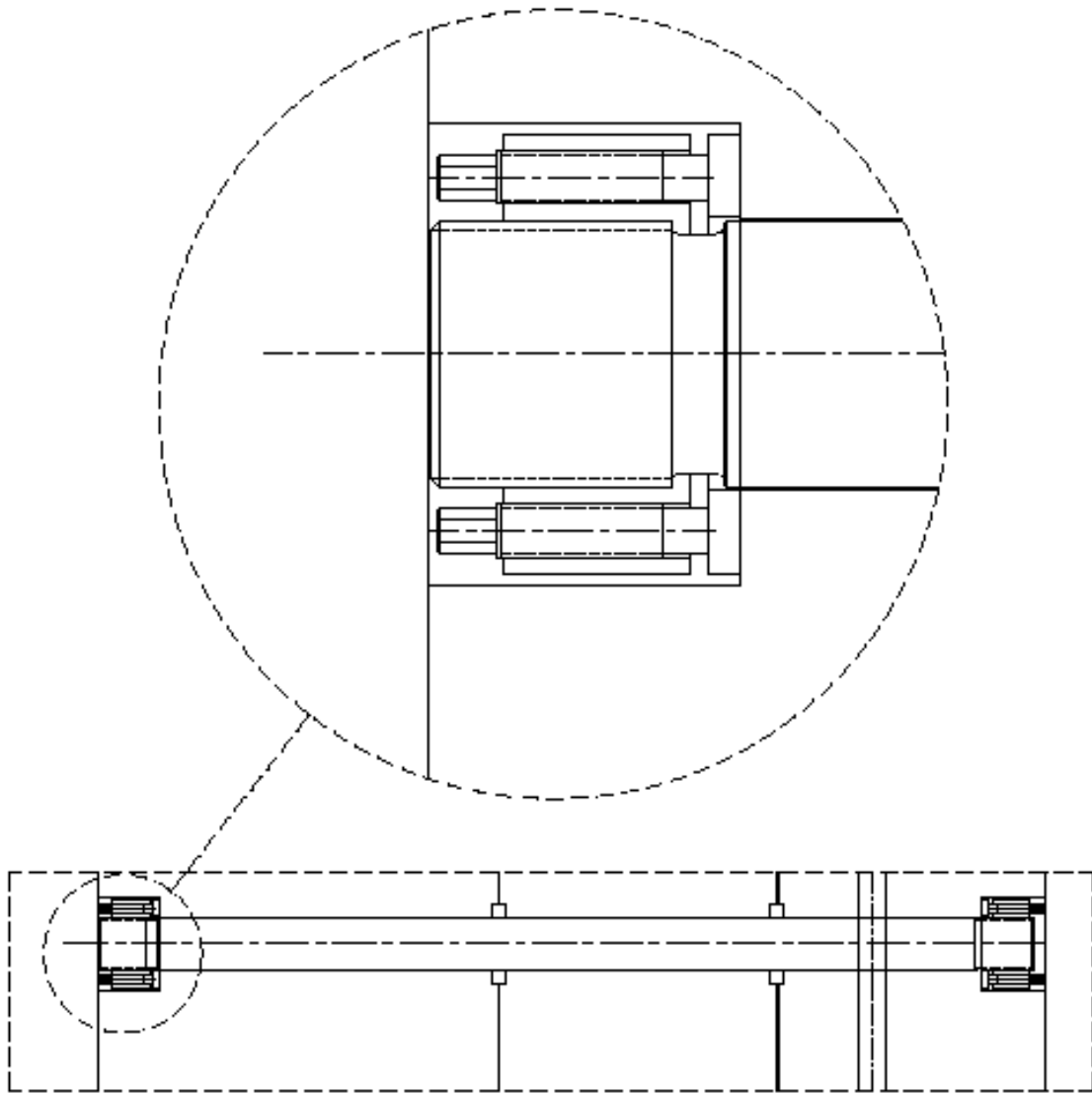


Fig. 8.16: Connection between sectors.

A cover plate is shown in the drawing. The plate serves two purposes:

1. To contain the pins against the magnetic force.
2. To provide a flat surface for mounting of other components, such as support posts for the chambers.

Cyclic loading analysis of the sector connections is similar to that for the centre ring and is being carried out in conjunction with studies of joint preload.

**Fig. 8.17:** Tie rod between nose and YE1 showing detail of nut.

8.2.13 Tie Rods

The maximum forces on the tie rods between the nose and YE1 is 2.62 MN for a 24-sector construction (section 0). For a 20-sector construction the maximum force would be about 3.1 MN. This gives a stress of 617 MPa for an 80 mm diameter tie rod.

The tie rod is made from alloy steel, AISI 4340 (EURONORM 83 35CrNiMo6), with

material properties as shown in Table 8.7.

Table 8.7
Material properties of tie rods.

Yield strength	980 MPa.
Tensile strength	1090 MPa
Hardness	38 RC
Elongation	12 %
Endurance strength	620 MPa (for 10^4 cycles)
Working strength	350 MPa (machined surface, 99% reliability, 0.7 size factor)

With this material the safety factor for static stress is 1.6. The effects of cycling loading and preload are under investigation at this time.

8.2.14 Disk Material

The material for the endcap will be low-carbon steel. This is the material of choice for its magnetic properties, however it has relatively low strength. The CMS endcap is under severe loading. This is in contrast to many conventional magnet yokes. A balance between good magnetic properties and moderate strength has to be achieved.

Chemical Requirements

The disk material will be AISI-SAE 1008 grade low carbon steel with chemical composition as shown in Table 8.8. Testing of each heat will be required to ensure compliance with these values.

Table 8.8
Disk material chemical composition.

Carbon	0.08% nominal, (0.10% max.)
Manganese	0.30% - 0.50%
Sulfur	0.05% max.
Phosphorous	0.04% max.

Mechanical Requirements

The mechanical properties of the disk steel material will be as shown in Table 8.9. These are nominal minimum values based on steel specifications.

Table 8.9
Disk material mechanical properties.

Yield Strength	240 MPa min
Tensile strength	350 MPa min
% elongation in 50 mm	22% min

As the rolled or forged plates for the endcap steel are very thick, it is anticipated that

mechanical properties will vary through the thickness as well as with direction. Testing of the material will be required to ensure compliance with these minimum values at all locations within the plates and in directions normal and parallel to the surface.

Magnetic Requirements

The relative permeability of the steel material will be as shown in Table 8.10. As shown in the magnetic section, most of the endcap steel is in saturation. The induction is via the superconducting coil. Therefore the absolute value of relative permeability is not of primary concern. However, uniformity of permeability is very important as it has an impact on coil forces. Requirements for uniformity are under investigation at this time. It is anticipated that sectors cut from a single rectangular plate will be used on diametrically opposite sides of a disk to help ensure magnetic symmetry.

Table 8.10
Disk material magnetic properties.

Relative permeability at 1.8 Tesla	155 min
Variability among all pieces at 1.8 Tesla	155-165

Size and Tolerance

The size of the raw plate material and the tolerances on size and form are dependent on fabrication processes chosen by the vendor. The design shows finished blocks. It will be up to the vendor to procure material consistent with the finished block sizes.

8.2.15 Fabrication

The fabrication process is very dependent on the chosen design and the capabilities of the vendors. It is anticipated that the fabrication process should be generally as outlined below:

- Special thick plates of appropriate composition and size are manufactured at a steel mill. It should be noted that there are only a few places in the world that can make plates this thick. Once the thickness criterion is met, the overall size of the plate is of major concern. It is unlikely that many mills could produce a plate large enough to yield two sectors of a 20 sector construction. If only one sector is cut from a plate, the waste would be too great and most likely render the process uneconomical. In such a case a larger number of sectors would have to be chosen.
- Rolling of plates. It is anticipated that a moderate amount of rolling is required in the plates to achieve the proper mechanical strength. It is unlikely that many mills can produce plates thick enough to get the required amount of reduction. It is also unlikely that any other process, with the possible exception of forging, can render a useful plate. This, again, limits the number of mills that can produce these plates.
- Preassembly and/or welding of sectors. It is possible to weld, or equivalently fasten, smaller sections to form a sector. This can be chosen by steel mills who cannot make large enough plates.
- Cutting of plates. Plates are cut to form rough sectors. It is anticipated that only the sides of the block need to be cut and that the two faces of the block are left in the as rolled condition. The type and amount of cutting should be minimised. It should also be done to reduce the total amount of waste. Cutting as close to the net shape is,

of course, desirable as it minimises the machining.

- Weld repair. It may be necessary to repair damaged plates during the fabrication process. The damage may occur during cutting or may be due to a void in the plate, or other similar anomaly. This is allowed. The type of weld has not been determined. It is anticipated that most conventional welding processes will be acceptable.
- Block machining. Each block will have to be machined flat and true to form on three surfaces. The two surfaces mating with adjacent blocks and the surface mating to the centre ring. It is anticipated that the surfaces forming the outside of the disk are left as rough cut. However, holes and other features for mounting of muon chambers will be required on these surfaces. The last block is machined after assembly of remaining blocks.
- Machining of holes and other features. Locating features and hole are machined in pairs of blocks. This is done to ensure proper fit during assembly.
- Preassembly. Each disk is entirely assembled at the factory. This is a requirement. It is important that all mating surfaces and features be verified and corrections be made at the factory. If there are joints that can be assembled only once, it is important that they be verified and partial trial joint assemblies be made at this time. As mentioned earlier, this is not possible for a fully welded option. In this case, sufficient preassembly must be done to verify correct assembly on site.

8.2.16 Assembly

In figure 8.18 through figure 8.21, the assembly operations are schematically shown. The main point about this scheme is that it is erected vertically. This will save floor space and eliminates the need for a turning fixture. It can also be erected directly on the cart.

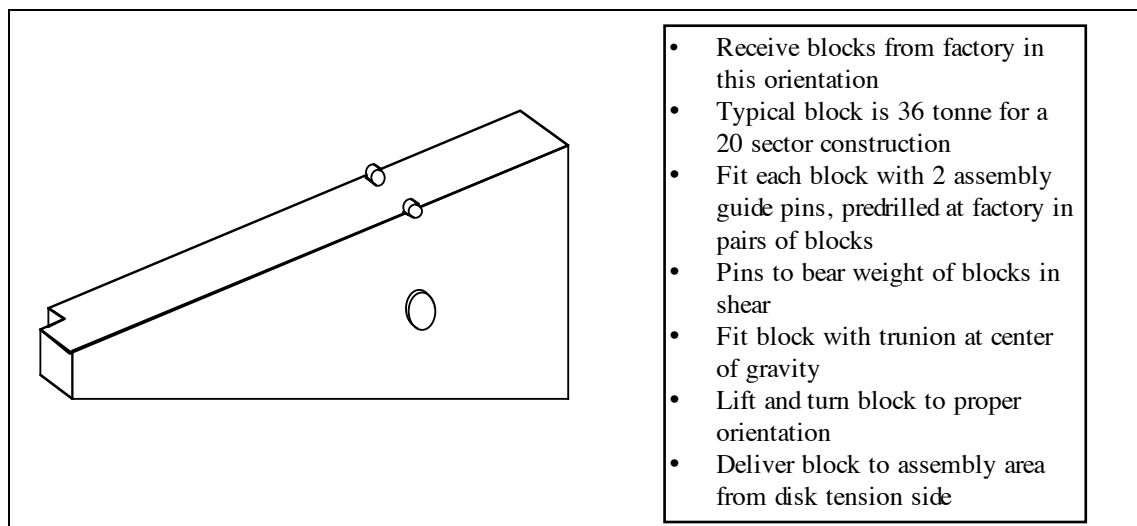


Fig. 8.18: Block pre-assembly preparation.

Horizontal assembly is also possible. This may have advantages in joint design and construction. However, it requires a very large turning fixture to make it vertical and other operations to position it on the cart. The vertical assembly is a goal to minimise time and space requirements.

8.2.17 Endcap Calorimeter Connection

The endcap calorimeter is attached to YE1 as one piece. The attachment scheme is shown in Fig. 8.22. The calorimeter is built in the horizontal position on the plate YN1. It is then turned to the vertical position as shown in this figure. The attachment is carried out by moving YE1 into position and engaging the conical interface. The main tie rods and on the outer radius and the smaller tie rods on the inner radius are then used to fasten the calorimeter in place. Fig. 8.23 shows the complete assembly.

Prior to calorimeter assembly, plate YN1 is fastened to YE1 and the magnetic test is conducted. This is done in order to have a complete magnetic assembly in place for the magnet test.

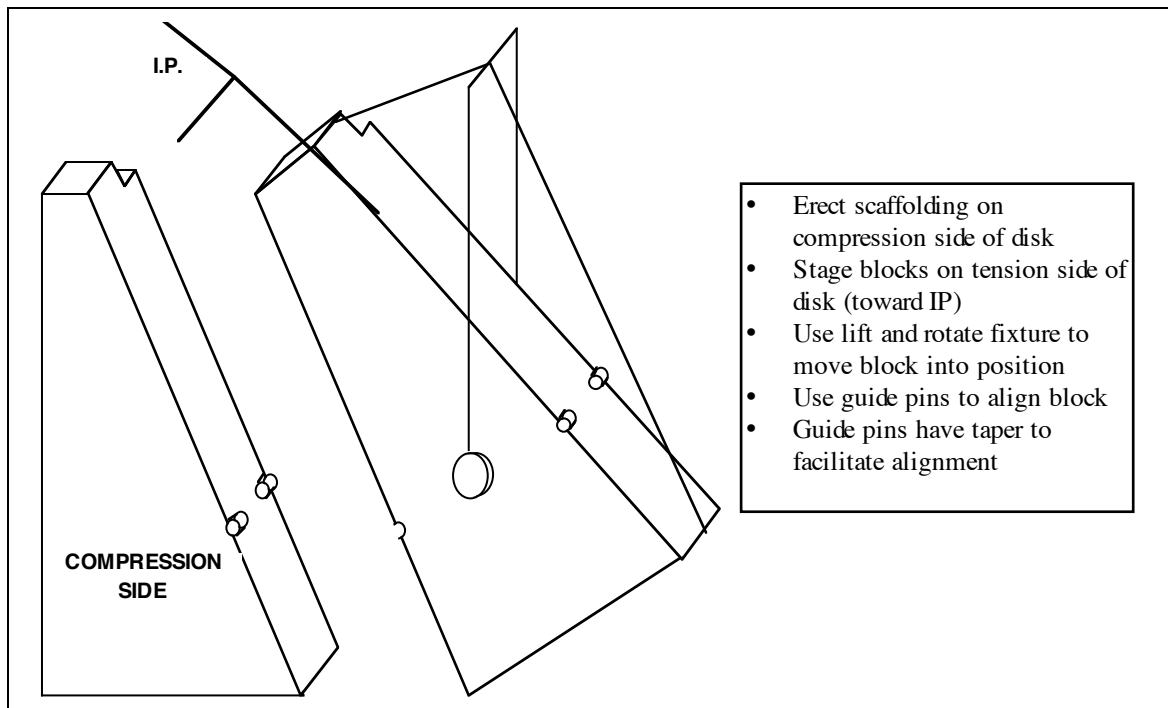


Fig. 8.19: Block rigging and positioning.

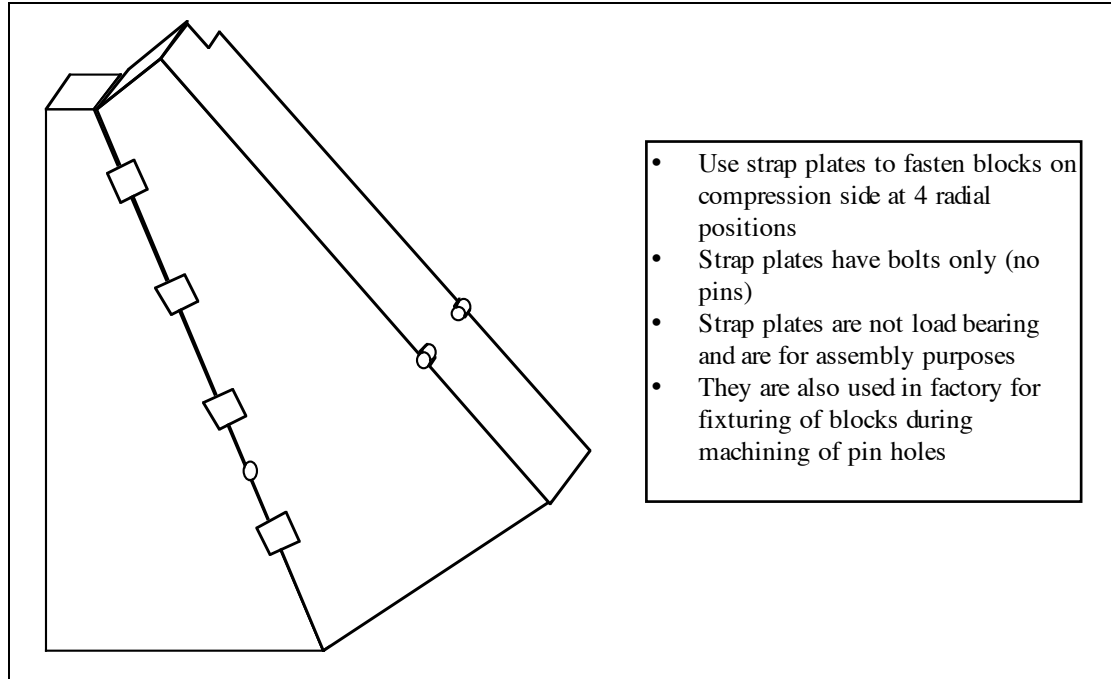


Fig. 8.20: Assembly of compression side (away from IP).

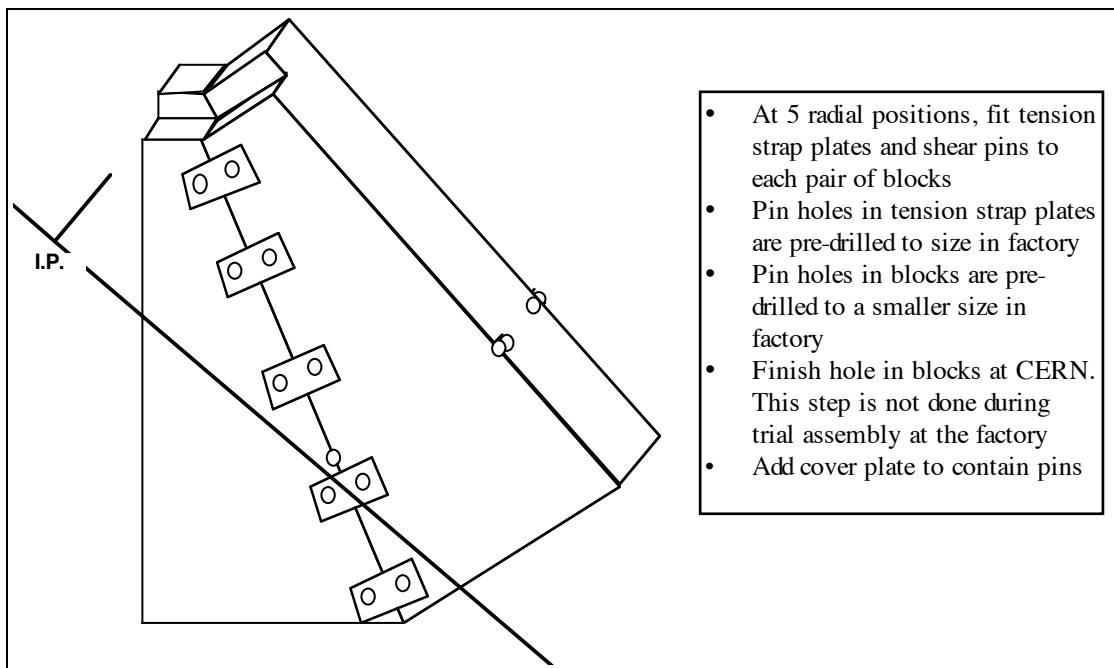


Fig. 8.21: Assembly of tension side (toward IP).

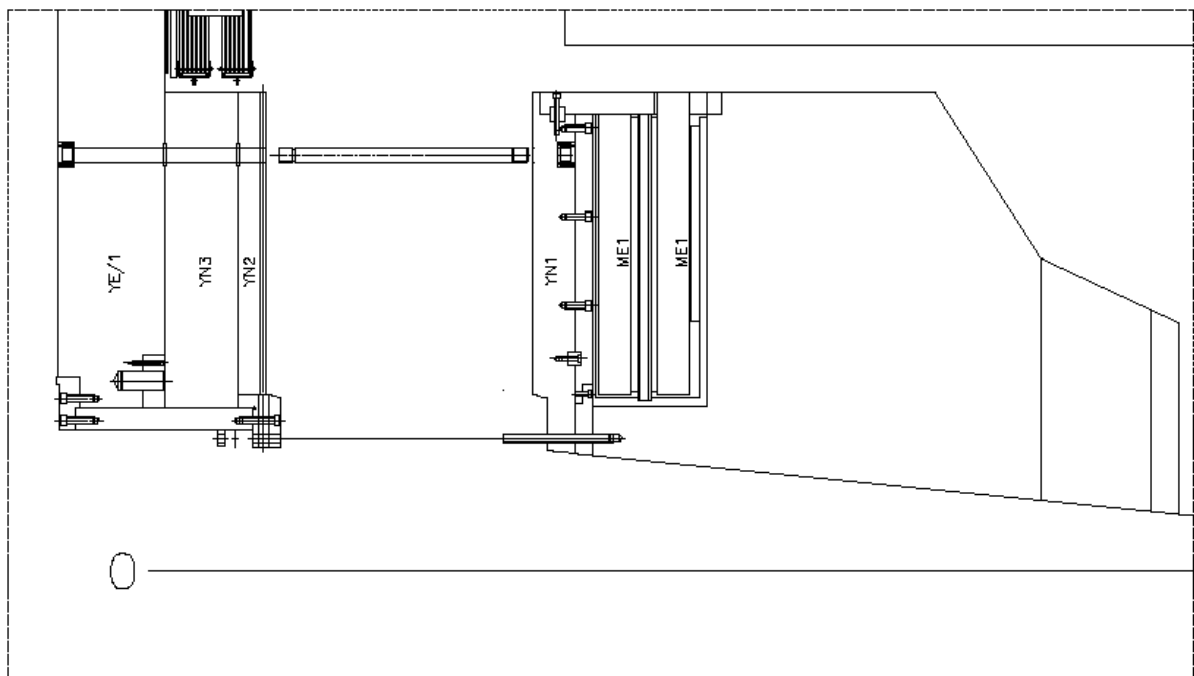


Fig. 8.22: Endcap calorimeter before attachment to YE1.

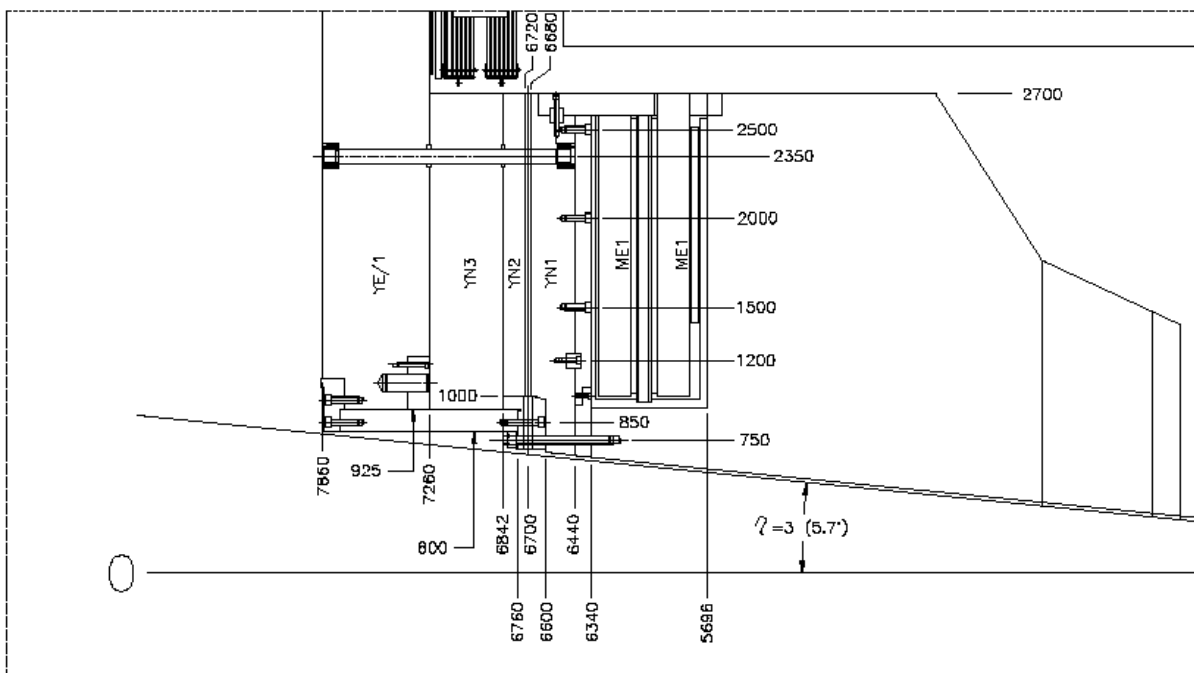


Fig. 8.23: Endcap calorimeter after attachment to YE1.

8.3 SUPPORT SYSTEM

This section contains the description of CMS endcap support and systems. There will be two endcaps. Each endcap consists of disks and each disk will have a separate cart. Therefore, there will be a total of 6 carts. The general arrangement of the carts is shown in Fig. 8.24. YE1 and the endcap calorimeter are shown in Fig. 8.25.

The carts will support the disks as they are installed in their final position within the CMS detector. They will also be used for support of the disks during construction on the surface hall, for motion of the disks during construction, and for detector opening and access.

Once all of the disks are fully constructed and instrumented with all detectors, the disks will be attached to form 2 integral endcaps. After this step, each endcap is one object and moves as one unit. The system is designed to use rollers, but studies going on to incorporate the same kind of air pad system that will be used for the barrel.

8.3.1 Stability

The disks are very large and relatively thin. A criterion for the stability must be chosen. We have designed for a width of support to height of centre of gravity ratio of 30%. This means that a force equal to 15% of disk weight is required to destabilise it. This is admittedly a large force, but the magnetic load on YE1 is about 7 times its weight. Obviously if the magnet is turned on while the disks are locked in any position but not closed fully against the barrel, the 15% lateral stability is insufficient and interlocks must be incorporated to avoid this situation.

The other issue is stability during possible earthquakes. At this writing, this has not been determined. We believe that the above criterion will satisfy this requirement.

Due to proximity of the disks, if all three disks were supported on one rail system, this number would be only 14%, which is quite low. Once we decide to support on two rails, 30% is easily attainable by alternating the support points between the inner and outer rails.

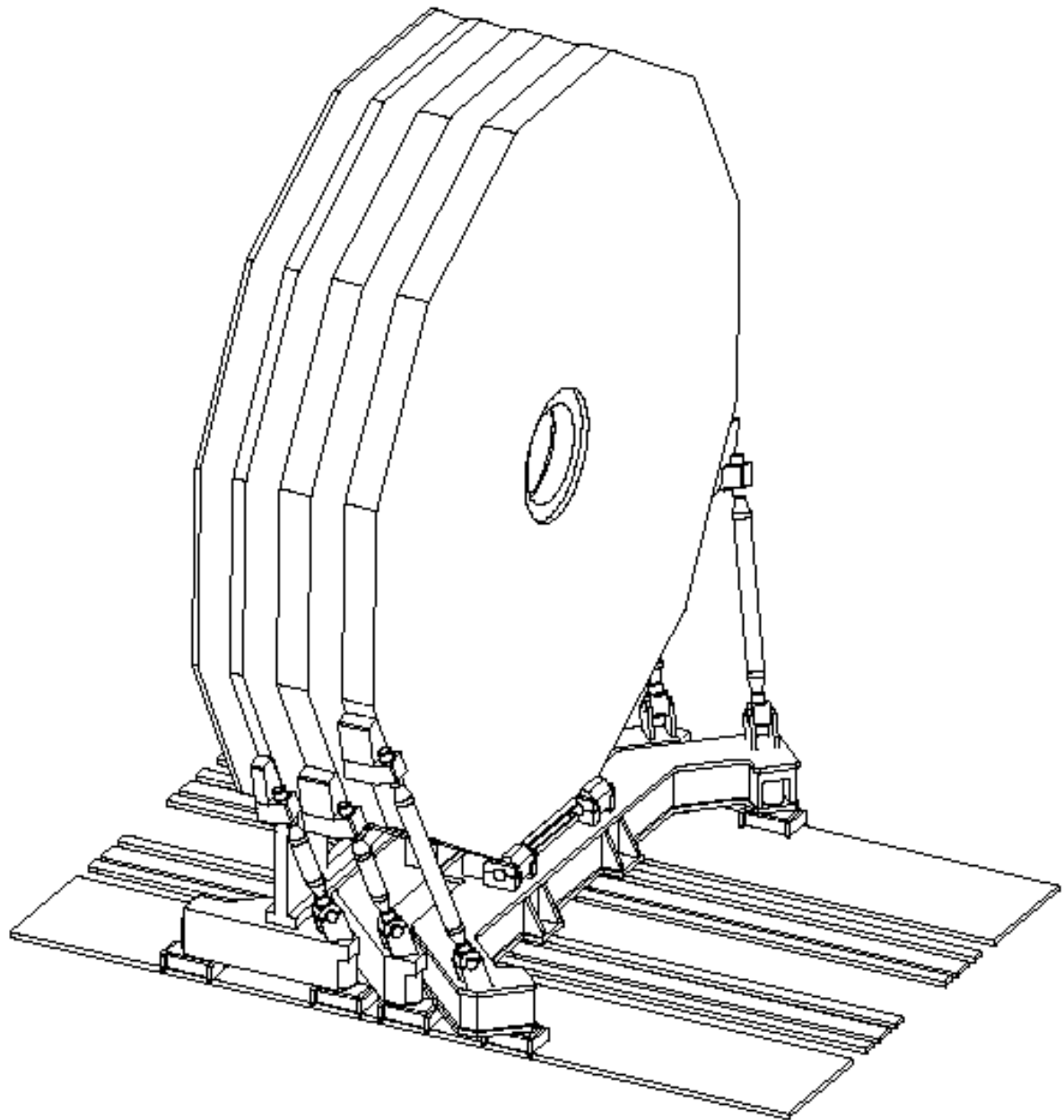


Fig. 8.24: Endcap disks shown on their individual carts in the closed position (ME4 shield wall is also shown).

8.3.2 Cart Design

Below are design parameters for each of the carts. YE1 cart had the most demanding requirements because of the large cantilever load of the endcap calorimeter.

- Each cart has a set of four movers which consist either of a roller or airpad with a hydraulic cylinder directly on top. The choice between rollers and airpads is currently under investigation.
- The movers are on inner and outer set of rails alternatively for YE1 and YE2, and on the outer rails for YE3.
- Each cart has a pair of braces to stabilise the disks. The braces reach as high on the

disk as possible. This is particularly important for YE1 where the brace reaches to 4 and 8 o'clock positions.

- Each brace had provisions for length adjustment to position the disk vertically.
- Each cart has a hinge connection to the disk. This is required due to the distortion in the disk as a result of the magnetic force.
- Each disk has an extension into the cart between the hinge shafts. This is designed such that if the braces were removed the disk will not fall.
- Each cart has provisions to rest on the inboard set of rails on sliding plates directly under the centre of gravity.

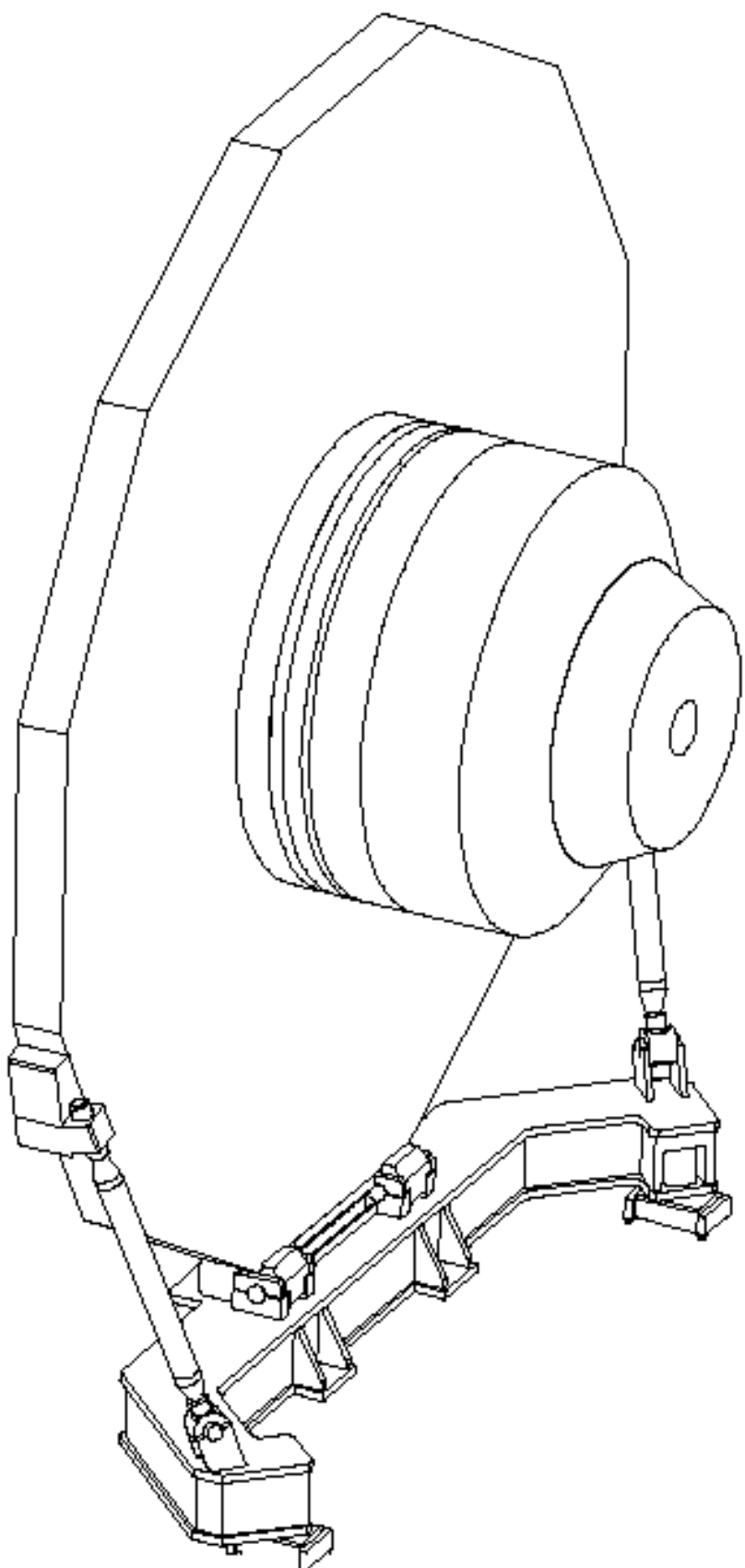


Fig. 8.25: YE1 disk on its cart with endcap calorimeter attached.

8.3.3 Operation

- Below is a general description of the operation of the support system.
- The endcap rides on the movers with the main jacks locked at a height slightly above final height.
- The endcap is brought close to the barrel but not touching.
- The main jacks are unlocked and the disks are lowered, with height control, on all four jacks to keep them level.
- The disks are set on grease pads which are on the inboard rails and under the centre of gravity. This sets the vertical position at the final height.
- Connections to barrel are engaged. These will be 4 hydraulic cylinders at f angle of roughly 75, 115, 255, 285 and accessible from the walkways.
- The main jacks are unloaded to a nominal constant force (pressure) of about 50 tonnes each. This maintains contact between rollers and the rails.
- The endcap is pulled on the grease pad against the barrel by the hydraulic cylinders.
- The hydraulic cylinders are maintained at a constant force. This force is greater than what is required to keep the disk from going downhill.
- The magnet is energised.
- The grease pads and the rollers allow the perimeter of the disk to move in Z away from the IP. Most of the load is on the grease pads.
- By maintaining only a small pressure in the main jacks, the cart and the brace will not be overstressed. The hinge between the disk and cart also aids in this respect.
- The hydraulic cylinders also allow this motion but maintain a constant force against the barrel.
- This procedure requires the operation of the main jacks in two modes: position control and force control. The hydraulic supply units must be capable of both modes. The hydraulic systems must be active during detector operation and appropriate interlocks must be incorporated.

9. VACUUM TANK

This system constitutes the external part of the solenoid cryostat. The vacuum tank, made of stainless steel, is cantilevered from the central ring of the barrel yoke. It houses and supports the superconducting coil, and must resist the unbalanced magnetic forces due to centring faults or misalignment of the solenoid, with respect to the return yoke. The inner cylinder, equipped with two horizontal rails, supports the weight and induced moments of the inner detectors, mainly the hadronic calorimeter barrel (HB). The outer shell is also used as a support for the cabling and piping of the inner detectors.

The vacuum tank consists of two concentric cylindrical shells connected through structural welds by two end flanges. Two chimneys are situated near the top of the vessel, on each side of the central ring of the barrel yoke. Their purpose is the following:

- i) the vertical chimney contains the cryogenic lines, maintaining the solenoid at 4 K during operation,
- ii) the second one, inclined at 30° to the vertical, contains the electrical leads, and is also used as the main pumping and venting line.

The design of the vacuum tank is made in such a way that the connection of the thermal shields with their pipework, and the tightening of the suspension and tie rods, remain possible even though structural welding must be performed to close the vessel.

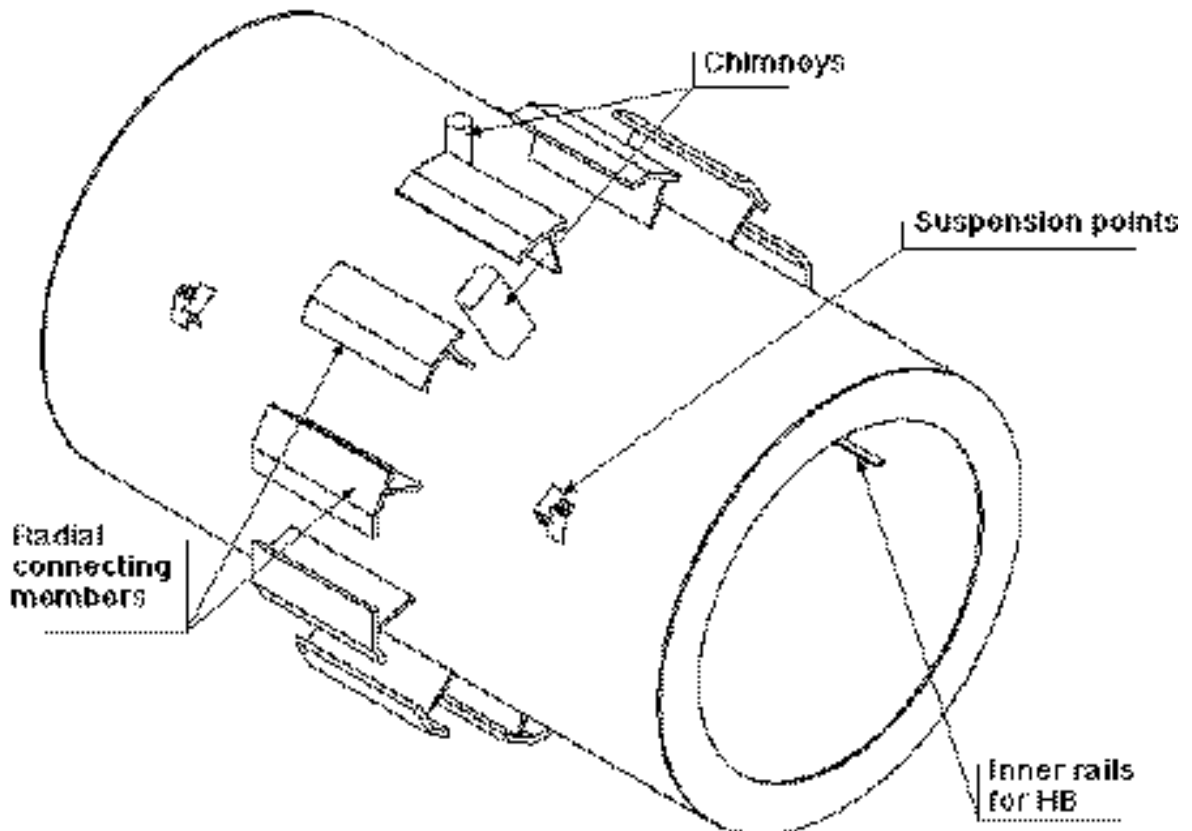


Fig. 9.1: Vacuum Tank general overview.

9.1 STRUCTURAL ANALYSIS OF THE VACUUM TANK

9.1.1 Introduction

Three independent Finite Element Analyses (FEA) of the vacuum tank have been performed, at CERN, FNAL and CEA Saclay.

The results are very similar and a combination of the three studies is presented in this report.

9.1.2 Material properties and allowable stresses

The material proposed for the vacuum tank components is stainless steel. A common steel used for such vessels is SA-240 SS304. The ASME Code is used throughout to verify the integrity of the vacuum tank components.

Table 9.1
Material properties used for the vacuum tank.

Material	SS304
Young's modulus	190 GPa
Poisson's ratio	0.3
Density	8000 kg/m ³
Elastic limit	205 - 230 MPa
Ultimate Tensile Strength	670 MPa
Allowable stress intensity	138 MPa

9.1.3 Dimensions and loads

The main geometrical dimensions of the vacuum tank are given in Table 9.2.

Table 9.2
Main geometrical dimensions of the vacuum tank.

Length	13000 mm
Outer shell external diameter	7600 mm
Inner shell inside diameter	5940 mm
Length of HB supporting zone	8864 mm
Inner shell thickness	60 mm
Outer shell thickness at $z < 2300$ mm	60 mm
$z > 2300$ mm	30 mm
End flange thickness	50 mm

The loads acting on the vacuum tank are the following:

- i) The external atmospheric pressure (103 kPa),
- ii) the weight of HB, electromagnetic calorimeter EB, and the Tracker for a total of

- 1050 tonnes,
- iii) the reaction forces of the cold mass supporting and preloading system, including maximum unbalanced forces, as shown in Fig. 9.2. This situation exists at two locations (see Z-coordinates of Table.9.3).

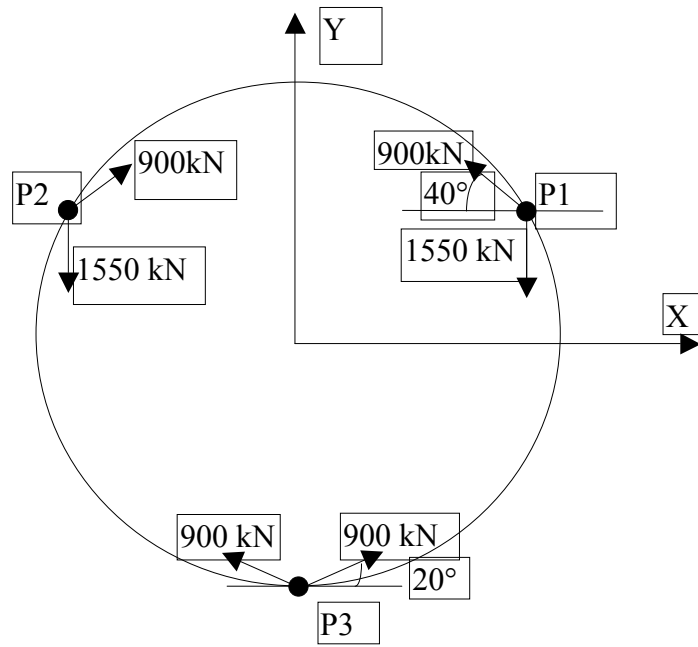


Fig. 9.2: Reactions of the cold mass supporting system.

Table 9.3

Coordinates and values of the reaction forces of the cold mass supports.

Point	Coordinates in mm (origin at interaction point)		
	X	Y	Z
P1	3265	1885	± 4000
P2	-3265	1885	± 4000
P3	0	-3770	± 3750

9.1.4 FEA Models and Results

Several independent models have been made to prove the sound design of the vacuum tank. Whereas the CERN/CEA analysis [9-1] aimed to verify the total integrity of the chosen wall thicknesses and the buckling safety, the more detailed FNAL study [9-2, 9-3] concentrated on the design of the rails which support the hadronic calorimeter barrel and the impact of the suspension points that house the coil suspension bars and the coil prestressing belt system.

The FNAL analysis has been performed using ANSYS; the CERN/CEA one was done with CASTEM 2000. Figure 9.5, p. XX shows the 3-D model of the vacuum tank. Around the suspension points a reinforced area of 45 mm thickness has been meshed with a finer grid. In Fig. 9.6 only the external part (30 mm) of the outer vacuum tank shell is shown. The deflection values are given in millimeters and indicate that the prestressing and suspension forces acting on the suspension shoulders create an inward-outward oscillation of radial displacement. The maximum inward deflection at the location of the shoulders is of the order of 9.5 mm. The points of maximum outward deflections are situated at an angle of + and -30

degrees in azimuth from the shoulders. It is of the order of 5.5 mm. To calculate the stresses in the rail that is welded to the inner vactank shell, the following approach has been made:

A coarse model of 1/4 of the vacuum vessel and rail was created in which the rail and inner vactank shell were modelled with solid elements while all other components were modelled with plate/shell elements. The welds were not explicitly modelled but considered only as line contact between the rail and vacuum tank. The hadronic calorimeter (HB) was modelled as a perfectly rigid plate acting on the vacuum tank through 40 spring elements. A refined submodel with explicit weld modelling was created with its center at the location of highest stress as indicated by the coarse model. The coarse model displacements were used for the displacements at the outer boundary of the submodel.

Finally, rail, weld and inner vacuum tank stresses were extracted from the submodel and compared to allowable stresses for SS 304 weldments.

Figure 9.7, p. XX shows the peak stresses at $z = 4432$ mm, i.e. at the end of the hadronic calorimeter loading. Assuming fully radiographed weld and primary membrane and bending stresses, ASME Section VIII, Div. 2 gives the following criteria for stress intensity:

- Primary membrane stress intensity limit = 138 MPa (20 ksi).
- Primary membrane + bending stress intensity limit = 205 MPa (30 ksi).

When the stresses in the most highly stressed region of the submodel are linearised to eliminate peak stress contributions, the following values are found:

- Primary membrane stress intensity = 113 MPa, therefore < 138 MPa.
- Primary membrane + bending stress intensity = 160 MPa, therefore < 205 MPa.

These values are clearly inside the target values. Nevertheless, full radiography of the welds is mandatory due to the high loading and disastrous consequences of failure.

In Figure 9.8 the sum of U_x and U_y displacements is plotted. The maximum displacement of the inner shell is + and -12 mm due to the bending moment induced by the hadronic calorimeter.

The complete deformation of the vacuum tank can be seen in Fig. 9.9, p. XX where the undeformed shape is shown in blue and the deformed in red. Amplification factor is 50.

The overall Von Mises stresses in the vacuum tank are shown in Fig. 9.10, p. XX. The highest value of only 102 MPa and the very low stress gradients prove the well designed distribution of material thicknesses in this highly loaded system.

To check if stability, i.e. collapsing of the vacuum tank, could be a problem, a buckling analysis on the base of eigen-values has been undertaken. The obtained values are 6.4 for the first and 7.7 for the second mode of buckling. Multiplying the actual loads by these values would lead to buckling. The buckling modes occur at the pre-stress locations due to the fact that the forces are applied very locally. The safety value against buckling is thus 6.4 for the lowest mode.

9.2 CONSTRUCTION CONCEPT

9.2.1 Transportable components

Due to its size and overall dimensions (13 m long x 7.6 m diameter), the vessel must be fabricated in transportable sections which will be assembled by structural welds after delivery to the CERN site.

The outer shell, which has a diameter exceeding transport limitations, will be split in three longitudinal sections (a central one about 4.6 m long, and two outer ones slightly shorter), each section being again split into two half shells (see Fig.9.3, items 1-6).

The inner cylinder which has a diameter within the transport limitations will be transported to CERN in the form of two half-length sections each 6.5 m long and 5.9 m in diameter (see Fig.9.3, items 7 and 8).

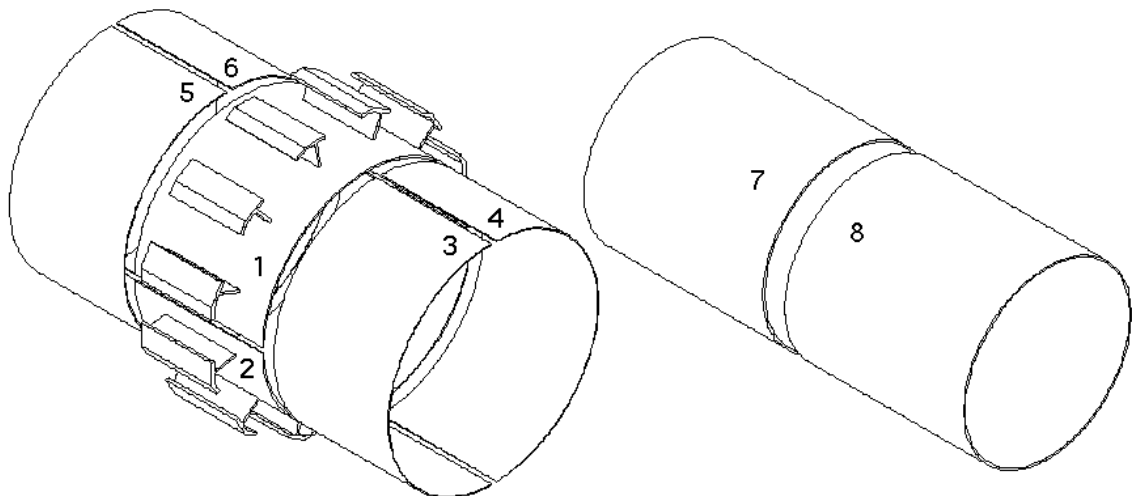


Fig. 9.3: Split outer and inner shell.

9.2.2 Manufacture of the outer shell

The central section of the outer shell is used for the pre-assembly of the central barrel wheel as it is described in Chap. 7.2. Hence its manufacture will be different from the two outer sections.

An internal structure acting as reinforcement and skeleton for the jig will be produced in two halves, each one comprising six radial webs converging onto a corresponding split bushing. Each half internal structure will be accurately machined on its mating surfaces in order that they assemble together precisely.

A previously rolled half-cylinder will then be fitted and mechanically constrained onto the pads of the half jig by tack welding. Once this operation has been repeated for the other half shell, the two components will be assembled together, precisely checked for geometry, then provisionally welded at the diametrically opposite seams using temporary straps.

The twelve outer radial connecting members will be fitted and welded to the shell in correspondence with the reinforcing webs. After stress relieving heat treatment, the complete structure will be placed on a vertical lathe and the corner pieces, situated at the extremities of the connecting members, accurately machined to provide a perfect dodecagonal profile for the trial assembly at the factory, (see Fig. 9.4).

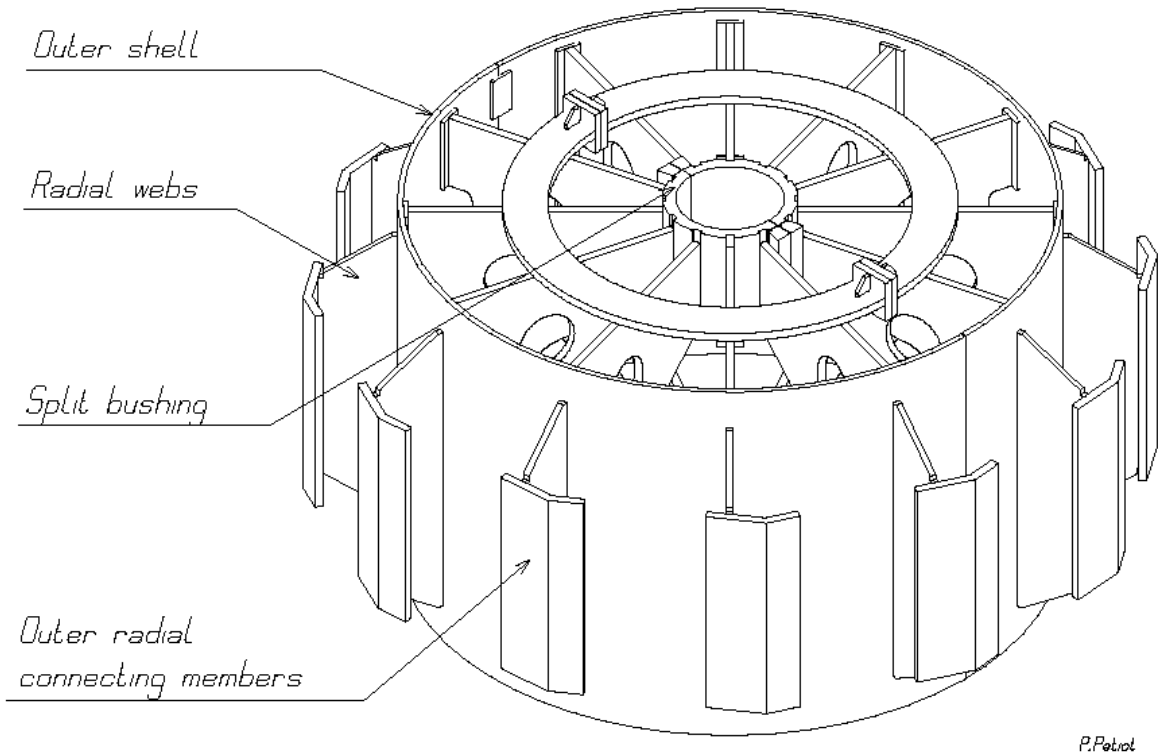


Fig. 9.4: Central section of the outer shell. This will be used as assembly jig in the Ferris Wheel for the central barrel yoke.

9.2.3 Manufacture of the outer shell end-sections

The 30 mm thick plates of the end-sections will be rolled to the specified radius. An internal structure will be inserted, to provide the rigidity during transport and machining.

The mating surfaces of each half shell, together with their internal structures, will be accurately machined. The two halves will then be assembled, checked for geometry, and provisionally welded at the diametrically opposite seams using temporary straps. The complete structure will be placed on a vertical lathe and precisely re-adjusted. It will then be separated again in two halves for transport.

9.2.4 Manufacture of the inner shell

The inner shell will be constructed as two complete cylinders, 5.9 m in diameter and 6.5 m long. Some temporary internal structural reinforcement may be added to maintain geometry.

The pre-machined support rails will be attached to the inside walls by structural welding. The temporary internal reinforcement will be completed, nevertheless leaving sufficient space for the insertion of a dedicated milling machine tool head. The complete assembly will be placed on a vertical lathe and the rail bearing surfaces and cylinder end faces machined to the required tolerances. The use of the temporary internal reinforcement will ensure geometric integrity and maintain the rail system tolerances.

This internal reinforcement will remain in place until the final welding of the inner shell to the end flanges at the CERN site.

It should be noted that as each hadron calorimeter half-barrel will be inserted from the corresponding end of the vacuum tank (see Chapt. 26), there is no strict geometrical relationship to be maintained between the rail system of one half-shell and its counterpart.

9.2.5 Trial Assembly

Before transportation the main components will be presented together at the factory, as if to be welded, to check the general geometrical conformity. Due to the presence of the inner reinforcement structures which maintain cylindricity, it will not be possible to perform the trial assembly of the full vacuum tank. However meaningful checks are still possible.

In particular, the two inner shell sections will be properly aligned to check the rail system and the interface with the end flanges.

Similarly, the outer shell end-sections will be presented to the outer shell mid-section, during trial assembly of the central barrel wheel.

9.2.6 Transport

Transport from the factory to the CERN site of the main items (8 in total for a gross weight of about 240 tonnes) will require road transportation for the last leg of the journey and sizes of pieces to be transported are very important.

All parts will include reinforcing structures to ensure geometrical stability and subsequent precision during final assembly. The maximum overall dimensions given below take into account this reinforcement; some protection should also be accounted for.

– outer half shell centre section: (2 off)	4.5 m by	5.5 m by	11.0 m
– outer half shell end section: (4 off)	4.3 m by	4.5 m by	9.0 m
– inner half-shell: (2 off)	6.0 m by	6.0 m by	6.5 m

Each item will be transported with its axis of revolution horizontal. The first two columns above are thus showing either the width or the height of each transported item.

9.3 FINAL ASSEMBLY

9.3.1 Reconstruction of the shells on the CERN Site

The two vacuum tank outer half-shells will first be mounted on the Ferris Wheel and welded together thus providing the assembly jig to be used for the central barrel ring (YB0) construction, as described in Chapt. 26, and as can be seen in Fig. 26.13-A, p. XX. When the assembly of YB0 is finished, the internal structure will be removed.

The four outer half-shell end sections will then be welded to the central section and the internal reinforcement structures will be removed completing the outer shell assembly. It may be possible that external reinforcement will be required, before the removal of the internal structures to maintain cylindricity near the end flanges. The outer shell of the vacuum tank will then be ready to receive the coil as seen in Fig 26.14, p. XX.

The two sections of the inner shell of the vacuum tank will be welded together on the turning system used previously to place the coil in the horizontal position. The same system will be used to place the inner shell in the horizontal position, ready to receive the coil itself as described in Chapt. 19 and 26, before closing the cryostat.

9.3.2 Closing of the Vacuum Tank

The vacuum tank must be closed around the coil by structural welding in the region of the end flanges, to transfer the loads generated by supporting the inner detectors. To allow disconnection of the coil from the turning device, and to allow completion of the coil ends as described in Chapt. 19, the inner shell will initially be connected to the outer shell by radial beams thus providing the structural integrity, but nevertheless allowing access to the inside of the vacuum tank. This access is needed for removal of the welding thermal protection and the completion of the thermal shield and super insulation facing the end flange regions.

The openings between the radial beams will then be closed by welding on thin closing plates.

10. PRE-INDUSTRIALISATION AND TESTS FOR THE YOKE CONSTRUCTION

Different issues have been studied for the yoke construction and for the displacement of the magnet elements in the surface assembly hall and in the cavern.

10.1 HIGH PRESSURE AIR PAD MOVING SYSTEM

As explained later in Chapt. 26, the magnet will be built in heavy segments (up to 2000 tonnes) which will have to be displaced during the assembly process to insert the coil and the vacuum tank inner shell. These heavy pieces will also be moved more than 100 m over the shielding plug before being lowered to the underground area. Once installed inside the underground area, access for maintenance of the subdetectors will require the endcap disks to be retracted. Maintenance of the barrel muon chambers will also require the outer barrel rings to be moved (see Chapt. 4). A heavy duty moving system is therefore required.

An air pad suspension system has been chosen which due to very low friction allows easy displacement of the heavy loads in all directions. Modern techniques using high working pressures have made these machines small and reliable. The choice of the system was straightforward since there is only one manufacturer in Europe if not in the world. These high pressure heavy duty air pads, used in civil engineering and in shipbuilding construction, are manufactured by the firm Noell. A labyrinth type rubber seal of 1.1 m dia. in contact with the floor surface and working at 30 bar gives a nominal lift of 250 tonnes. These air pads are usually coupled with hydraulic jacks to equalise their individual lifts and to raise and/or to lower the suspended load once it has reached its prescribed position.

Four such air pads and built-in jacks have been purchased, and a platform for a nominal 1000-tonne load has been constructed at CERN (see photographs in Fig. 10.1-A and Fig. 10.1-B, p. C-36).

Several tests have been carried out on a flat floor in order to learn how to use the pad system and to measure the friction coefficient. This was measured on different floor surfaces (plain concrete, painted concrete, steel plates, etc.), with the help of a lubricant e.g. glycol emulsion. Results were always in the order of 0.2%.

Some dynamic tests have also been made in order to simulate a sudden braking action (either a lack of air pressure or by hitting an obstacle). The system behaves as a mass supported on springs, represented by the air layer inside the air pads themselves, fully over damped.

To prepare for the displacement inside the underground area, a more realistic test has been set up, using an inclined cast concrete floor with a slope of 1.23% corresponding to the situation in the cavern. The first results, as predictable from results obtained on a horizontal floor, show that the friction is not sufficient to retain the load on the cavern floor. Consequently some form of retaining action will be needed when displacing the magnet elements in the negative Z direction.

The present retained concept is to use two pairs of hydraulic winches working in opposition (one pair on each side of the heavy elements to be displaced) and connected by their cables which will always be pulled in tension. The connections will be first fastened to the load and the air pads will be pressurised, then the winches will move the system up or down the slope. After reaching the correct position the air pads will be depressurised and the

connections removed from the load. The cables could then be connected to another load or stored into the cable drums fixed to the winches thus freeing the area of the temporary obstruction.

The development of 350-tonne air pads is being carried out by Noell. Four of these units will have the capacity of moving the first endcap disk YE1. A full series of qualification tests is foreseen for these units. If successful it is also planned to use the air pad system to move the endcap disks. This would considerably simplify the logistics inside the surface hall, and more important, inside the underground hall.

10.2 DRILLING OF DOWEL HOLES

It has been explained in Chapt. 7 that the barrel rings need doweling between their constitutive iron slabs and assembly brackets to withstand the shear forces generated by gravity loads. In order not to require high machining tolerances it has been decided to drill the locations for these dowels after each layer of slab has been assembled. Drilling must thus be performed in-between matched iron blocks of different grades.

Three drilling tests have been performed using a special drilling head (see photograph in Fig. 10.2-A, p. C-37) to drill the holes of 70 mm dia. and 800 mm deep between matched iron blocks of the same grade and of different grades. The first series was between St 360 / St 360; the second between St 360 / St 560; and the third between St 360 / high resilient StE 500. Results were very good with a hole diameter tolerance of 0.1 mm and an almost perfect straightness of the hole, less than 0.3 mm over the total depth of 800 mm (see photograph in Fig. 10.2-B, p. C-37).

A fourth test will be conducted to prove the validity of the technique using a lower grade steel, e.g. St 310, which is still acceptable for the barrel ring construction. This test will be carried out for the worst cases, St 310 / St 560 and St 310 / StE 500.

10.3 ASSEMBLY TECHNIQUES

Different tests are under consideration or development to determine the final assembly of the barrel rings and the endcap disks. These tests should also indicate the working behaviour of the components. They are aimed at two major objectives:

- i) to ensure sufficient reaction against the magnetic forces in beam direction Z (about 1800 tonnes, as explained in Chapt. 6). These forces develop between the corresponding slabs of the second and third layers of the barrel rings due to the fact that they are not retained by Z-stops as is the case in the first layer;
- ii) to make the endcap disks (supporting the large magnetic forces of 12000 tonnes, see Chapt. 8) almost like solid disks.

The first objective will be achieved in two different ways: circumferential welding of the 70 mm dia. dowel pins, and partial gluing (epoxy resin and/or anaerobic glue) of the surfaces in contact between the slabs and the assembly brackets. Tests showed that welding and/or gluing will be able to withstand all the applied forces by itself, thus giving a safety coefficient of 2 should both techniques be applied.

Concerning the second objective, several tests have been carried out during the last three years to see if the endcap disks could be assembled, on the CERN site, using the Electroslag technique. Tests have been done in collaboration with ESAB and TTS [10-1]. These tests have been done on 600 mm thick blocks, using two opposite welding shoes rising

vertically and moving the melting baths upward at a speed of 0.75 m per hour (see photograph in Fig. 10.3-A, p. C-38). An iron spacer of section 300 x 30 mm² was inserted between the blocks to maintained their geometry after welding (see photograph in Fig. 10.3-B, p. C-38). The gaps left on both sides of the spacers were the starting points of the baths which were fed with the usual metallic wires and fluxes. First results were promising in terms of overall deformation which was kept small, however cracks were discovered by macro inspection. They were mainly due to grain growth during solidification and by too much constraint induced by the spacer.

More tests have recently been done to understand the reason for the crack formation. EMPA and ESAB have just finished examination of a fairly good weld [10-2 and 10-3], presenting only microcracks which may be due to the fact that the base material is of low quality. Nevertheless it has been judged that the Electroslag process, although very attractive [10-4], will take too much time to be operational and too complicated to use in the assembly hall, so it has been abandoned. As explained in Chapt. 8 the present solution for assembling the disks, which are now made in sectors, is by mechanical fastening with bolts and/or pre-stressing techniques.

11. COLD MASS DESIGN CONCEPT

The cold mass is defined as the part of the CMS solenoid which operates at liquid helium temperature. It consists essentially of the superconducting winding and the quench back external cylinder to which the LHe cooling circuit is attached.

11.1 DESIGN CONSIDERATIONS

The physics requirements for the CMS magnet are a 4 T magnetic field at the centre of the detector, (see Chapt. 2). The main magnetic and geometrical design parameters of the cold mass are given respectively in Table 11.1 and 11.2.

Table 11.1
Magnetic Characteristics.

Magnetic induction at interaction point	4.0	T
Magnetomotive force	42.29	MAt
Conductor peak magnetic field	4.6	T
Winding overall current density	12.68	A/mm ²
Stored energy	2.69	GJ
Magnetic radial pressure	6.4	MPa
Axial compressive force at mid plane	148	MN
Operating current	19.5	kA
Inductance	14.15	H
Total number of turns	2168	
Turns per layer	542	
Dump resistor	0.050	W
Dump voltage	1000	V
Dump time constant	283	s

Table 11.2
Overall geometrical parameters.

Magnetic length	12.4	m
External diameter (without cooling tubes)	6.976	m
Internal diameter	6.360	m
Overall radial thickness	308	mm
Winding thickness	296	mm
Quench tube thickness	12	mm

Total mass (without supports)	220	t
-------------------------------	-----	---

In December 1994, the CMS Technical Proposal [1-1] included a complete design of the superconducting coil system. According to a general recommendation of CERN to build most of the large LHC components out of CERN site, the coil structure was designed to be compatible with road transportation; the coil was split into 4 longitudinal sections to be built in factories using the inner winding technique and then assembled in the CMS surface hall [11-1].

After detailed analysis of the challenges raised by the design presented in the TP, it was decided that, to simplify the design, a solution was to build the coil winding as a single unit provided that the winding operation could be carried out on the CERN site. In this case, the mechanical structure necessary for containing and assembling separate modules, consisting of a thick cylinder and thick flanges, could be eliminated and an external winding technique became feasible. This important evolution in the construction process interacts on the coil definition but keeps the basic concept in stabilisation, cooling mode and quench protection.

The CMS coil design is based, as for a number of existing large detector superconducting solenoids, on the enthalpy stabilisation concept. In this type of stabilisation method, only limited thermal disturbances can be tolerated in the superconducting winding, as opposed to the cryostability method. This concept has been successfully applied to detector solenoids because they are not subjected to substantial external sources of disturbance like fast varying magnetic field or particle radiation and they are operated in DC mode with low energising rate.

The basic features which have demonstrated the high quality and reliability of such magnets are the following:

- high purity aluminium stabilised conductor,
- compact impregnated winding and indirect cooling mode,
- quench back protection process.

Important information can be gained from the previous designs and construction techniques. The ALEPH solenoid, designed and built by Saclay [11-2], has been used in many ways as a reference model for the design of the CMS coil. But the CMS coil cannot be simply extrapolated from ALEPH, because of the very large increase in magnetic field from 1.5 T to 4 T and the requirement of limited radial thickness [11-6]. The main changes introduced in the coil design are:

- four layer winding instead of a mono layer one,
- self supporting winding structure based on a mechanically reinforced conductor, instead of a soft aluminium conductor,
- stronger aluminium alloy as structural material to withstand higher operating stresses due to both the higher field and the coil thickness requirement.

11.2 COLD MASS DESCRIPTION

The cold mass has an overall thickness of 308 mm. It is composed of a 296 mm thick superconducting winding and is surrounded by a 12 mm thick cylinder which acts as both cooling wall and quench back cylinder.

This cold mass is supported inside the vacuum vessel by the tie rod system described in Chapt. 18.

The winding consists of four concentric layers made from a 72 x 22.3 mm² compound superconducting conductor wound on its shorter edge. The conductor, described in Chapt. 12 and shown in Fig. 11.1, includes a high purity aluminium component as stabiliser and a high strength aluminium alloy component as the mechanical reinforcement, making the winding a self supporting structure.

The external cylinder provides both the cooling wall and the quench back cylinder. To improve the thermal conductivity in the longitudinal direction 1 mm thick high purity aluminium strips are laid down between the winding and the external cylinder.

The LHe cooling circuit consists of a network of pipes attached to the external side of the cylinder. Longitudinal manifolds are installed at the top and bottom of the coil and supply the semi-circular branches of the circuit. This parallel flow system works in a thermosiphon circulating mode which insures a homogeneous and stable flow distribution as demonstrated on the ALEPH solenoid [17-2], (see also Chapt. 17).

All the electrical insulation is made from glass epoxy composites. The ground insulation situated between the outermost layer and the external cylinder has a total thickness of 2 mm, that is 1 mm on each side of the aluminium strips. The inter layer and the inter turn insulation being respectively 1 mm and 0.5 mm thick.

The relatively small coil thickness results from the physics requirement for such a high compactness. It has two important consequences: first, a radial strain under field of 0.15% and secondly the stored energy density of 12.2 J/g. These basic characteristics, significantly larger than for previous detector solenoids, are fully taken into consideration in the present design.

11.3 THE CURRENT AND THE CURRENT DENSITY

These two determinant parameters are related to the coil stability and to the quench protection and they result from iterative calculations which are presented in the following chapters. However, the basic considerations are briefly resumed here to give a general understanding of the coil design.

The operating current I, and the current density J, in the pure aluminium can be related to the stored energy Es and the dump voltage U across the dump resistor by the following relation F(T), assuming an adiabatic behaviour and no normal zone propagation. This figure provides a basis for the preliminary design but it is also useful for understanding the interdependence of the parameters.

$$F(T) = \int_{T_0}^{T_m} \frac{C_p}{\rho} \cdot dT = \frac{J^2}{I} \cdot \frac{E_s}{U}$$

T_0 and T_m are respectively the initial and the hot spot temperatures, ρ the aluminium resistivity and C_p the conductor heat capacity per unit volume.

The stability criteria of such type of solenoid cannot provide absolute values for the parameters. It is based, in a large extent, to comparative characteristics. For the CMS coil the current density and the current sharing temperature have been determined respectively at $J = 28 \text{ A/mm}^2$ and $T_{cs} = 6.5 \text{ K}$, for providing the same stability conditions than the ALEPH solenoid as presented in Chapt. 15. For comparison, in the ALEPH solenoid, the current density is $J = 40 \text{ A/mm}^2$.

For a hot spot temperature of $T_m = 100$ K the above relation gives a value of 20 kA for the current. In practice the coil dimensioning is based on a value of 19.5 kA. This leaves a 500 A safety margin to compensate for a possible lower filling factor.

Measurements on the ALEPH solenoid have shown that the temperature rise following a fast dump is actually much lower than the prediction given by this simplified criteria. This is mainly due to the fact that the normal zone propagation is dominated by transverse diffusion of the heat released into the external cylinder by eddy currents. Computations of the quench behaviour of the CMS coil show a similar situation and are shown in Chapt. 16. The typical calculated results are 60 K for the hot spot and 56 K for the final temperature.

The hypothetical case of the failure of the quench protection system, which is the worst case, has also been analysed. In the first period the normal zone develops without inducing significant currents in the external cylinder, but after a delay of about 80 seconds the current decay becomes fast enough to initiate the quench back effect, thus protecting the coil. The coil maximal temperature is then 146 K.

11.4 SELF SUPPORTING WINDING STRUCTURE

In the CMS coil, the aluminium alloy is not used in the shape of a thick external cylinder as was the case for the previous solenoids of this type, but is directly attached to the conductor [11-6, 11-7]. This mechanically reinforced conductor configuration has been designed essentially for mechanical reasons. However, it also provides significant advantages for stabilisation and quench protection because it increases the conductor enthalpy.

In the CMS coil, the only structural component is the conductor itself. Two requirements led to this concept:

- The first requirement is to keep a low level of shear stress between the insulating material and the aluminium alloy.
- The second requirement is related to the 0.15% hoop strain at nominal field, resulting from the radial compactness of the coil required by the CMS detector. Under this operating condition the pure aluminium component undergoes cycles in the plastic domain. It is fundamental to control the cycles of the pure aluminium by tightly fixing it to the aluminium alloy. The bonding must have a good mechanical performance and must be of a metallic nature.

11.5 NUMBER OF LAYERS

The operating current, the total number of turns and the conductor size are summarised in Table 11.3. The number of layers however is still a free parameter at this stage.

Table 11.3
Design parameters independent of the number of layers.

Operating current	19.5	kA
Total number of turns	2168	
Total length of conductor	45.400	km
Conductor cross sectional area (insulated)	1606	mm ²

The choice of the number of layers will fix the conductor aspect ratio and the unit

length as shown in Table 11.4. As there is no mechanical support structure an even number of layers is necessary to compensate the conductor hoop force at the extremities of the layers. This is done by mechanically tying the conductor ends from adjacent layers and also from the first and the last layers.

From the beginning, the reference models were the existing mono layer or two layer solenoids. For the 4 Tesla CMS coil, the required number of turns cannot be contained in a two layer winding. The minimum number of layers is four and this extrapolation was found acceptable from the steady state thermal calculations, the maximum temperature difference being lower than 50 mK. However it must be kept in mind that this is only an extrapolation and that it is not easy to predict the stability behaviour when increasing the thermal barrier between the helium heat sink and the high field innermost layer. A large number of layers clearly increases this thermal barrier. Provision must also be taken for the conductor junctions inside the winding.

Table 11.4
Conductor unit length and aspect ratio vs. number of layers.

Number of layers	Conductor size mm ²	Unit length km
2	144.0 x 11.2	22.3
4	72.0 x 22.3	11.3
6	48.0 x 33.4	7.6
8	36.0 x 44.6	5.7
10	29.0 x 56.0	4.6
12	24.0 x 66.8	3.8
14	20.6 x 78.4	3.2

The evolution of the winding concept into one single section and the use of an external winding method could lead to a reconsideration of the number of layers because the winding may look easier to make, bending the conductor on its smallest inertia being simpler.

It is known by experience that square shape conductors are more difficult to properly dispose in a winding, and that an aspect ratio larger than two is always preferable. Table 11.4 shows that the configurations using 6 to 10 layers use conductors of low aspect ratio cross section. A 12 layer winding uses a 24 x 66.8 mm² conductor of 3.8 km unit length. But it must be recalled that an increase of the number of layers brings important drawbacks, because it increases:

- the number of end junctions,
- the inter layer junction overall dimension in the axial direction,
- the number of epoxy layers and thus the thermal gradient through the winding,
- the coil geometrical defects which are cumulative with the number of layers.

This last point is one of the most important because the winding requires a high geometrical quality in order to ensure a good performance of the coil especially to prevent conductor slips or dangerous stress concentration. Winding the conductor with its smallest inertia in the axial direction greatly facilitates the stacking.

After comparing different configurations, it has been concluded that a limited number of layers and the radial orientation of the largest conductor side are favoured to build a uniform and well stacked winding, and the four layer winding has been retained.

11.6 PURE ALUMINIUM BEHAVIOUR

There are two consequences, coming from the low yield strength of the pure aluminium with respect to the coil operating point, that must be considered in more detail: first the structural function of the pure aluminium and second the evolution of its properties when accumulating cold work.

11.6.1 Structural function

The CMS coil is designed so that the aluminium does not have any mechanical structural functions because, at nominal field, the operating point will be in the plastic domain, even if improved strength aluminium is used. The pure aluminium and the aluminium alloy components have the same elongation and the respective stresses are shared according to their respective mechanical characteristics. The mechanical computations show that, at the nominal point, the aluminium is necessarily in the plastic domain. At the contrary, the aluminium alloy works far below the elastic limit with a maximum Von Mises stress of 140 MPa. The yield strength of the aluminium is improved by the cold work accumulated by the magnetic field cycles so that the pure aluminium will support a larger and larger fraction of the magnetic load. From the mechanical point of view the most stringent situation is thus the first energisation.

It is difficult to predict in which metallurgical state the pure aluminium will be in, because it will be partly affected by the assembly of the alloy over the insert and also by the curing of the epoxy resin. As a basic principle the performance of the CMS coil should not depend on the mechanical state of the pure aluminium. The reference mechanical computations have been performed using the characteristics of fully annealed aluminium. For a more realistic comparison characteristics measured on the ALEPH conductor have also been used. Before winding, the ALEPH conductor gave a yield strength of 40 MPa at 4.2 K which indicates a high level of cold work obtained by the final calibration operation through a Turk head [11-9].

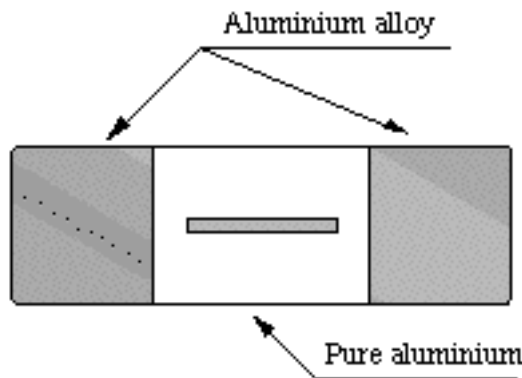


Fig. 11.1: Block conductor geometrical arrangement.

A proper geometrical arrangement for the conductor components is required to satisfy the above requirements for the pure aluminium. The best arrangement, called the box configuration, is a conductor where the alloy completely surrounds the aluminium (see also

Chapt. 12). Unfortunately it is too complex to build so a compromise has been made by using another configuration which is the block conductor [11-8]. It consists of a central aluminium insert containing the superconducting cable and two aluminium alloy sections of the same width welded on each side as shown in Fig. 11.1. The conductor is wound on its shortest side thus orienting the large side perpendicular to the magnetic field axis. This results in a winding composed of concentric cylinders in which the aluminium alloy provides the elastic mechanical structure, as can be seen on Fig. 11.2.

11.6.2 Electrical effect of the cyclic plastic strain

The electrical and thermal properties of pure aluminium change with cold work, but contrary to the mechanical effects, this evolution is a degradation. The increase of electrical resistivity is almost independent of the aluminium quality and is proportional to the total accumulated plastic strain [11-3]. In principle the resistivity and the thermal conductivity [11-4] of the aluminium can be deduced from the total amount of cold work seen by the aluminium, however, this is somewhat complicated since the degradation is partly cancelled when warming up to room temperature [11-5].

For the quench protection and stability computations the number of times the magnet is cycled is important, thus two reference values have been considered: 50 cycles for the first two years of operation and 300 cycles for the following twenty years. Table 11.5 gives the evolution of the RRR for these two values, without taking into account recovery due to the yearly warming up.

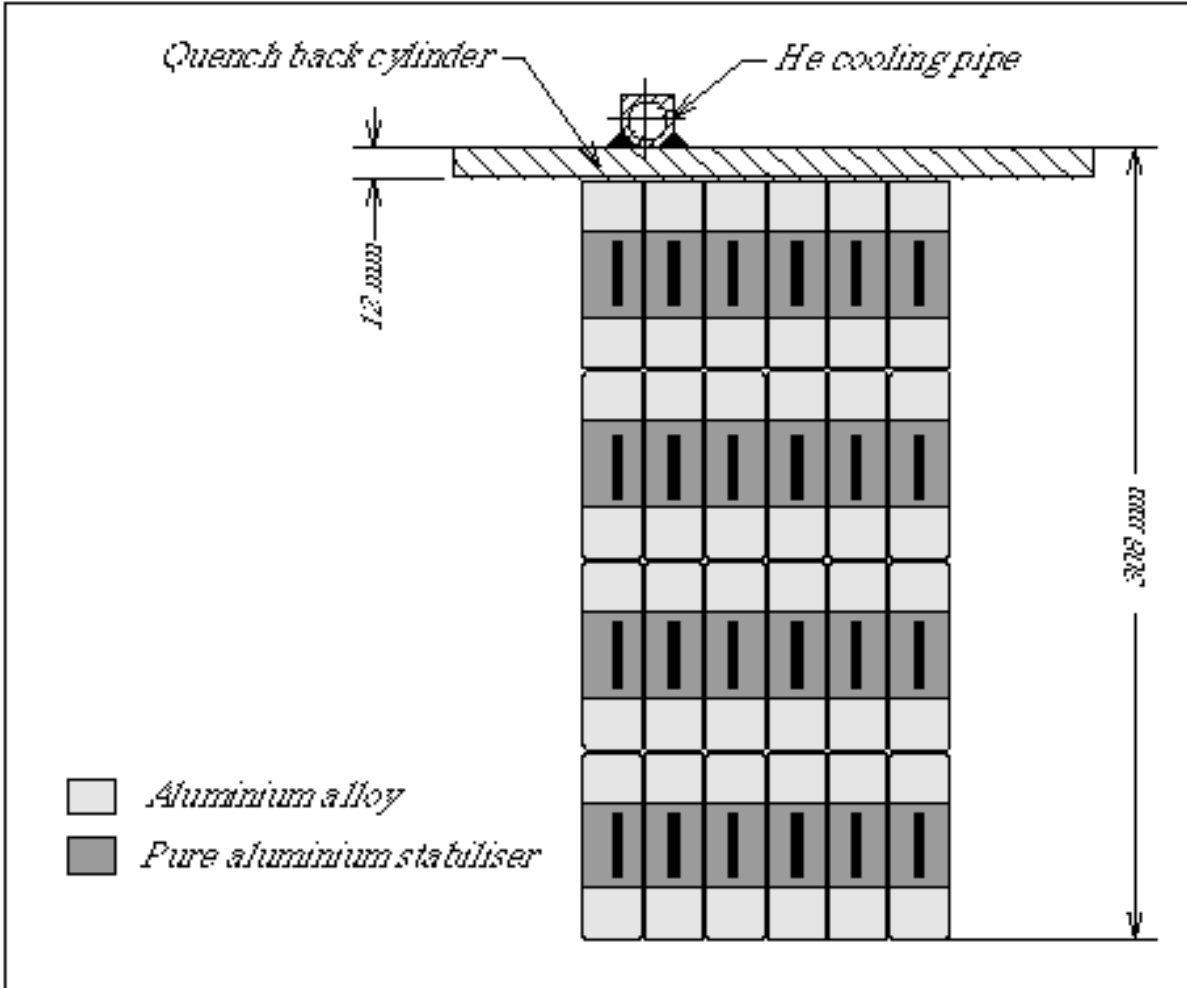


Fig. 11.2: View of the winding showing the structure in concentric cylinders.

Table 11.5
Aluminium RRR evolution.

Initial RRR	1500	1000	800
50 cycles			
Effective RRR	893	688	588
300 cycles			
Effective RRR	576	483	431

Both the stability and the quench protection analysis (see Chapt. 15 and 16) show that a RRR value of 400 is still acceptable: the long term evolution of the pure aluminium characteristics due to cyclic plastic strain will not affect the CMS coil performance.

12. CONDUCTOR

12.1 INTRODUCTION

The design of a self supporting structure obtained by mechanically reinforcing the conductor makes this component more complex than other aluminium stabilised conductors previously used for thin solenoids. The conductor must satisfy simultaneously mechanical and industrial feasibility requirements. This fact has been identified since the beginning of the project and it has lead to developments in several parallel directions. The overall dimensions and the sub component proportions are determined by the general coil design, according to mechanical strength, quench protection and stability requirements. However, these requirements can be met by many different conductor configurations. Three of all possible configurations have been studied at length and the results of the investigations have been presented in intermediate reports, based on the information available at that time.

These studies have lead to reduce the spectrum of options and the conductor structure and possible fabrication technologies have been decided. This has resulted in the so called “block” conductor configuration which satisfies both mechanical and fabrication requirements.

12.2 THE CMS CONDUCTOR

12.2.1 Conductor overall characteristics

The CMS conductor comprises 3 components: the Rutherford type superconducting cable, the high purity aluminium stabiliser and the aluminium alloy reinforcement. The overall characteristics are given in Table 12.1.

Table 12.1
Conductor overall characteristics.

Nominal design current	20.0 kA
Rated current	19.5 kA
Critical current at 4.2 K and 5 Tesla	62.5 kA
Total length of conductor	45.4 km
Overall dimension (bare section)	72 x 22.3 mm
Component cross sectional areas	
Pure aluminium area	659 mm ²
Aluminium alloy area	892 mm ²
Superconducting cable overall area	53.6 mm ²
Cu area	24.2 mm ²
NbTi area	22.2 mm ²
Void fraction	7.2 mm ²
Total weight of components	
Pure aluminium	81 t
Aluminium alloy	109 t
Superconducting cable	16 t
Cu	9.9 t
NbTi	6.1 t
Conductor	222 t

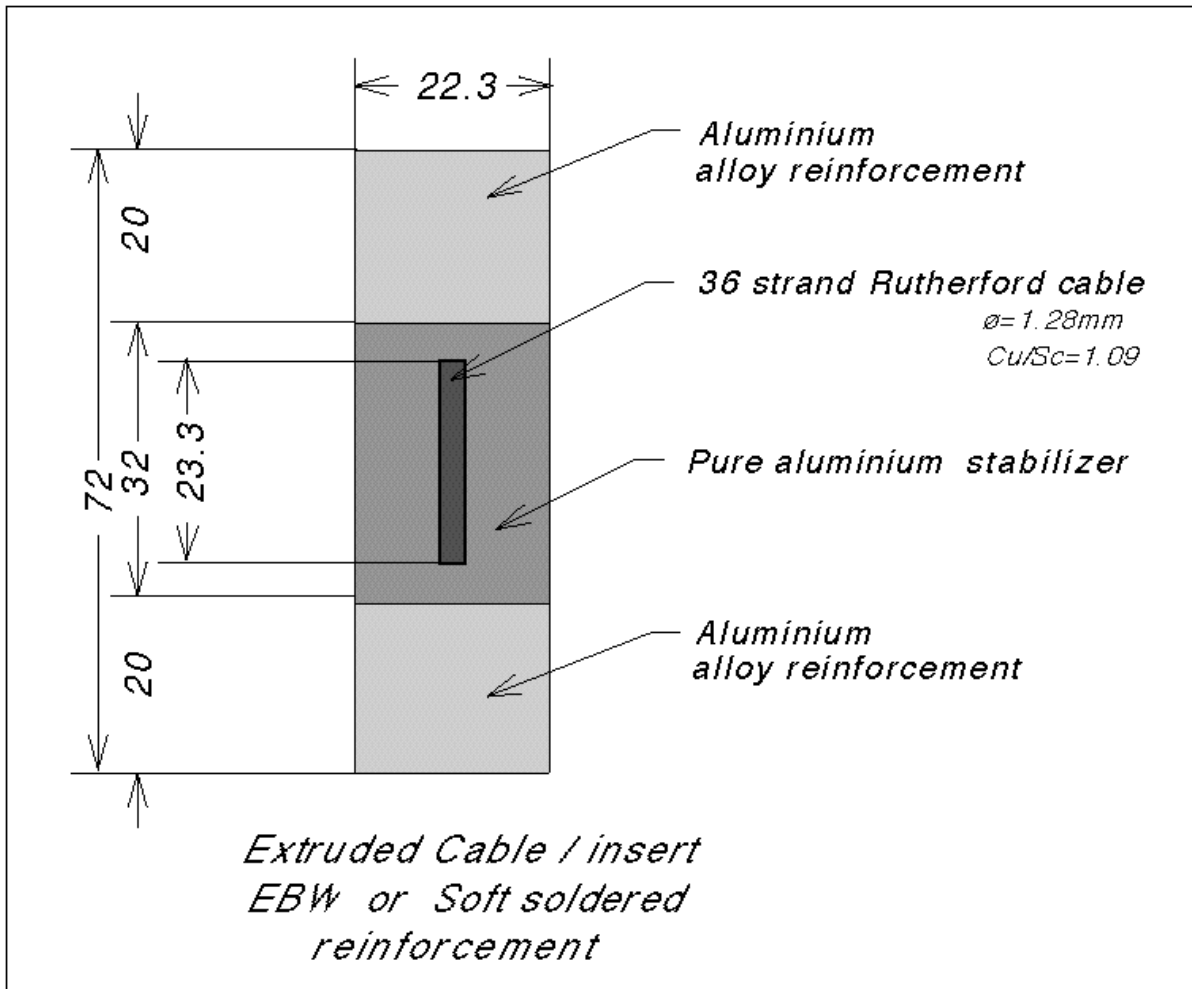


Fig. 12.1: Conductor cross section.

12.3 MECHANICAL CONSIDERATION

The thin, aluminium stabilised, solenoids developed in the past 15 years show common characteristics. As an example for all these magnets (CDF, TOPAZ, VENUS, H1, ZEUS, DELPHI, ALEPH, ...) the hoop strength is provided by an aluminium alloy cylinder, which contains the winding. Since the first development of the CMS solenoid design, it was clear that such a solution would lead to a not well balanced mechanical structure, because four layers of soft aluminium conductors should have been contained inside a thick (190 mm) aluminium alloy cylinder, in order to limit the hoop strain to 0.15% (see also Chapt. 11). This solution minimises the bonding area between conductors and reinforcement leading to some disadvantages.

- The structural part is far from the conductor, so that its heat capacity plays no role (or a minor role) in determining the stability margins.
- The total axial force (120 MN) is transferred to the reinforcement through the bonding of the outermost layer. This bonding becomes very critical for the shear strength resistance.
- The axial thermal contraction of the coil, affected by the insulating material, does not match the cylinder thermal contraction, leading to a further increase of the shear stress at the cylinder-winding bonding.

These drawbacks can be reduced by increasing the bonding area between pure-aluminium conductor and reinforcement so that a simple solution consists in distributing the reinforcement inside the winding. From a mechanical point of view, the best choice is to couple as strongly as possible the pure aluminium to the aluminium alloy, allowing a safe transfer of axial, radial and hoop magnetic force from the conductor to the mechanical structure. In this framework the heat transfer is optimised too. These preliminary considerations led to the concept of a new conductor, which provides the hoop strength (due to the inclusion of the reinforcement in the conductor structure). A solenoid can be *simply* made by winding the reinforced conductor onto a temporary mandrel and by impregnating the turns.

Three configurations, shown in Fig. 12.2, have been assessed in detail.

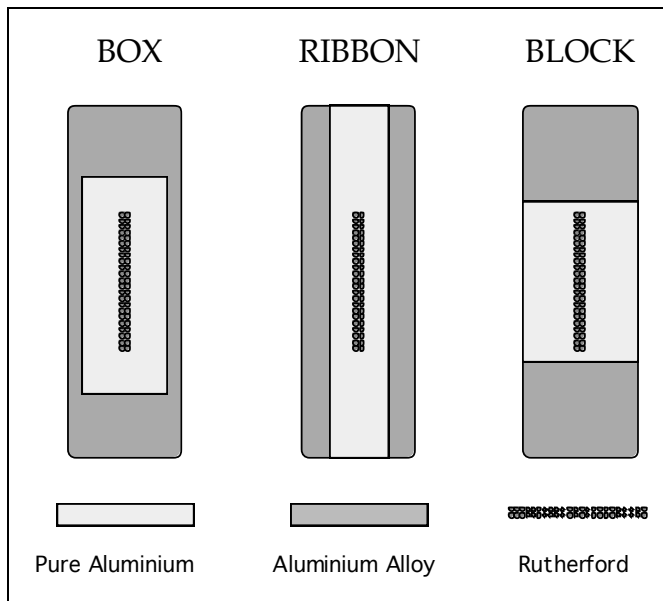


Fig. 12.2: Conductor geometrical configurations.

As it will be shown in the next chapters, these solutions are not very different as far as stability, enthalpy margin or stress distribution in the winding is concerned.

The critical issue in the choice of one or another conductor design is the working condition of the pure Al stabiliser. In fact, it is important that the structural contribution of the pure Al should be minimal. In this respect the box design seems to be the most suitable together with the block design, whereas the ribbon design seems inappropriate.

The results of the FEA carried out so far indicate that the box configuration is potentially the best one. However, in designing this kind of conductor, the manufacturing aspects should be taken into considerations. The block configuration appears as the best compromise between mechanical requirements and feasibility of long lengths.

12.4 CONDUCTOR COMPONENTS

12.4.1 SC Wire

The SC strand has been designed based on the experience acquired in the development of wires for previous Al stabilised solenoids and for the LHC superconducting dipoles. The strand layout must be optimised in order to minimise electrical properties degradation due to

the conductor manufacturing process. This is very important bearing in mind that around 5 tonnes of NbTi will be needed for the whole winding.

A critical current density of 2700 A/mm^2 at $B = 5 \text{ T}$ and $T = 4.22 \text{ K}$ can be assumed as design value for the finished conductor. This value can be reached, for example, by starting from an initial critical current density of 3000 A/mm^2 and a maximum total degradation of 10% due to the manufacturing process, as recently demonstrated on a test run [12-6]. To obtain these critical current densities should be considered one of the goals of the pre-industrialisation program. The NbTi area has been sized in such a way that the current sharing temperature is equal or higher than $T_{cs} = 6.5 \text{ K}$ for the peak field value at each layer. In order to save superconducting material, NbTi content for the cable destined to each layer could be graded according to the peak field of the layer, in such a way that the current sharing temperature is the same for each layer.

The strand diameter has been chosen to be smaller than 1.3 mm in order to keep cabling degradation within few percent, as shown by the R&D activities carried out by CERN and ETH over the last four years in collaboration with industry.

The characteristics chosen are shown in Table 12.2.

Table 12.2
SC strands parameters.

Parameters for wires used in innermost layer	Value
Strand diameter	$1.28 \pm 0.005 \text{ mm}$
Cu/SC ratio	1.09
Filament diameter	$< 50 \mu\text{m}$
I _c at 5 T and 4.2 K	= 1700 A
Twist pitch	about 20 mm
RRR of copper matrix	> 100
Critical current density at 4.22 K and 5 T	2700 A/mm^2

Before closing this section it is important to stress some technological aspects.

Although NbTi wires are well known, it is necessary:

- to optimise the electrical properties at the operating peak magnetic field (4.6 T),
- to develop a suitable quality control to guarantee the electrical performances,
- to optimise the price in relation to the quantity of wires to be produced.

CMS member states companies have the know-how to produce wires of good quality. This will be ascertained through limited production runs.

12.4.2 Rutherford type cable

The superconducting strands are assembled to form a flat cable of the Rutherford type. The characteristics are shown in Table 12.3. The chosen conductor is very similar to the one developed through the CERN R&D programme (32 strand cable of 1.3 mm diameter and Cu/SC = 1.3). Unit lengths of 12 km are within industrial capabilities, as long as strand cold welds are allowed.

In this type of conductor it is recommended to use a low compacting ratio both to ensure a small critical current and to improve the bonding between the cable and the aluminium.

Table 12.3
Cable Parameters.

Number of strands	36
Cable width	23.3 mm
Cable thickness	2.34 mm
Transposition pitch	~ 200 mm
Compacting ratio	< 0.9
Cable critical current at 4.22 K , 5 T	62.5 kA

Figure 12.3 shows the I(B) diagram with the 4.5 K, 5.5 K and 6.5 K characteristics, together with the peak field load line. At constant peak field of 4.6 T the nominal current is 1/3 of the critical current.

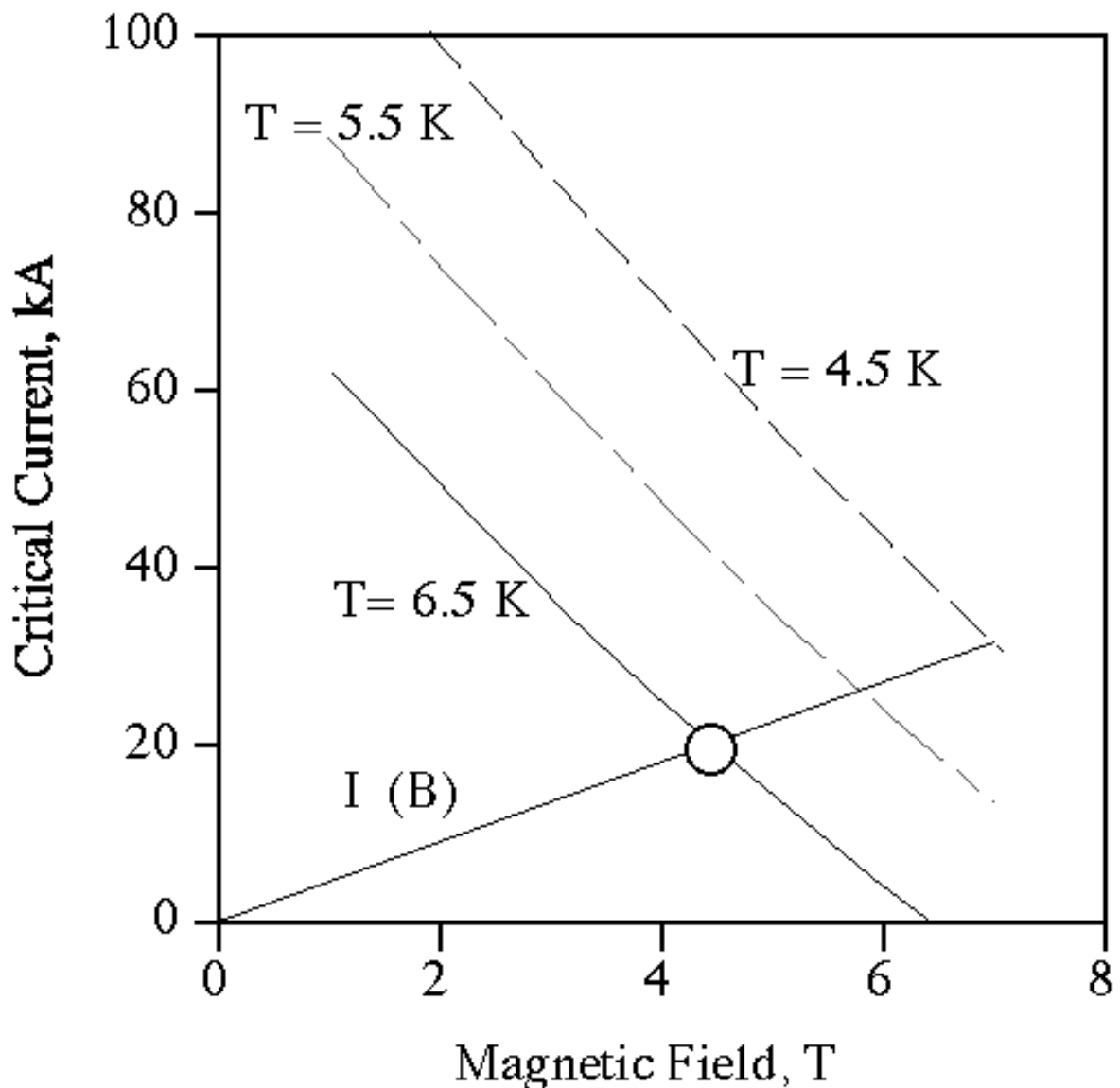


Fig. 12.3: CMS conductor current - field diagram.

12.4.3 Insert

The Rutherford is enclosed inside the aluminium stabiliser through a coextrusion process. This assembly is named *insert*. The coextrusion process requires to heat the aluminium up to 420 °C. Experiments have demonstrated that the critical current degradation can be less than 10% when the manufacturing parameters are properly adjusted. Tests are in progress to measure the performance degradation as a function of the duration of the interruption of the extrusion process.

Although the production of 12 km unit lengths of insert is in principle feasible, one must be ready to accept shorter lengths and to make a limited number of joints of good quality inside the coil. In fact, starting from a 12 km Rutherford cable, the extrusion process will be carried out until the process must be interrupted for any reason. If long enough, say more than 2 km, this length will be accepted as a production length. The lengths of insert will be joined together on the CERN site (see 12.4.5 and Chapt. 23), to provide the 12 km long insert required to wind one layer, before adding the reinforcement. Thus CMS requires long unit lengths of insert, to limit the number of joints inside a layer, however, no strict value will be imposed for the definition of a unit length, but the permissible number of joints will be limited.

If necessary, in order to improve the mechanical properties of the insert, some cold work can be obtained by bending and straightening the conductor prior machining.

Development programmes through several industrial contracts both for CMS and ATLAS conductors have demonstrated the industrial feasibility of the extrusion process on samples more than 300 m long.

12.4.4 Mechanical Reinforcement

In order to obtain the final conductor, the insert must be mechanically coupled to the aluminium alloy reinforcement. For the manufacturing of the “block” conductor two different techniques are being considered; the two reinforcement sections, which are made from a high strength aluminium alloy, are joined to the stabiliser either by soft soldering or by electron beam welding.

Different techniques, as coextrusion in one or two steps, were studied in the framework of an R&D program financed by CERN in 1993 through the LHCC Magnet Advisory Group (MAG). They were abandoned because extrusion of the aluminium alloy has to be done at a too high temperature for the superconductor.

Electron Beam Welding (EBW)

Electron beam welding is an assembly technique which allows to make high quality welds in a continuous process. It can be applied for the CMS conductor to fix a reinforcing section on each side of the extruded insert.

The electron beam makes a narrow heated region just at the metal interface and practically the temperature rise of the conductor components, the superconducting cable, as well as the aluminium materials, is limited. Measurements have shown that the temperature does not exceed 160 °C at a distance of 5 mm from the weld.

The process must be applied under vacuum in a special welding equipment which has to be continuous and fully automated. There are several industrial applications of this type in continuous operation showing that dynamic gating is an operational technique.

It must be stressed that the “block” configuration is particularly suitable for this assembly method, because the weld depth is minimised.

The use of the Electron Beam welding technique for adding the reinforcement is the retained solution as extensive laboratory tests have shown the good quality of the solution. The EB process presents some difficulties due to the short distance between the cable and the insert interface, which may lead to overheating in case of accident during the welding operation. On line protections, control and checks will have to be implemented.

Soft soldering technique

This technique, already used for conductor assembly and for conductor joints, has been considered at a time for assembling the aluminium alloy over the extruded insert.

At the present stage, developments for fixing the reinforcement by soft soldering are still in progress in parallel with the extrusion and the EB welding processes, as it presents an alternative to the base solution, should any unexpected difficulty be discovered later.

At the end of the reinforcing operation an electrolytic anodisation can be foreseen to improve the bonding and the electrical insulation performances.

12.4.5 Conductor joints

There are two types of conductor joints foreseen in the coil:

- layer to layer joints located at the end of the coil and thermally coupled to a liquid helium heat sink,
- joints inside the coil. As explained in 12.4.3, this case is mandatory for the extruded insert solution but it could also be required in any accidental case in which already manufacture lengths have to be repaired. Clearly these joints cannot be cooled locally by a liquid helium heat exchanger. The joining process must thus be fully qualified in order to produce reliable joints of high quality, especially offering an electrical resistance lower than 10^{-9}W .

The joining technique is developed in Chapt. 23.

12.5 RECENT PROGRESS IN ALUMINIUM STABILISED CONDUCTOR PRODUCTION

In addition to the production of testing lengths for the CMS project, members institutes of the CMS magnet project have been also involved recently in the industrial production of stabilised aluminium conductor for several coils destined to physics experiments.

- ATLAS race track conductor: [12.1, 12.2] based on the excellent experience gained with the development of the aluminium stabilised test conductor for the CMS detector magnet in summer 1994, CERN has put ETH Zürich in charge of manufacturing one 200m long conductor for the ATLAS race track coil. For this application, the aluminium stabilised conductor consists of a Rutherford type superconducting cable, which is surrounded by a high purity aluminium stabiliser. The Rutherford type cable itself is twisted out of 32 superconducting strands of 1.23 mm diameter and with a critical current, at 4.2 K and 5 Tesla background field, of about 1550 A each.
- Fermilab D0: [12.3] to further improve our experience, in February 1996 we finished the production of 4.5 km long aluminium stabilised superconductor for the Fermilab D0 detector magnet. Because of the small cross section of the aluminium stabiliser

we have developed a new process line by using a Conform extrusion machine.

- KEK Belle Conductor: [12.4] last year, for the manufacturing of 16 km aluminium stabilised conductor for the KEK Belle detector magnet in Japan, we have developed a conductor together with Outokumpu Oy/Superconductors. By means of already developed equipment and using the process developed for the Atlas and Fermilab D0 conductors this work could be finished in July 1996.
- The BABAR conductor: [12.5] just recently six aluminium stabilised superconductor unit lengths of about 1.8 km each have been manufactured for the BABAR detector at SLAC. This work was carried out in collaboration with INFN Genoa, Europa Metalli, Cable Cortaillod and ETH Zürich.

13. INSULATION

13.1 INTRODUCTION

The technical solution proposed for the insulation of the CMS coil makes use of the semi-wet pre-preg technique. This method, employing pre-impregnated tapes was selected after exhaustive consideration of the three major processing techniques: wet winding, vacuum impregnation and pre-impregnated tape, in relation to cost, complexity, technical suitability and feasibility.

This method has already been used in the past for other similar solenoids. The coils for DELPHI and H1 for example, were manufactured using pre-impregnated tape and both coils have worked successfully for a number of years [13-1].

The CMS coil will be manufactured using a process similar to the one developed at Rutherford Appleton Laboratory for DELPHI.

13.2 TECHNICAL REQUIREMENTS

The coil is constituted of four layers of 542 turns each. This includes:

- a) conductor insulation between turns, made from a semi-wet pre-preg 0.125 mm thick and wrapped around the conductor with a 50% overlap,
- b) ground insulation:
 - at the inner diameter,
 - between layers,
 - between the last layer and the thermal drains,
 - between the drains and the quench-back cylinder,
 - between the quench-back cylinder and the cooling pipes to guarantee a good thermal bonding.

During the numerous stages of the coil life, the insulation will have to meet various requirements: electrical, mechanical and thermal.

Electrical requirements

During a fast discharge into the 0.05 W dump resistor, the maximum voltage expected across the coil is $U = 1000 \text{ V}$, and $\pm 500 \text{ V}$ with respect to ground (Chapt. 20).

The design value for the insulation has been set at 3 kV at each point, corresponding to $2U + 1000 \text{ V}$, that means three times the maximum voltage developed during a fast dump (Chapt. 16), as shown in Table 13.1.

Table 13.1
Maximum voltage developed inside the solenoid.

between turns	< 2 V
between layers	530 V
to ground	$\pm 500 \text{ V}$
across the coil	1000 V

The turn to turn insulation will not be tested at 3 kV even if the insulation process will be qualified for this value. The layer to layer insulation however, will be fully tested at 3 kV after curing the previous layer and before winding the next one.

The breakdown voltage of the glass/epoxy system is about 50 000 V/mm, this means a minimum insulation thickness of at least 0.06 mm is needed to withstand 3 kV. The design thickness of the insulation is 0.5 mm inter turn and 1 mm inter layer, this is well above the required values.

Mechanical requirements

The reinforced conductor is designed to be self supporting and the monolithic winding coil design has been produced to minimise the level of stress in the insulating material.

As explained in Chapt. 14 a Mohr-Coulomb criterion has been adopted for the insulation. The ($s_{\text{mean}}, t_{\text{max}}$) distribution at 4.5 K and nominal field is shown in Fig. 14.6 and Fig. 14.7. An analysis is being carried out to assess the influence on the stress field of the winding helix and conductor corner fillet. Some experiments are underway in order to test and validate a strain based Mohr-Coulomb criterion.

Another mechanical requirement for the insulation is to ensure the mechanical continuity and allow the coil to support the gravity stress during assembly and handling, for these calculations an acceleration factor of 1.2 g has been used.

The insulation will also have to withstand the maximum pressure exerted by the tooling equipment during winding.

The mechanical calculations were made using the insulation thickness of the coil as shown in Table 13.2.

Table 13.2
Insulation Thickness.

Insulation	Thickness (mm)
inner Insulation	1
between Turns	0.5
between Layers	1
between Layer and Aluminium Strips	1
between Aluminium Strips and Quench Back	1

Thermal Requirements

The indirect cooling technique relies on thermal conduction through the coil. This means that, in addition to meeting all other mechanical and electrical requirements, the thermal conductivity of the winding must also be maximised. This requires that the bonding between the insulation and conductor and also between the layers has to be very good, therefore imposing certain requirements on the surface preparation for the conductor and on the winding process itself.

A high quality bonding between the quench-back cylinder and the cooling pipes is also needed to obtain good thermal conductivity.

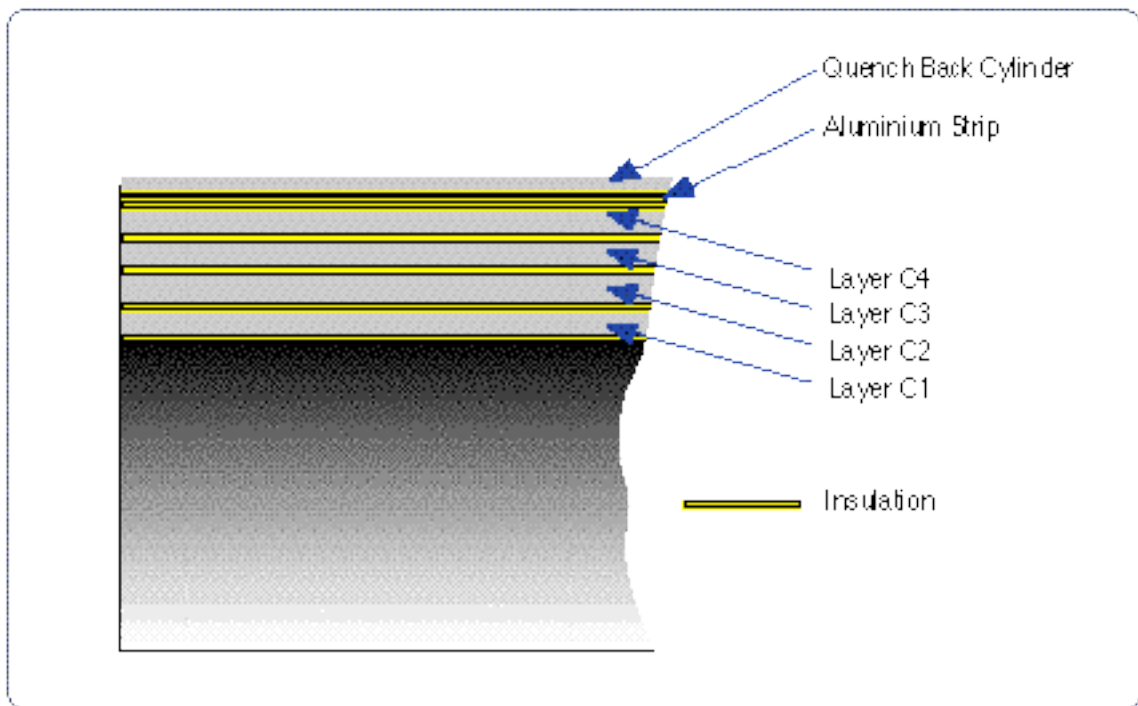


Fig. 13.1: Position of the coil insulation.

13.3 INSULATION PROCESS

The final choice for the insulating process, consists of winding the insulation with a semi-wet pre-preg technique similar to the one developed by the Rutherford Appleton Laboratory and successfully used for the DELPHI solenoid.

The winding process is carried out on a vertical mandrel using the outer winding technique as described in detail in Chapt. 19.

During winding the resin is partly released from the pre-preg due to the pressure applied. This leads to a slight decrease in the insulation thickness. During a short time creeping is expected to occur in the turns as they are wound, the insulation will then remain at the same thickness until curing. No displacement between the mandrel (or previous cured layer) and the winding will occur if both the coil and mandrel are maintained at the same temperature. For this purpose the winding mandrel has to be built in aluminium alloy to reduce differential thermal expansion.

The interlayer insulation is applied during the winding of the conductor by wrapping the insulation around the layer. A stripping cloth is then placed over it to absorb the excess resin. Some form of protection will be used to avoid exposure to humidity.

If required during the insulation process, but before the curing, it will be possible to unwind some of the turns. This requires maintaining the tensile force on the conductor and axial pressure on the winding.

Curing is carried out layer by layer and, in order to avoid any possible displacement along the mandrel or in the previous cured layers, the axial pressure

provided by the winding machine will be maintained constant.

A radiant screen will be used to heat the coil. The mandrel will also be heated to avoid differential displacements between the solenoid and the mandrel, and guarantee a small temperature gradient in the coil ($\leq 15^{\circ}\text{C}$).

To ensure the full homogeneity of the insulation, a two step polymer curing process will be established at approximately 100°C and 125°C .

After the first layer is cured the second is then wound and cured. This continues up to the fourth layer when the ground insulation is wrapped on top of it. The pure aluminium thermal drains are put into place before curing the last layer.

The quench-back cylinder, made from an extruded aluminium alloy profile, is then wound over the outer insulation and welded on line using a laser technique. Computations have shown that the temperature under the profile should remain below 100°C .

When the cold mass is completed a final curing of the full coil will be carried out to guarantee optimum polymerisation.

The insulation process requires that the wrapping of the insulation around the conductor is done during the winding of the conductor, as near as possible to the coil itself, and that the material used for the insulation has to be protected from humidity and dust throughout the whole winding process, in addition the completed turns should be protected as soon as possible.

13.4 DRAWBACKS OF ALTERNATIVE METHODS

This process has been selected after considering alternative methods for both the impregnation process and the curing process. The reasons are explained below.

13.4.1 Alternative impregnation processes

Vacuum impregnation technique

For a coil of this size the risks associated with vacuum impregnation have been considered too high, as any accident will mean a total rejection of the coil.

As only reliable high quality tooling is acceptable it would be both complex and expensive to use this method on a large “one off” coil.

Wet winding

The wet winding process presents many problems, it is unpleasant to use, has health and safety risks and is technically difficult to apply to a large coil. For these reasons this solution has been abandoned, as it was also abandoned for the DELPHI and H1 coils.

B Stage pre-preg

This solution was considered for a long time. Nevertheless it appears that during the curing phase axial pressure has to be maintained on the winding in order to follow the decrease of the pre-preg thickness when the resin becomes liquid. The estimated length reduction of the coil is several centimetres. The displacement of the insulated winding occurs against the full length of the previous cured layer and this

could produce unacceptable voids.

13.4.2 Alternative Curing processes

Curing the whole coil in one go

This process is very challenging. It requires the use of a resin with a very long working life at room temperature, due to the duration of the complete winding process.

It also requires maintaining each completed layer under tension and axial compression while continuing to wind the other layers. It is practically impossible to prevent the first layers from moving during the winding of the last layers.

Curing in parallel with the winding

This technique requires the insulation to be heated locally, on line with the winding. A thermal gradient appears in the winding during curing and cool down to room temperature, this creates additional stresses in the insulation. Furthermore this process does not allow completed turns to be unwound if needed.

13.5 MATERIAL SELECTION

Insulating material

In order to fully quantify the process, the resin used to manufacture the wet pre-impregnated ribbon has to cope with the following requirements:

- it has to be chemically stable and in a viscous state at room temperature,
- it has to react slowly, during curing, avoiding high exothermic and fast liquid/solid transitions,
- it is required that the resin in the tape be viscous during the winding stage in order to provide good wetting, ensure that it will flow, to allow the conductor turns and layers to be compacted and have a good bonding,
- it must have a good hygroscopic behaviour because of the long duration of the winding.

Glass fibre reinforcement

The need to wrap the insulation around the conductor requires the use of a ribbon that does not risk having the fibres pulled out at the ribbon edges.

A pliable tape is required to ensure that the tape follows precisely the form of the conductor when wrapping, without leaving any unfilled gaps between the tape and the edges of the rectangular conductor.

Stripping cloth and barrier film

In order to absorb the surplus of resin released during winding, a stripping cloth is wrapped around the interlayer insulation. It has to be easily removable after the curing process, leaving a smooth surface with good bonding properties ready to start the winding of the next layer.

During the winding operation a protection system will be wrapped around the layer to layer insulation to limit its contact with air and moisture.

Bonding of the cooling pipes

The glue used to bond the cooling pipes requires a good thermal conductivity with respect to the polymer properties at low temperature.

Manufacturing method for the insulation material

The technique used to impregnate the glass fibre ribbon with resin has to fulfil the following requirements:

- it should not allow any delamination of the ribbon wedges,
- it should completely evaporate any solvents used to reduce the viscosity of the resin during the impregnation phase. Such solvents could lead to bubbles forming during the curing of the insulation,
- excess resin has to be present to ensure the tackiness of the impregnated ribbon.

Curing schedule and thermal environment

During the initial curing cycle of each layer, the resin has to be in a low viscosity state in order to complete the wetting of the conductor and eliminate any trapped bubbles that could be present after wrapping.

Up to five successive cure cycles have to be done on the resin without any consequences to the mechanical properties of the fully cured material.

The maximum temperature during the curing process should be approximately 50°C lower than the temperature at which a degradation of the polymer could start.

Storage without any degradation has to be possible for at least six months at room temperature and for two years at -18°C.

13.6 QUALIFICATION OF THE PROCESS

Starting from the results obtained at RAL for DELPHI, a series of tests has been carried out at Saclay to understand the behaviour of the resin and the preimpregnated tapes, [13-2] to [13-9].

However, to fully qualify the processes described above, it is foreseen to make a series of tests in parallel with the pre-industrialisation programs for the fabrication of the winding and the conductor manufacture.

The following paragraphs resume these activities.

Wetting

Good wetting is one of the main requirements when selecting the resin, as a reliable bond between the insulation and the conductor at cryogenic temperatures is considered to be a direct consequence of good wetting.

Viscous flow of the excess resin

As explained above, the pre-impregnated tape needs to have a excess of resin in order to flow, wet the conductor, and fill any gaps between the turns. This flow continues until the thickness of the glass fibre ribbon is reached. The ability to reach the final insulation thickness defined by the ribbon itself will have to be controlled.

Surface preparation of the conductor

The surface preparation will be qualified through bonding tests at cryogenic

temperatures, similar to the wetting tests. The influence of the rugosity and the surface activity of the conductor will need to be estimated and controlled.

Local overpressure

Tests will have to be carried using the pressing system, to determine how much local over-pressure can be tolerated without damaging the fibres.

Bonding

Bonding between the insulation and the conductor has to be controlled and related to the wetting properties of the resin and the preparation of the conductor. The aim is to obtain a bond that is stronger than the resin itself, thereby designating the failure strain of the matrix material as the limiting criterion for mechanical safety at cryogenic temperatures.

Electrical tests

Electrical tests have to be undertaken to ensure that the final insulation fulfils the electrical specifications.

14. COIL MECHANICAL ANALYSES

In this chapter we will summarise the main results of the 2-D axisymmetric mechanical analyses carried out to date on the CMS coil. A quick outline of on going and future activities will also be given [14-1].

The coil has been simulated at two of its operating conditions:

- Coil at 4.5 K.
- Coil energised (4.5 K, 19.5 kA, 4.05 T).

Several simulations have been carried out for different conductor configurations [14-2], [14-3]. The results presented in this chapter are those obtained for the block conductor (see Fig. 12.1).

The analyses have been carried out in parallel at INFN-Genova and CEA-Saclay using two different FE codes (ANSYS and CASTEM respectively) [14-4].

The results of the analyses for the previous CMS coil configurations as well as for the windings with different conductors can be found in several technical notes issued both by INFN and CEA-Saclay [14-5], [14-6], [14-7], [14-8], [14-9], [14-10], [14-11].

14.1 MAGNETIC FEA

14.1.1 The magnetic FE model

A magnetic FEA was performed to calculate the Lorenz force distribution to be used in the stress FEA. The calculation is non linear due to the B-H curve of the iron. More detailed magnetic computations are reported in Chapt. 6.

The geometry of the iron yoke used in the magnetic analysis is shown in Fig. 14.1. The following approximations have been made in the model:

- the dodecagonal prisms of the barrel and the end-cap are transformed into cylinders of the same cross sectional area,
- the hole of the chimney in the barrel has been neglected,
- the current (19.5 kA) in the winding has been modelled as uniformly distributed in 4 shells of the same radial thickness of the Rutherford cable.

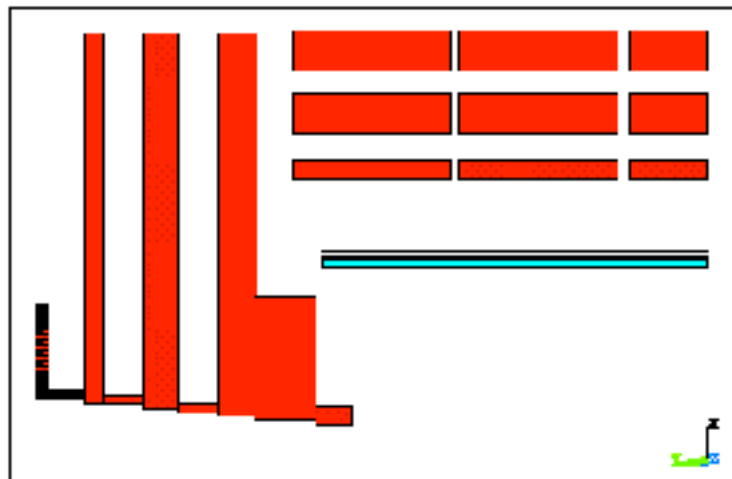


Fig. 14.1: Iron yoke geometry used in the magnetic FEA.

14.1.2 Magnetic FEA results

The B field contour plot and the integral axial force as a function of z are shown in Fig. 14.8, p. C-39 and Fig. 14.2.

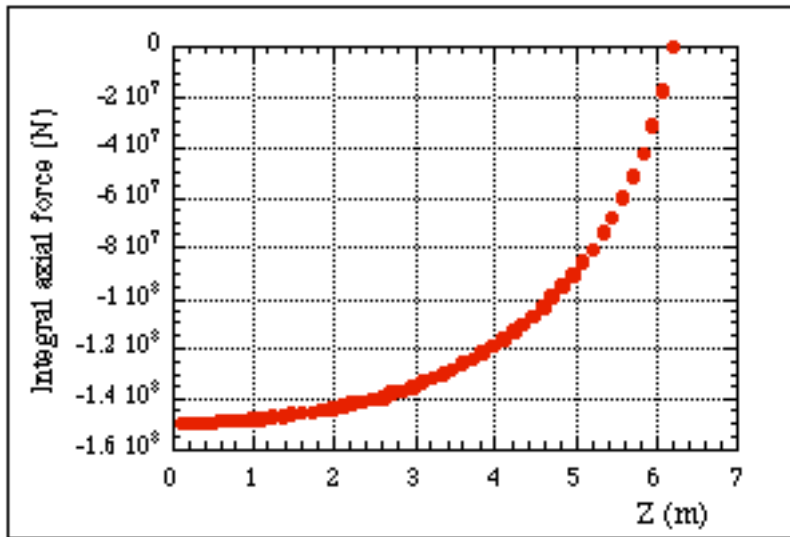


Fig. 14.2: Integral axial force as a function of Z.

14.2 STRESS FEA

14.2.1 Material properties

The behaviour of the different materials has been modelled as follows:

- Electrical insulation: elastic and orthotropic material.
- Aluminium alloy: elastic and isotropic material.
- Pure aluminium: elasto-plastic isotropic material with kinematic hardening rule.

The experimental stress strain curves measured at 4.2 K are shown in Fig. 14.3 for annealed and cold worked Al (after 4-5 energisation cycles) [14-12].

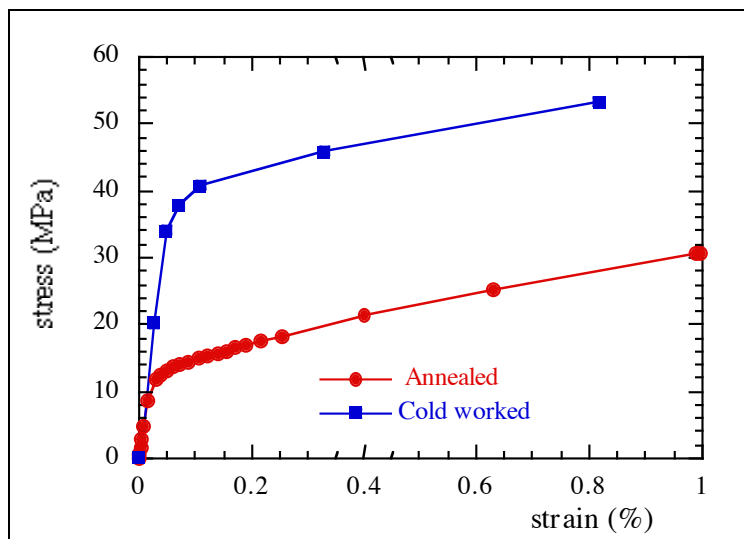


Fig. 14.3: Experimental stress strain curves, measured at 4.2 K, of pure Al both fully annealed

and cold worked after 4-5 energisation cycles.

Table 14.1
Material properties used in the FEA.

Material	Temperature K	Young's Modulus GPa	Poisson's ratio
Al	4.2	see Fig. 14.3	0.49
Al-alloy	4.2	77.7	0.327
Sc strand	4.2	130	0.3
Fibre glass epoxy // to fibre direction	4.2	20	0.21
Fibre glass epoxy ^ to fibre direction	4.2	12.5	0.21

Table 14.2
Mean integral thermal expansion coefficients used in the FEA.

Material	Mean integral thermal expansion coefficient 293 K - 4.2 K K ⁻¹
Aluminium	14.23 10 ⁻⁶
Al-alloy	14.16 10 ⁻⁶
Sc strand	8.79 10 ⁻⁶
Fibre glass epoxy // to fibre	8.45 10 ⁻⁶
Fibre glass epoxy ^ to fibre	25.5 10 ⁻⁶

14.2.2 The mechanical FE model

The coil has been simulated with an elasto-plastic 2-D axisymmetric FE model. A sub-modelling technique had to be used for the FEA due to the size of the problem and its non-linearity, which comes in with the plastic flow of pure aluminium. Two locations: coil end and coil centre were chosen for the sub-modelling. Each sub-modelling location comprises 4 layers and 8 turns.

Several sub-models (see Fig. 14.4 and Fig. 14.5) for different locations and different degrees of detail have been run. No major differences were found between the stress distribution of the aligned turn and the staggered turn winding configuration. The results presented here are those of the sub-model with aligned turns.

As already mentioned at the beginning of the chapter, the stress analyses have been carried out for two main operating conditions:

- Coil at 4.5 K.
- Coil at 4.5 K energised.

The real load history of the coil should in principle have been taken into account in our modelling, as the problem is non conservative (i.e. history dependent) due to the plastic flow of pure Al. However, for these analyses, one single load step both for cool-down and

energisation has been used. This is a fair approximation if one assumes monotonic cooling and energisation.

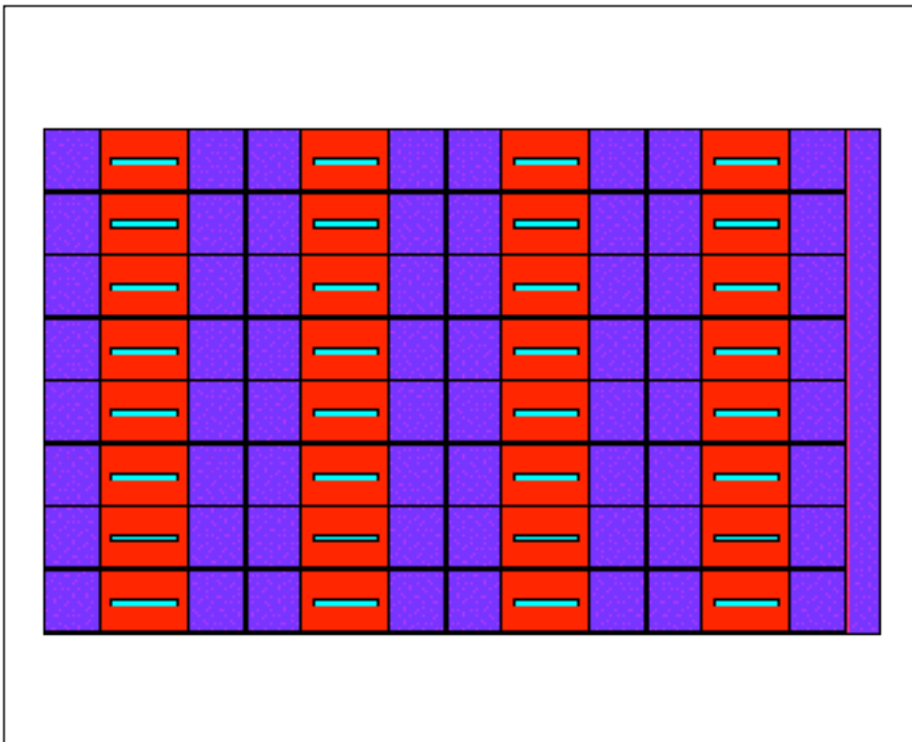


Fig. 14.4: Sub-model with aligned turns.

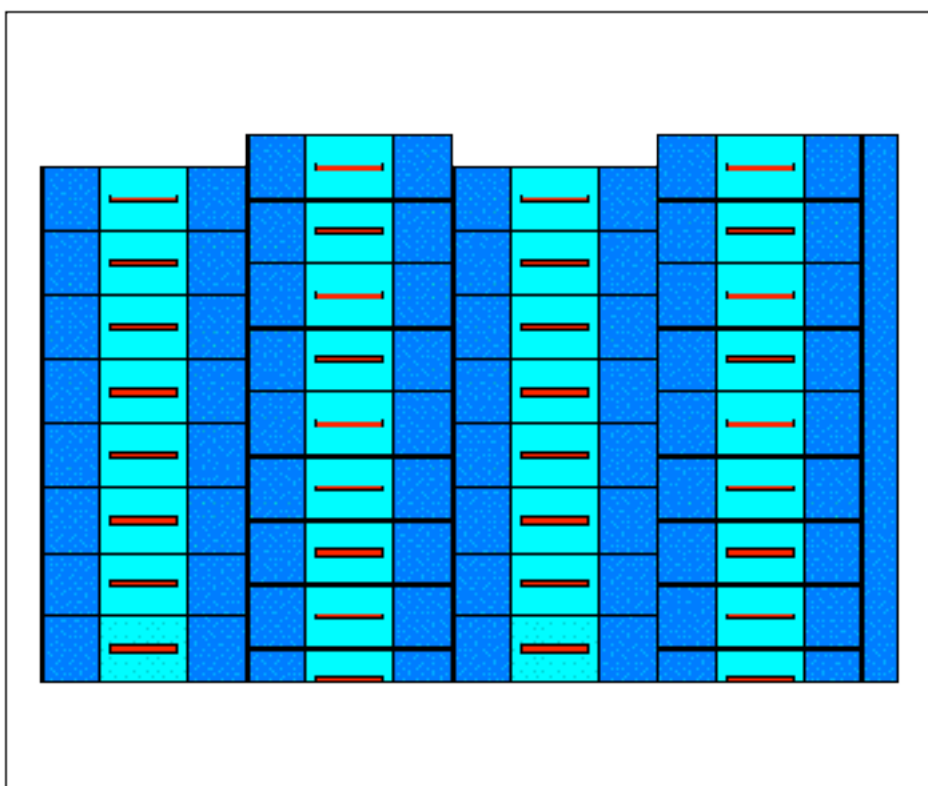


Fig. 14.5: Sub-model with staggered turns.

14.2.3 Stress FEA results

Analyses criteria

The Von Mises criterion has been used for all ductile materials present in the winding.

For the insulation, which behaves in an elasto-brittle way, a criterion which takes into account the hydrostatic component of the stress tensor must be used. In our case the Mohr-Coulomb criterion has been adopted. According to this criterion the calculated distribution of points ($s_{\text{mean}}, t_{\text{max}}$) must lay within an experimental failure envelope. If the material is isotropic the implementation of Mohr-Coulomb is straightforward. In the case of an anisotropic material, on the other hand, the use of this criterion is not trivial due to the fact that the envelope is not univocal. One way around this problem is to consider the most restrictive envelope. However, since the scatter of the failure envelopes in terms of stress is greater than those in terms of strain, a strain based Mohr-Coulomb criterion should be used [14-4], [14-13]. In order to do so the experimental strain failure envelope is needed. At present, the only experimental information available is relative to stress envelopes. So, even if not ideal, the results of the analyses are presented here in terms of stress.

For the interfaces the results were extracted from the FEA in a form which could be compared with the experimental data available.

Stresses in the conductor

The pure aluminium has been modelled with annealed state properties. This has been done in order to calculate the maximum strains seen by the winding throughout its working life. The stress values obtained in this analysis are obviously lower than those obtained with a cold worked aluminium. When comparing FEA with experimental results one must bear in mind the Al properties used in the modelling.

A summary of the results is given in Tables 14.3, 14.4 and 14.5. The maximum stress levels are shown together with the location.

Table 14.3
Maximum Von Mises stress in conductor's components.

Material	Von Mises stress, MPa Coil End	Von Mises stress, MPa Coil centre
Coil at 4.5 K		
Pure Aluminium	2 - 21	4 - 21
SC Cable	200 - 246	200 - 246
Al alloy	0 - 62	0 - 62
Coil at 4.5 K, energised		
Pure Aluminium	9 - 23	9 - 25
SC Cable	80 - 191	38 - 200
Al alloy	62 - 100	112 - 139

In the loadcase of the Coil at 4.5 K the maximum Von Mises values found in the pure Al are in fact stress concentrations localised around the Rutherford cable.

Peak Von Mises stresses only increase by few MPa's when the magnet is energised. However, it must be noted that, in this loadcase, high Von Mises stress values appear all over

the cross section of the Al-stabiliser.

Stress contour plots of the different details of the winding are shown in Figs 14.9 and 14.10, p. C-40 to Figs 14.11 and 14.12, p. C-41.

Table 14.4

Maximum Von Mises and Shear stresses at interfaces (Al side): Coil end.

Material Bonding	Max Von Mises stress MPa	Max Shear stress MPa
Coil at 4.5 K		
SC Cable ÷ Pure Aluminium	15 - 21	12
Pure Aluminium ÷ Al Alloy	7 - 17	10
Coil at 4.5 K, energised		
SC Cable ÷ Pure Aluminium	13 - 23	13
Pure Aluminium ÷ Al Alloy	12 - 19	10

Table 14.5

Maximum Von Mises and Shear stresses at interfaces (Al side): Coil centre.

Material Bonding	Max Von Mises stress MPa	Max Shear stress MPa
Coil at 4.5 K		
SC Cable ÷ Pure Aluminium	15 - 21	12
Pure Aluminium ÷ Al Alloy	7 - 17	10
Coil at 4.5 K, energised		
SC Cable ÷ Pure Aluminium	14 - 24	13
Pure Aluminium ÷ Al Alloy	11 - 19	10

Stresses in the insulation

Maximum and minimum values of shear at the interface are given in Tables 14.6 and 14.7. The (s_{mean} , t_{max}) distributions shown in Fig. 14.6 and Fig 14.7 fall well within the failure envelopes found in the literature [14-14].

Table 14.6

Maximum values of shear stress at insulation-conductor interface.

Coil at 4.5 K	Shear stress MPa
Coil end location	10
Coil centre location	10

Table 14.7

Maximum values of shear stress at insulation-conductor interface.

Coil at 4.5 K, energised	Shear stress MPa

Coil end location	10
Coil centre location	10

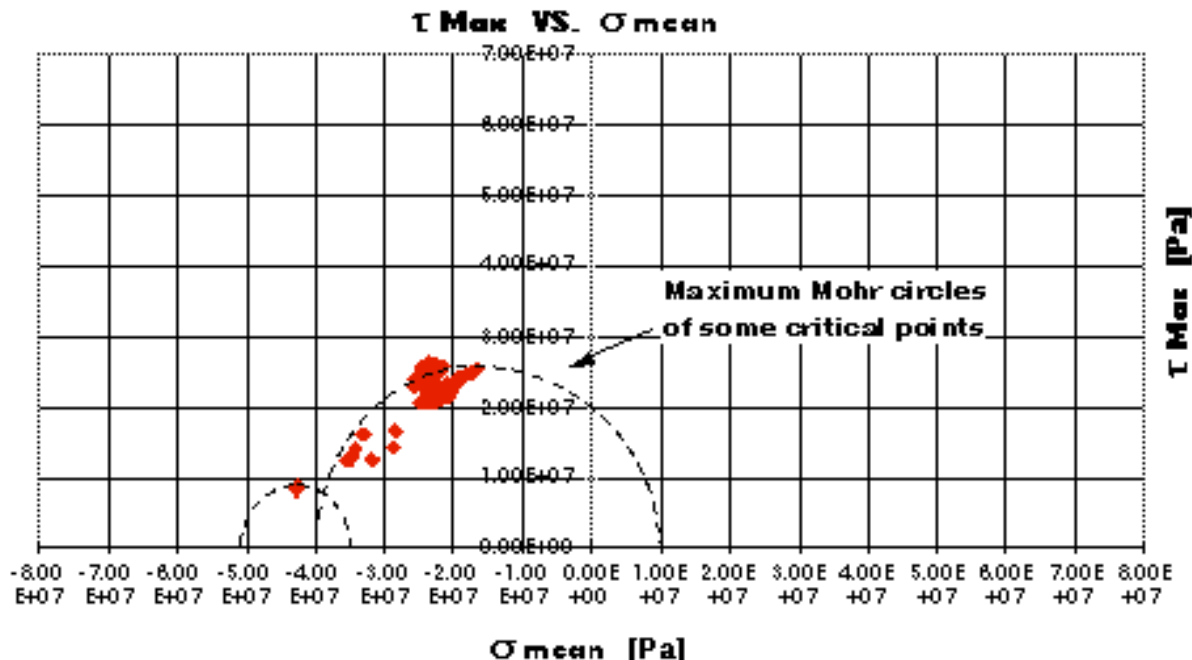


Fig. 14.6: Coil centre location - Coil at 4.5 K: (σ_{mean} , t_{\max}) distribution in the insulation.

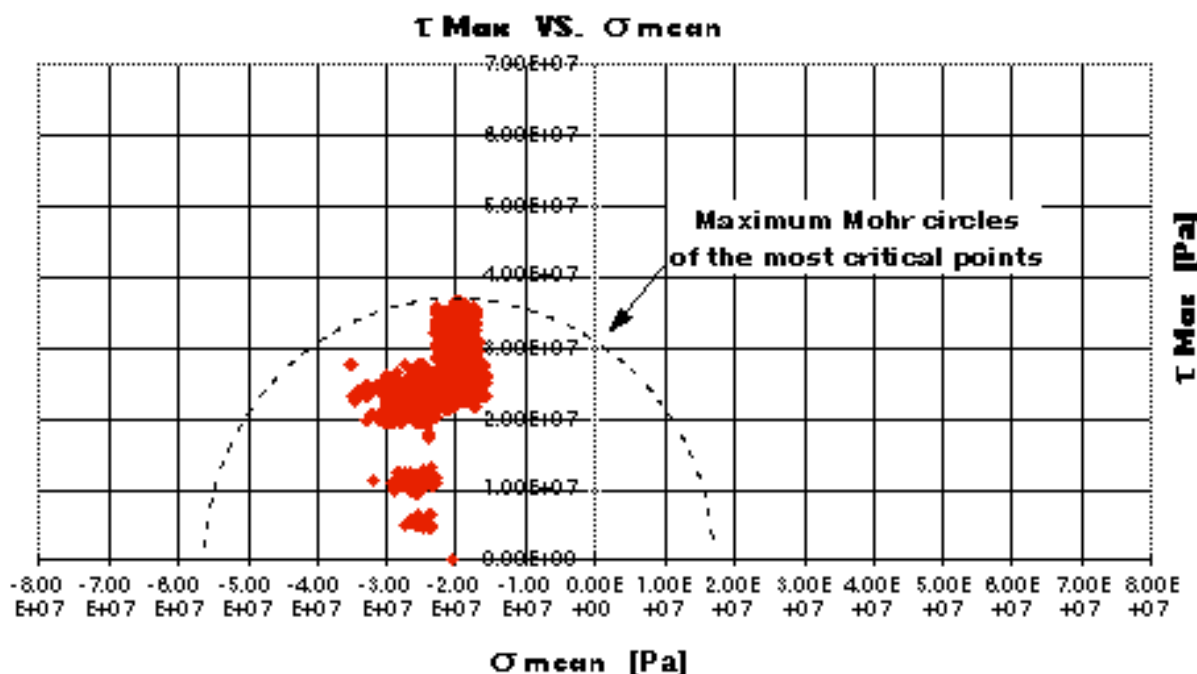


Fig. 14.7: Coil centre location - Coil at 4.5 K, 4T: (σ_{mean} , t_{\max}) distribution in the insulation.

14.3 CONCLUSIONS

Insulation

Cool down gives the largest contribution to the stress field in the insulation, on the other hand the effect of the EM forces seems to be relatively small.

Some analysis is under way to investigate the influence of the winding helix on the stress field in the insulation. Another important outstanding issue is the effect of the conductor corner fillet.

On the experimental side a set of samples is being designed, at CERN and CEA, Saclay, in order to validate a Mohr-Coulomb strain based failure criterion to be used in our future FEA's. Other tests to study the failure mechanism at the interface are also being considered.

Aluminium

The pure Al stabiliser is well into the plastic domain. The present conductor geometry has been chosen to minimise most of the structural function of the pure Al. Tests have been planned at CERN and ETH on several issues regarding the Rutherford/Al interface [14-15].

15. STABILITY AND THERMAL ANALYSIS

15.1 INTRODUCTORY CONSIDERATIONS

The main topic of this chapter is *stability*. In this case the term *stability* means, the ability of the coil to support local or distributed temperature rises above the nominal temperature without quenching. Before giving details, it is important to define some important parameters to prevent misunderstanding.

The critical temperature, with no current flowing in the conductor, T_c , only depends on the magnetic field. For NbTi the critical temperature is according to:

$$T_c(B) = T_{c0} \left(1 - \frac{B}{B_{c20}}\right)^{0.59}, \quad (15.1)$$

where T_{c0} is the critical temperature at $B = 0$ ($T_{c0} = 9.3$ K), and B_{c20} is the critical field at $T = 0$ ($B_{c20} = 13.9$ T). At $B = 4.6$ T, the CMS peak field, $T_c = 7.35$ K. Considering that a current I_0 flows in the conductor, a new critical temperature T_{cs} is defined as the maximum temperature for which the current I_0 can flow with no dissipation in the superconducting part. T_{cs} is called the current sharing temperature.

$$T_{cs} = T_c - (T_c - T_0) \frac{I_0}{I_c(T_0, B)}, \quad (15.2)$$

where $I_c(T_0, B)$ is the critical current at nominal temperature and peak field. For CMS, T_{cs} has been fixed at 6.5 K, allowing the magnet to operate at 1/3 of the critical current.

In order to organise the concepts related to the stability, three cases of heat dissipation inside the coil may be distinguished:

- a) A fixed amount of energy E_0 is released as heat inside the winding (localised or also distributed) in a given time, t_0 , in such a way that the temperature rise in the winding will not be higher than $T_{max} < T_{cs}$.
- b) A steady state power dissipation occurs inside the winding. The heat is drained away by the LHe coolant, through the thermal conductance of the cold mass, in such a way that the maximum temperature does not exceed T_{cs} .
- c) A fixed amount of the energy E_0 is locally released as heat inside the winding in a given time, t_0 , causing a local increase of temperature over the critical temperature $T_{max} > T_{cs}$.

It is possible to find for each case the conditions at which the coil can operate without quenching.

For case a) we can define the maximum energy for unit volume $E_{u.v}$ causing a temperature rise within T_{cs} . $E_{u.v}$ is related to the distributed heat released in large volumes (up to the complete coil). For a safe design the value of $E_{u.v}$ should be as high as possible. The question is *how large should $E_{u.v}$ be?* or in other words *what is the reference energy to be compared with $E_{u.v}$?* There are two possible answers to this question:

- a) $E_{u.v}$ should be compared with values of existing running coils of the same kind;
- b) An analysis should be carried out in order to evaluate the reasons leading to energy releases in a large fraction of the coil.

These points are addressed in section 15.2, which discusses all these topics grouped together in a single subject called Enthalpy Margin.

In case b) there are steady heat inputs to a given zone of the coil, due to several reasons such as a conductor joint, eddy currents during charging and discharging or heat conduction through the supports. The heat is drained away by the cooling system through the conductance of the cold mass and a temperature gradient results inside the cold mass. The aim of the design is to have a cold mass conductance (in every direction) and a cooling capacity so high that reasonable heat sources can only cause negligible temperature rises (not higher than 50 mK). These topics are more related to the cooling system and are not discussed in this chapter.

In case c) we analyse the situations for which localised quenches occur. The aim of the analysis is to understand the conditions needed to restore to a fully superconducting state, ($T < T_{cs}$). In principle it should only be necessary to answer the following three questions:

- a) Does a threshold value of localised disturbance energy exist, for which the local transition grows (quenching the coil) or recovers ?
- b) What is the definition of a localised disturbance? What happens for distributed disturbances?
- c) What are the possible sources of the disturbances?

These topics, which are related to concepts such as Minimum Quench Energy and Minimum Propagating Zone, constitute the main part of the stability chapter and are discussed in sections 15.3, 15.4, and 15.5.

15.2 ENTHALPY MARGIN

As was discussed in the previous section the current can flow with no dissipation in the superconducting cross section up to a temperature of 6.5 K. In the temperature range 6.5 K - 7.34 K, the current is shared between the superconductor and the matrix. Fig. 15.1 shows the critical current scales for field and temperature. The load line of the peak field intercepts the critical curve $I_c(B)$ at 20 kA for a temperature of 6.5 K. An interesting parameter is the enthalpy variation from 4.5 K to 6.5 K:

$$E_{u.v.} = \int_{4.5}^{6.5} Cp(T)\delta dT, \quad (15.3)$$

where $Cp(T)$ is the specific heat (in J/Kg) and d the density. By averaging the thermal properties among the four parts of the winding (Aluminium, Copper, NbTi and fibreglass epoxy), we find $E_{u.v.} = 2550 \text{ J/m}^3$. This enthalpy margin can be re-written in a more convenient way as energy per unit conductor length, resulting in $E_{u.l.} = 4.2 \text{ J/m}$. About 50% of the enthalpy margin is provided by the structural material (Aluminium alloy) tightly coupled to the conductor.

As stressed in the previous section, the aim of the design consists in maximising the enthalpy margin. At a fixed magnetic field, the only way to increase the margin is to increase the superconducting cross section. It is interesting to graph the enthalpy margin as a function of the superconducting cross section as shown in Fig. 15.2. The maximum margin is 3890 J/m^3 , corresponding to $T_{cs} = 7.35 \text{ K}$,

requiring an infinite superconducting cross section. The actual choice of 22.3 mm^2 , gives a margin of 2550 J/m^3 (65% of the ideal maximum one) and can be considered a good compromise. As an exercise, doubling the present cross section will increase the margin to 3200 J/m^3 . Unfortunately this modest growth (25% more) has a big impact on the conductor cost.

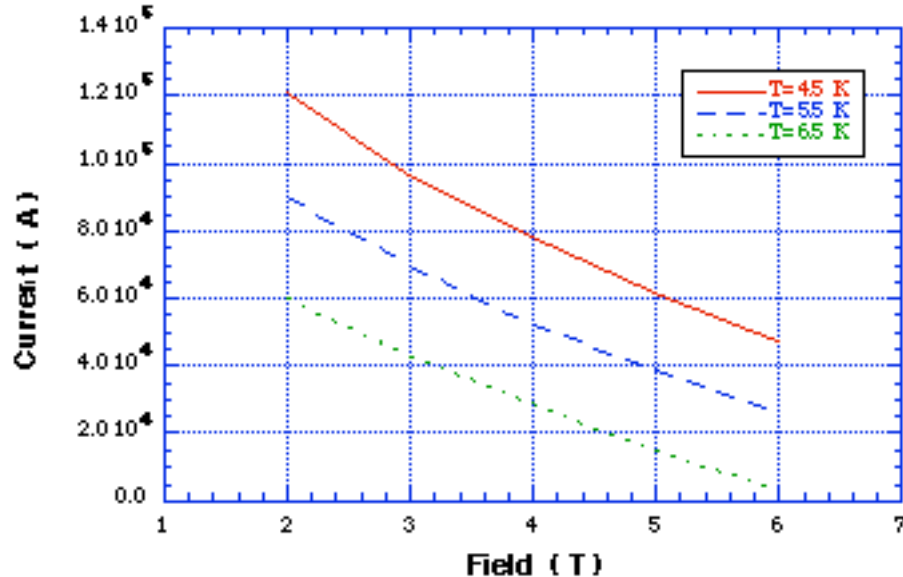


Fig. 15.1: Critical current Vs magnetic field at 3 different temperatures, intercepting the peak field load line.

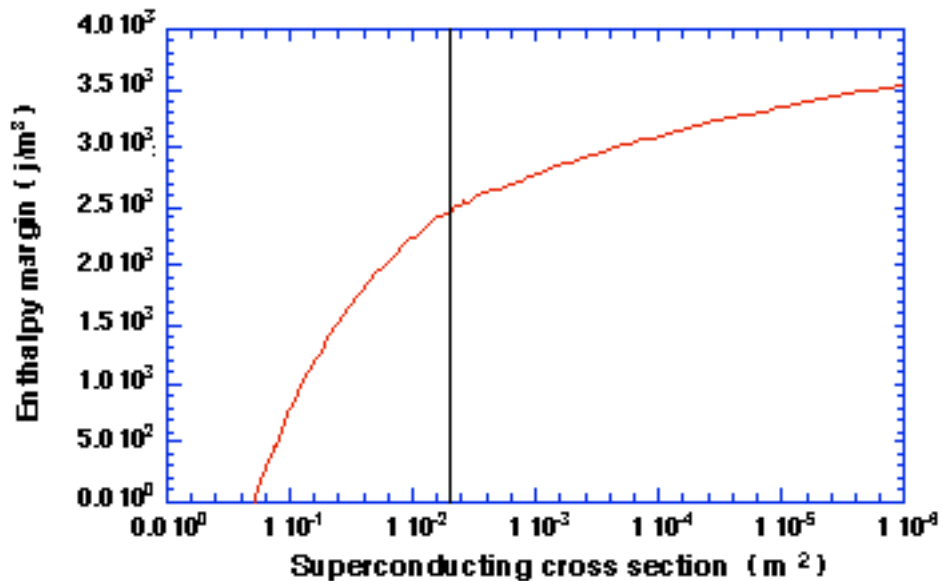


Fig. 15.2: Enthalpy margin Vs the superconducting cross section.

In the introduction section it was stated that in order to understand how large is the enthalpy margin, it is useful to perform comparisons with existing running coils of the same kind. For this comparison we chose the superconducting thin solenoids of the CDF and ALEPH experiments. CDF was chosen as a reference coil because it is one of the oldest thin solenoids of large dimensions still working today. Furthermore

it is particularly critical from the stability point of view. ALEPH is the biggest existing thin solenoid and its design is particularly well known to the CMS design team. The parameters of interest for stability computations are shown in Table 15.1. Using that data the enthalpy margin for ALEPH and CDF is calculated to be respectively 2800 J/m^3 and 1300 J/m^3 . In terms of energy per unit length we have respectively 0.4 J/m and 0.1 J/m . It is clear that from the point of view of any disturbance directly released inside the conductor or close to it, the energy per unit length is more significant.

Under this view, the CMS conductor could seem to be much more stable due to its large cross section: we have a factor of 10 with respect to ALEPH and 35 with respect to CDF. Unfortunately the larger margin of the CMS coil with respect to ALEPH and CDF, does not necessarily mean higher stability, because we have not yet compared the margin with the disturbance sources in the cold mass of the three coils. Section 15.4 is devoted to such considerations, involving the disturbance spectrum in large Al-stabilised and indirectly cooled superconducting coils.

Table 15.1

Parameters used for stability computation on CMS, ALEPH and CDF coils.

Parameters	CMS	ALEPH	CDF
Layers	4	1	1
Conductor width (mm)	22.3	3.6	3.89
Conductor thickness (mm)	72	35	20
Turn/turn insulation(mm)	0.27	0.27	0.2
Cylinder thickness (mm)	12	50.0	16.0
Ground plane insulation (mm)	0.94	0.6	1
Bath temperature (K)	4.5	4.4	4.5
Peak field (T)	4.6	2.0	2.5
Nominal current (A)	20000	5000	5000
I/I _c	30%	40%	60%
Sharing temperature (K)	6.5	6.8	5.8
Critical temperature (K)	7.35	8.5	8.2
Current density in the Al matrix			
(A/mm ²)	28	40	64

15.3 TRANSIENT ANALYSIS. LOCALISED DISTURBANCES

In this section we will study the effects of perturbations causing localised transition to normal state ($T > T_{cs}$). In general it is supposed that a time dependent disturbance $G(t)$ is released as heat inside the winding. In that zone, the critical temperature is exceeded causing a dissipation, $\dot{Q}(t)$, which depends on how much current is transferred from the superconductor to the aluminium matrix and also how the current is shared by the superconductor and the aluminium. From a mathematical point of view this situation can be studied by solving the heat transient diffusion equation by numerical methods. The approach to the problem consists in imposing a given disturbance and solving the equation describing how the normal

zone (if any) increases, causing a quench, or reduces, restoring full superconducting state.

The heat dissipation

When the temperature T is higher than the sharing temperature T_{cs} , the current is transferred to the matrix, causing a dissipation of unit volume:

$$\dot{Q} = \rho_{eff} J^2, \quad (15.4)$$

where ρ_{eff} is essentially the resistivity of the pure aluminium matrix, and J is the current density in the same metal. The current I_{Al} flowing through the aluminium depends on temperature: at $T = T_{cs}$, $I_{al} = 0$, at $T = T_c$, $I_{Al} = I_0$ (i.e. all the current). Eq. 15.4 is based on the assumption that the excess current in the superconductor can be immediately shared by the whole aluminium matrix. Unfortunately this assumption does not reflect the real situation occurring in a large Al-stabilised conductor. The current cannot be shared instantaneously by the aluminium matrix because of the eddy currents. The most appropriate description is given in terms of a diffusion of the electrical field according to the equation:

$$\Delta \vec{E} = \frac{\mu_0}{\rho} \frac{\partial \vec{E}}{\partial t}, \quad (15.5)$$

The heat dissipation is strongly modified by (15.5). Since it is difficult to take into account at the same time both the current sharing effect and the current diffusion effect, we used a simplified model for the heat generation by assuming that the heat dissipation starts when the temperature exceeds $T_s = (T_{cs} + T_c)/2$. As an example Fig. 15.3 shows the heat generation versus time using a numerical solution (for this solution we used the standard general purpose F.E. code ANSYS rev. 5.2) for the CMS conductor. At a time of a few milliseconds after the transition ($T > T_s$) the current remains in the Rutherford cable, causing heat generation of up to 100 times higher than the computed value using (15.4).

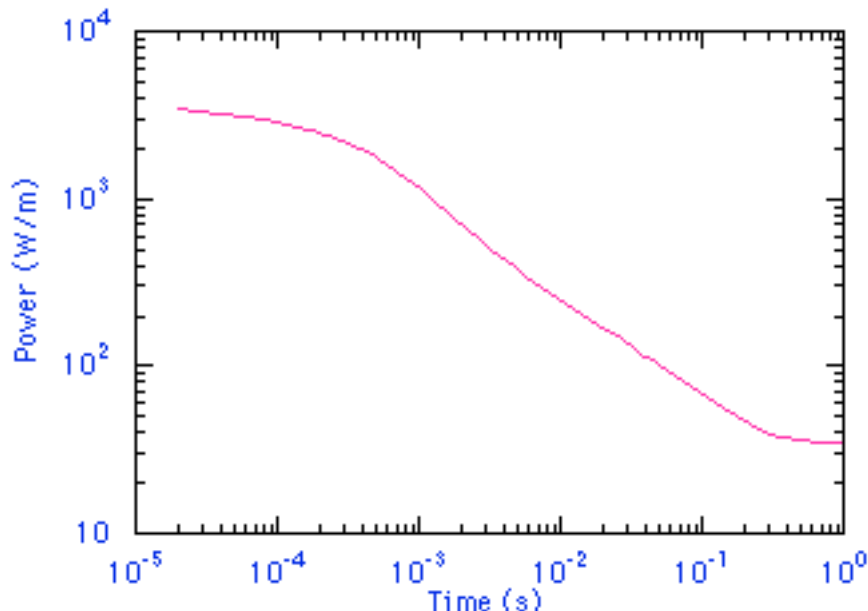


Fig. 15.3: Time dependent heat dissipation due to the current diffusion.

Approximately 1 second after the quench, the current in the Rutherford cable is close to being equally distributed in the whole aluminium cross section.

The disturbance

The disturbance is assumed to be a constant power dissipated for a given time in a given region. The time duration of the disturbance and the dimensions of the region where the energy is released are two very important parameters and will be discussed later.

Numerical solution of the heat conduction equation

The heat conduction equation was solved numerically by using a 3-D F.E. code for transient thermal problems (HEATING-7.2 developed at Oak Ridge National Laboratory). The code was implemented with a routine to compute the heat generation taking into account the effects of several parameters such as:

- a) the material thermal and electrical properties as functions of field and temperature [electrical resistivity $r = r(T, B)$, thermal conductivity $k = k(T, B)$, specific heat $C = C(T)$],
- b) the critical temperatures $T_{cs}(B, I_c)$ and $T_c(B)$,
- c) the heat generation, including as an option, the current diffusion effect as expressed by (15.5).

Model for numerical computation

The winding is usually schematised as a solid parallelepiped, of which the plane X-Y represents a small portion of the Z-R cross section of the coil with a fixed number of adjacent turns. The longitudinal direction (Z) represents the coil azimuthal direction. The longitudinal length of the model should large enough that the results are not affected by changing this parameter (several meters are used).

The symmetry of the problem allows to use only a quarter of the model, cutting down the number of nodes and CPU time.

Figure 15.4 shows a cross section of the CMS winding model (plane X-Y corresponding to the plane Z-R of the coil) with 5 adjacent conductors for each layer, which the symmetry reduces to 2 and a half conductors. The four layers of the coil are represented. The thin supporting cylinder is not modelled for reasons explained later.

All the components of the winding (Rutherford, pure Al, Al alloy, insulation) are modelled. Since the localised disturbance is put in the central conductor of the first layer (at $X = 0, Y = 0$), only the first layer is completely modelled. For the remaining 3 layers the Rutherford cable and the aluminium stabiliser are grouped by averaging the electrical and thermal properties.

The system is assumed to be adiabatic with an initial temperature equal to the operating temperature ($T_0 = 4.5$ K).

The model was suitably meshed using parallelepiped elements. Each element is defined by 8 nodes. The total number of nodes ranges from 10000 to 17000. In order to use a reasonable CPU time, attention must be paid to minimising the number of the nodes. A model with 13000 nodes requires 46 h CPU time on a Digital ALPHA VAX to perform a transient analysis of 0.7 s.

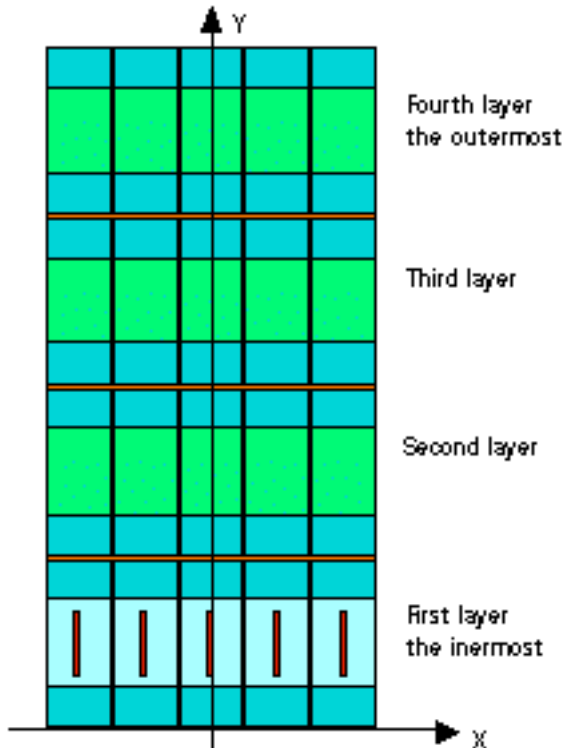


Fig. 15.4: Cross section (plane x-y equivalent to the z-r plane) of the CMS winding model.

Stability analysis

The analysis is carried out by imposing a disturbance and computing the time evolution of the temperature distribution. The disturbance is modelled by releasing a fixed amount of power for a given time in a given region. For CMS, as modelled in Fig. 15.4, the power was deposited in the central conductor (of 5) of the first layer, in a longitudinal length of 1 cm and for a time of 10 ms. A more complete discussion about the disturbance modelisation will be made in a later section.

The results can be usefully represented through a graph showing the quenched region in the longitudinal direction along the central conductor. In this case we assume normal zones to be the regions having temperature $T > T_s = (T_{cs} + T_c)/2$. Figs 15.5 and 15.6 show the time evolution of this transited length (with pure aluminium RRR = 800) in two different cases:

- a) instantaneous current diffusion (Fig. 15.5),
- b) finite current diffusion (Fig. 15.6) according to Eq. 15.5.

We showed the results for the Minimum Quench Energy for both cases because our model can be pessimistic when considering the current diffusion. In fact due to the difficulty to consider both the current sharing and the current diffusion effects, the transition to normal was schematised as a process occurring sharply at a temperature T_s intermediate between the sharing temperature T_{cs} and the critical temperature T_c . The simulations showed that large zones of the winding remain in the range T_{cs} to T_c . However the results obtained with instantaneous current diffusion give an upper limit to the stability.

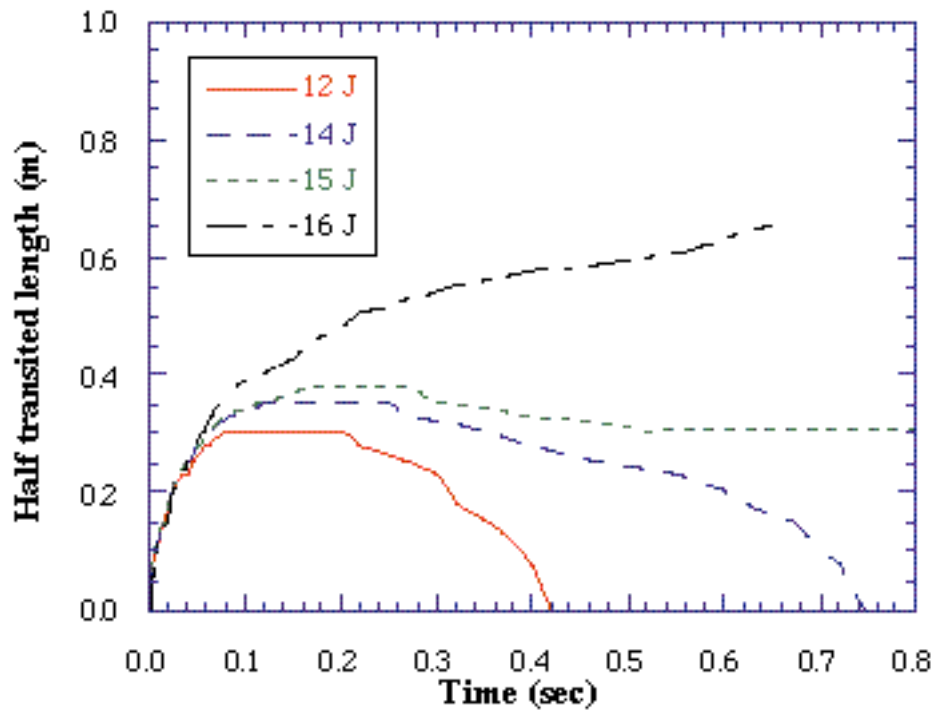


Fig. 15.5: Time evolution of the normal zone in the case of instantaneous current (and ideal) diffusion.

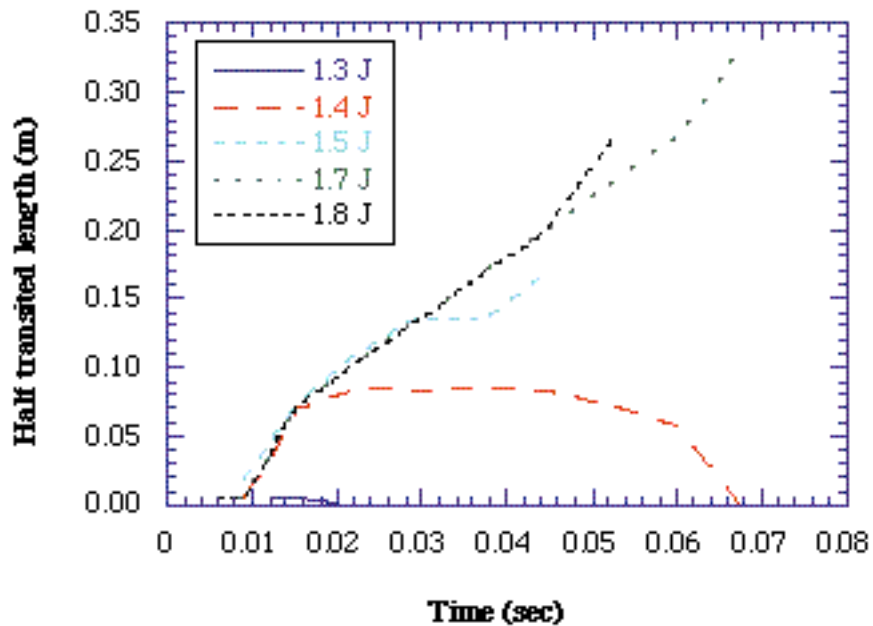


Fig. 15.6: Time evolution of the normal zone in the case of finite (and real) current diffusion.

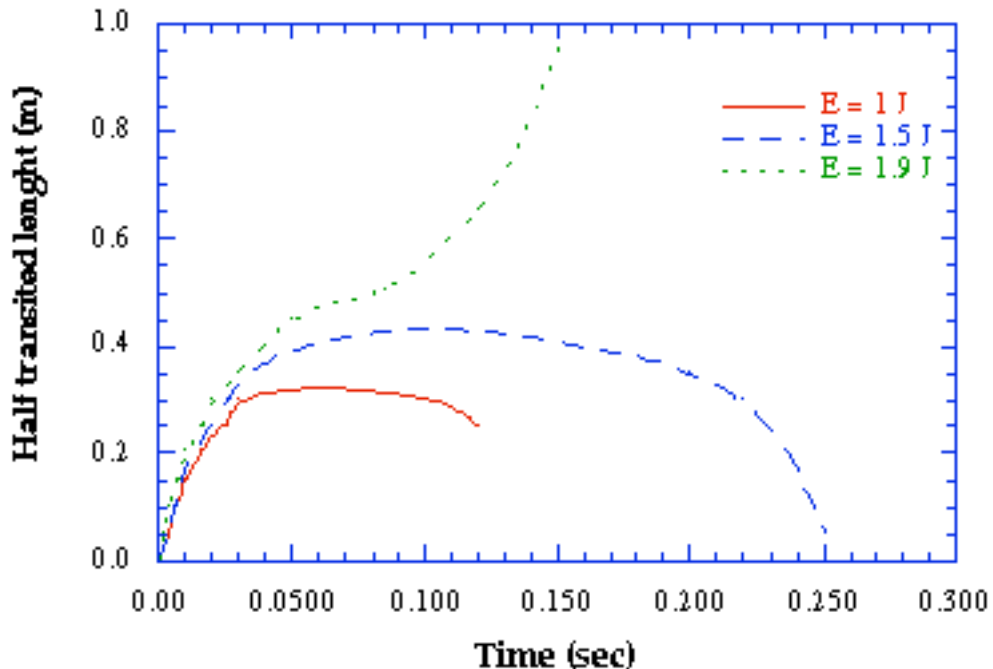


Fig. 15.7: Time evolution of the normal zone in the case of finite current diffusion for the ALEPH coil.

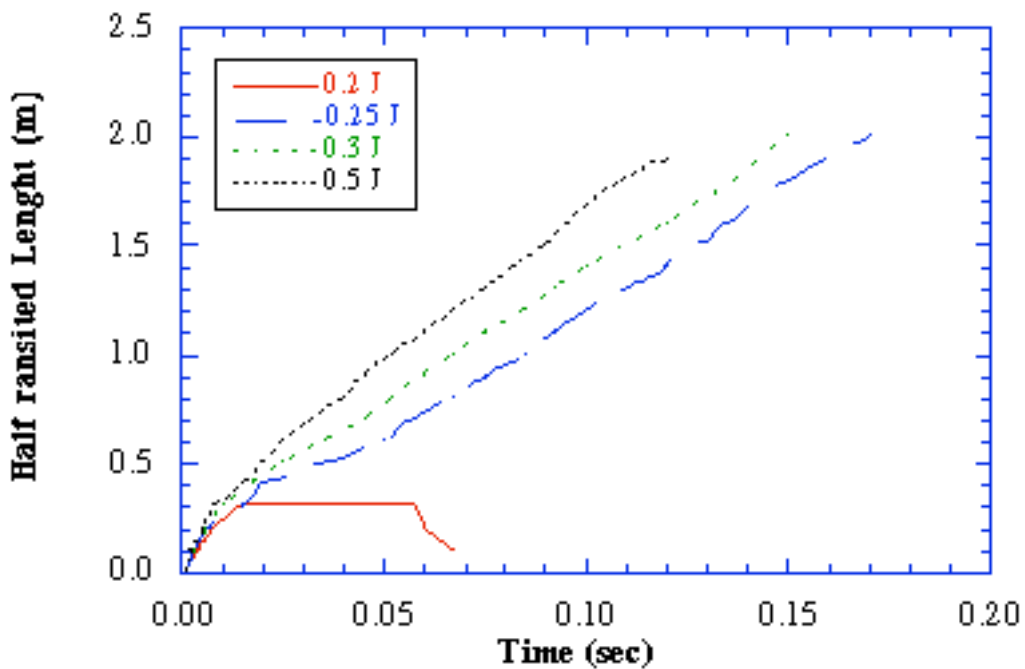


Fig. 15.8: Time evolution of the normal zone in the case of finite current diffusion for CDF coil.

Time $t = 0$ is defined as the starting time of the disturbance. The disturbance energy is used as a parameter.

Several interesting considerations can be made looking at these results:

- For both cases there exists a threshold energy at the border between propagation and recovery behaviours. This energy, which we will call Quench Energy, stays

between 15 and 16 J in the case of the instantaneous current diffusion and between 1.4 and 1.5 J in the more realistic case of finite current diffusion. Similar analyses on different magnets confirmed that the energy release, dividing propagation from recovery, really stays in a very narrow range, as shown in Fig. 15.7 and 15.8 for ALEPH and CDF.

- b) At initial times the transited length grows in the same way for every value of the energy disturbance. The initial growth is followed by a stop of the normal zone propagation if the energy release is less than the Quench Energy. For CMS the propagation stops in a time of 100 ms for the instantaneous current diffusion case and 15 ms in the other case. The quenched zone is stable for some time, and then decays up to a point where the superconductivity is restored. The quenched zone, after the initial growth, continues to grow with a different velocity, if the energy release is close to, but higher than the QE. A possible interpretation could be as follows. The localised disturbance generates a normal region which rapidly grows up to a fixed length (70 cm in the instantaneous current diffusion case and 16 cm in the other case). The flat of the curves represents a metastable region where the heat generation is compensated by the thermal conduction. Since the two contributions are not exactly equal, there is a prevalence of one, causing a quench or a recovery. We think that the flat represents a metastable region, which can be considered as analogue of the so called Minimum Propagating Zone, i.e. a normal zone in thermal equilibrium with the surrounding superconducting environment.
- c) The effect of the current diffusion strongly affects the stability, reducing by one order of magnitude the available Quench Energy in the ideal case of instantaneous current diffusion.

An important question is related to the meaning of localised disturbance. We computed the Quench Energy Vs the disturbance duration at a fixed value of the disturbance length (1 cm), as shown in Fig. 15.9. Furthermore, the Quench Energy was computed vs. the disturbance length at a fixed value of the disturbance duration (10 ms) as shown in Fig. 15.10.

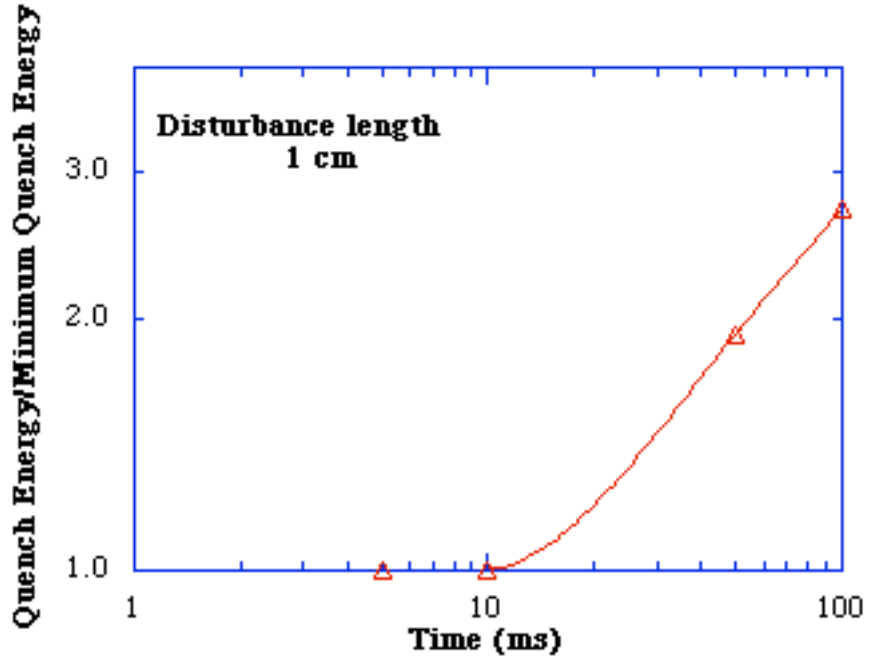


Fig. 15.9: Quench Energy vs. the disturbance duration at a fixed value of the disturbance length (1 cm).

As figures show, the Quench Energy is not depending on the disturbance, for disturbances of lengths up to 3 cm and time durations of up to 10 ms. Since Fig. 15.6 shows that the metastable region (or MPZ) is 16 cm and a time of 15 ms is required to form it, the previous statement is equivalent to saying that the disturbance can be considered localised if its length and duration are respectively smaller (but not necessarily much smaller) than the MPZ length and the time interval to set it. We can define the lowest value of Quench Energy, independent of disturbance length and duration, as the Minimum Quench Energy.

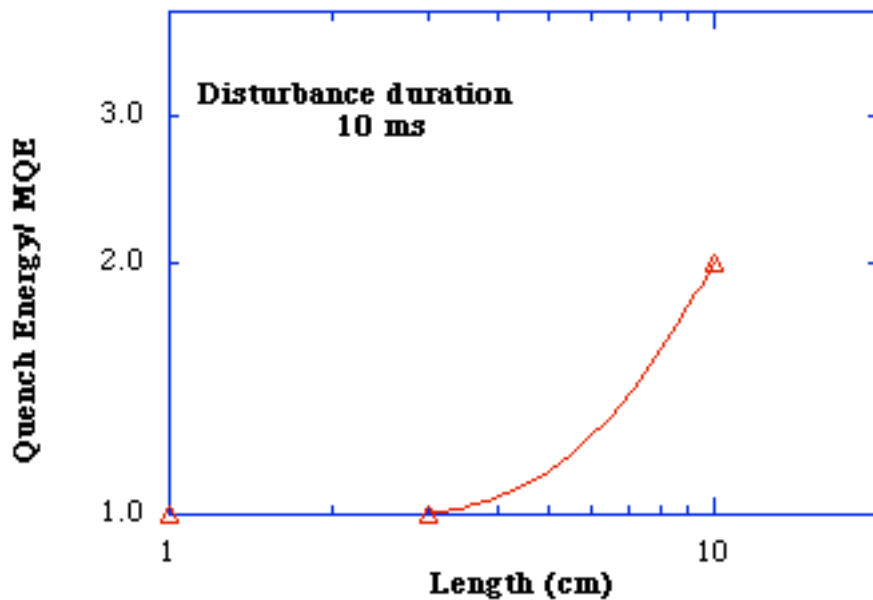


Fig. 15.10: Quench Energy Vs the disturbance length at a fixed value of the disturbance duration (10 ms).

15.4 POSSIBLE DISTURBANCE SOURCES

In this section we briefly analyse the possible heat releases inside the winding, trying to get an idea about the order of magnitude of the released energy or power. The heat releases of a mechanical nature generated directly inside the coil are due to un-reversible phenomena like movements, breakages or slippings, related to basic mechanisms such as stress above the yield limit, shear failure or bonding failure. Though formal and rigorous analysis is a very hard task, some special cases can be analysed.

Pure aluminium in plastic regime

It has been stressed in previous chapters that the hoop force puts the pure aluminium beyond the elastic limit. During a cycle of the magnetic field the energy dissipated per unit volume is given by the integral of the stress over deformation:

$$E = \int \sigma d\epsilon. \quad (15.6)$$

In our case, this integral, calculated using the curves with 40 MPa yield strength, gives $E = 2.9 \cdot 10^4 \text{ J/m}^3$. Considering a total cold mass of pure aluminium of 28 m^3 , we have a total dissipation of $8.1 \cdot 10^5 \text{ J}$. The power generation depends on the charge time as discussed in Chapt. 17. This power can be easily drained away by the cooling circuit with no problems. In this case we have a heat dissipation of mechanical nature, but not strictly related to the coil stability because the phenomenon is in a steady state.

Bonding failure

A bonding failure can occur at several interfaces: Rutherford-pure aluminium, pure aluminium - reinforcement, conductor - insulation, turn to turn, layer to layer. In each case energy could be dissipated. The most dangerous case occurs when the heat is released very close to the Rutherford, so that the cable-pure aluminium bonding must be carefully studied. The mechanical analysis showed that a shear stress of 20 MPa exists at this interface. This shear stress is due to the differential thermal contraction between pure aluminium and the Rutherford cable. Since pure aluminium contracts, from RT. to 4.5 K, much more than Copper and NbTi, the Rutherford is put in compression, while the pure aluminium is in tension. Since the Rutherford is completely surrounded by the pure aluminium, we would also have the same stress if there was no bonding at the interface. As a consequence a failure of this bonding should not be dramatic from the point of view of the release of elastic energy. In case we have an extruded insert, it can be argued that the failure of the bonding could allow micro-movements of the strands under the action of the magnetic field. Looking at typical cross section of Rutherford cable inside pure aluminium, we can observe the existence of voids. The Rutherford is compacted with a filling factor of around 85%. The worst situation happens when under the action of the axial force, one half of the Rutherford moves against the other half. Since the gap between the two halves is $s = 0.05 \text{ mm}$, the energy dissipation per unit length is $W = B I s = 4.3 \cdot 10000 \cdot 5 \cdot 10^{-5} = 2.15 \text{ J/m}$ (we have used a current of 10 kA because only half the Rutherford moves). This energy dissipation is well within the enthalpy margin (4.2 J/m).

Epoxy cracks

Since the epoxy contracts much more than aluminium when cooling down from RT. to 4.5 K, the epoxy is put in tension. The stored elastic energy can be written as :

$$E = \frac{3}{2} Y \epsilon_0^2 \frac{1}{(1-2\nu)}, \quad (15.7)$$

where Y is the Young's modulus (8 GPa), ϵ_0 is the strain due to the differential contraction (of the order of $8 \cdot 10^{-3}$), ν is the Poisson ratio (0.21) and V is the volume. The elastic energy is of the order of 10^6 J/m^3 . This energy constitutes a potential disturbance source. Nevertheless in order to have significant disturbances (of the order of the enthalpy margin), a big fraction of epoxy should crack in a large volume. As an example the Enthalpy Margin (4.2 J) is roughly equivalent to the energy stored in the conductor insulation for a length of 25 cm. The complete -insulation crack along 25 cm all around the conductor is quite an improbable occurrence.

15.5 COMPARISON WITH LARGE RUNNING COILS

In the previous sections we discussed the basic concepts to carry out stability transient analyses on an aluminium stabilised superconducting winding. These ideas were preliminary tested by predicting the amount of localised energy necessary to quench a mock up of the DELPHI coil. The predicted values (using 3 different numerical codes HEATING, CASTEM and RALTRAN) and the experimental measurements of MQE ranged within a factor 2. On the basis of these results we think that the developed methods for stability analysis, involving the use of 3D Finite Element Codes, can give realistic information. However if this analysis is applied not only to the magnet under design but also to different (and existing) magnets, one can have comparative results of interest for the design itself.

In this framework we made a comparison of the computed MQE for some aluminium stabilised solenoids with the results obtained for CMS. As for the enthalpy margin the solenoids ALEPH and CDF were considered. In performing comparative studies it is important to consider that the MQE depends on the RRR, which depends on several factors such as the aluminium purity and the stress level in the conductor. Since this information is only partially available, we preferred to compute the MQE for a wide range of values of the RRR at $B = 0 \text{ T}$, so that a more general picture about stability is given. The results are shown in Fig. 15.11 and 15.12 for the two cases of instantaneous and finite current diffusion.

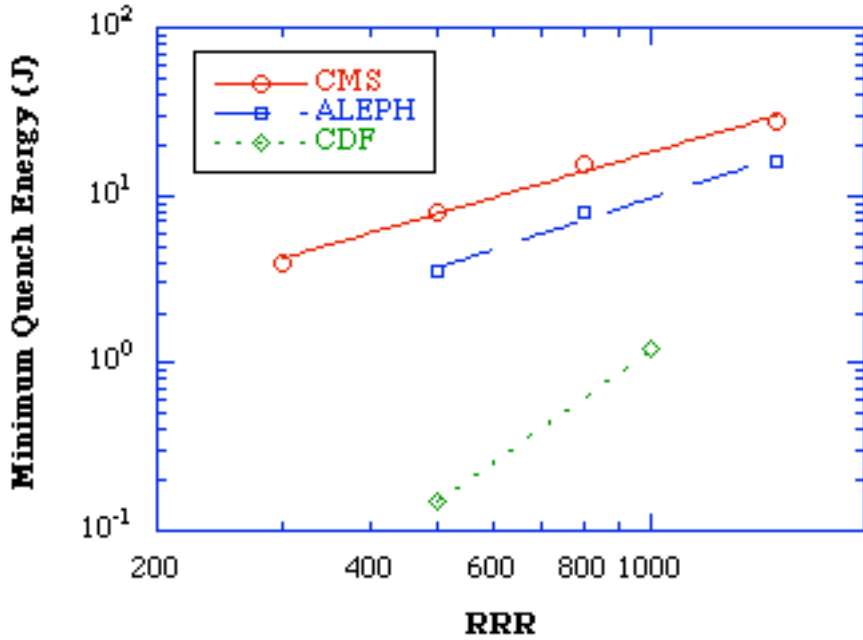


Fig. 15.11: MQE vs. RRR for CMS, CDF and ALEPH solenoids in the case of instantaneous current diffusion.

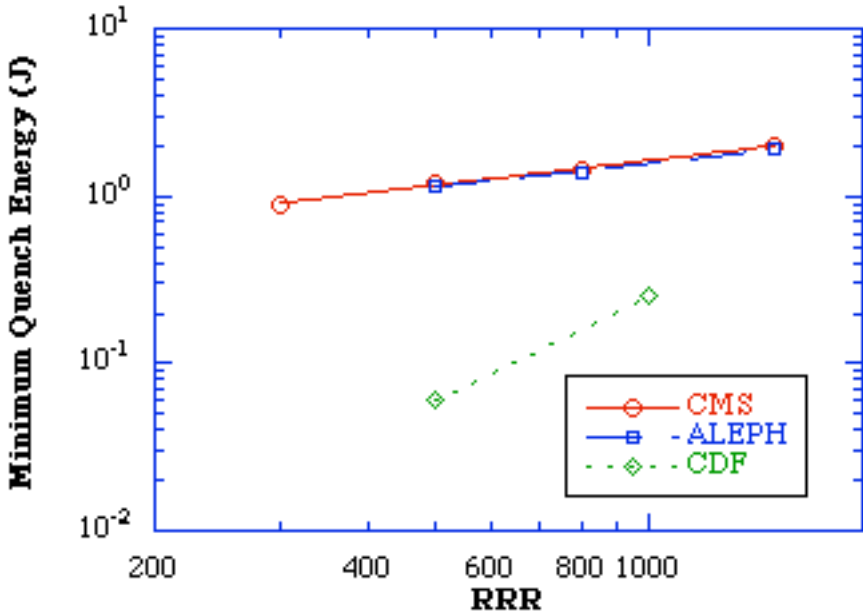


Fig. 15.12: MQE vs. RRR for CMS, CDF and ALEPH solenoids in the case of finite current diffusion.

From the point of view of our interest, i.e. the optimisation of the CMS winding and conductor, we could infer that the stability margin against localised disturbances of CMS is at least of the same order as the ALEPH margin and much higher than the CDF one. Nevertheless a more accurate discussion about this result is needed, because we must relate the calculated stability margin with the level of disturbances.

If we had information about the stress distribution for the three magnets, we should be able to find a correlation between stress (and then possible mechanical

disturbances) and stability margins. Since the insulation is the weakest part of the winding, it would be interesting to know the stress distribution in that part.

We carried out this exercise by computing the stress distribution in the insulation of ALEPH and CMS. As parameter for comparison we choose the principal stress S1. Figures 15.13 and 15.14, p. C-42, show a detail of insulation stress in ALEPH and CMS due to the thermal contraction. Fig. 15.15, p. C-43, shows how the CMS insulation stress barely increase due to the magnetic load, as can be seen by looking to Fig. 15.14 which is repeated on the same page to ease comparison.

15.6 CONCLUSIONS

These previous results clearly show that the stresses in insulation are very similar for ALEPH and CMS. They are mainly due to the cool-down from RT. to operating temperature. The potential disturbances for unit volume coming from breaks of insulation or in the epoxy should be the same for both coils.

Since the Enthalpy margin for unit volume and the MQE are similar for both coils, it is possible to conclude that CMS is as stable as ALEPH with respect to localised and distributed disturbances in insulation.

16 QUENCH ANALYSIS

16.1 INTRODUCTION

The coil protection system, as shown in Fig. 16.1, is based on a Quench Back Cylinder (QBC)/dump resistor concept. The winding/QBC assembly works essentially as a current transformer, in which the winding acts as the primary circuit and the QBC as the secondary.

During normal coil operation, the power dissipated in the QBC due to eddy currents is negligible, given the very low current change rate. The ramp up time is 5 hours and the slow dumping, which is performed into a 2 mW resistor, has a time constant of 2 hours, as described in Chapt. 20.

During a fast dump on the other hand, the power dissipated in the QBC effectively contributes to driving the whole winding to a normal state.

The quench protection analysis is based on the electrical circuit shown in Fig. 16.1. Two different scenarios have been considered:

- normal external fast dumping,
- failure of the protection system.

Finite Element and analytical calculations were carried out to analyse the quench protection. The failure of the protection system has only been modelled by analytical calculations.

The calculations on the quench back give an average coil final temperature after fast discharge of 56 K, which corresponds to about 80 % of the 2.7 GJ initial magnetic energy extracted in the 50 mw protection resistor. The aluminium RRR influences the quench back characteristics when the RRR is less than 500; the average coil final temperature is calculated to reach just over 60 K and the energy extracted in the protection resistor is 74% of the initial magnetic energy.

A failure of the protection system has also been studied. In this case the maximum calculated temperature in the winding reaches about 150 K and there is a dependence on the aluminium RRR when the RRR is less than 100.

The stresses induced in the magnet due to current discharge are kept at a low level, i.e. a few MPa in the quench back cylinder.

16.2 QUENCH BACK PROTECTION

Rapid discharge mode creates a current decay which induces losses in the structure especially in the external cylinder, large enough to raise the temperature of the winding and to quench the layers successively in a typical time of 5 to 10 seconds. Joule effect due to the current in the aluminium stabiliser reinforces the quench back mechanism. The whole winding being entirely in the resistive state and the layers being in good thermal contact, the energy deposition in the winding is quite uniform.

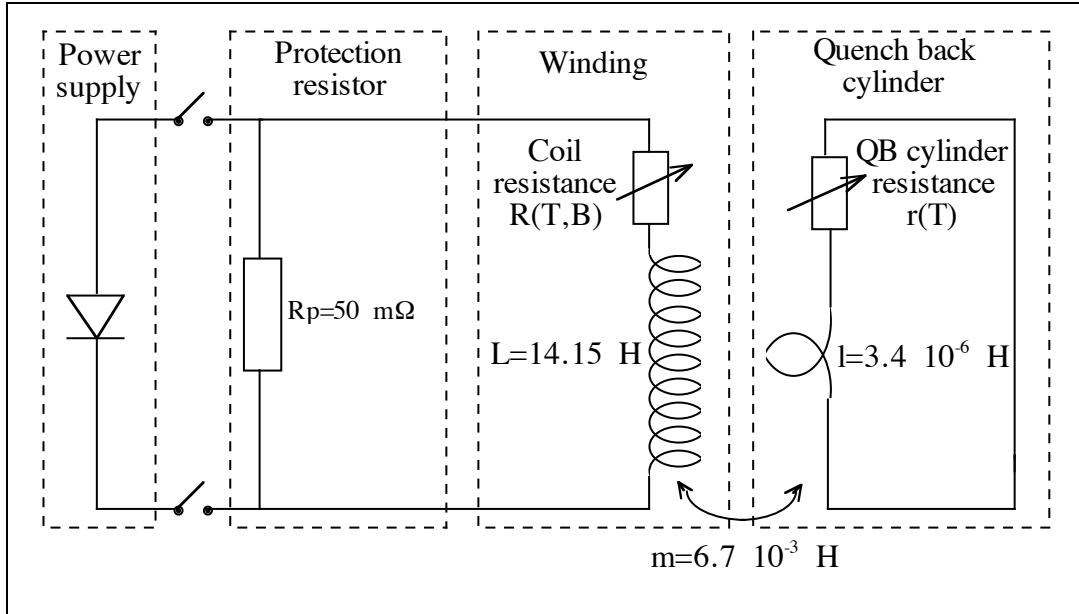


Fig. 16.1: Equivalent electrical circuit of the winding/shell configuration.

16.2.1 Quench back typical results

The post-quench-back coil temperature distribution has been estimated by finite element analysis [16-1, 16-2] and by analytical computations [16-2, 16-3, 16-4].

Typical results lead to the characteristics provided in Table 16.1. They are obtained by analytical calculations. These results correspond to the 12 mm thick quench back cylinder, the dump resistor of 0.050 W and an aluminium RRR of 1000.

Other simulations have been made by varying the following parameters: aluminium RRR, external cylinder thickness, dump resistor value. All calculations show that the quench back protection is efficient and leads to high extracted energy ratio of about 80% hence to low final temperatures in the coil together with a good temperature uniformity. The maximum temperature gradient calculated is 16 K, and thus the thermal stresses in the winding are therefore kept at an acceptable level. The current diffusion effect has not been taken into account as it increases the local dissipated power, hereby the propagation velocities, and therefore acts favourably for protection. It has been studied in [16-5].

Table 16.1
Quench back typical results.

Initial quench time	No quench	0 s	0 s
Breaker opening delay	0 s	0 s	16 s
Quench back delay *	7 s	7 s	7 s
Average coil final temperature	56 K	56 K	56 K
Hot spot temperature	-	61 K	70 K
ΔT max. within the coil	2 K	7 K	16 K
Extracted energy ratio	77 %		
Effective time constant **	212 s		
Magnet final resistance	0.05 W		

* delay to have the 4 layers quenched after breakers open.

** time when the current is $I = I_0 / e = 7173 \text{ A}$.

16.2.2 Comparison of the methods

The comparison of the results given by the FE calculations and the analytical calculations (see Table 16.2) show that the former calculations give lower coil temperature and higher extracted energy ratio than the latter calculations, since the analytical calculations do not take into account the heat conduction in the winding and the heat exchange with the quench back cylinder [16-2].

Nevertheless, the temperatures obtained with the analytical computations are presented for the quench back analysis as conservative upper bound temperatures.

Analytical computations:

The temperature dependence of the material specific heats and electrical resistivities are calculated with power law functions on given temperature intervals. The magnetic field effect is taken into account by adding to the resistivity at $T = 4.2 \text{ K}$ and 0 T a term corresponding to the magnetoresistance at $T = 4.2 \text{ K}$ and 2 T . The properties of aluminium at 0 T are provided in Table 16.3 for a RRR of 1000.

The propagation velocity calculations are performed with the material heat conductivities at liquid helium temperature, which lead to the following values:

- axial velocity: 0.09 m/s ,
- radial velocity: 0.13 m/s ,
- azimuthal velocity: 1.39 m/s (along the conductor).

Finite element computations:

The FE analysis takes into account the magnetic field and temperature dependence of the material thermal and electrical properties: the electrical resistivity, specific heat, heat conductivity values are obtained from the Cryocomp software database. The FE analysis also calculates the critical and current sharing temperatures as a function of the magnetic field in each layer, the effect of the magnetic field variation due to the eddy currents in the quench back cylinder, and the energy extracted by the liquid helium remaining in the cooling pipes at the beginning of the discharge until it is completely evaporated. Indeed, when the protection is triggered, the LHe feeding is stopped, but the cooling circuit is still full of liquid helium which extracts a small portion of energy from the magnet. Each layer is totally quenched when the temperature in this layer reaches the critical temperature threshold.

Table 16.2
Comparison of the calculation methods (RRR Al = 1000).

	FE calculations	Analytical calculations
Average final coil temperature	44 K	56 K
ΔT max. within the coil	15 K	16 K
Extracted energy ratio	84%	77 %

Table 16.3
Aluminium properties at 0 T for analytical calculations (RRR Al = 1000).

T (K)	4.2	10	15	20	30	40	50	60	70
r (10^{-10} W.m)	0.250	0.258	0.291	0.378	0.898	2.3	5.25	10.5	17.2
Cv (10^3 J/m 3 .K)	0.759	4.01	11	24	85.1	210	395	579	764

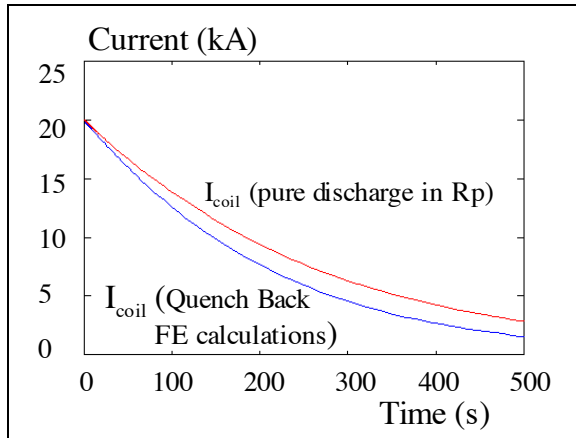


Fig. 16.2: Coil current during a fast discharge compared to a pure discharge in a L/Rp circuit.

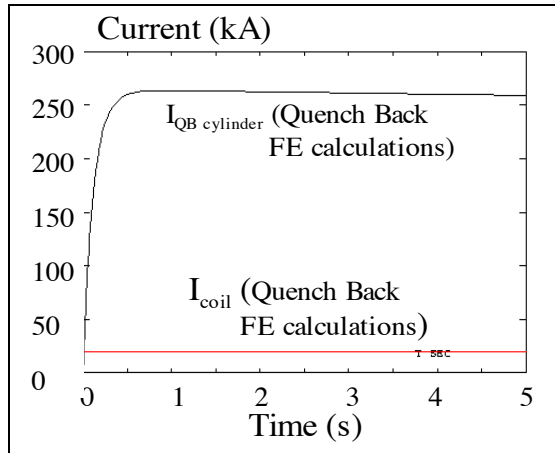


Fig. 16.3: Currents in the coil and the 12 mm thick quench back cylinder.

16.2.3 Quench back process

The FE calculations include the thermal diffusion and provide accurate description of the magnet behaviour during quench back. Typical graphs are provided on Fig. 16.2 and Fig. 16.3, and Fig. 16.5 to Fig. 16.8. These graphs correspond to an aluminium RRR equal to 1000. The inductances are constant. The eddy currents in the quench back cylinder increase rapidly during the first seconds following the trigger of the fast dump (Fig. 16.3).

The voltage at the connections of the coil during fast discharge is estimated at the beginning of the discharge to be 1000 V with a 0.050 W protection resistor bank. The voltage is distributed across turns and layers. The maximum resistive voltages are obtained between layers at their extremities according to Fig. 16.4. The maximum value obtained from these calculations is 530 V [16-6] for V2 and V3 (see Fig. 16.4). The insulation thickness is 1 mm and 0.5 mm respectively for layer to layer insulation and turn to turn insulation. These thickness allow to withstand high voltages so that the magnet is safe from over voltage during

quench back.

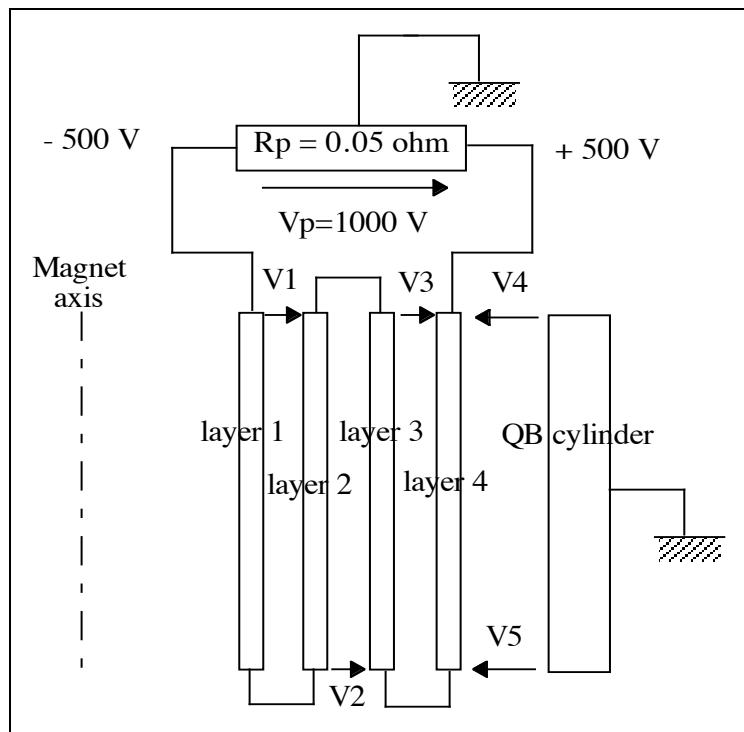


Fig. 16.4: Electrical connections between layers.

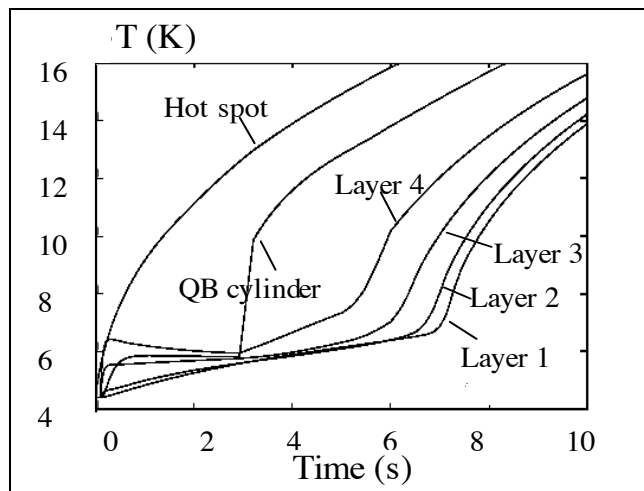


Fig. 16.5: Temperature increase at the beginning of fast discharge.

The first layer to quench is the fourth one, which is the closest to the quench back cylinder, then the neighbouring layer quenches and so on, as shown on Fig. 16.5 and Fig. 16.7.

It is possible to grade the conductor to have different material cross sections from one layer to the other, keeping the overall conductor cross section identical in the 4 layers.

The grading allows to diminish the required superconducting material quantity and to get the same enthalpy margin in each layer. It results in a more uniform heat dissipation in the 4 layers (Fig. 16.8) and it increases the stability margin.

The possible grading of the CMS conductor is described in a specific technical report [16-7]. The gradation parameters are:

- the aluminium stabiliser cross section,
- the superconducting material cross section.

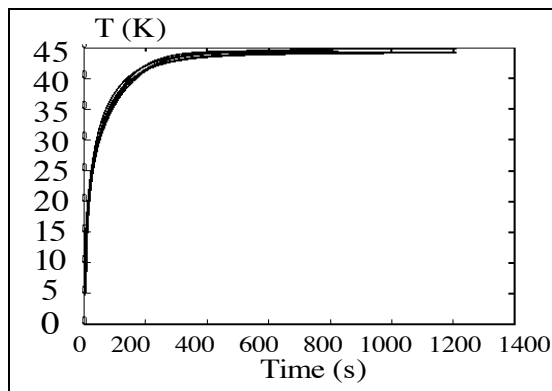


Fig. 16.6: Temperature increase during a fast discharge.

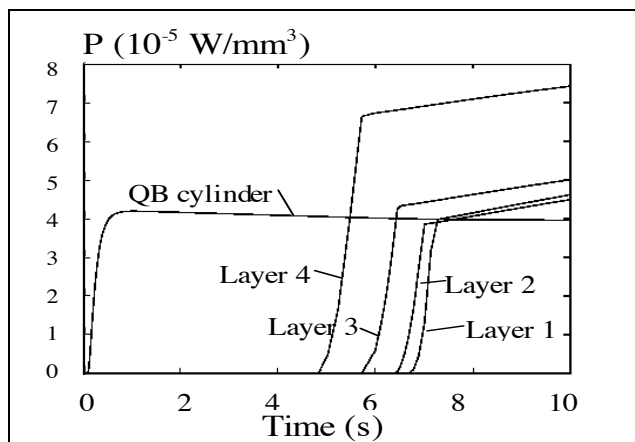


Fig. 16.7: Joule heat source in each layer and QB cylinder at the beginning of a fast discharge.

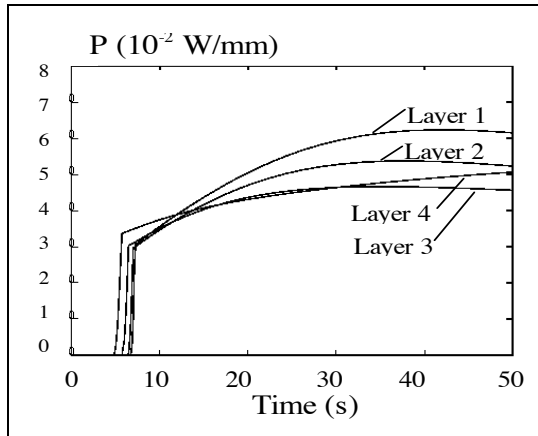


Fig. 16.8: Joule heat source in each layer: effect of grading.

16.2.4 Influence of parameters

Temperatures in the coil and extracted energy ratio have been calculated by varying the following parameters:

1. Quench back cylinder thickness : 5, 12, 18, 50 mm

The eddy currents in the quench back cylinder reach a value which depends on the thickness of the quench back cylinder, whereas current density stays constant at about 1.8 A/mm^2 .

The part of the initial magnetic energy that is extracted in the protection resistor R_p is about 80%, when the thickness ranges from 5 to 50 mm.

The layers quench faster with thicker quench back cylinder: 11 s with a 5 mm thick cylinder, 3 s with a 50 mm thick cylinder.

The quench back cylinder thickness does not show a great influence on the quench back characteristics.

2. Protection resistor bank: 0.050 W and 0.025 W

Typical results of the influence of the protection resistor are given in Table 16.4, and [16-1, 16-2].

3. Aluminium RRR from 50 to 2800 taking $\text{RRR} = r(273 \text{ K}) / r(4.2 \text{ K})$

The aluminium RRR influences the final temperature and a variation of the extracted energy ratio is mainly noticeable for RRR values lower than 500, as shown on Fig. 16.9 and Fig. 16.10, where R_p is equal to 0.050 w.

Table 16.4
Influence of R_p on quench back characteristics (RRR Al = 1000).

	$R_p = 0.050 \text{ W}$	$R_p = 0.025 \text{ W}$
Quench back delay *	7 s	20
Average final coil temperature	56 K	72 K

Hot spot temperature (no breaker opening delay)	61 K	86 K
Hot spot temperature (16s breaker opening delay)	70 K	97 K
Extracted energy ratio	78 %	48 %

* delay to have the 4 layers quenched after opening of the breakers.

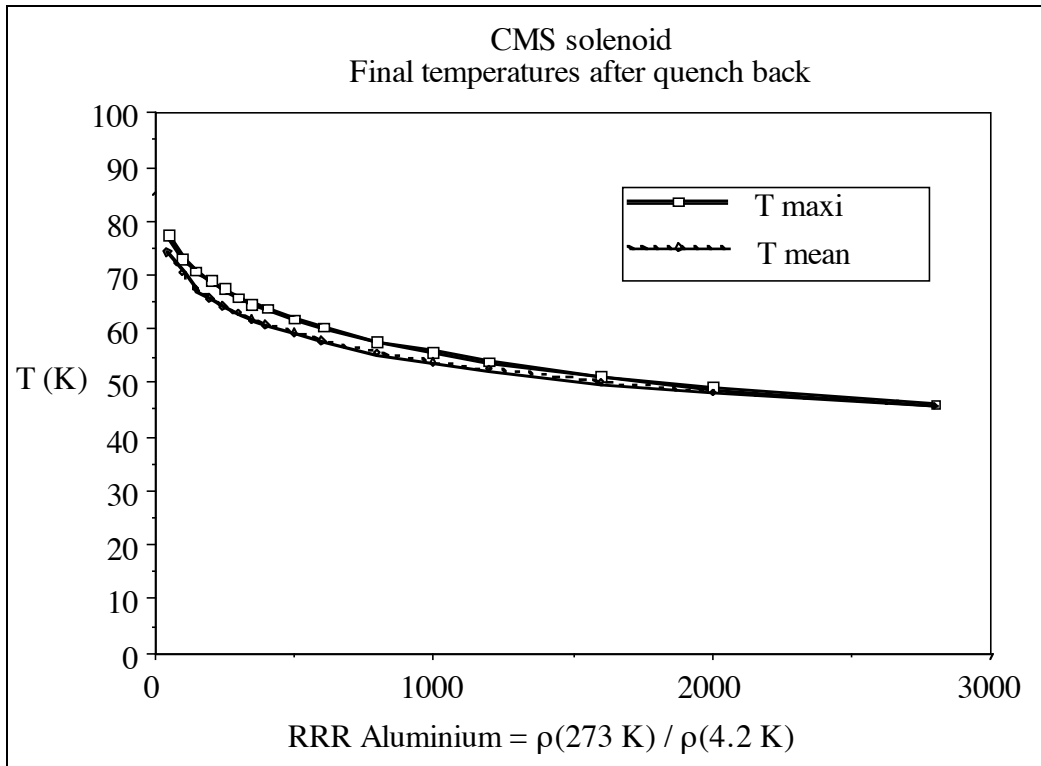


Fig. 16.9: Coil final temperature after quench back versus aluminium RRR.

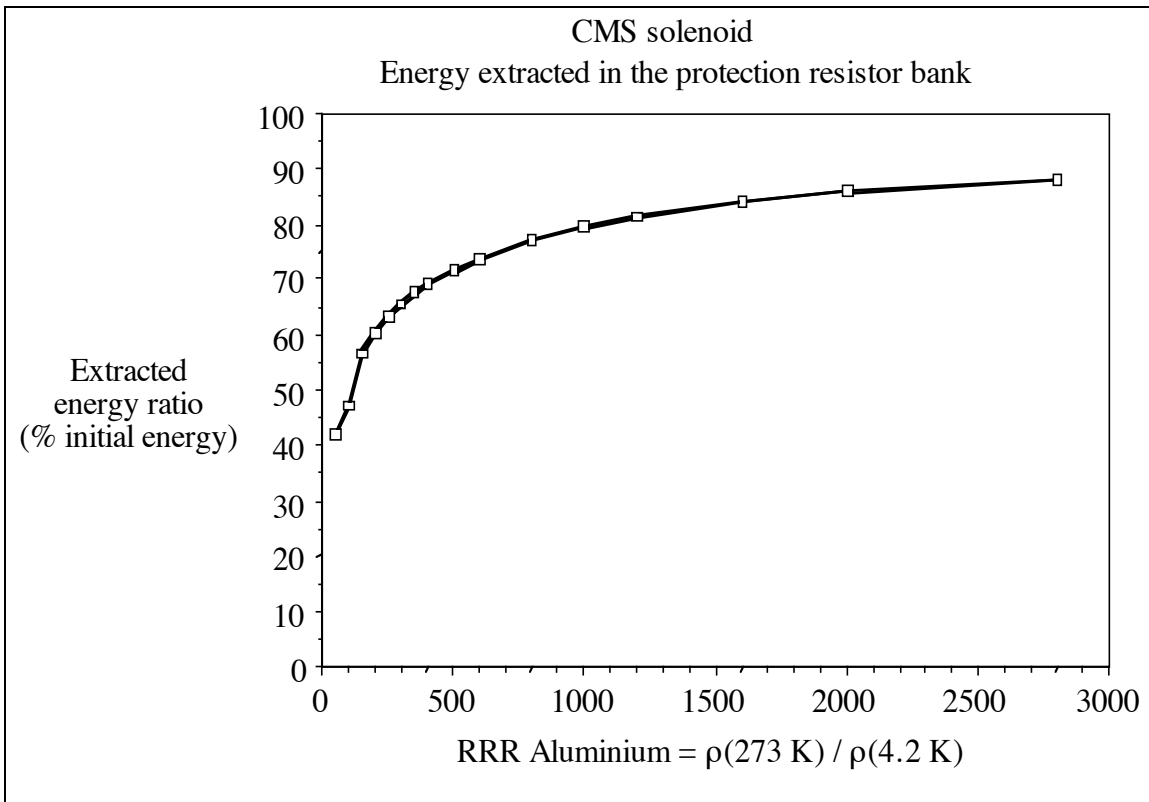


Fig. 16.10: Ratio of extracted energy versus aluminium RRR.

16.3 PROTECTION SYSTEM FAILURE

The entire stored energy will be dissipated within the coil in case of a protection system failure. The specific magnetic stored energy per unit mass is about 12.2 kJ/kg. When uniformly released into the coil it rises the temperature to 89 K.

Analytical computation results are presented in this chapter. As mentioned earlier, they do not include the effects of the heat conduction in the winding and heat exchange with the quench back cylinder. The temperatures obtained with the analytical computations are presented for the quench back analysis as conservative upper bound temperatures.

A finite element analysis will allow to confirm these results and will provide a calculated temperature field map to determine the stress level inside the winding after quench. The effect of discharging at low currents will also be studied.

16.3.1 Quench propagation typical results

Analytical computations have been performed to calculate the temperature distribution in the coil due to a quench located at the end of the coil [16-8]. This is a worst case situation which will causes both the highest temperature and the highest temperature gradient in the coil.

Typical results are reported in Table 16.5. In a first step the normal zone propagates at constant current. When the voltage across the coil reaches the capability of the power supply, as the normal zone develops both in length and temperature, the current starts to decrease and the quench back mechanism starts but much more slowly than in a normal dump.

Typical coil current profile is given on Fig. 16.11 where the quench back current profile

is also plotted. Typical temperature profile is provided on Fig. 16.12 together with the quench back temperature profile.

Table 16.5

Quench values in case of protection system failure (RRR Al = 1000).

Effective time constant *	270 s
Axial quench velocity	0.09 m/s
Quench back delay **	100 s
Maximum temperature	146 K
Magnet final resistance	0.17 W

* time when the current is $I = I_0 / e = 7173$ A.

** delay to have the 4 layers quenched.

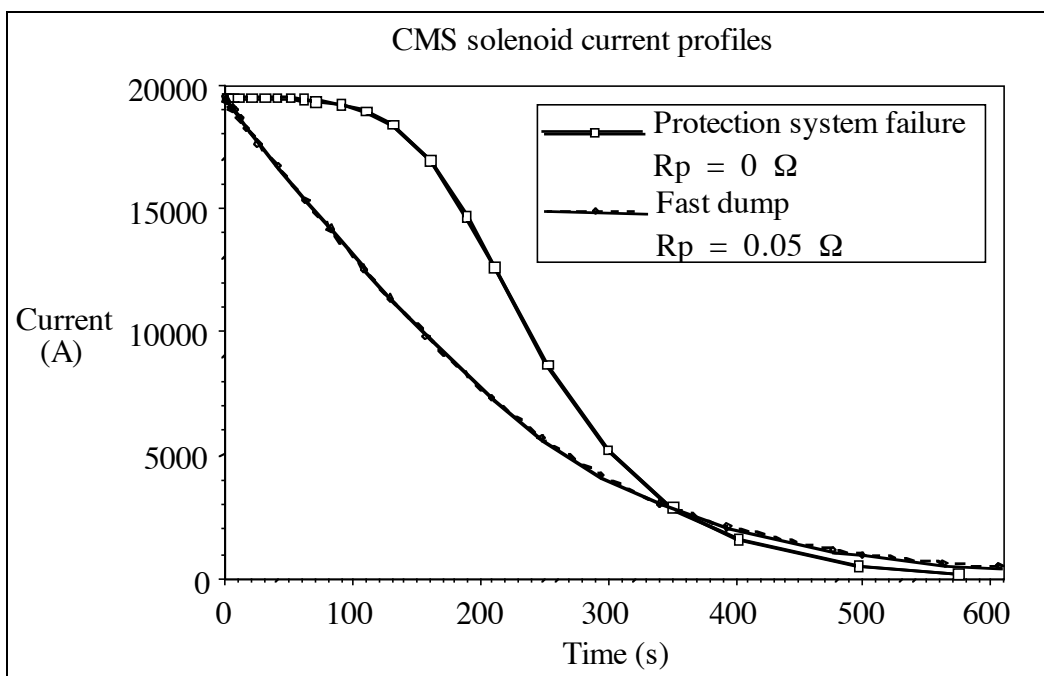


Fig. 16.11: Comparison of the current profiles with protection system failure and with fast dump.

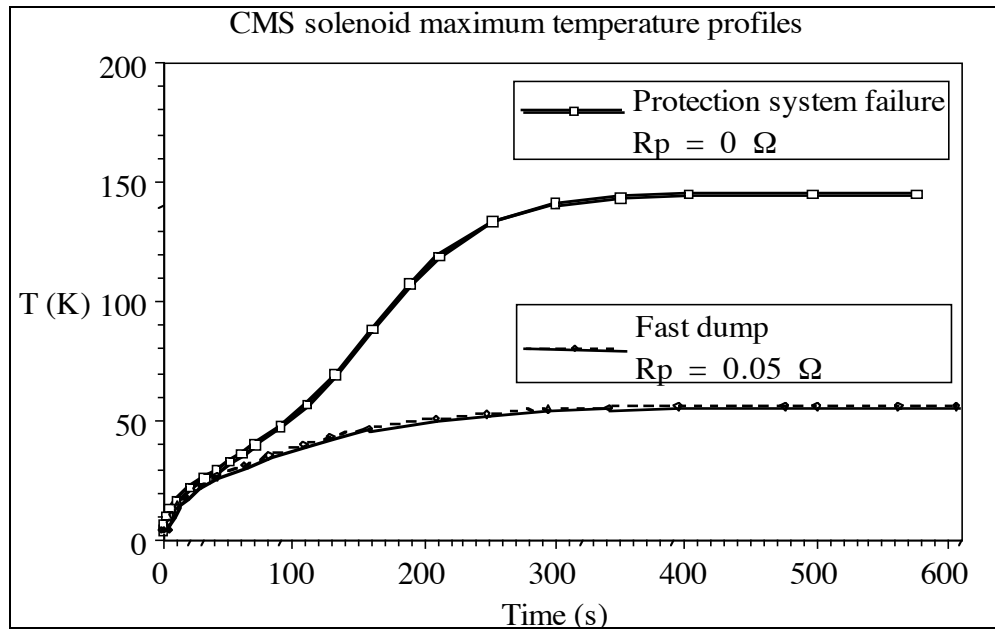


Fig. 16.12: Comparison of the coil temperature profiles with protection system failure and with fast dump.

16.3.2 Influence of parameters

The maximal and minimal temperatures have been calculated for several RRR by the analytical computation (Fig. 16.13).

For RRR greater than 100, these analytical calculations indicate after quench, a maximal temperature of about 150 K and a temperature difference within the coil of about 110 K.

16.4 INDUCED FORCES DURING DISCHARGES

As shown on Fig. 16.11, both in case of a normal external fast dump and a failure of the protection system, a fast decay of the current occurs in the winding, resulting in a fast decrease of the magnetic flux. Therefore eddy currents appear in the magnet elements which are electromagnetically coupled with the coil, i.e. the quench back cylinder, the external and internal vacuum tank, the screens and the iron yoke. Lorentz forces induce mechanical stresses in those elements.

At nominal current operation, the winding hoop strain is 0.15 %. The quench back cylinder strain is also 0.15 %, as it follows the coil expansion. This strain leads to a hoop stress of 125 MPa, in a quench back cylinder made of a 6082 aluminium alloy with a Young's Modulus of 77 Gpa.

During discharges, the stresses in the quench back cylinder due to the Lorentz forces are added to the above values. The results are given in Table 16.6 [16-9, 16-10]. Because of the low eddy current density in the quench back cylinder (1.8 A/mm^2) the Lorentz forces are low, hence the induced stresses are negligible compared to the stresses due to the coil deformation.

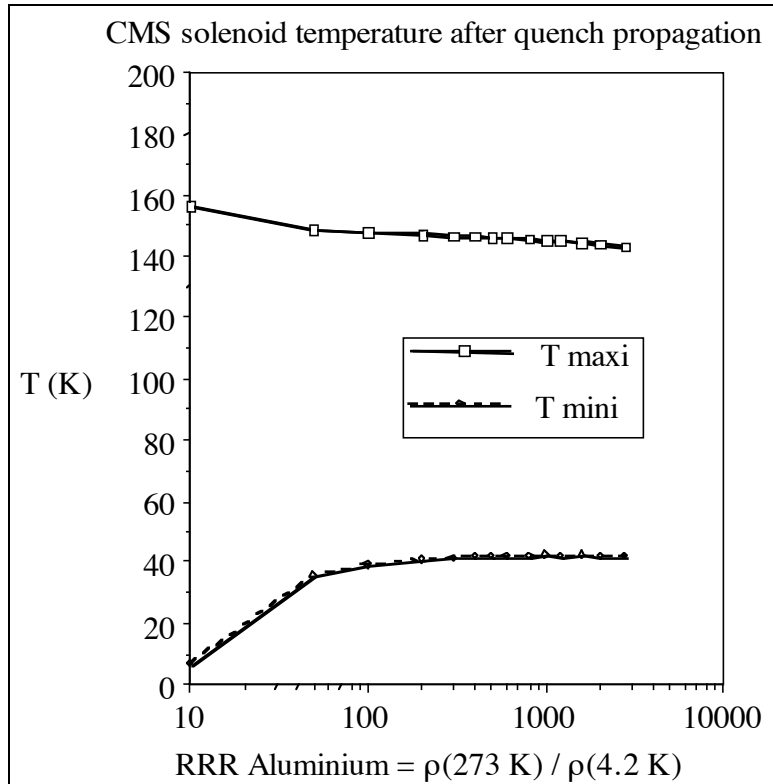


Fig. 16.13: Maximal and minimal temperature versus aluminium RRR, in case of failure of the protection system.

Table 16.6
Hoop stresses in the quench back cylinder.

	Lorentz forces	0.16% coil deformation	TOTAL
<i>Nominal current operation</i>		125 MPa	125 MPa
Normal external fast dumping	5 MPa	125 MPa	130 MPa
Protection system failure	7 MPa	125 MPa	132 MPa

In a first approach, one can say that the mutual and self inductances of the internal and external vacuum tanks are close to the quench back cylinder ones because of there similar geometries. As the electrical resistivity of stainless steel at room temperature is about 40 times greater than that of 6082 aluminium alloy at 4.4 K, the eddy currents in the vacuum tank are low. As a result the induced stresses are negligible.

To contain the forces on the screens, due to eddy currents during the discharge to acceptable levels, the screens will be cut into sectors.

A FE analysis to be done soon will allow to estimate the forces in the screens, the external and internal shells of the vacuum tank, and iron yoke, from the magnetic field map obtained with the FE computations.

17. COIL CRYOGENIC SYSTEM

17.1 INTRODUCTION

The CMS solenoid cryogenic system is composed of two sub systems: the cryogenic plant and the coil cryogenic system these are defined as located outside and inside the coil vacuum vessel.

The cryogenic plant is presented in Chapt. 21. It is a dedicated helium refrigerator which produces and delivers the cryogenic power to the coil cryogenic system through an intermediate 5000 l LHe vessel installed on the side of the CMS magnet yoke, (see Fig. 26.8, p. C-58).

The CMS coil cryogenic system is composed of the 220-tonne superconducting coil working at liquid helium temperature, the thermal shield system cooled by a flow of helium at 60 K to 80 K, and the vacuum vessel. It also includes two chimneys crossing the iron yoke, one for the 20 kA helium cooled current leads, the control wiring and the pumping, and the other one for the cryogenic lines. The latter one ends at the top of the magnet, above the yoke, in an ancillary cryogenic vessel which houses the helium phase separator and the helium manifolds.

The main features of the coil which characterise the CMS cryogenics are:

- the cold mass of 220 tonnes,
- the magnetic stored energy of 2.7 GJ,
- the coil indirect cooling mode using a thermosiphon process.

Another specific aspect is the quench back mechanism: fast dumping the magnetic field spontaneously quenches the coil. This sensitivity to fast field variation brings certain advantages for the quench protection but must not be used for normal operation because 20% of the stored energy is released as heat in the coil, raising its temperature up to 50 K; a period of about 3 days is then necessary for re-cooling. So fast dumping must only be used in emergency cases such as a quench.

The slow dumping sequence, which does not quench the coil, lasts about 5 hours. The main function of the 5000 l vessel is to secure the cryogenic power supply so that the field can always be dumped slowly.

17.2 CRYOGENIC LOADS

17.2.1 Radiation heat flux

The heat radiation is the predominant component of the cryogenic loads because of the large dimension of the solenoid. Multilayer superinsulation is inserted on both sides of the thermal shields and the radiation heat loads are calculated as shown in Table 17.1.

Table 17.1
Multilayer insulation parameters.

	Surface area m ²	Number of layers	Heat flux W/m ²	Heat load Watt
Cold mass at 4.4 K	560	5	0.2	120
Thermal shield	560	30	5	2800

17.2.2 Cryogenic coil Supports

The 18 axial tie rods and the 12 radial belts of the solenoid are made of titanium alloy (Chapt. 18). Their temperature profiles must be independent of the refrigerator availability so there is no thermal or mechanical link between them and the shield system. Table 17.2 gives the dimension and heat input of the axial and radial cold mass tie rods.

Table 17.2
Cold mass tie rod parameters.

Rod	Section (mm ²)	Length (m)	Heat input per rod (W)	Quantity	Total heat load (W)
Axial tie rod	3612	12.70	0.4	18	7.2
Radial tie rod	2700	1.60	2.4	12	28.8

The system holding the shield consists of a set of rods made of low conductivity material, connecting the shield panels to the vacuum vessel. One end of each panel is rigidly fixed and the other allowed to move in the panel plane to accommodate the thermal contractions. Total heat input to the shield is 500 W.

17.3 CRYOGENIC LOAD AT LIQUID HELIUM TEMPERATURE

The saturated helium pressure of the coil cooling circuit is controlled by the refrigerator at a constant value of 1.25 bar providing a boiling temperature of 4.45 K. The losses at this temperature level are given in Table 17.3 at the nominal coil current of 20 kA.

Table 17.3
Steady state heat input at nominal coil current.

Total static heat losses at nominal current = 185 W		
Radiation heat load	120	W
Holding system	40	W
Phase separator and valves	20	W
Conductor junctions	5	W
Current lead LHe mass flow rate	2.5	g/s

When ramping up or down the coil current, eddy current in the coil structure and pure aluminium plastic strain build up additional losses summarised in Table 17.4.

Table 17.4
Dynamic heat loads due to field ramping.

Dynamic heat loads during ramping up and slow discharge of current		
Mean dynamic power dissipated in the coil	70	W
Peak value of dynamic heat load	240	W

17.3.1 Thermal shield cryogenic load

Table 17.5 indicates the heat load on the thermal shield system.

Table 17.5
Thermal shield heat load.

Radiation heat load at 60-80 K	2800	W
Supports	500	W

17.4 INTERNAL COOLING CIRCUITS

The flow chart of the solenoid cooling system is pictured in Fig. 17.1. It consists essentially of two independent cryogenic circuits.

- The coil cooling circuit using saturated liquid helium circulated in a thermosiphon mode. It is a closed loop including the phase separator vessel in elevated location, the cooling tubes attached on the coil external cylinder, the connecting manifolds and one feeding valve. This circuit also supplies the current leads with LHe.
- The thermal shield cooling circuit using forced flow helium gas.

These circuits, including the separator vessel and the current leads, are designed to support a pressure of 18 bars.

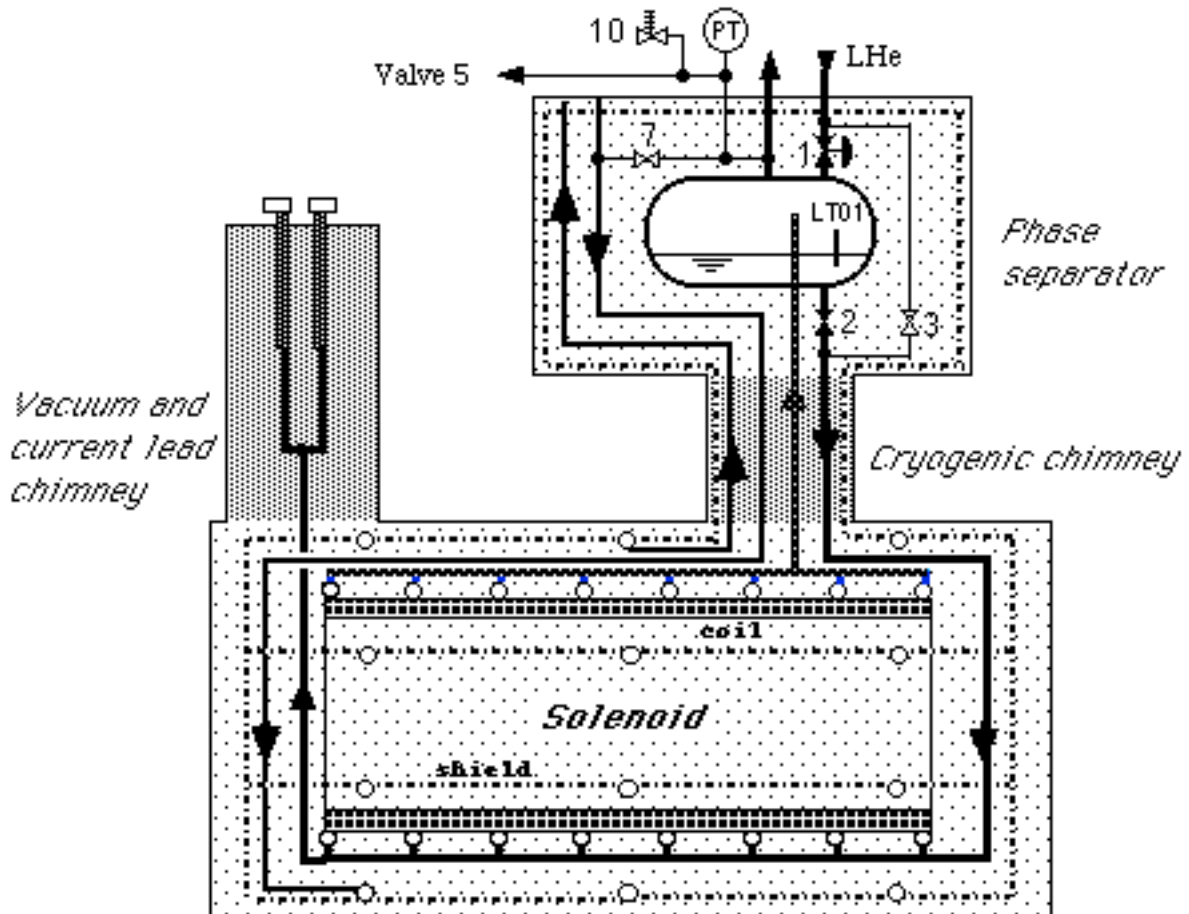


Fig. 17.1: CMS coil cooling circuit.

17.4.1 Thermal shield system

The thermal shield system is composed of 36 independent panels attached to the inner and outer vacuum vessel walls and closing plates at both ends of the coil. This system is designed to accommodate thermal contraction. Each shield panel is made of 5 mm thick aluminium plate with a cooling pipe welded on it.

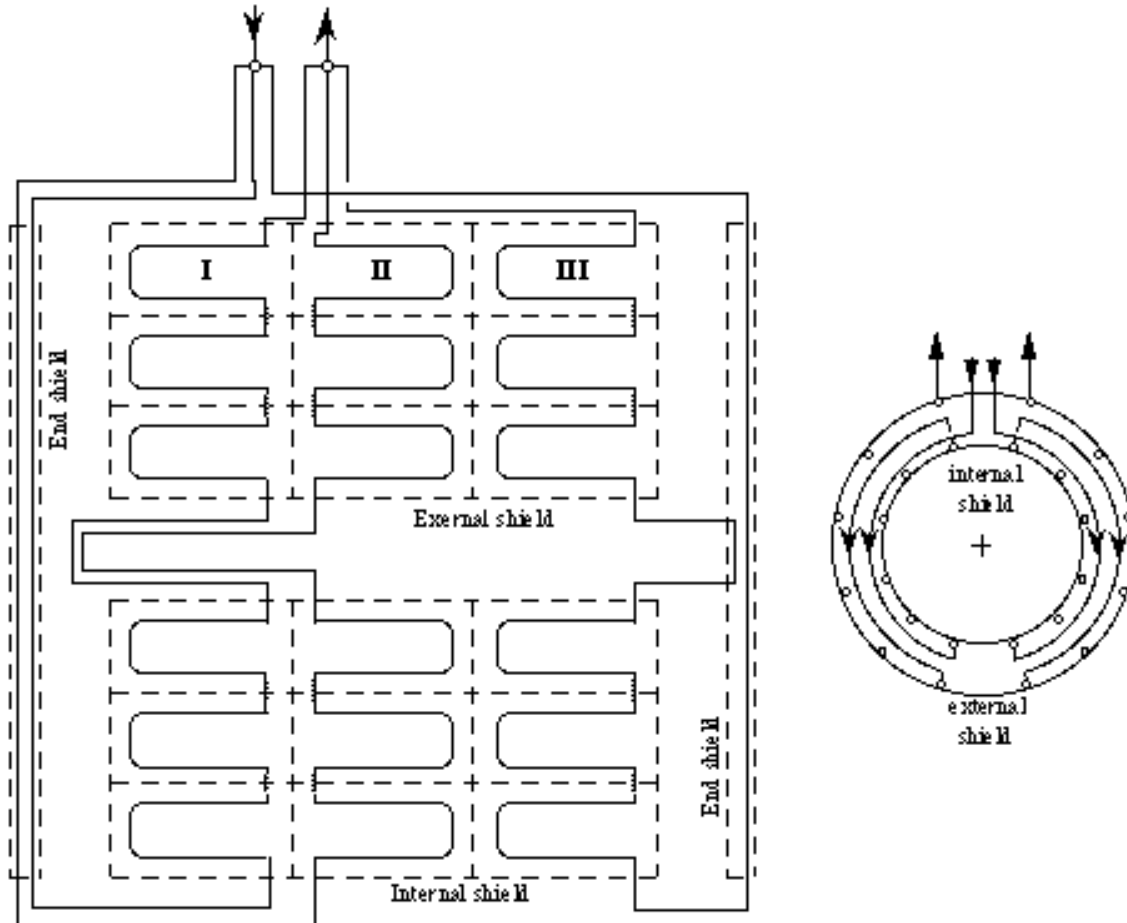


Fig. 17.2: Thermal shield helium circuit.

In normal conditions the thermal shield is cooled by forced flow helium gas provided by the helium refrigerator. In case of a momentary refrigerator stop, it is supplied by the coil circuit helium boil off (valve 7 opened). The cooling power in this second configuration is actually larger than in the normal operation configuration one, resulting in a lower shield temperature.

Table 17.6 and Table 17.7 gives the operating parameters respectively in normal operation and when the shield circuit is supplied with the boil off from the phase separator vessel.

The helium circuit is a low pressure drop network [17-1]. It consists of 6 parallel branches, each of them supplying 6 shield panels in series, as pictured in Fig. 17.2. The inlet and outlet of each branch connections to the main helium lines are installed in the separator vacuum vessel, this allows for a possible adjustment of the parallel flow distribution. Temperature sensors are installed on all the return lines.

Table 17.6
Thermal shield working parameters in normal operation.

Inlet temperature	60	K
Outlet temperature	80	K
Operating pressure	5	bar
Mass flow rate	35	g/s
Cooling power 60K to 80K	3300	W
DT (hot point - helium)	10	K
Length of a branch	110	m
Inner diameter	20	mm
Total shield pressure drop	80	mb

Table 17.7
Thermal shield working parameters when supplied from the phase separator boil off.

Inlet temperature	5	K
Return temperature	80	K
Operating pressure	1.1	bar
Mass flow rate	20	g/s
Total shield pressure drop	60	mb

17.4.2 Thermosiphon circuit

The so-called indirect cooling method is defined by the local heat sinks situated on the outer side of the coil. It is opposed to the hollow conductor or LHe bath cooling method. The indirect cooling can be used for low loss superconducting coils and requires a good thermal conduction throughout the cold mass. It also requires that helium is circulated through the cooling pipes.

The thermosiphon process is a method which provides the required helium circulation. The principle is to use the density difference, between the pure liquid and a two phase mixture made up of liquid and vapour, as driving head in a U shaped circuit configuration as sketched in Fig. 17.3. A vessel, located in an elevated position, allows the helium phase separation. The pure liquid is re-cycled to the cooling circuit while the vapour returns to the refrigerator which continuously supplies the boiled liquid fraction.

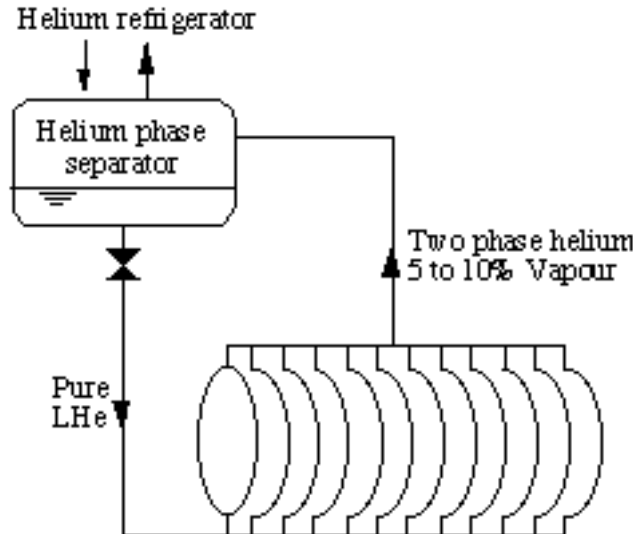


Fig. 17.3: Thermosiphon circulating principle.

This type of system has already been used successfully on the ALEPH solenoid [17-2]. It has the advantage of reliability because it does not have any moving parts such as cold pumps. It is also efficient as the temperature is uniform, due to the fact that the cooling helium flow spontaneously adapts to the heat load distribution. This process also allows the use of short cooling pipes supplied in parallel.

This arrangement also limits the quench pressure. When a quench is detected, the supply valve (V2) is closed and the helium in the cooling tubes is rapidly evacuated to the phase separator vessel due to the fast temperature rise. This surge process limits the pressure rise to few bars without venting any helium to atmosphere.

As the thermosiphon is essentially driven by gravity, the cooling tubes must be vertically orientated. They are semi-circular segments connected at the bottom and top to the supply and return manifolds. These cooling tubes are attached to the outer side of the external cylinder every 260 mm.

The thermosiphon circuit is made up of 8 independent sub-circuits. Fig. 17.4 represents the schema of half of the helium distribution for the thermosiphon cooling circuit. Each sub-circuit can be manufactured and leak tested before assembly on the coil.

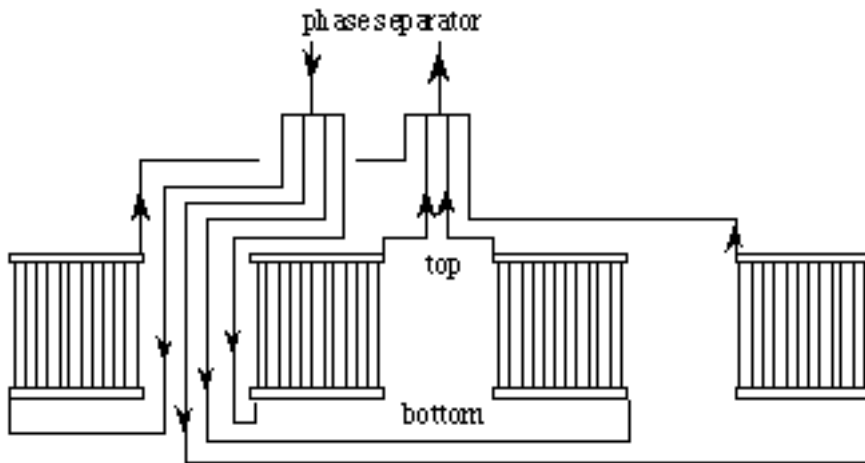


Fig. 17.4: Cooling circuit configuration (half of the thermosiphon circuit).

The piping lengths and diameters are given in Table 17.8. This system is calculated in order to keep the quantity of vapour in the return line lower than 10%.

Table 17.8
Thermosiphon piping parameters.

	Inner diameter mm	Length m
Inlet line	23.7	22
Feeding manifold	23.7	3
Return manifold	23.7	3
Cooling tubes	14	11
Return line	23.7	8

17.5 COIL TEMPERATURE DISTRIBUTION

At constant current the cold mass is subjected to heat radiation (0.2 W/m^2), conduction from the supports and localised internal sources due to the conductor junctions at each layer end and inside the winding (0.4 W per junction).

In varying current regime there are additional transient losses:

- eddy currents in the quench back cylinder,
- eddy currents in the pure aluminium,
- plastic strain of pure aluminium.

AC losses in the strands or filaments are negligible, as are eddy currents in the aluminium alloy.

Computations on the temperature distribution in the cold mass show that the temperature difference is lower than 50 mK at constant nominal current.

The dynamic losses due to eddy currents and aluminium plastic strain are both function of the current intensity and the rate of current variation [17-3]. When ramping up the current at constant dI / dt eddy current losses are almost constant but the heat generated by plastic strain is zero up to the aluminium elastic limit and then roughly increases as B^2 per unit time.

It is at a maximum when it reaches the nominal current. There are some uncertainties when estimating the temperature rise because the metallurgical state of the aluminium is not well defined. Calculations show that temperature differences can be of the order of 0.1 K. This winding temperature has to be monitored during the energising of the coil and the power supply voltage must be adaptable to reduce the energising speed if needed.

17.6 CRYOGENIC SEQUENCES

The operation of the CMS solenoid includes 5 cryogenic sequences [17-4], (see also Chapt. 21):

- cool down,
- normal operation,
- slow discharge in case of main's failure,
- post quench re cooling,
- warming up.

During cooling down the coil cooling tubes are supplied with forced flow helium. The cooling down speed is controlled in order to limit the temperature difference to 50 K maximum over the winding.

The helium refrigerator is dimensioned for the normal operational cryogenic loads. Additional power is required to cool down the 220 tonne cold mass in about 3 weeks. This is done by supplying LN₂ to the refrigerator cold box. The total helium flow delivered by the cycle compressor is used to transfer the cooling power to the coil. The thermal shields are not supplied until the temperature is lower than 120 K. At this temperature level the cold box expansion engines are started and the shields are also cooled down. The cool down curve is shown in Fig. 17.5.

Table 17.9
Cool-down helium flow parameters.

Outlet pressure	bar	7
Mass flow	g/s	150
DP on internal circuit at 300 K	bar	3.5

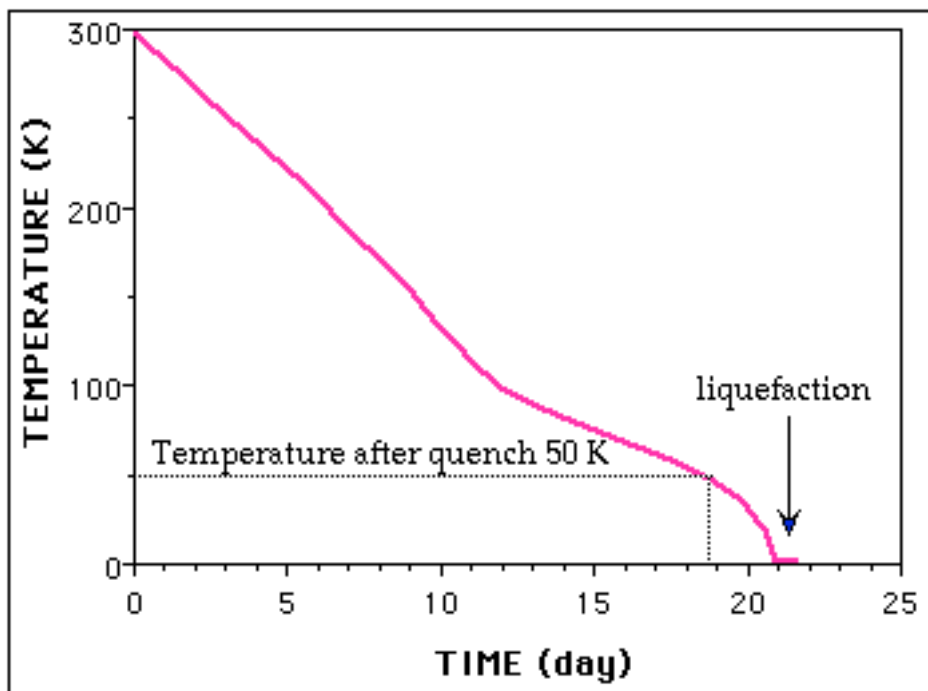


Fig. 17.5: Cooling down of the CMS coil.

18. SUPPORT SYSTEM

18.1 INTRODUCTION

The support system has to ensure the precise and rigid suspension of the cold mass inside the vacuum tank. The loads to be supported are the 220 tonnes weight of the cold mass and the magnetic forces due to the decentring and misalignment of the coil with respect to the return yoke. The design must also take into consideration the shrinking of the coil during cooling and its deformation under magnetic forces. The system has been analysed at Saclay [18-1] and FNAL [18-2].

18.2 DESCRIPTION

The support system consists of a set of rods made out of titanium alloy (see Fig. 18.1) and the photograph of a mock-up in Fig. 18.5, p. C-44. The longitudinal forces are taken by the pre-stressed antagonist pulling rods, called the longitudinal tie rods (see Chapt. 18.5). The weight and radial forces are taken by pre-stressed belts in two different sections of the solenoid, called “radial belts” (see Chapt. 18.6), they are grouped in sets of three. The studies of the support system are made for three different working conditions:

- Room temperature: 300 K;
- Cryogenic temperature and no field: 4 K, 0 T;
- With the solenoid energised: 4 K, 4 T.

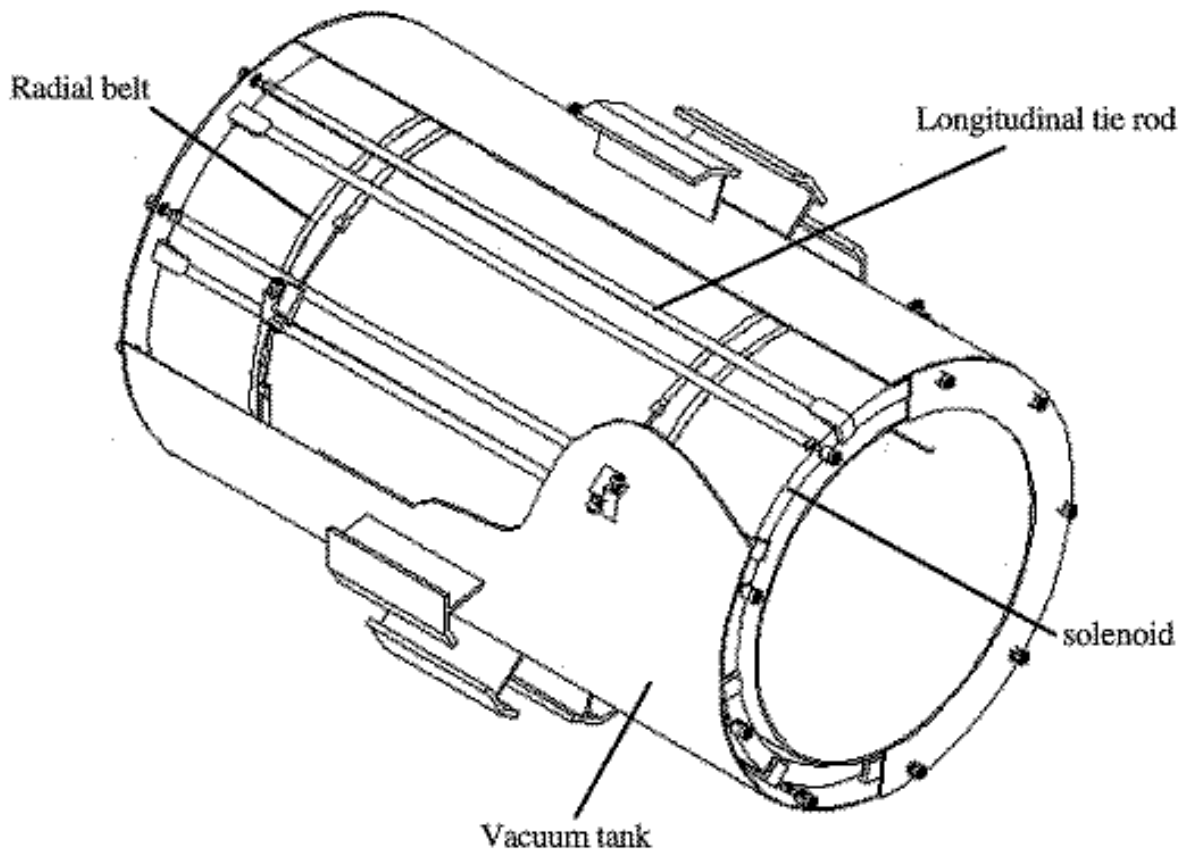


Fig. 18.1: General view of the support system.

18.3 LOADS AND DEFORMATIONS

18.3.1 Mechanical loads

Figure 18.2 shows the cold mass, its axis and the possible displacements caused by decentring and misalignment.

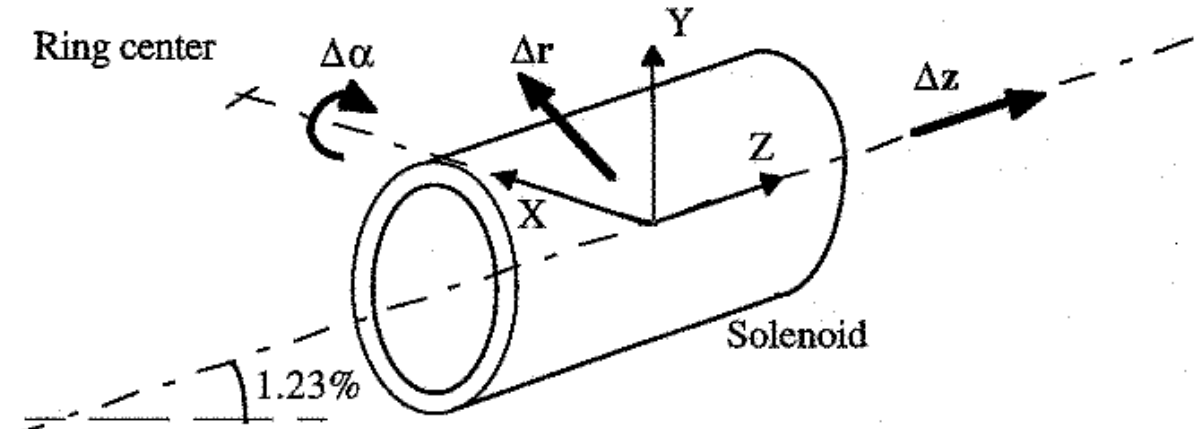


Fig. 18.2: Displacement components.

The loads acting on the suspension system are the following:

a) Weight of the solenoid (2200 kN):

The calculation also takes into account a 1.2 g acceleration during handling. This value is low because when the system is being moved, it will always be supported by the hydraulic dampers provided by the air pad system and its associated hydraulic jacks (see Chapt. 10 and 26).

b) Loads due to a magnetic misalignment:

As an hypothesis, the solenoid axis must lie within a 10 mm radius, centred around the magnetic axis, see Chapt. 18.8, where the alignment procedures during the first energisations are described.

The worst scenario loads, taking into account the results of Chap. 6-7, are indicated in Table 18.1.

Table 18.1
Solenoid misalignment and induced loads.

Solenoid misalignment	Corresponding loads
$Dz = 10 \text{ mm}$	$Fz = 1100 \text{ kN}$
$Dr = 10 \text{ mm}$	$Fr = 110 \text{ kN}$
$Da = 5'$	$Mx = 2730 \text{ kN}\cdot\text{m}$

where Dz , Dr , and Da are defined as follows:

- Dz : Displacement in Z direction,
- Dr : Displacement in the plane X, Y,
- Da: Rotation around X.

18.3.2 Coil shrinking and deformation under field

During cooling-down the coil diameter and its length are reduced in the same ratio:

$$\text{DR} / R (300 / 4 \text{ K}) = \text{DL} / L (300 / 4 \text{ K}) = -4.15 \cdot 10^{-3},$$

giving: $\text{DR}_1 = -14 \text{ mm}$, and $\text{DL}_1 = -50 \text{ mm}$.

During the energisation of the solenoid, the coil diameter increases and the length decreases by the following values:

$$\text{DR} / R (0 / 20 \text{ kA}) = +1.5 \cdot 10^{-3},$$

$$\text{DL} / L (0 / 20 \text{ kA}) = -8.22 \cdot 10^{-4},$$

giving: $\text{DR}_2 = +5.5 \text{ mm}$, and $\text{DL}_2 = -11.4 \text{ mm}$.

18.4 REQUIREMENTS

The rigidity of the support system is designed to limit any additional misalignment to 2 mm in any direction from an original misalignment of 10 mm, thus preventing any large displacement of the coil position. The stress in the support system components must always be inferior to the allowable stress. The Titanium alloy chosen is TA6V which presents the following mechanical properties:

- Young's modulus: 110 GPa,
- $R_{p0.2}$: 900 MPa,
- allowed stress: 600 MPa.

18.5 LONGITUDINAL TIE RODS

As explained in 18.2, the longitudinal tie rods are pulling in opposite directions. They are attached to the solenoid, at a temperature of 4.2 K on one side, and pulled from the vacuum tank flange at room temperature on the opposite side, and have a length of 12500 mm. Fig. 18.3 shows schematically how the solenoid is centred longitudinally inside the vacuum tank by the antagonist tie rods. A detail of the mock-up can be seen on the photograph of Fig. 18.6, p. C45.

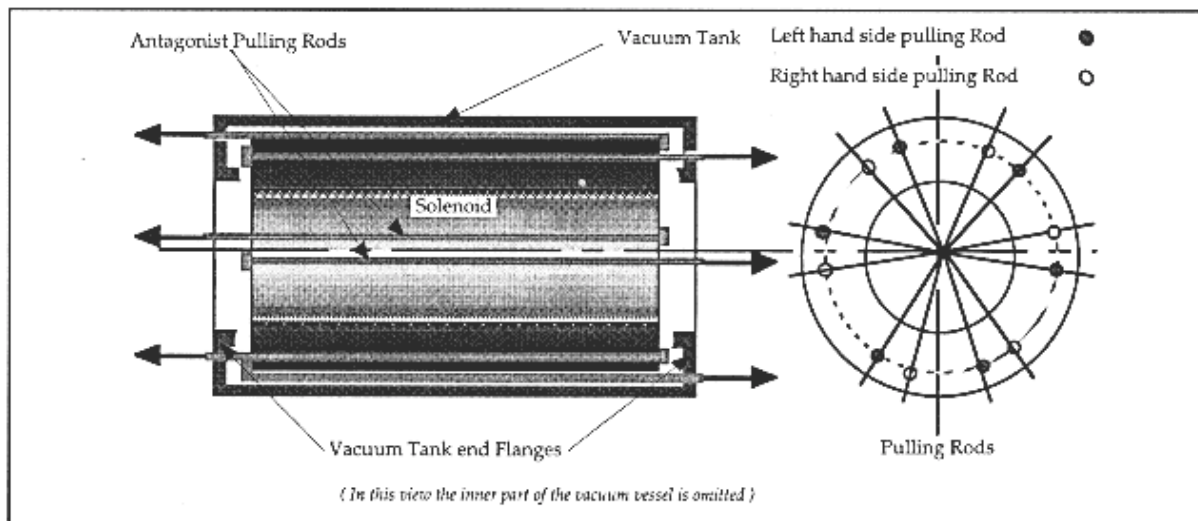


Fig. 18.3: Longitudinal positioning system of the solenoid.

The main mechanical parameters of the longitudinal tie rods are given in Table 18.2.

Table 18.2
Main mechanical characteristics of the longitudinal tie rods.

Material	TA6V
Number of tie rods	Two sets of 9
Cross sectional area	3 600 mm ² (200 mm x18 mm)
Pre-stress	196 MPa
Maximum axial displacement	2 mm

The stress in the longitudinal tie rods varies with the loading conditions. The maximum values are indicated in Table 18.3.

Table 18.3
Maximum stress in the longitudinal tie rods.

Working conditions	300 K	4 K, 0 T	4 K, 4 T
Maximum stress (MPa)	197	86	53

The thermal loss from 300 to 4 K, per longitudinal tie rod, is found to be 0.4 W, without taking into account any intermediate heat interception.

18.6 RADIAL BELTS

Two sets of three “U” shaped radial belts distributed at 120° are attached to the solenoid at 4.2 K on one side, and pulled from the outer shell of the vacuum tank at room temperature on the other side. Fig. 18.4 shows schematically how the solenoid is centred radially in the vacuum tank by antagonist radial belts every 120°

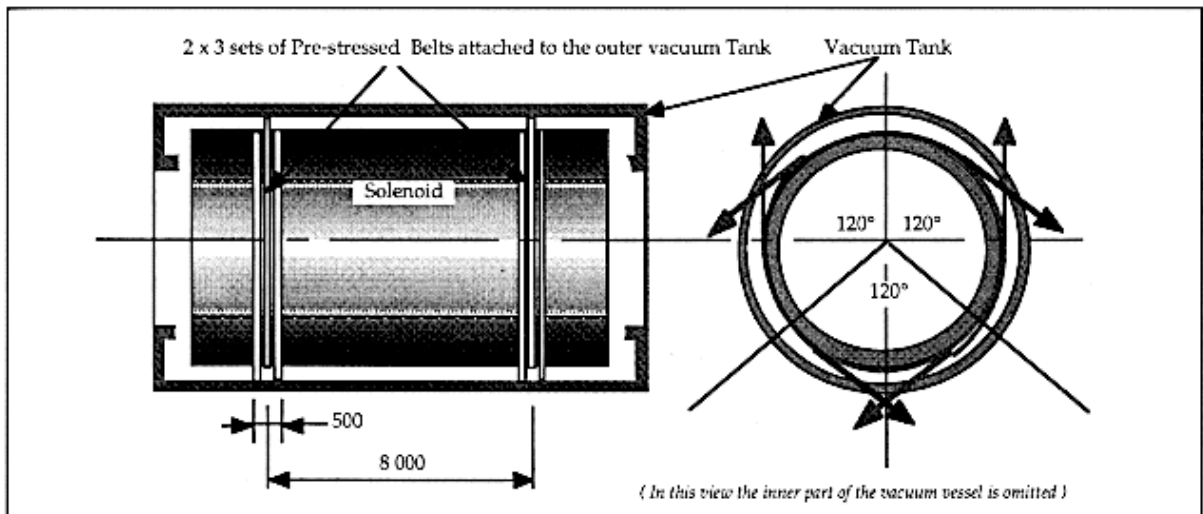


Fig. 18.4: Radial positioning system of the solenoid.

The main mechanical parameters of the radial belt system are given in Table 18.4.

Table 18.4
Main mechanical characteristics of the radial belt system.

Material	TA6V
Number of tie rods	two sets of 3
Cross sectional area	2 700 mm ² for 60 mm dia.
Pre-stress	510 kN
Maximum radial displacement	2 mm

The stress in the radial belt system varies with the loading conditions. The maximum values are indicated in Table 18.5.

Table 18.5
Maximum stress in the radial belt system.

Working conditions	300 K	4 K, 0 T	4 K, 4 T
Maximum stress (MPa)	450	280	410

The thermal loss from 300 to 4 K, per radial tie rod, is found to be 2.4 W, without taking into account any intermediate heat interception.

18.7 INDUCED STRESSES ON THE COIL

A first study has shown that the stresses induced on and in the coil by the supporting system are acceptable. A full 3-D finite element analysis will be carried out to check the result in detail and to properly design the attachment points.

18.8 ADJUSTMENT PROCEDURE

In order to accurately centre the solenoid it is necessary to measure the unbalanced forces by applying a small current to the coil and then make a step by step adjustment of the coil position. Using the pre-stressing equipment of the tie rods it will be possible to move the coil inside the vacuum tank and obtain, when the magnet is at full field, the same force in corresponding tie rods. Strain gauges will be attached to the support system to obtain these measurements which will be carried out during a test of the coil in the surface hall. This adjustment procedure will be performed with the two hadronic barrels HB inserted, to have the final deformations of the vacuum tank.

To gain access to perform the radial adjustment of the coil inside the vacuum tank both endcaps and the two outer rings YB/2 and YB/-2 will need to be moved. The axial adjustment however will only require moving the two endcaps (see Fig. 4.3, p. C-5). All tie-rods are equipped with bellows to ensure air tightness when connecting to the vacuum tank. In case a leak occurs in the bellows of a radial tie rod, the coil can be temporarily supported by installing a second tie rod system from the cold mass belt system during the repair or replacement of the bellows.

19 COIL MANUFACTURING AND ASSEMBLY

19.1 INTRODUCTION

The CMS Superconducting Coil will be wound as a single module of four pre-impregnated insulated layers, each layer being cured one after the other. Winding will take place on the CERN site in the surface building SX5 (see Chapt. 25 and 26).

The conductor will be assembled and machined on the winding site starting from the extruded insert and the extruded reinforcement profiles spooled onto large take-off drums. Each unitary length of conductor will be completed before starting to wind the corresponding layer (Chapt. 12 and 23). The winding process will be carried out by winding externally on a mandrel with a vertical axis (Fig. 19.1). Each layer will be wound starting from the bottom but in the opposite direction with respect to the previous one.

Layers 1 and 3 will be wound clockwise while layers 2 and 4 will be wound anti-clockwise.

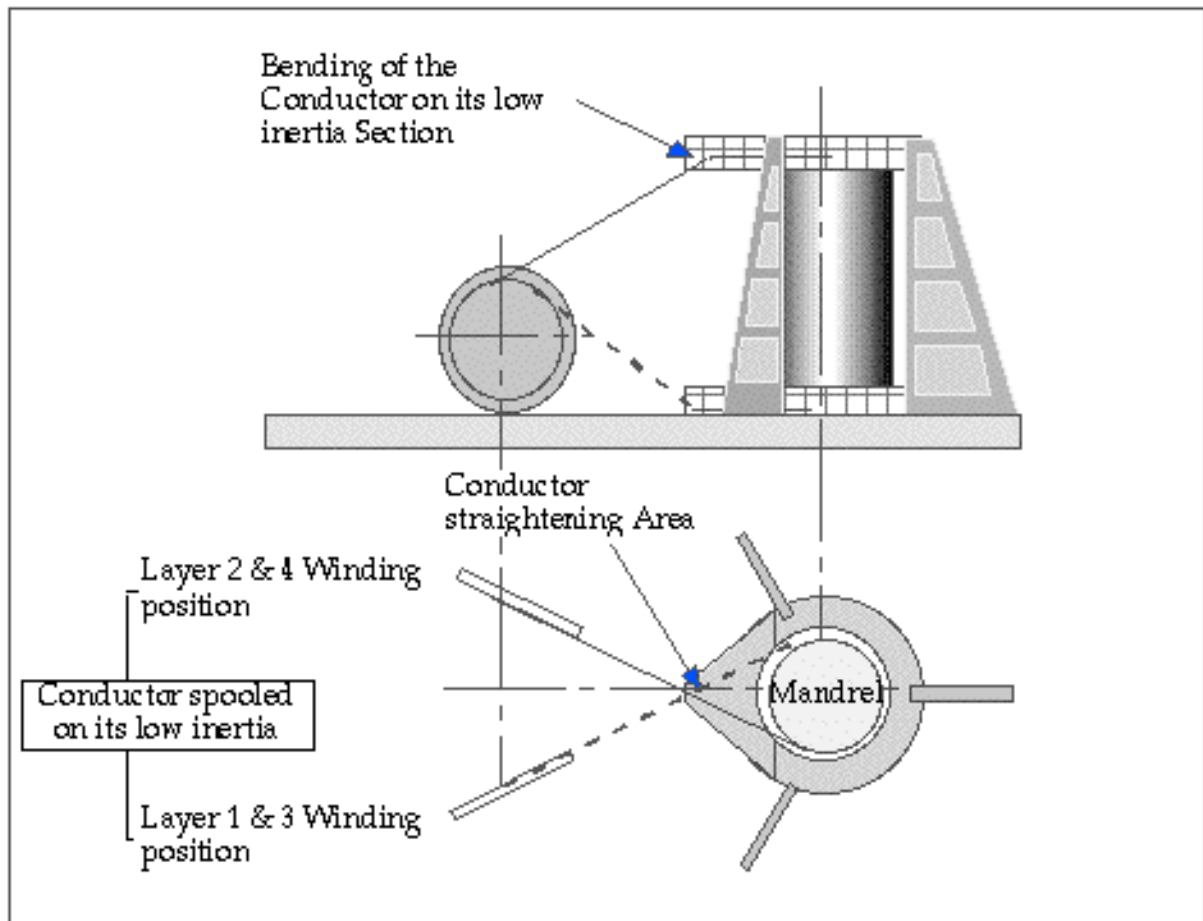


Fig. 19.1: Winding machine overview.

The insulation, in the form of pre-impregnated tape (semi-wet pre-preg), will be cured in two steps: first at a temperature of approximately 100 °C and finally 125 °C, (Chapt. 13).

The winding mandrel will also be used as a handling device to insert the coil

horizontally inside the outer shell of the vacuum tank.

19.2 DESCRIPTION OF THE WINDING MACHINE

19.2.1 Winding Machine principle

As stated earlier, the winding machine is essentially composed of a vertical rotating mandrel, and it is not excluded that this equipment can be produced by adapting an existing vertical lathe to the required needs.

It must be equipped with an adjustable speed system adapted to the different phases (winding, machining, insulating, winding of the quench back-cylinder etc.) and be able to ensure that the conductor is always kept under tension, even in case of equipment breakdown or loss of mains power.

The mandrel speed will be adjustable between 0 and 1 revolution/minute.

To wind the conductor under constant tension (see Fig. 19.4), at least three methods are possible:

- Winding the conductor by simply pulling it onto the mandrel.
- Winding the conductor by pulling it and at the same time pushing it toward the axis of the mandrel.
- Pre-bending the conductor at the correct radius before winding it on the mandrel.

These possibilities will be tested during the pre-industrialisation program described in Chapt. 24, and the technique which appears to be the simplest and the most reliable one, with respect to the precision of conductor positioning and risks of damaging the insulation, will be chosen. The prestudy has been done using the second technique, however, from early studies, the pre-bending technique looks like a promising one.

The position of the conductor during the winding process must be permanently controlled:

- radially to get a straight cylinder, Fig. 19.7.
- axially to get the highest filling factor, Fig. 19.8.

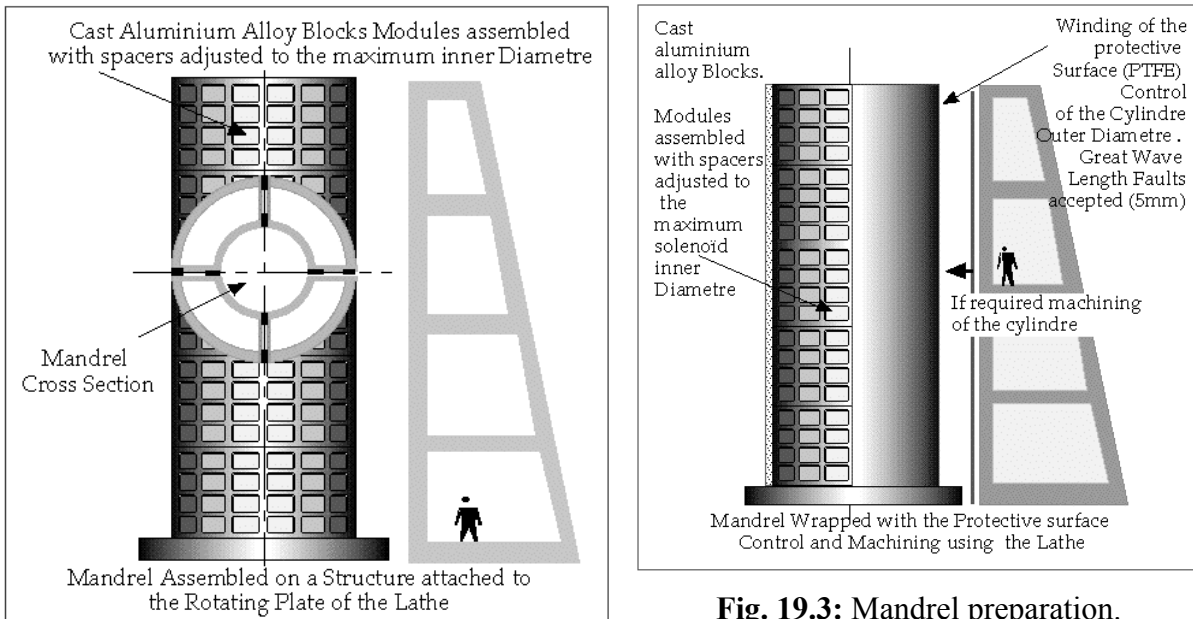
Figure 19.9 shows the principle of the conductor positioning control.

19.2.2 Winding Mandrel

The mandrel is made from cast aluminium alloy blocks assembled directly on the rotating plate. The mandrel is wrapped with a thick layer of polyethylene to facilitate coil removal.

The mandrel will be used as the handling structure for the coil, and it must be collapsible to allow its extraction, after the coil has been inserted and supported inside the outer shell of the vacuum tank (Fig. 19.2).

The general tolerances required for the mandrel are large; long ‘waving’, of the order of 5 mm over 5 m, can be tolerated, however, if necessary, it could be machined using the winding machine and the lifting platform structure as a lathe (Fig. 19.3).

**Fig. 19.2:** Mandrel assembly.

19.2.3 Applying the winding tension on the conductor

The winding tension on the conductor is obtained through caterpillar belts driven by an electromagnetic clutch (Fig. 19.4, 19.11 and Fig. 19.12). This system is designed so that the winding direction can be reversed, without changing the tension on the conductor. In case of power supply failure, the clutch is locked keeping the tension of the conductor unchanged.

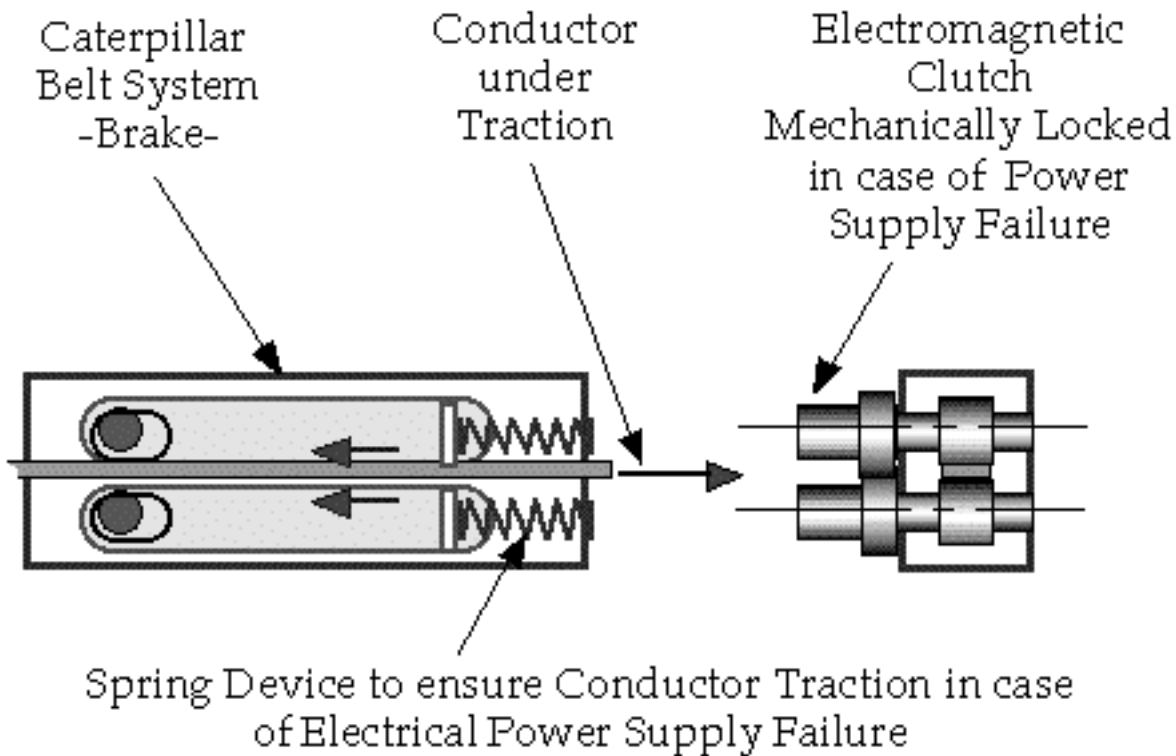


Fig. 19.4: Caterpillar belt system -Brake.

19.2.4 Positioning the conductor

The final “laying-down” of the conductor on the winding is a crucial phase to avoid damage to the insulation. For this purpose, a guide for the conductor will be installed just after the insulation checking box (Fig. 19.12).

The fact that the conductor is wound on its higher section inertia simplifies its positioning on the winding (Fig. 19.5 and 19.6). The ideal situation is obtained when the conductor lands exactly in its final position; then no sliding under pressure is required either along the mandrel or the previously wound layer.

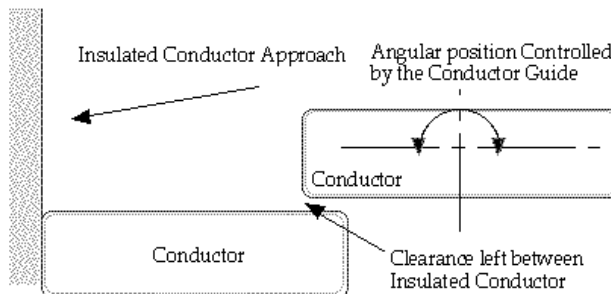


Fig. 19.5: Conductor laying-down:
Phase 1.

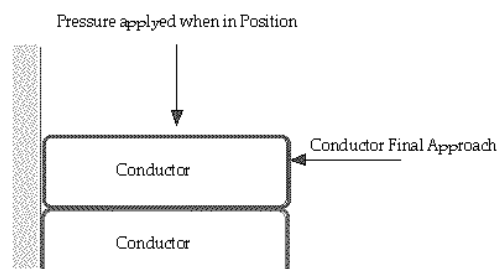


Fig. 19.6: Conductor laying-down:
Phase 2.

19.2.5 Controlling the filling factor

To obtain the correct position, and hence a good filling factor (Fig. 19.8), the conductor is pressed with a controlled force against the previous turn by means of rollers (36 appears a good number) equally distributed around the mandrel (Fig. 19.9). The force applied by the rollers can be adjusted to prevent horizontal misalignment of the conductor, nevertheless, this force being limited so as not to damage the insulation. The position of the rollers is permanently monitored, using the reference helicoidal wedge placed on the rotating table of the winding machine, to ensure the proper winding pitch (Fig. 19.10).

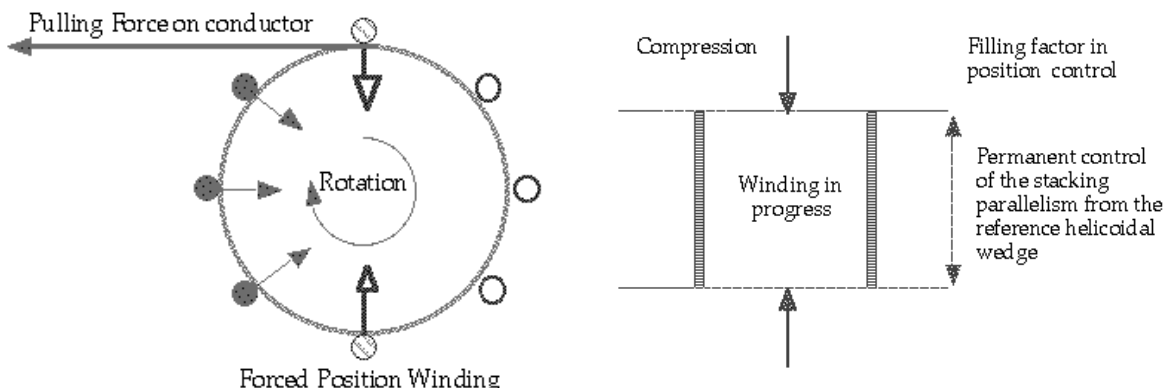


Fig. 19.8: Turn stacking control.

Fig. 19.7: Winding principle.

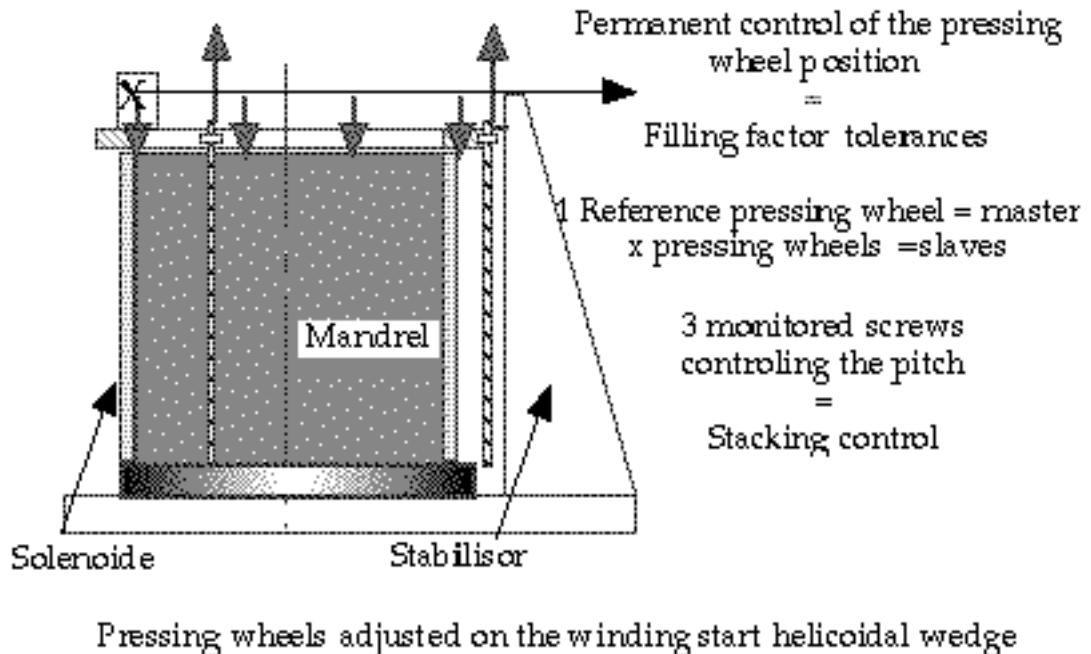


Fig. 19.9: Filling factor control principle.

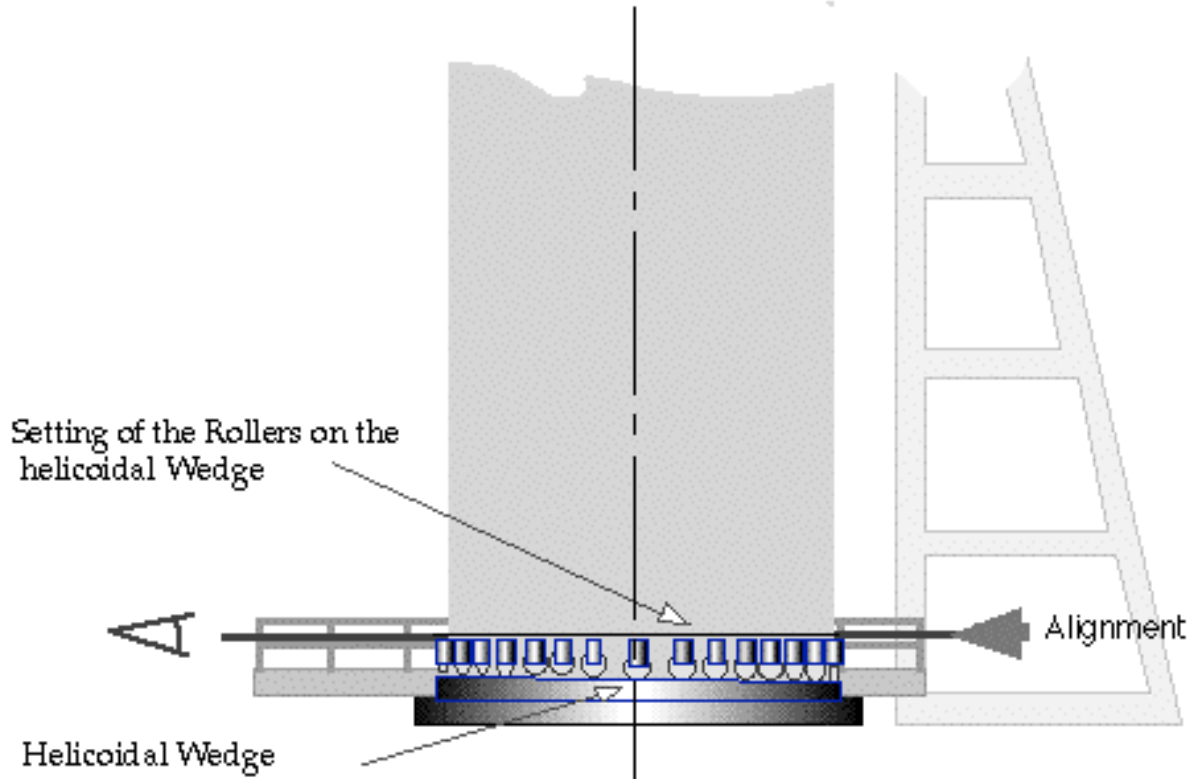


Fig. 19.10: Setting of the axial rollers.

The magnetic computations have been performed taking a safety margin on the filling factor, the nominal current being fixed at 20 kA, although the operating current is expected to be 19.5 kA (Chapt. 6). This will help to compensate for a lower filling factor.

To compensate for a higher filling factor, provision will be made to wind more turns than the nominal number, thus allowing to take the winding to its nominal dimension. Consequently, some extra length will be foreseen for each unitary length of conductor.

19.2.6 Insulating the conductor

The conductor insulation process is carried out on the winding line (Fig. 19.11). This operation is foreseen between the brake and the insertion point, the conductor being first cleaned and dried to ensure good bonding (Fig. 19.12).

The insulation is made of semi-wet pre-preg 0.125 mm thick, wrapped around the conductor with a 50% overlap (Chapt. 13).

The insulation with respect to ground is monitored continuously on line, to check the continuity of the wrapping and to detect the presence of metallic particles in the insulation.

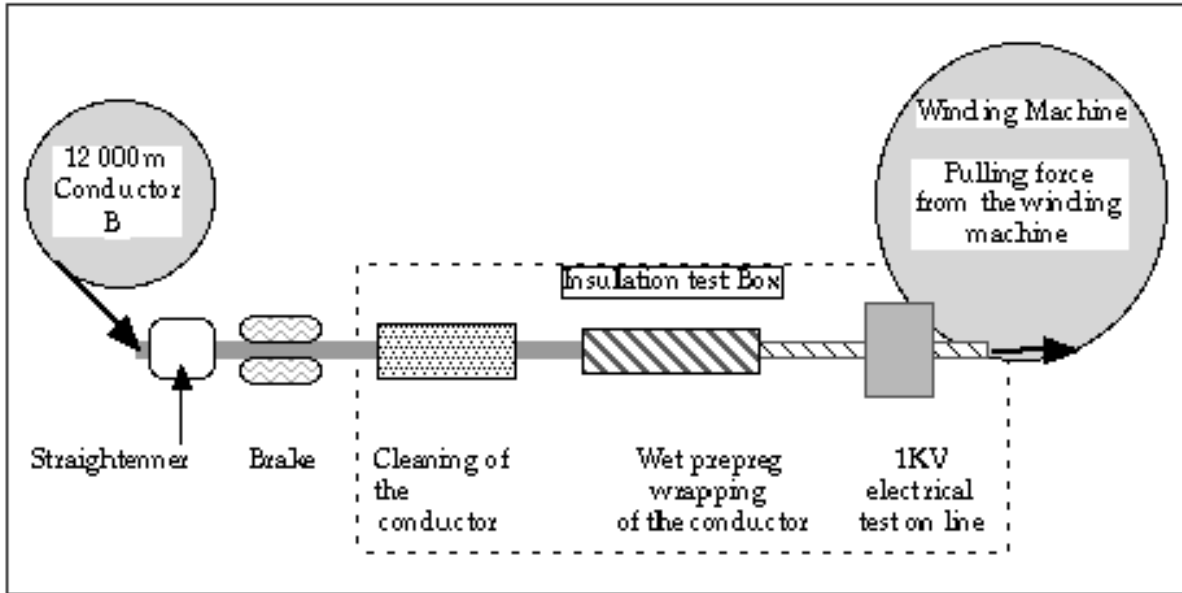


Fig. 19.11: Conductor insulation process on the winding machine.

19.3. DESCRIPTION OF THE WINDING PROCESS

19.3.1 Winding of the layers

The first operation is the installation of an angular wedge to generate the winding pitch. This wedge, one turn in length, is bolted directly on the table of the winding machine. With the wedge in position, the axial pressure rollers, foreseen to control the filling factor, will be adjusted.

The conductor, fed from the insulation testing box (Fig. 19.11), is pulled towards the winding table and attached to it. Its end is prepared for the joint to the next layer. The winding of the layer can then proceed.

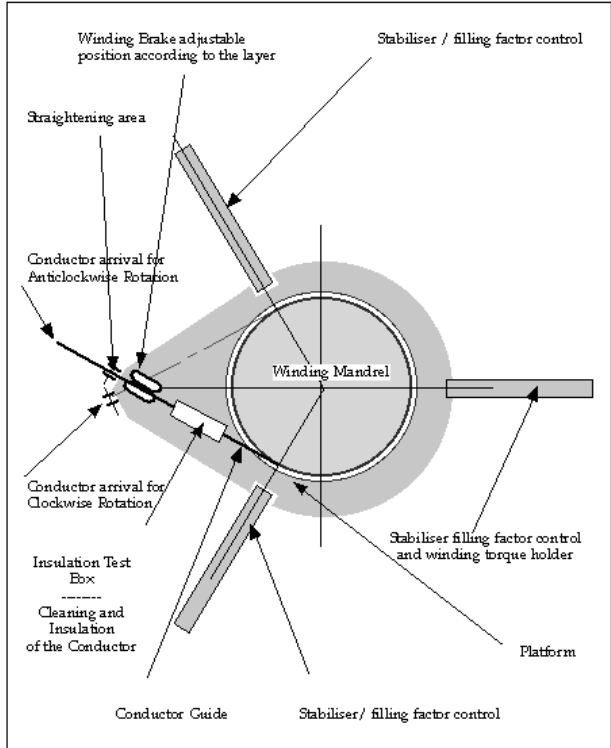


Fig. 19.12: Winding machine pressure plate.

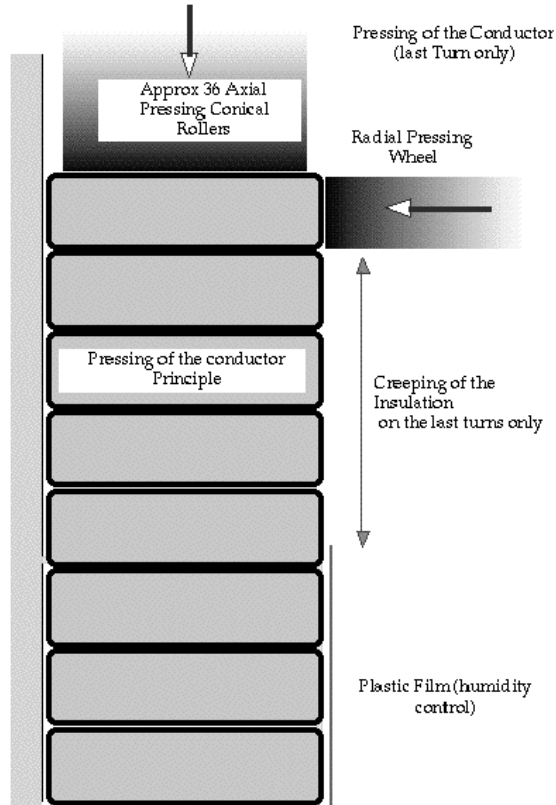


Fig. 19.13: Winding process steps.

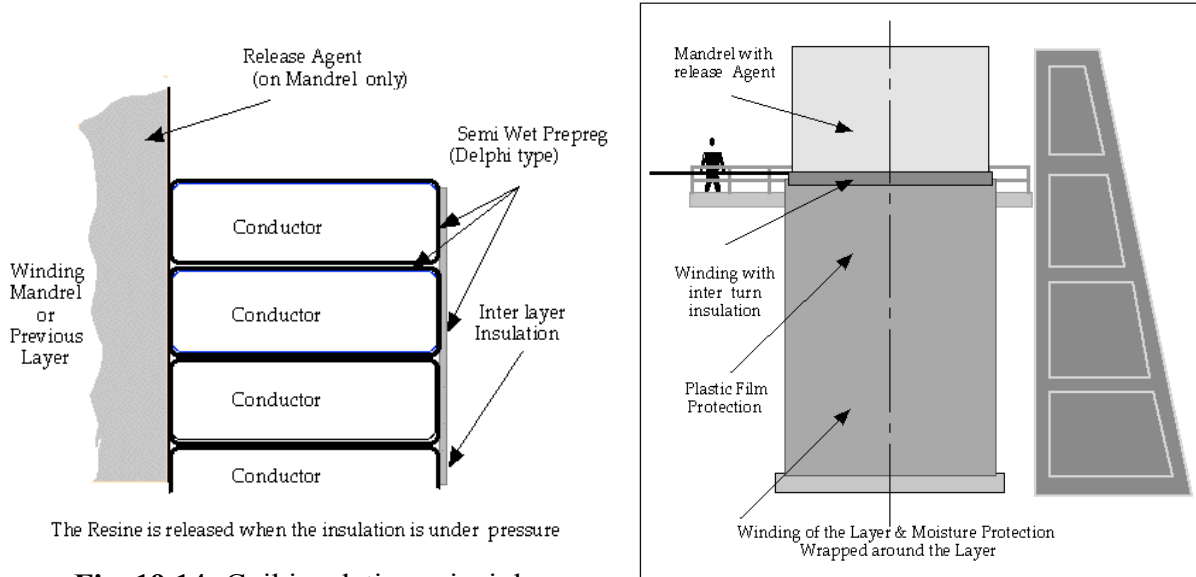
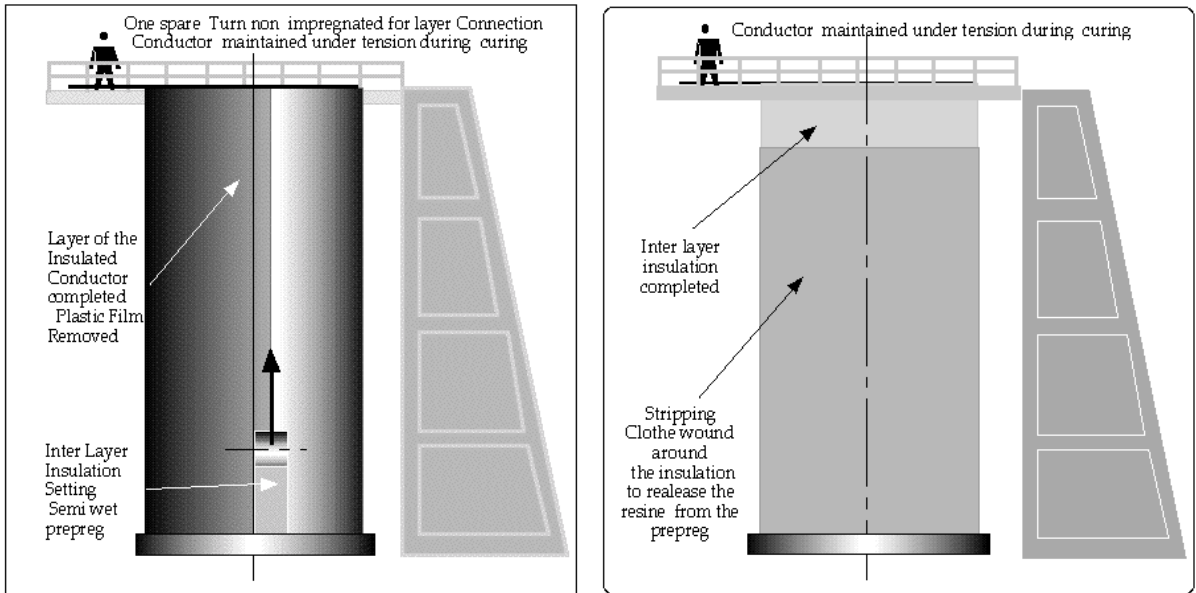
During the winding operation (Fig. 19.13), resin is partly released from the pre-preg, due to the pressure which is continuously applied, and this process slightly decreases the thickness of the pre-preg. This creeping is expected to occur only during the first two hours following the application of the pressure, and thus it concerns only the last turns wound.

The insulation process needs a fairly clean environment and protection from moisture. To satisfy these requirements various solutions can be envisaged, from the simplest, consisting of a plastic film around the coil (Fig. 19.15), to the most sophisticated, such as a humidity controlled clean room.

To terminate the winding of a layer, the conductor is maintained under the correct tension, and clamped to the mandrel. The end of the layer will be used to make the lead termination at the completion of the process (Fig. 19.19).

19.3.2 Applying the inter-layer insulation

After having wound a layer of insulated conductor, the protective film will be removed, and the inter-layer insulation will be placed longitudinally (Fig. 19.16). This insulation, made of 0.250 mm thick pre-preg (twice the turn to turn insulation) with an overlap of 50%, is placed vertically on the face of the cylinder. Once this insulation is positioned, a striping cloth is wrapped to release part of the resin out of the pre-preg and to absorb the excess of resin. The conductor is maintained under tension, at the top of the solenoid, until the winding is locked (Chapt. 19.3.5) and the curing is finished.

**Fig. 19.14:** Coil insulation principle.**Fig. 19.15:** Winding in progress.**Fig. 19.16:** Inter layer insulation setting.**Fig. 19.17:** Stripping cloth setting.

It must be emphasised that during the winding of a layer, the resin remains liquid enough, allowing reversal of the winding process. The resin also acts as a lubricant, allowing the conductor to creep to its final position with only a small force being required.

19.3.3 Curing of a layer

The curing of the coil is carried out layer by layer, using a radiant screen. The

mechanical structure of the mandrel must be heated too, to avoid displacements due to thermal contraction, between the solenoid and the mandrel.

Curing is done at a temperature of about 100 °C and the complete cycle, is foreseen to last of the order of two weeks.

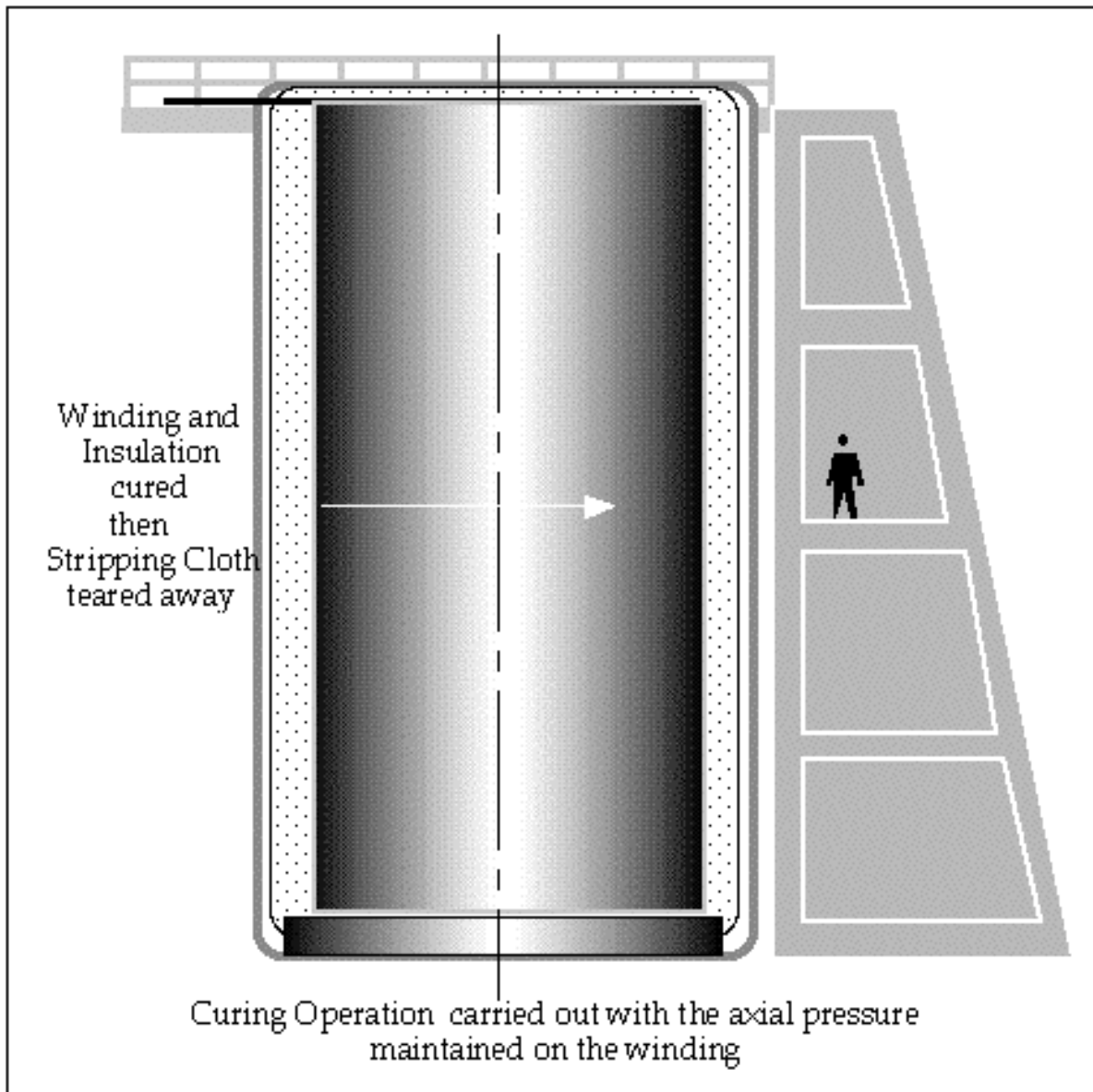


Fig. 19.18: Curing.

After curing, the stripping cloth will be removed. The whole surface will be checked to verify that the geometry of the resulting cylinder is within tolerances. The general aspect must be smooth and exempt from surplus resin. In particular, dry drops of resin will be removed, and filler will be used, through a process to be determined, to compensate for possible local lack of resin. Even at this stage, where the interlayer insulation is not complete, the insulation will be submitted to a test voltage of 3 kV.

19.3.4 Making the layer to layer joints

The interlayer connections, between layers 1 and 2 and layers 3 and 4, are located at the bottom of the winding. These joints could be made before starting the winding of a new layer. The joint is carried out by soft soldering (or welding) the two inserts together over a length at least equal to the transposition pitch of the Rutherford cable (Fig. 19.19).

The continuity of the reinforcement will be ensured by mechanical means (Fig. 19.20). After being assembled, the system is slowly put under tension, and when the nominal winding force is reached, the locking clamps are removed.

The process described for the first layer will be repeated for subsequent layers.

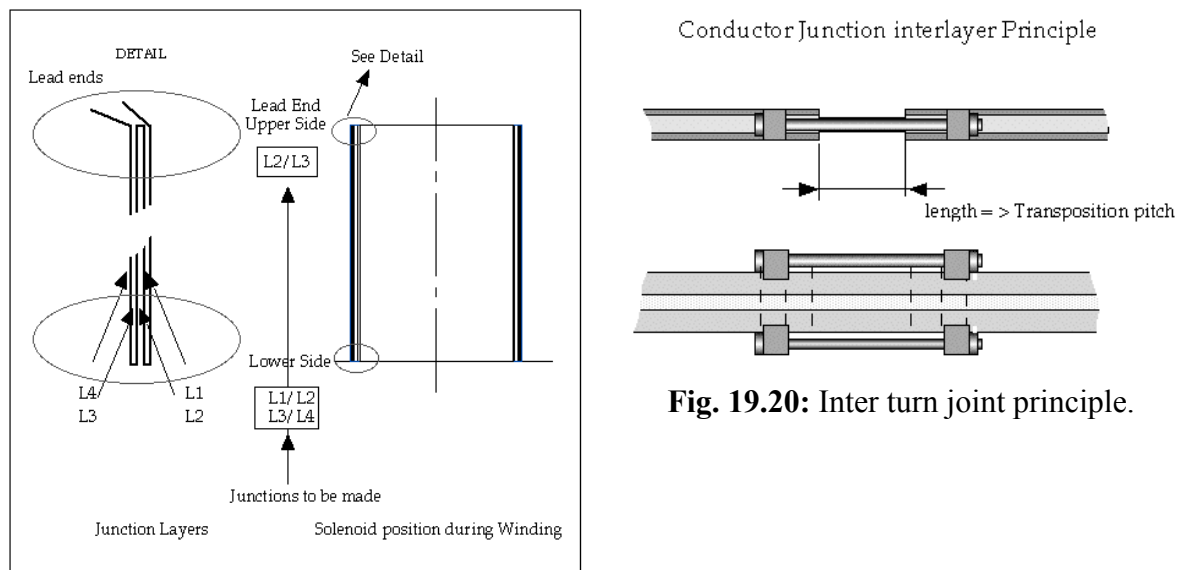


Fig. 19.19: Solenoid joints.

19.3.5 Making lead ends and locking the winding

To ensure equilibrium of the winding forces in the coil, the extremities of the first and last layer will be locked mechanically by linking the two lead ends together through an insulated clamp (Fig. 19.21).

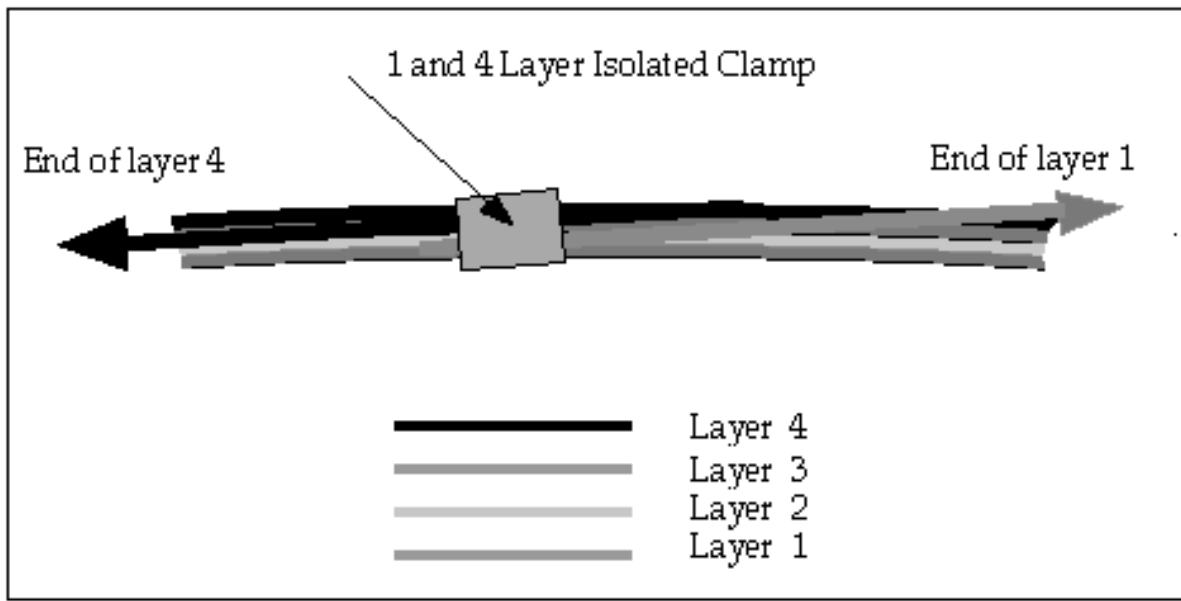


Fig. 19.21: Lead end joint principle.

At this stage the three first layers have been cured. The fourth layer is cured after clamping the two lead ends.

19.3.6 Laying down the longitudinal thermal drains

To improve the axial thermal conductance, 1 mm thick strips of pure aluminium, acting as thermal drains, are placed longitudinally to completely cover the length of the final layer; each drain being electrically isolated from the others (Fig. 19.23). These aluminium foils are bonded in place using the same pre-preg insulation technique as the inter-layer insulation. An additional insulation thickness of 0.75 mm thick pre-preg strips is then placed between the thermal drains and the outer insulation. The outer insulation of the final layer is then completed before starting the winding of the quench-back cylinder.

The uncured pre-preg is wound onto a spooling device with a vertical axis, positioned near the winding machine to facilitate the re-spooling.

The pre-preg is wound on the coil, with an overlap of 50%, under a slight tension to release some resin from the cloth.

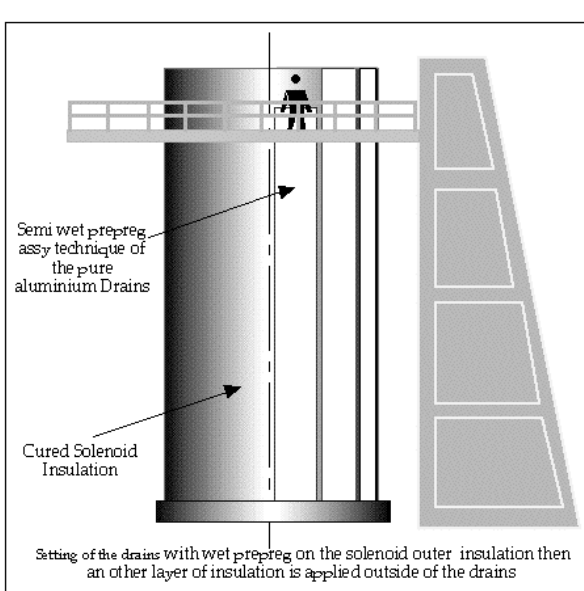


Fig. 19.22: Positioning the thermal drains.

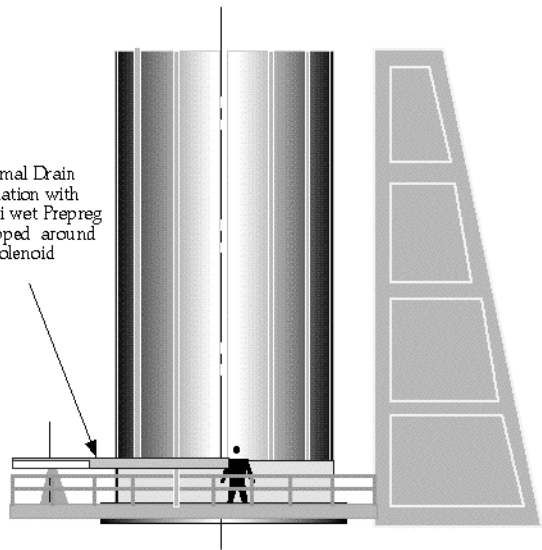


Fig. 19.23: Thermal drain insulation.

19.3.7 Winding of the quench-back cylinder

The quench-back cylinder is made from an extruded aluminium alloy profile, wound directly over the insulation layer covering the thermal drain.

This profile will be wound as a helix and welded to form a continuous cylinder. A suitable welding technique must be chosen to make sure that the temperature under the profile will not be detrimental to the insulation or the conductor that are located just behind the quench back cylinder (Fig. 19.24 and Fig. 19.25). The laser welding technique appears to be well adapted, and computations show that the temperature under the profile could remain below 100 °C. Real tests are in progress to fully qualify this method.

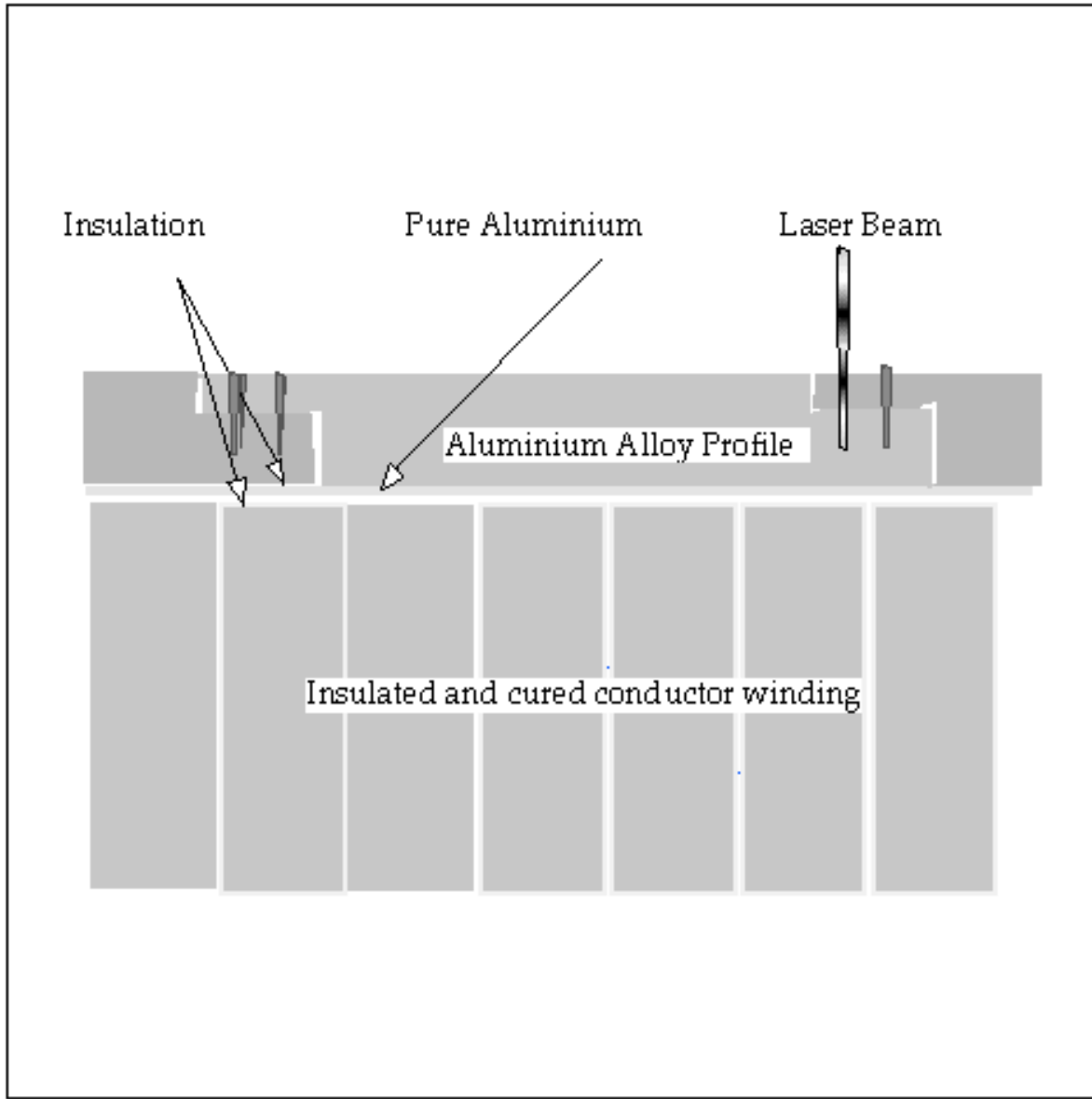


Fig. 19.24: Quench-back cylinder welding detail.

19.3.8 Adding the radial belts and cooling circuits

Six supporting belts are attached to the solenoid to support its weight and allow accurate adjustment of the position of the coil inside the vacuum tank (Chapt. 18).

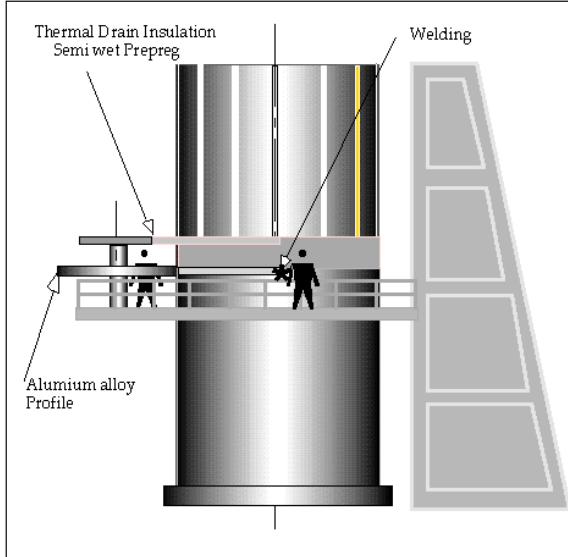


Fig. 19.25: QBC winding & welding.

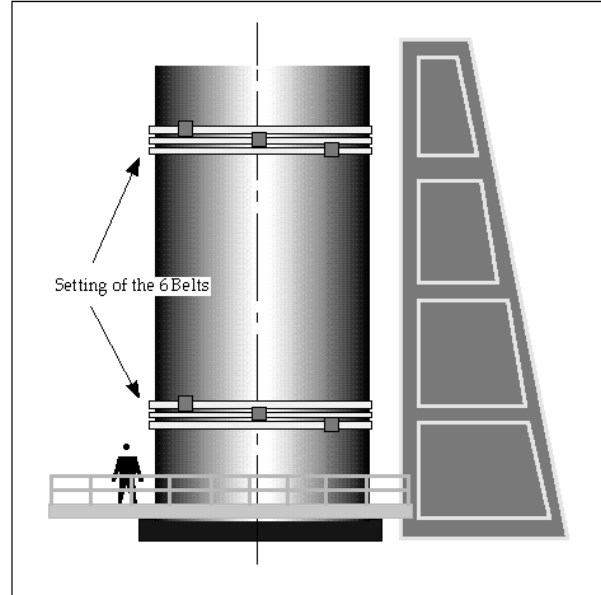


Fig. 19.26: Installation of the 6 radial belts around QBC.

The helium cooling circuits are placed over the quench-back cylinder (QBC), using the same semi-wet pre-preg technique as used for the thermal drains. The cooling circuits are maintained in contact with the quench-back cylinder by prestressed collars. Thermal conductivity is ensured by the resin contained in the semi-wet pre-preg, and the collars and the prestressing tie rods are dimensioned to support the 0.15% hoop strain which is also applied to the cooling circuit (Fig. 19.27 and 19.28).

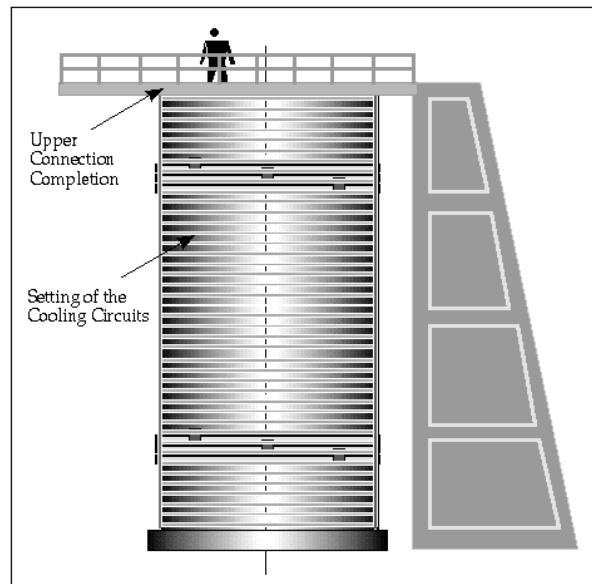
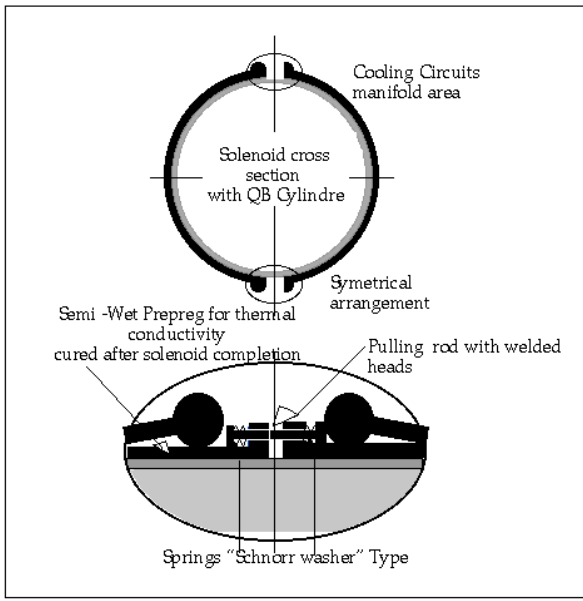


Fig. 19.27: Cooling circuit detailed fittings.

Fig. 19.28: Installation of the cooling circuits.

19.3.9 Final curing of the whole coil

After having completed the cooling circuits, the layers of insulation placed inside and outside the thermal drains and under the cooling circuits are cured. For this curing, the complete solenoid will be heated to the final curing temperature (125°C), to obtain complete polymerisation everywhere and thus ensure the optimal mechanical properties of the insulation (Fig. 19.29).

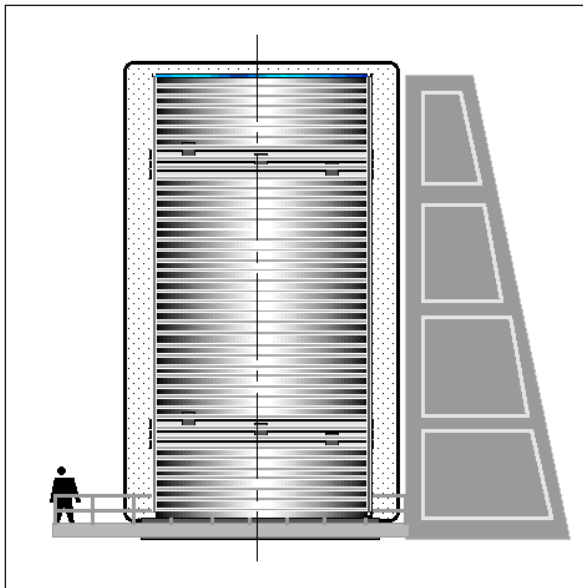


Fig. 19.29: Final curing.

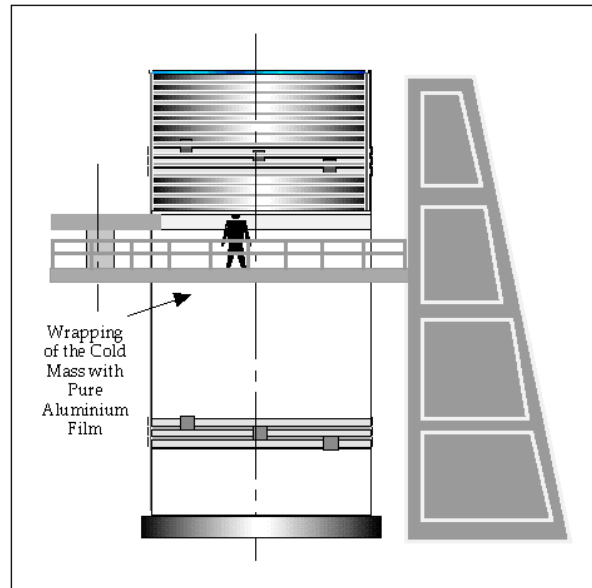


Fig. 19.30: Pure aluminium film winding.

19.4 COMPLETION OF THE COLD MASS

To complete coil fabrication the final operations are:

- the wrapping of a pure aluminium film,
- the fitting of the solenoid equipment,
- the installation of the thermal shields.

19.4.1 Wrapping the pure aluminium film

A foil of pure aluminium is wrapped around the solenoid with a small overlap to improve the emissivity of the cold mass (see Chapt. 17 and Fig. 19.30).

19.4.2 Mounting the solenoid equipment and the thermal shields

The tie rods of the longitudinal support system are put in place and temporarily attached at the ends of the solenoid. The pipework for the cryogenics is prepared and the bus bars are laid down (Fig. 19.31).

The thermal shields, made from at least two sections, are placed around the solenoid using the travelling crane (Fig. 19.32). They will be temporarily attached to the solenoid, to avoid any movement during the swivelling operation.

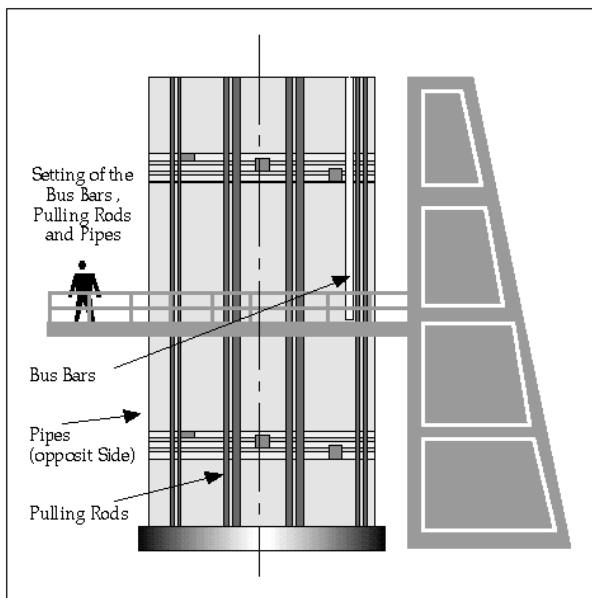


Fig. 19.31: Pipes, bus, pulling rod fitting.

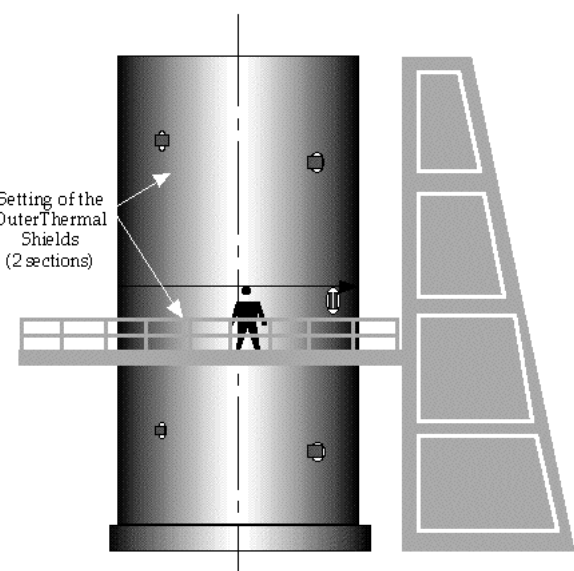


Fig. 19.32: Outer thermal shield installation.

19.4.3 Swivelling the coil to the horizontal position

The winding operation has been carried out on a spacer (approximately 2500 mm thick) to which the mandrel was attached. This spacer, temporarily linked to the winding table, is designed to be the main part of the swivelling device. After installation of the outer thermal shield, the swivelling system is built from the spacer (Fig. 19.33) and the solenoid, previously oriented in the correct angular position, is ready for insertion into the vacuum vessel.

The concrete floor of the building is locally reinforced to accept the maximum reaction forces generated during this operation. The rotation will be carried out in 3 steps.

1. Tilting of the solenoid:

To ease the passage of the centre of gravity (C of G) from one side to the other side

of the vertical line going through the axis of rotation, a removable water tank acting as a counterweight is integrated into the device. The water tank is first filled with water, then, using a gantry crane, the solenoid is tilted to bring the C of G close to the vertical line going through the axis of rotation. The system is secured by cables retained by a winch (or a hydraulic actuator).

2. The crane is stopped and the water is drained out of the tank, thus changing slowly the position of the C of G which will cross the vertical line going through the axis of rotation. The winch (or the hydraulic actuator) is used to restrain the system and complete the rotation of the solenoid to its horizontal position.
3. When close to the horizontal position, tie rods are attached to the anchoring points to secure the system.

The whole rotation operation is shown in Fig. 26.14.

19.5 COMPLETION OF THE SOLENOID

19.5.1 Wrapping of the superinsulation around the thermal shield

Once the solenoid is in the horizontal position, the superinsulation is wrapped around the outer shield using lifting platforms.

19.5.2 Insertion of the solenoid inside the vacuum vessel

The central barrel ring, equipped with the outer shell of the vacuum vessel, is moved toward the solenoid (Fig. 19.33/1) on the air pad system (Fig. 19.33/2 and 26.14). When in position, the 12 tie rods of the radial belt system are linked to the solenoid. The four tie-rods supporting the weight are put under a slight tension (Fig. 19.34/3). The mandrel is then collapsed to its smaller diameter and extracted by sliding out the central barrel ring (which now supports the solenoid via the two radial belts), away from the turning device (Fig. 19.34/4).

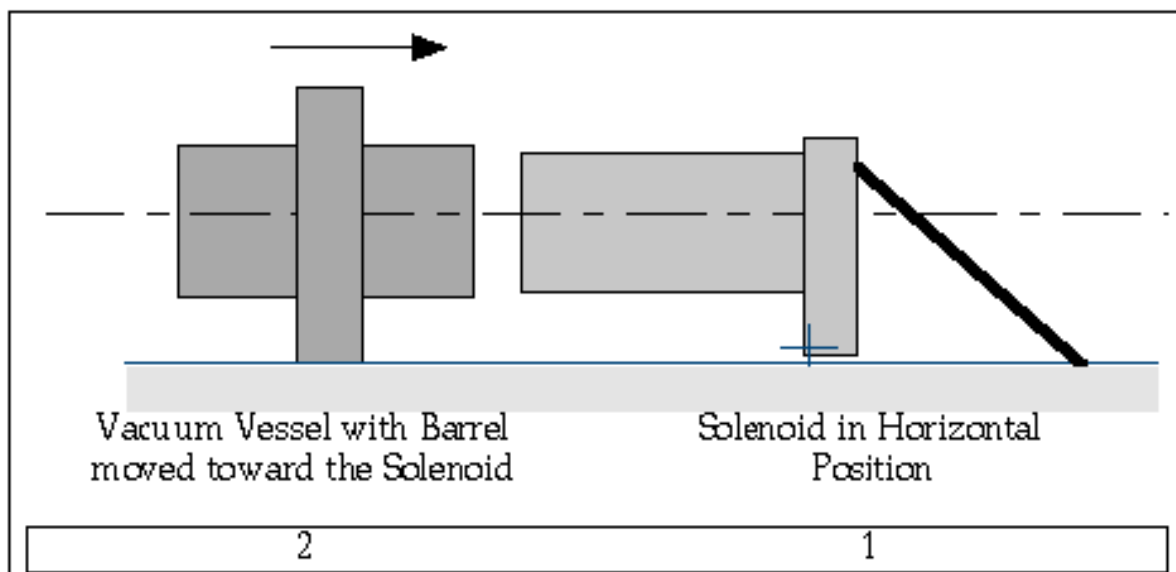


Fig. 19.33: Solenoid insertion into the vacuum vessel.

The pipework of the cooling circuits and of the thermal shield may now be installed.

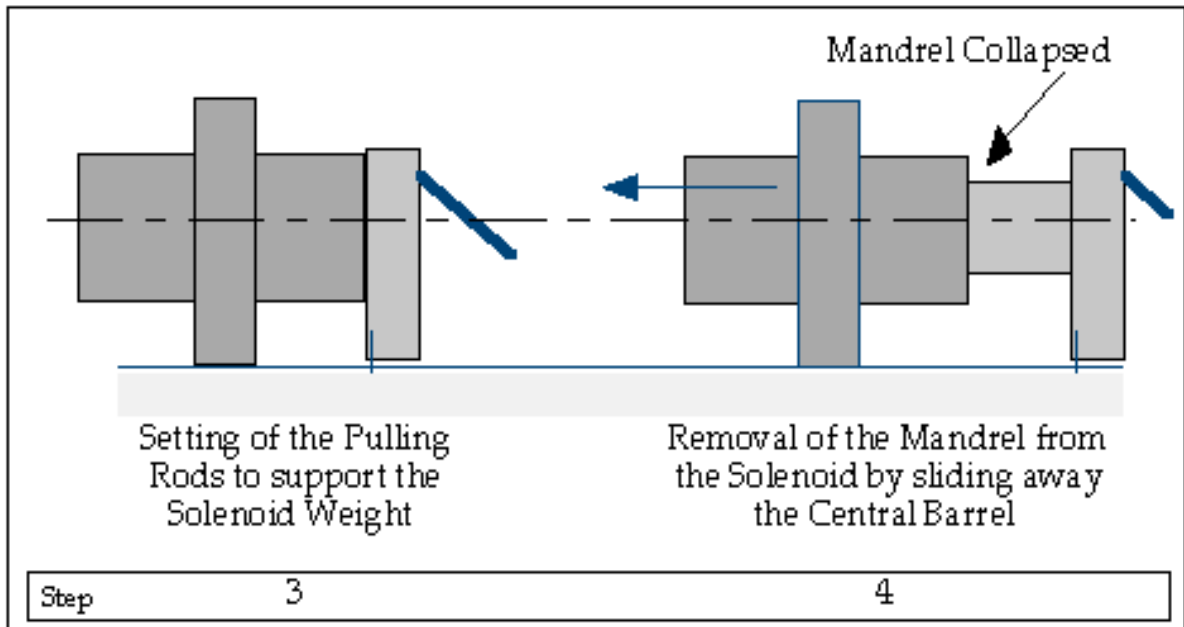


Fig. 19.34: Mandrel removal from the solenoid.

19.5.3 Completion of the ground insulation

With the mandrel removed, the inner surface of the solenoid is checked and cleaned. Then the ground insulation, foreseen on the inner surface, is completed using glass cloth and a resin curing at room temperature. When cured, this insulation will also be tested at 3 kV, applied between the inner surface of the insulation and the first layer of conductor.

19.5.4 Re-constructing the inner vacuum vessel

The mandrel is removed from the turning device, leaving room free for mounting on it the two halves of the inner vacuum vessel. The two shells will be assembled on the winding table in the correct angular position, then welded and fully tested to re-construct the inner shell of the vacuum tank (see Chapt. 9). When completed, the inner shell of the vacuum vessel will be turned to the horizontal position using the same device and procedure as used previously for the solenoid.

In the mean time the end face of the solenoid which was against the winding table will be completed (Fig. 19.35/6 & 7).

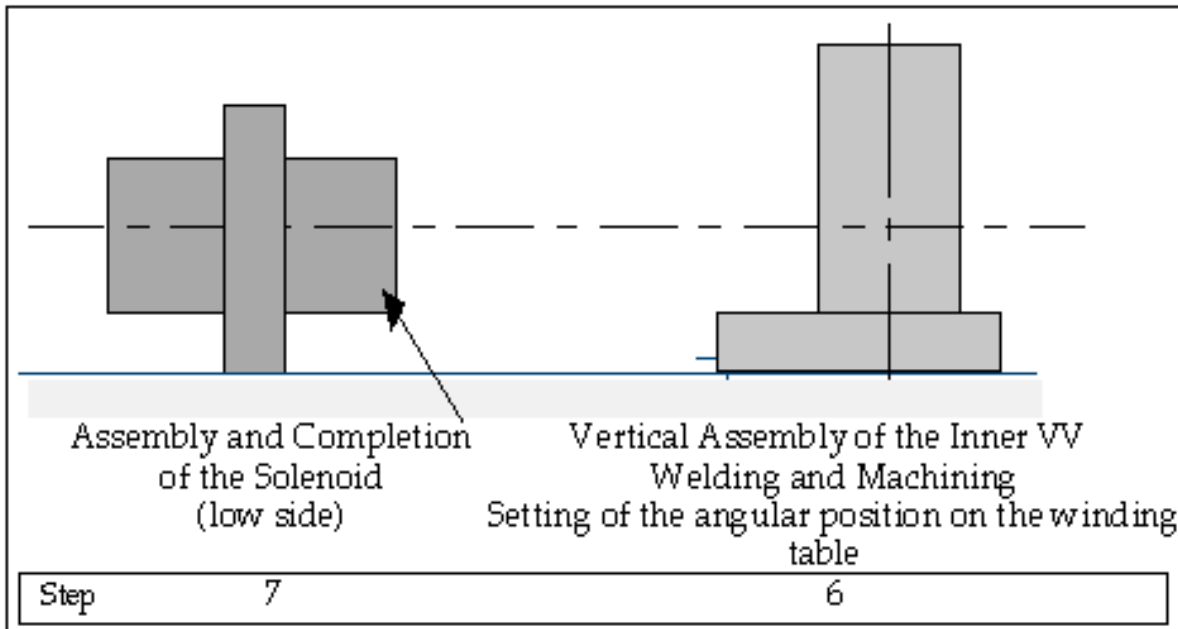


Fig. 19.35: Solenoid completion and inner vacuum vessel assembly.

19.5.5 Mounting the thermal shield and the superinsulation

The inner vacuum vessel is swivelled from the vertical to the horizontal position and the inner multilayer insulation is wrapped around it, using lifting platforms. Finally, the inner thermal shield and associated pipework are mounted over the inner shell of the vacuum tank. When ready, the solenoid supported by the central barrel ring, is slid over the inner shell of the vacuum vessel equipped with the inner thermal shield (see Fig. 19.36/9).

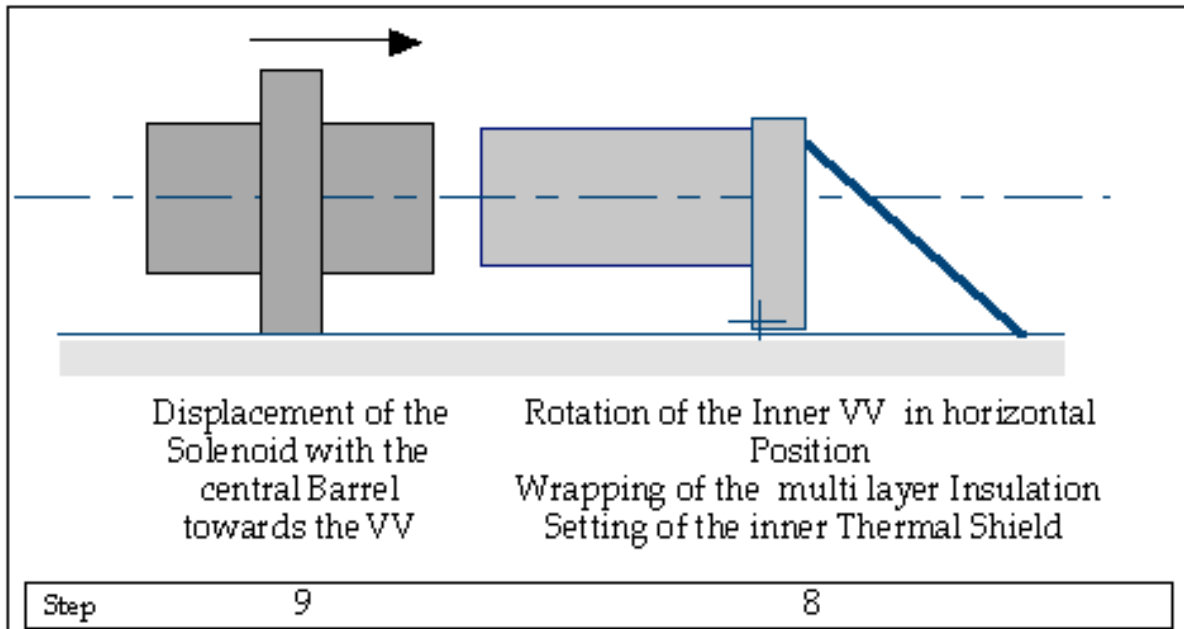


Fig. 19.36: Inner thermal shield assembly and inner shell insertion in solenoid.

19.5.6 Completing the vacuum vessel

Thermal protections are placed inside the vacuum vessel to prepare for welding, on the left side, of the spacers connecting the inner and the outer shells of the vacuum tank (Fig. 19.37).

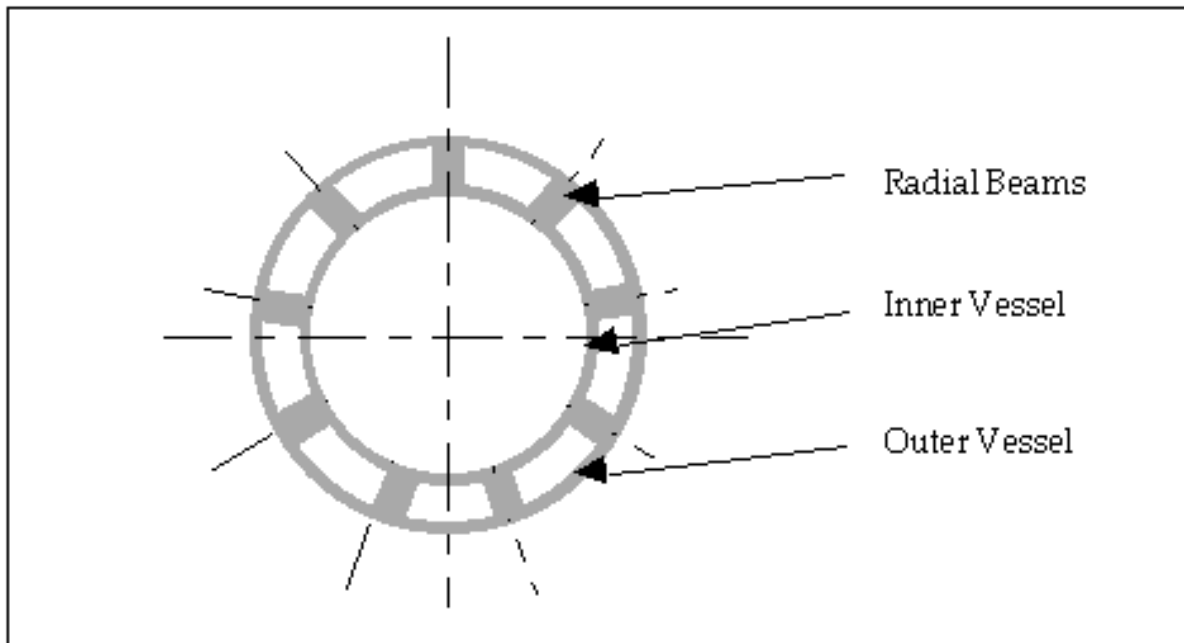


Fig. 19.37: Radial beams on vacuum vessel ends.

The temporary fixtures used for the longitudinal tie rods are removed, and the left hand

side radial beams are welded to connect the outer and inner shells of the vacuum tank. The welds are then verified.

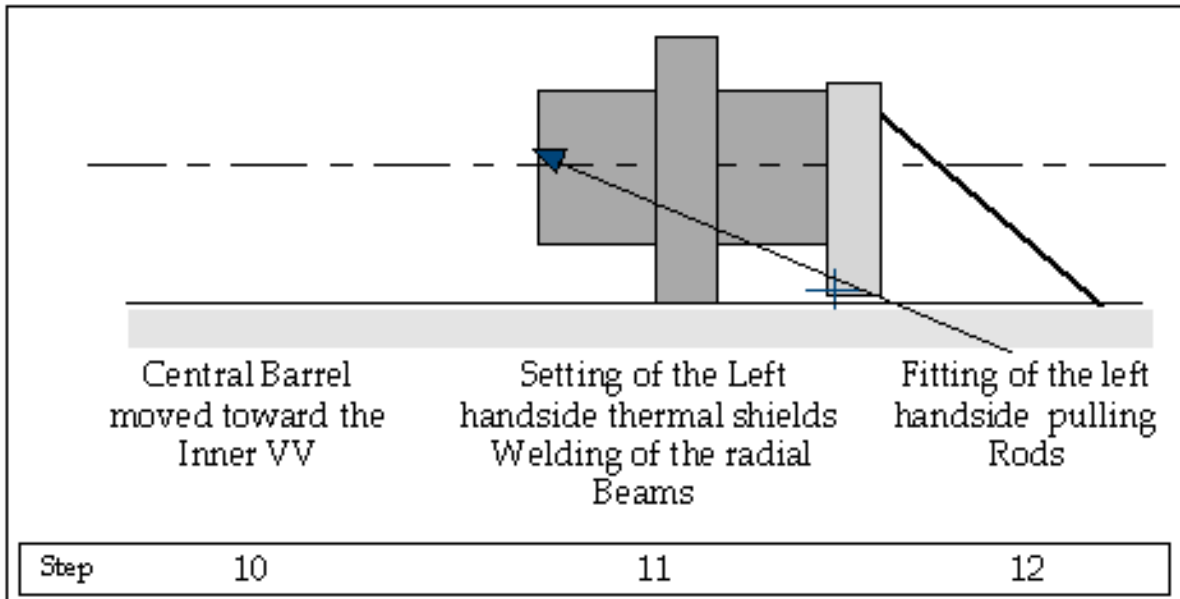


Fig. 19.38: Completion of the left hand side of the solenoid.

Welding protections are installed, through the swivelling device end plate, and three radial beams are welded to connect the right-hand side inner and outer shells of the vacuum tank. The temporary inner vacuum vessel clamps and reinforcement which were maintaining the cylindricity of the shell are removed.

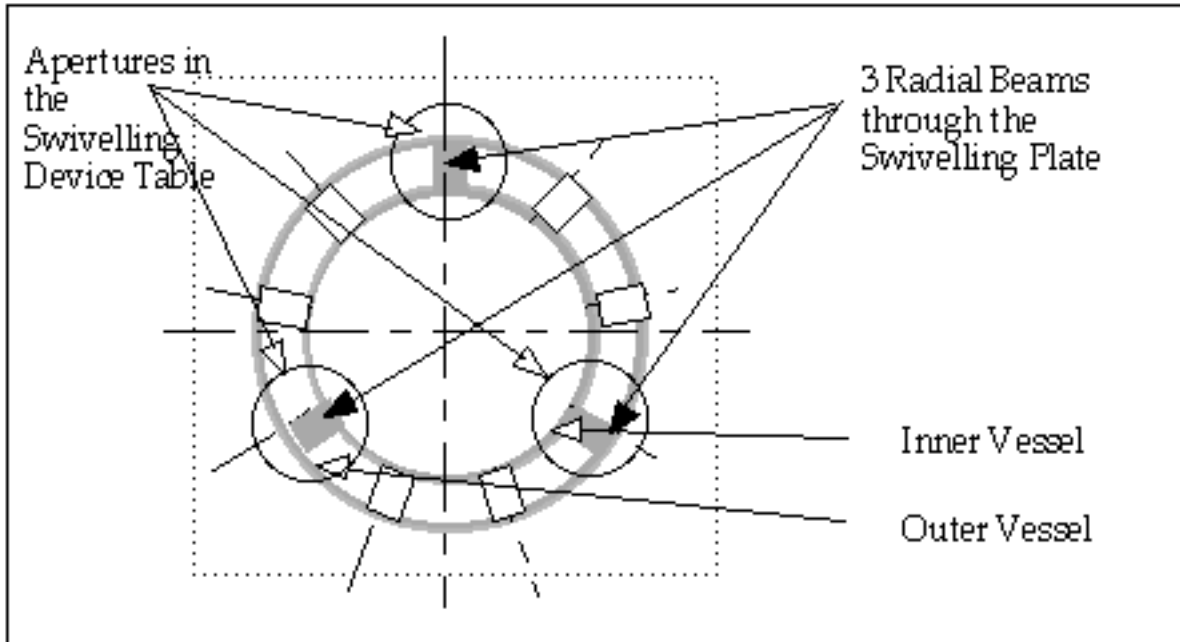


Fig. 19.39: Installation of the radial beams through the swivelling table apertures.

The central barrel is slid away from the turning device, and the six remaining radial

beams, connecting the inner and outer shells of the vacuum tank, are adjusted and welded after having installed adequate thermal protections. The welds are verified using non destructive methods, and the thermal protections removed. The longitudinal tie rod jacks are set, but not yet prestressed.

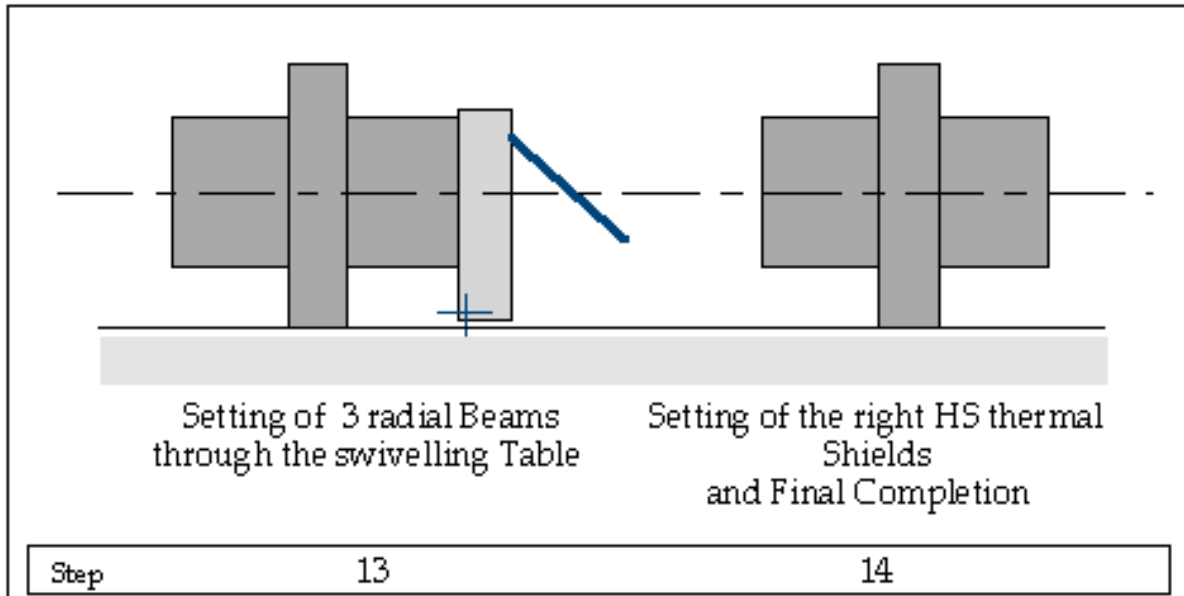


Fig. 19.40: Installing 3 radial beams through the swivelling table end plate.

19.5.7 Completing the cold mass and closing the vacuum vessel

During this phase, the end thermal shields are completed at both extremities, as well as the instrumentation, pipework, and fitting of all tie rods. This will be followed by the completion of the chimneys (cryogenic and electrical), and pressure testing of the helium pipes.

The vacuum tank will be closed by welding on end plates and will be pumped down and leak tested. The general leak test will be performed with the pipework under He pressure. The final operation consists of adjusting and pre-stressing all the tie rods. This will be done according to the procedure described in Chapt. 18.

20. ELECTRICAL CIRCUIT AND POWER SUPPLY

20.1 INTRODUCTION

This chapter describes the electrical system which provides the power for the solenoid and ensures its safety in the event of a quench or in case a fault has been detected.

The electrical circuit of the CMS solenoid is shown in Fig. 20.1.

20.1.1 General description

The power supply has a +16 V, 20000 A output with two circuit breakers CP1 and CP2 connected between the dc outputs and the two main electrical supply lines to the magnet. The dump resistor RD is composed of $5 \times 10 \text{ m}\Omega$ resistor elements linked in series and mounted in parallel to the two breakers CR1 and CR2 which are doubled for safety. Depending of the position of the CR breakers the dump resistor can either be in the fast discharge configuration or in the slow discharge configuration. In the first case the CR breakers are keeping open the 5 elements in series hence a dump resistor of 50 mΩ while in the second case the CR breakers are maintaining closed the 5 elements in parallel hence a dump resistor of 2 mΩ.

The middle of the solenoid is indirectly grounded by means of a resistor tapped into the central point of the bridge. This grounding line is protected against over-current by a breaker. By grounding the magnet in the middle the “dump voltage to ground” is divided by a factor of two and also allows the leakage current to be monitored thus making it possible to detect a short with respect to ground.

For safety reasons two breakers are used which open both polarities and also:

- quickly separate the magnet from the power supply for easy checking of the insulation,
- protect the power supply against the high voltage developed during the energy dump.

20.1.2 Protection concept

The protection of the solenoid is based on the classical concept of the extraction of the stored energy into an external resistor. It also benefits from the presence of the outer cylinder which produces eddy currents during the current decay and creates heat, initiating quenches in all solenoid layers. Therefore the maximal temperature and the temperature gradient in the winding is moderate. Quench analysis is treated in Chapt. 16.

The value of the dump resistor limits the maximum voltage across the solenoid terminals to 1000 volts, that is normally $\pm 500 \text{ V}$ with respect to ground.

20.2 ELECTRICAL COMPONENTS

20.2.1 DC Power Supply

The power supply is a thyristor D.C. generator. It delivers up to 20000 A, at 16 V maximum, and is operated in voltage control mode during ramping up of the current, and in current control mode during steady state operations. It is provided with free wheel diode system and needs demineralised water cooling. Its main parameters are given in Table 20.1.

The power supply has a size of about 3 m x 4 m with a height of 2.5 m and a weight of about 7 tonnes. It is located inside the cryogenic cavern USC5, see Fig. 26.8, p. C-58.

Table 20.1
DC Power Supply Parameters.

Current rating	20000	A
Voltage	16	V
Ramp up time	5	h
Stability	$\leq 1.10^{-4}$	
AC power,	800	kVA
Ripple, 10 Hz-10 MHz	0.8	V rms

20.2.2 Breakers CP

The two 20 kA breakers are air cooled and must support an opening voltage of 1000 V. They are of the "normally open" type.

They are housed in a cabinet attached to the power supply in the cryogenic cavern USC5 of about 3 m x 4 m, height 2 m and weight about 5 tonnes, see Fig. 26.8, p. C-58.

20.2.3 Dump resistor and breakers CR

In all operation phases, except the slow discharge one, the CR breakers are open. This is the fast dump configuration with the 5 resistors in series providing a total resistance of 50 mΩ.

For the slow discharge phase the CR breakers are closed. The 5 resistors are coupled in parallel providing the slow dump configuration of 2 mΩ resistance. In case of a quench during the slow dump, the CR breakers are opened commuting to the fast dump configuration.

The stainless steel dump resistor is air-cooled through convection cooling. It is designed to absorb the total solenoid magnetic energy with a temperature increase of 300 °C at its hottest point.

The associated CR breakers are four pole air-breakers for 8000 A and must support an opening voltage of 1000 V. They are of the "normally open" type.

The estimated volume of the dump resistor housing and its electrical lines is about 100 m³. The resistor is fixed to the wall of the shaft above the platform covering the experimental cavern, see Fig 26.8, p. C-58. The CR breakers are located beneath the five elements of the dump resistor on the platform itself [20-1].

20.2.4 Grounding circuit

As shown in Fig. 20.1, the grounding circuit is composed of a resistor bridge in series with a ground resistor and the over current protection breaker CM. These 3 resistors have the same value of 40 Ω. Normally the electrical circuit is grounded at the electrical middle point. Monitoring the leak current through the grounding resistor allows to follow the insulation evolution.

20.2.5 Electrical lines

The 20 kA electrical buses between the power supply, the solenoid and the dump resistor are made of water-cooled copper cables [20-2]. The copper cross-section limits the

voltage drop to less than 2 V. Table 20.2 indicates the main parameters of the cable buses. No break in the cables between the solenoid and the dump resistor can be allowed at any time, therefore, in the event of a lack of coolant at full current, the integrity of the cables must be ensured. Temperature of the junctions will be permanently monitored. All the bus sections will be fully protected to detect and prevent any accidental short circuits.

The space occupied in section by each cable bus is of 450 x 450 or 900 x 200 mm², depending whether the cables are disposed in a flat or square arrangement.

Table 20.2
Electrical Cable Bus Parameters.

	Solenoid - Power Supply		Solenoid - Dump Resistor	
Length per polarity	50	m	40	m
Cable number per polarity	4		4	
Section of copper per polarity	23800	mm ²	23800	mm ²
Resistance of bus feed and return	0.075	mΩ	0.060	mΩ
Total voltage drop	1.5	V	1.2	V
Water flow per cable	8		l/mn	
Temperature increase	<10		°C	
Holding time without flow	13		h	
Holding time without water	4.5		h	

20.2.6 Current leads

Cryogenic current leads are sensitive parts of superconducting magnet circuitry because they have to conduct the nominal current between room temperature and liquid helium temperature while not consuming too much helium for cooling. The continuity of lines between the magnet and its dump resistor is of major importance. The main considerations for the current leads is their robustness and their holding time without helium cooling.

The leads must be able to carry the nominal current in case of coolant flow loss for a duration of several minutes (say between 5 and 10) without suffering any thermal damage. This time provides a safety margin for the safe discharge of the solenoid.

The projected structure of the current leads is a copper cable in a stainless steel conduit, identical to the one at ALEPH.

20.3 DISCHARGE MODES

Three modes for discharging the solenoid are available.

- Slow discharge through the slow-dump-configured resistor.

This is the regular mode of decreasing the solenoid current to zero, along with the safety mode of discharging the solenoid in the event of a minor fault described in paragraph 20.2.

The time constant of the slow discharge is 6750 s. To quickly lower the solenoid current, a fast discharge is commanded by opening the CR breakers when the current goes below 2000 A.

A slow discharge can be interrupted when the fault is cancelled: the operator can recover the process and reset the current to its initial value.

- Fast discharge through the fast-dump-configured resistor.

This is the emergency mode of discharging the solenoid in the event of a major fault, described in paragraph 20.2.

The time constant is 210 s due to the winding resistance developed during the quench of the solenoid (280 s if there were no quench).

- Free wheel discharge through the diodes of the power supply.

This is not considered a regular mode for operation; nevertheless it is available and its duration which is related to the resistance's of the diodes and the electrical buses is estimated to about 18 h.

20.4 SAFETY VS FAULTS

20.4.1 Fault interlocks

The diagram of the safety interlocks is shown in Fig. 20.2. Two levels of faults are shown.

- First the major faults which imply the fast discharge of the stored energy through the 50 mΩ dump resistor. As the fast dumps cause large perturbations on the physics experiments and need several days to re-cool, their number must be reduced to the minimum. The fast dump faults are the following:
 - quench of the superconductor,
 - excessive temperature of current lead heat exchangers,
 - other emergency cases still to be defined.

The fast dump operation is initiated by:

- opening the CR contactors,
- opening the CP breakers,
- opening the main power supply breaker.

- Secondly, the minor faults which only imply the slow discharge of the stored energy through the 2 mΩ dump resistor. These faults are the following:
 - excessive current lead voltage drop,
 - low helium flow in current leads,
 - low vacuum pressure,
 - water cooling failure of the bus,
 - overheating the bus junctions,
 - other faults still to be defined.

The slow dump operation is initiated by:

- closing the CR breakers,
- opening the CP breakers,
- opening the main power supply breaker.

- Furthermore, a safety interlock checks the connection of the dump resistor every time the solenoid is excited in current, by monitoring the dump resistor voltage. Lack of voltage commands the ramping back of the power supply current to zero.

20.4.2 Fault repertory

Ground insulation failure

All the components of the solenoid electrical circuit - power supply, breakers, dump resistor, winding - are entirely insulated from earth, but as already mentioned in paragraph 20.2.4 the middle of the solenoid is indirectly grounded. A degradation of the solenoid insulation to earth will allow leakage current through the grounding resistor whenever the solenoid voltage is not zero, *i.e.* whenever the field is changing.

Monitoring the leakage current allows the evolution of the insulation to be controlled and to detect a short-circuit. The level of the leakage current which triggers the opening of the breaker must be set low enough to prevent the generation of an arc which could cause damage to the conductor in the event of a single coil short.

Most critical situations arise if multiple shorts to ground exist at the same time, creating a shorted winding section. Whenever the field is changing, circulating currents are induced into the shorted section. The faster the field change, the higher the current in the shorted section. Consequently these currents will be maximum during a fast dump commanded by a conductor quench. The difference between the currents of the normal and shorted sections results in a redistribution of the forces inside the solenoid and also in an unbalance of the axial forces between the solenoid and the iron caps.

An analysis of the shorting effects is to be carried out.

Protection system failure

In case of a total failure of the protection system in presence of quench, the current will only begin to decay when the resistive voltage across the coil reaches the power supply voltage capability

If only the CR breakers fail to open, a slow dump into $2\text{ m}\Omega$ is performed in place of a fast dump into $50\text{ m}\Omega$, which is fairly similar to the above total failure case. In both cases, Chapt. 16 shows that the solenoid does not suffer damage from overheating or over-voltage.

Electrical buses failure

The continuity of the electrical lines between the solenoid and the dump resistor ensures the safety of the solenoid. In particular the lines and the junctions must be permanently monitored to avoid overheating.

Disconnection of the dump resistor

Disconnecting the dump resistor would be fatal to the solenoid. This could occur if the dump resistor is not reconnected after maintenance. To check the actual connection of the dump resistor across the solenoid terminals, the voltage of the resistor central element is monitored every time the solenoid is switched on: the absence of the dump resistor voltage commands the ramping back of the current to zero.

20.5 SURFACE MAGNET TESTS

It is planned to test the complete CMS solenoid, with its yoke closed, in the surface building around October 2003, before its transfer and final installation in the experimental cavern. The electrical circuit for these tests will make use of the final components, which will be later installed in the cavern, except the electrical buses (which may be simple copper cables) because the respective positions of the elements will be quite different in the cavern.

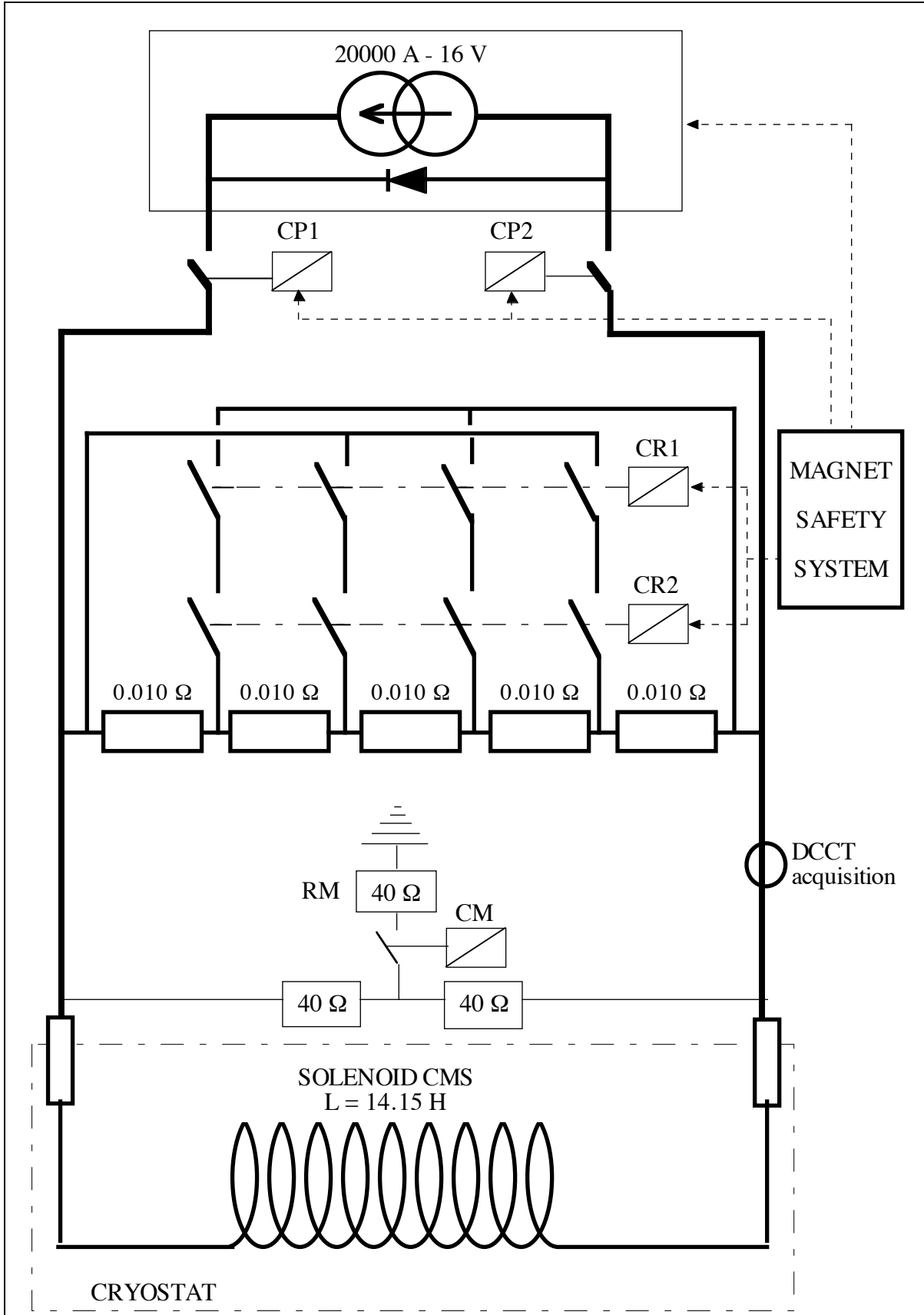


Fig. 20.1: Electrical circuit for the CMS solenoid.

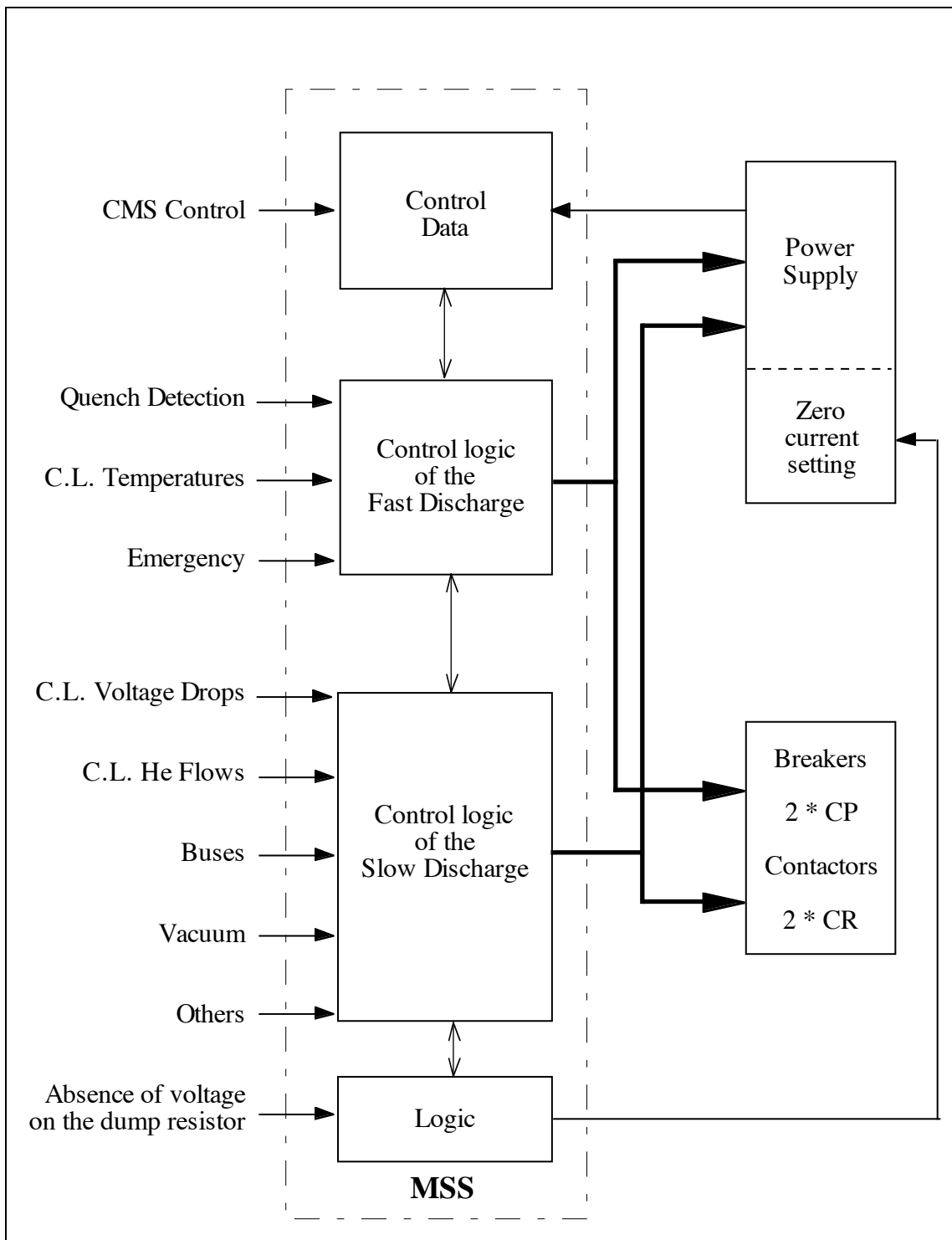


Fig 20.2: Diagram of the Safety Interlocks.

21. CRYOGENIC PLANT

21.1 REFRIGERATION PLANT (COMPRESSORS, REFRIGERATOR, TRANSFER LINES, LHE 5000 L DEWAR)

21.1.1 Compressors, helium gas and liquid nitrogen storage

The compression system will consist of two screw compressors installed at the surface of P5, in the purpose-built Building SH, (see Fig. 21.1, p. XX). They will be set in their final position from phase one and will be used first for the magnet test at the surface and then for the commissioning and operation in the experimental cavern. The nominal mass-flow of the compression system is ~ 180 g/s. The maximum pressure level is expected to be ~ 18 b. In the same building a third screw compressor with a capacity limited to 40 g/s, will be used for the recovery of helium gas from the magnet in the event of the main cryogenic plant being shut down. This gas will be compressed and stored without contamination and thus can be re-usable after the shut-down. Building SH will also house the complete oil removal and purifier system needed for the operation of the screw compressors.

The helium will be stored at the surface outdoors (see Fig. 21.1, p. XX) in two 250-m³ cylinders at 20 b. This storage capacity provides a supply of two full loads for the refrigeration plant and the magnet system. An addition helium supply can be provided by connection the CMS gas holders with those of the LHC accelerator, located at the same surface area.

A 50 000 l liquid nitrogen dewar for pre-cooling the magnet in the temperature range 300 to 100 K is also located at the surface. During this cooling phase, the expected liquid nitrogen mass-flow is 500 l/h. During the magnet testing period at the surface in Building SX, the liquid nitrogen dewar is located between Buildings SH, SX and the "Cryogenic Alcove" (SHL) which will temporarily house the cold box for the test. In the final phase, when the liquid nitrogen is supplied to the cold box in the experimental cavern, the dewar will be moved next to Building SDX so as to minimise the length of the required liquid nitrogen transfer line.

21.1.2 Cold Box, transfer lines and 5000 l liquid helium cryostat

On the base of the thermal loads of the superconducting magnet system and of the operating conditions (thermal sequencing during the technical shutdowns of the LHC, cooling-down time and quench recovery), it was agreed to use a refrigerator with a power rating of 1.5 kW @ 4.5 K (entropic equivalent).

The upper part of the cold box contains a set of liquid nitrogen/helium heat exchangers for magnet cooling down to 100 K. In addition the liquid nitrogen pre-cooling should allow to increase the helium liquefaction of the plant when necessary.

The cold box will be connected to the magnet via an intermediate cryostat (see Fig. 21.2, p. XX), which will house all the cryogenic valves needed to pre-cool the magnet and its heat shield. The intermediate cryostat includes a 5000 l reserve of liquid helium to allow the magnet slow discharge in the event of failure of the cryogenic system or other facilities.

The cold box will be connected to the intermediate cryostat by a single thermally shielded transfer line 600 mm in diameter and 30 meters long containing 4 separate lines.

Two for the magnet circuit helium, diameter of 80 mm at the outlet, 50 mm at the inlet and two for the heat shield circuit, 60 mm in diameter. The cryostat will be connected to the valve box and helium phase separator (on top of the detector) by means of 4 separate transfer lines performing the same functions as described above.

The magnet's heat shield will be cooled by tapping off the required mass-flow at the level of the outlet of the first expansion turbine of the cold box and reinjecting the shield return at the inlet to the second expansion turbine (in case of a cycle with only two turbines in series).

21.2 CRYOGENIC FLOW-SHEET AND PROCESS DEFINITION (COOL-DOWN, NORMAL AND RECOVERY CONDITIONS, WARMING-UP)

21.2.1 Cooling-down phase from 300 K to 100 K

The magnet will be pre-cooled using the liquid nitrogen/helium heat exchanger in the cold box designed for this purpose (see Fig. 21.2, p. XX). The 50 mm lines will be used (identical to those used for the liquid phase) to convey all the nominal mass-flow of the screw compressors (approximately 180 g/s with a total pressure drop across the system of 10 b at ambient temperature). Both the valve box and the intermediate cryostat have a bypass for this purpose. Valves V271, V272, V273 will be closed and valves V260, V290 open. By-pass V3 in the valve box will be used to allow the necessary mass-flow. The gas return from the magnet will be channelled inside the cold box to the appropriate temperature level. Assuming a maximum temperature gradient of 50 K, the cooling-down time to 100 K will be ~ 20 days. During this phase the expansion turbines are switched off and cooling of the heat shield has not yet started.

21.2.2 Final cooling-down phase from 100 K to 4.5 K

From this point onwards the cold box expansion turbines are in operation. Circulation in the magnet heat shield starts and in parallel a minimal mass-flow of 80 g/s is maintained in the circuits of the coil. At the same time, part of the main mass-flow is tapped off to cool the intermediate cryostat and the 5000 l liquid helium dewar. This final cooling phase will last approximately 10 days.

21.2.3 Normal operation at 4.5 K

The cold box with its own phase separator, upstream of V260, will supply the supercritical liquid helium at 3b to the 5000 l cryostat. V271 will allow the level of liquid helium in the dewar to be regulated. The pressure of the cryostat will be set at 1.5 by V273, located at the cold return to the cold box. Transfer to the magnet valve box and phase separator will be done by the supply valve V272. The shield will be cooled via valves V280 and V281 with a helium mass-flow of 35 g/s, at an input temperature of 60 K and an output temperature of 80 K. The input pressure will be 5 b and the pressure drop lower than or equal to 150 mb.

21.2.4 Operation at 4.5 K without cold box and with or without compression system

In case of failure of the refrigerating system, the dewar continues to supply liquid

helium to the phase separator of the valve box. The 5000 l capacity will ensure the supply of liquid helium to the magnet throughout the current slow discharge phase which takes approximately 4 hours. With the expansion turbines out of operation the heat shield is no longer cooled. After depressurisation of the shield circuits from the nominal operating pressure, the V7 by-pass valve conveys the flow evaporated by the magnet into the circuits of the heat shield. The evaporation rate of the magnet will be 20 g/s and the total expected pressure drop in the shield circuits is less than 120 mb (excluding atmospheric heat exchanger).

If the compressors for the cryogenic cycle are in operation, the helium from solenoid return and current leads may be recovered and stored in the gas holders. These flows will be injected at the low pressure level of the main compression system. In the event of total shutdown, including that of the cycle compressors, these flows will be recovered and stored by the recovery compressor, which must be connected to the auxiliary external safety services allowing its operation in the event of the main facilities failure.

Valve V283 controls the pressure in the phase separator of the magnet when the cold box is not in operation and the heat shield during depressurisation.

21.2.5 Fast energy dump

During rapid discharges

Valves V1 and V3 are closed and the expansion turbines are shut down. The cold box is isolated by valves V260 and V290, as is the 5000 l dewar by its valves. The cryostat has its own exhaust through V275 via a heat exchanger to the low pressure of the compression system.

Post-quench depressurisation

The "thermosiphon" circuit is depressurised by the V7 by-pass valve through the shield.

Post-quench cooling

Two options are being considered for thermal recovery of the magnet from the average temperature of 50 K reached after a fast energy dump. As there are no valves on the thermosiphon return, cooling may be done either by controlling the opening of the by-pass of the Joule-Thomson in the cold box so as to limit the pressure rise in the low-pressure circuit, or by supplying the magnet directly with liquid helium from the cryostat's 5000 l reserve. The time required to cool the magnet from 50 K to 4.5 K after a quench will be about 3 days. Assuming that only 20% of this stored energy is discharged in the cold mass.

21.2.6 Warming-up of the magnet

During the LHC technical shutdowns, it is agreed that the magnet will be electrically re-heated and decoupled from the cryogenic circuits to allow maintenance of the compressors, the refrigerator and auxiliary equipment.

21.3 VACUUM INSULATION OF THE MAGNET

The magnet's vacuum insulation will be done by:

- a primary pumping station consisting of two vane pumps and two 900 m³/h Roots pumps. These will be installed in the service cavern and connected by a 300 mm diameter pipe to the distribution pumps described below.

- a diffusion pumping station connected to the vacuum chamber of the magnet. One 8000 l/s diffusion pump will be directly connected by a 600 mm spool piece to the vacuum chimney (400 x 800 mm²). A second 2000 l/s pump will be directly connected to the vacuum chamber of the magnet's valve box.

21.4 CRYOGENIC PLANT FOR THE SURFACE TEST OF THE MAGNET

A test of the overall cryogenic plant and its auxiliary equipment is planned at the surface of LHC P5. The plant will be connected to the magnet system which, at that time, will be located in Building SX. Extensive magnet tests are planned before installation in the experimental cavern. For this purpose, the following cryogenic equipments are provided (see Fig. 21.3, p. XX):

- the complete compression system and its auxiliary equipment in Building SH,
- the helium gas holders opposite to building SH connected to the compressors,
- the cold box and its control equipment will be temporarily installed in the building known as the "Cryogenic Alcove" (SHL) adjacent to the Compressor Building SH (see Fig. 21.1, p. XX). The first floor of the Cryogenic Alcove will house the cold box and its auxiliary equipment, and the ground floor will house the main supply for the magnet and the pumping stations for the insulation vacuum.

As can be seen on the surface layout for the magnet test, the intermediate cryostat is located next to the magnet and forms an integral part of its structure. It is coupled to the valve box of the magnet by the required transfer lines. This unit is designed to move as one component when being lowered and installed in the experimental cavern.

From the layout studies it appears that the main transfer line (four in one) linking the cold box to the intermediate cryostat containing the 5000 l liquid helium dewar must be purpose-built for the magnet surface tests and cannot be reused for the final transfer system in the underground cavern. Nevertheless, it is intended to standardise the connection equipment of this transfer line to the cryostat.

21.5 INSTALLATION OF THE COLD BOX, TRANSFER LINES AND LIQUID HELIUM CRYOSTAT IN THE UNDERGROUND AREA

The final layout of the cryogenic equipment is shown in Fig. 21.4, p. XX. It should be noted that the cold box and its auxiliary equipment are now located in the service cavern, to which access is permitted at all times when the accelerator is in operation. Conversely, the magnet intermediate cryostat and valve box are located in the experimental cavern where access is not allowed when the beam is on (controlled access).

The transfer lines between the intermediate cryostat and the valve box remain unchanged after the surface test of the magnet. However, the multiple transfer line connecting the cold box to the intermediate cryostat will now be straight and at the same height. The main transfer line and the other gas lines or auxiliary pumping lines will pass from the service cavern into the experimental cavern via a hole in the concrete blocks of 1.2 m in diameter in accordance to the rules required by the radiation safety.

The pumping stations and power supply for the magnet will also be installed in the service cavern (see Fig. 21.4, p. XX). The magnet's power supply cables and the quench detection signals pass through the concrete wall in a specially-designed conduit.

21.6 TIMETABLE FOR THE CRYOGENIC EQUIPMENT INSTALLATION AND MAGNET TESTS

Below is the proposed timetable for the design studies, preparation of the specifications, procurement, installation and testing of the cryogenic equipment, coupling of the installation to the magnet, followed by tests at the surface and in the experimental cavern.

Design studies and definition of the process engineering 08/1997
Preparation of the equipment specifications	09/1997 - 06/1998
Market survey and call for tenders	03/1998 - 12/1998
Equipment orders placed	01/1999
Delivery of the equipment	06/2000 - 12/2000
Installation and testing of the cryogenic equipment (compressors + final infrastructure, cold box at the surface)	01/2001 - 12/2002
Test of the CMS magnet at the surface of P5	01/2003 - 10/2003
Transfer of the cryogenic system to its final position in the cavern - final installation of the equipment and transfer lines	11/2003 - 12/2004

22. MAGNET CONTROL SYSTEM

22.1 PRINCIPLES

The Magnet Control System (MCS) is integrated into the CMS Detector Control System (DCS) [22-1]. It is capable of working independently or as part of the overall CMS DCS. It includes four parts:

1.

The Sensors and Actuators of the magnet, auxiliaries and closely related infrastructure.

2.

The Programmable Logic Controllers (PLCs) including a Test and Development Station (TDS) for development, testing, commissioning and debugging of the process controls.

This process control sub-system is programmed for full automated functioning of the magnet system and ensures:

- working sequences of the proximity cryogenics, vacuum system, power supply,
- control of heating and gas flow regulation of the current leads,
- transmission of alarms and of all parameters readout.

3.

The Magnet Safety System (MSS) which aims, in case of fault, to secure in an entirely automatic mode the magnet and auxiliaries with hardware equivalent protections of two kinds:

- specific protection like Transition Detection System, current lead faults ...
- standard protections like usual interlock system acting on water flow limit, water leak detection, power supply fault...

Both are combined to trigger appropriate discharge of the magnet and hence eliminate any risk of damage. This system must provide the highest level of reliability.

One imbedded PLC in parallel allows on-line analysis of the safety parameters and offers redundancy in securing the magnet as well as more intelligent exploitation tools.

All necessary parameters and alarms related to this system are transmitted in real time (a few seconds) to MCS to enable supervision and fault analysis.

4.

The Magnet Supervisor (XMS) [22-2] which is a component of the CMS DCS and, as such, provides the user with all functionalities of a DCS component, includes:

- supervision and control facilities,
- operator's assistance and diagnostic facilities.

The user will be able to use a DCS operator desktop in the experiment control room, or in the service cavern or from remote locations. Different types of users have to be considered and will be described in parag. 22.3.

The conceptual control system structure is shown in Fig. 22.1. Fieldbus technology will be used at the level of the PLCs and at the level of the sensors and actuators. Provision will be made to have the possibility to revert to direct cabling of the sensors and act

uators to the PLCs if magnetic field or radiation effects happen to cause disturbance.

The partition of MCS in four parts can lead to the same partitioning in terms of procurement. Testing, installation and commissioning are independent of the availability of XMS.

PLCs with TDS can be treated in an industrial turn-key system approach, whereas XMS is produced as a DCS component.

MSS is an autonomous system using possibly custom design packages whose parameters are input to the PLCs.

Independent commissioning of sub systems is ensured. Local diagnostics and fault finding at commissioning as well as flexibility is provided with the help of TDS.

MCS control system is required to interface with other systems in CMS:

- Top level MCS experiment through DCS / CMS operations in CMS control room.
- MCS refrigeration plant (external cryogenics) and Central CRYO control room.
- LHC Machine operations / LHC control room.
- DEAS Detector and Experimental Area Safety System.
- Technical services (Technical Control Room TCR).
- Infrastructure and general services (relevant vital information will be acquired directly at the Infrastructure PLC level).
- Power Converter Service.
- Maintenance call and help service.

Interface requirements are partially detailed in 22.5 and will need special care.

Every effort will be made to standardise, as far as possible, the different Magnet Process Control Systems of the LHC experiments. This option presents obviously different advantages, but the most evident are those of minimising the number of staff having the same level of competence on the field, and reduce the storage of spare parts for the same level of reliability.

Wherever possible, one will try to take advantage from the choices adopted for the LHC machine, because CERN, as host laboratory, will have the heavy charge of satisfying reliable and inexpensive running of the LHC experimental complex.

Cryogenics is one of the most evident examples but other common fields are currently being investigated.

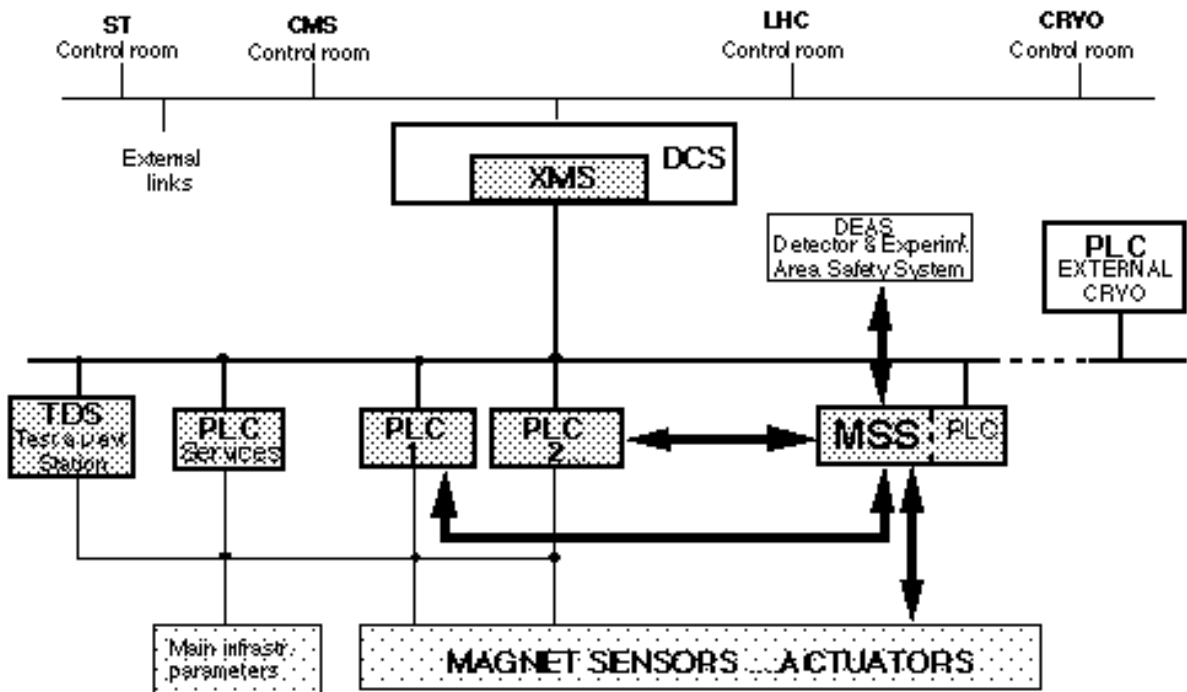


Fig. 22.1: Conceptual Control System Structure.

22.2 INSTRUMENTATION

There are many ways for connecting the sensors and actuators to the control systems. We have chosen to connect the sensors, actuators and the PLCs on the same fieldbus, a solution which offers several advantages; if this choice is impossible due to problems of radiation or magnetic field, we have the possibility to revert to hardwired lines. The design of the control system is detailed in Chapt. 22.3. For the instrumentation, the following possibilities are under study:

- connect all sensors to remote input-output modules,
- use smart sensors and actuators (as defined hereafter).

Each of these two possibilities allows to:

- minimise the number of cables between the magnet installation and the control system,
- transmit noise free data to the PLCs,
- adopt an advanced technology,
- optimise the maintenance.

The remote I/O systems are well developed in industry and are commercially available. The use of remote modules is now well-tested. These modules transmit values of all sensors and receive commands for actuators as numeric data through the fieldbus. They allow the following functionalities:

- diagnostics,
- wiring tests,
- power supply module monitoring,
- failure position,
- programmable filtering,

- status memory.

Nevertheless, the remote modules transmit only the values of the sensors. Any error in the measurement (noisy signal, shift or other deviation between real value and transmitted value) produces effects in the control system. However the use of smart sensors and actuators allows to minimise such effect. The smart sensors have local processing capability and a fieldbus port. This technology has the same advantage as the remote I/O module technology; moreover it ensures the following functionalities:

- transmit confirmed information on the fieldbus (e.g. the measured pressure value is linearised and temperature compensated),
- automatic control of the sensor internal processing,
- large range of measurement which may help to reduce the number of spare sensors.

The physical parameter measurement on the magnet installation are for the cryogenic part:

- flows,
- pressures,
- levels,
- temperatures,
- movement of cold mass.

For the magnet safety, the physical parameters are:

- currents,
- voltages,
- temperatures,
- pressures,
- levels.

These parameters are transmitted to the MSS as detailed in Chapt. 22.4.

The actuators are mainly analogue valves, flow valves and vacuum pumps. For the actuators, the same alternative solutions as for the sensor are under study, (i.e. remote module and smart actuators). The smart actuators are presently only in the prototype development stage. Therefore, the use of I/O modules for actuators is safer at the present time.

To resume, at present the following instrumentation is considered:

- sensors: smart sensors or sensors with remote modules on fieldbus,
- actuators: remote I/O modules (smart actuators are only in prototype state),
- safety signals to HL / MSS: electronic treatment in cavern and direct transmission to HL in MSS,
- safety signals to PLC / MSS: electronic treatment in cavern and transmission to be defined.

22.3 CONTROL SYSTEM

According to Fig. 22.2, the control/command design is composed of several PLCs.

Each of them controls an independent subsystem. This division conforms the installation functionalities and its advantages are:

- easy testing and debugging; each subsystem can be tested alone without waiting for the other subsystems to be operational,
- improvement of the maintainability and availability of the experiment,
- independent development of the PLC software.

Each subsystem ensures one or many functionalities in the experiment as indicated in the table below:

Table 22.1
Subsystem functionality.

Subsystem	Functionality
Cryogenics	<ul style="list-style-type: none"> - Cool down - Control loop for the exploitation parameters - Warm up
Vacuum	<ul style="list-style-type: none"> - Ensure a good vacuum
Alignment	<ul style="list-style-type: none"> - Alignment between the magnet and iron mass
Current leads	<ul style="list-style-type: none"> - Control loops: flows and temperatures at top of CL
Magnet Safety System (MSS)	<ul style="list-style-type: none"> - Quench detection - Detection of current lead fault - Communication with XMS
Power Supply	<ul style="list-style-type: none"> - Power supply parameters control

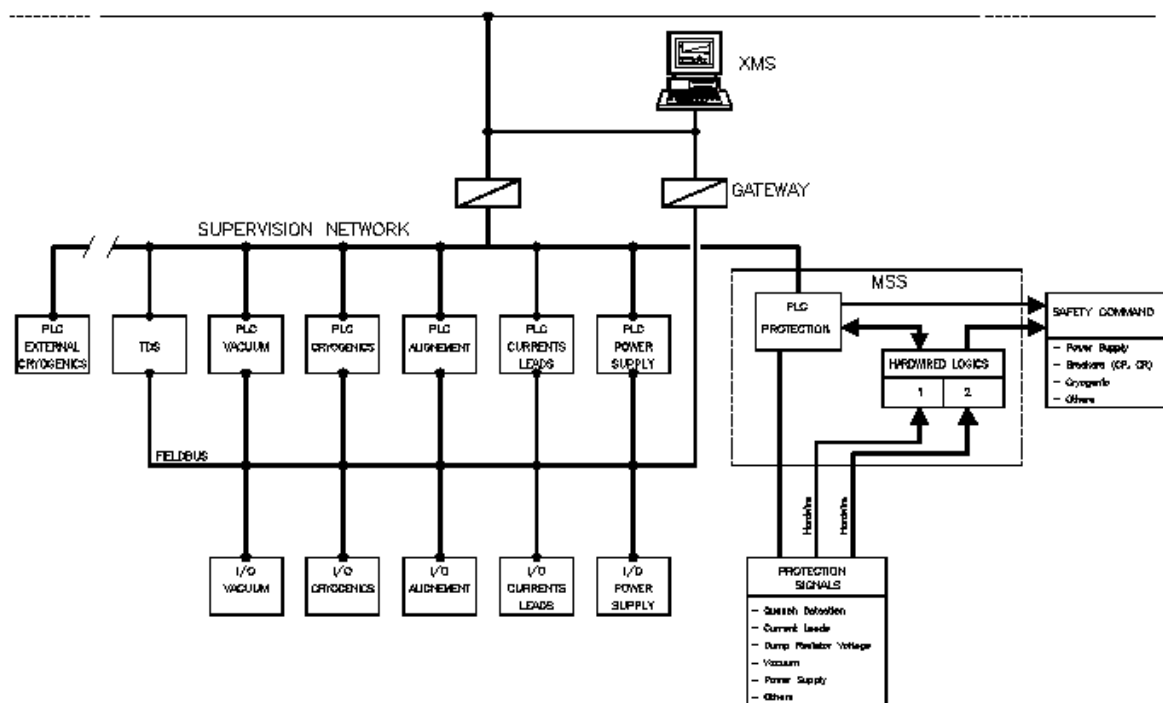


Fig. 22.2: Control system architecture.

The whole of the control/command is monitored by the XMS through two gateway s if these are requested by the communication protocols. Nevertheless, two connection l ines are necessary:

- the first one with the fieldbus for on-line monitoring of all control parameters,
-
- the second one on the supervisor network for diagnostics. The latter conn ection enables the understanding of the process, to ensure optimised maintenan ce, to monitor all states in the running mode.

This design is built with four kinds of users in mind:

- the operator: during running, he is the first user interested by the experim ent status,
- the maintenance leader: in case of failure in the process, he can analyse the different process states, effect a temporary remedy or ask the maintenance tea m for an emergency intervention,
- the experts: in the debugging phase, they analyse all the problems and the y need data close to the real process,
- the control system designers: will work with the experts in the debugging phase; they need data on the internal state of the PLCs, fieldbus, remote modul es

22.3.1 The PLCs

The PLCs are programmable electronic systems with microprocessors. They proc ess discrete, analogue or numeric signals in real-time.

They have the following advantages:

- processing time adapted to the cryogenic process,
- processing of analogue parameters,
- resistance to industrial environments,
- longer lifetime.

The PLCs allow the following processing:

- manage the operation of the installation,
- ensure control loop,
- ensure subsystem safety,
- help to run diagnostics.

The design of each PLC will be studied later taking into account the availability con straints.

22.3.2 The fieldbus

The fieldbus is the mean of communication between:

- the sensors-actuators and the PLCs,
- the PLCs themselves,
- the TDS and PLCs,
- XMS and the sensors/actuators.

The fieldbus protocol allows all PLCs to access all sensor values. This possibility simplifies the cabling in the case that several PLCs need to access the same sensor.

The choice of the fieldbus is not yet made. Nevertheless, the fieldbus will conform to the recommendations of the "Working Group on Fieldbuses" of June 26, 1996.

The parameters for the fieldbus choice are:

- critical time,
- transmission of data with determinist cycle,
- capacity for transmission of analogue data,
- total length,
- transmission speed,
- design simplicity.

If the fieldbus technologies present any problem with radiation or magnetic field, the connection design allows to transmit parameters with hardwired lines.

22.3.3 The supervisor network

The choice of the supervisor network depends of the communication protocol of the XMS. Nevertheless, the data in this network is intended for XMS. It is used for diagnostics, to understand the installation functioning, to monitor the installation state and maintenance. This network is not a critical element in the architecture because it is not essential for system operation.

22.4 MAGNET PROTECTION (MSS)

22.4.1 Principles

The CMS experiment must run for several months each year without interruption. The experiment monitoring will be done from a control room located in a surface building.

The magnet safety is ensured by two independent systems, using different technologies:

- Hardwired Logic (HL).
- PLCs.

The MSS design is shown in Fig. 22.3.

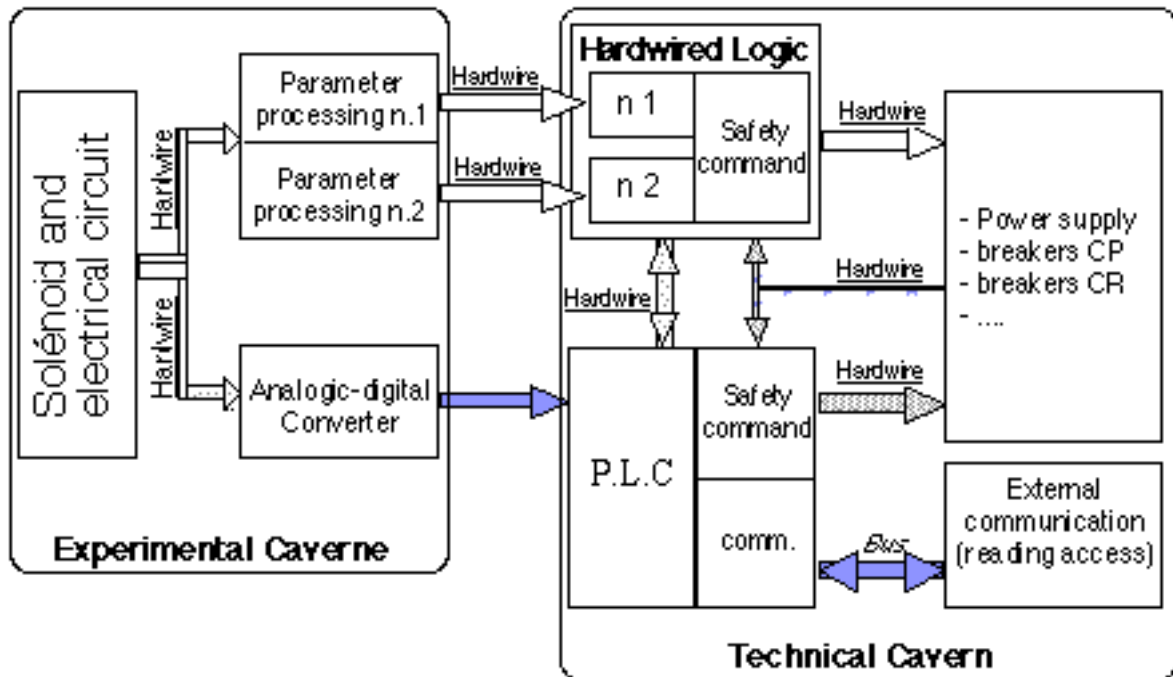


Fig. 22.3: Magnet Safety System Design.

22.4.2 Protection actions

The main purpose of the protection is to ensure CMS solenoid safety by discharging the stored energy in one of two modes:

- Slow Dump (SD),
- Fast Dump (FD).

The protection principles are detailed in Chapt. 20.

The Slow Dump is the regular mode of decreasing the current on operators request and the safety mode of discharging the solenoid in the event of minor faults. It is done by closing the breakers CR1 & CR2 and opening the breakers CP1 & CP2 (Fig. 20.1).

The Fast Dump is an emergency mode triggered by major faults giving a rapid discharge of the solenoid. It is done by opening the breakers CR1 & CR2 and opening the breakers CP1 & CP2.

22.4.3 Safety system reliability

The safety parameters are analysed on-line. Signal thresholds trigger appropriate safety commands (SD, FD, warning ...).

The two hardwired logic systems ensure a high dependability due to their structural and logical simplicities.

The PLC, along with its role for data acquisition, duplicates the same safety functions as the hardwired logics HL, but it works with signal thresholds set to lower values than those of the HL.

The association of HL with PLCs gives users several exploitation possibilities such as:

- memorisation of parameters in the pre- and post- quench period,
- memorisation of the parameters in normal continuous operation,
- on-line monitoring of the various parameters,
- monitoring the parameter shifts with time,
- automatic change of threshold related to parameter shift,
- ease of diagnostics in case of installation failure ...

22.4.4 Magnet Safety Interlocks

The safety signal treatment is ensured by two independent hardwired logic channels and a PLC channel. All safety sensors are doubled or perhaps tripled.

The hardwired logic parameters are processed by electronics located near the sensors in the experimental cavern, then transmitted to the MSS in the technical cavern.

For the PLC, the parameter signals will be transmitted between both caverns in a mode yet to be defined.

The magnet safety interlock scheme is shown in Fig. 22.4.

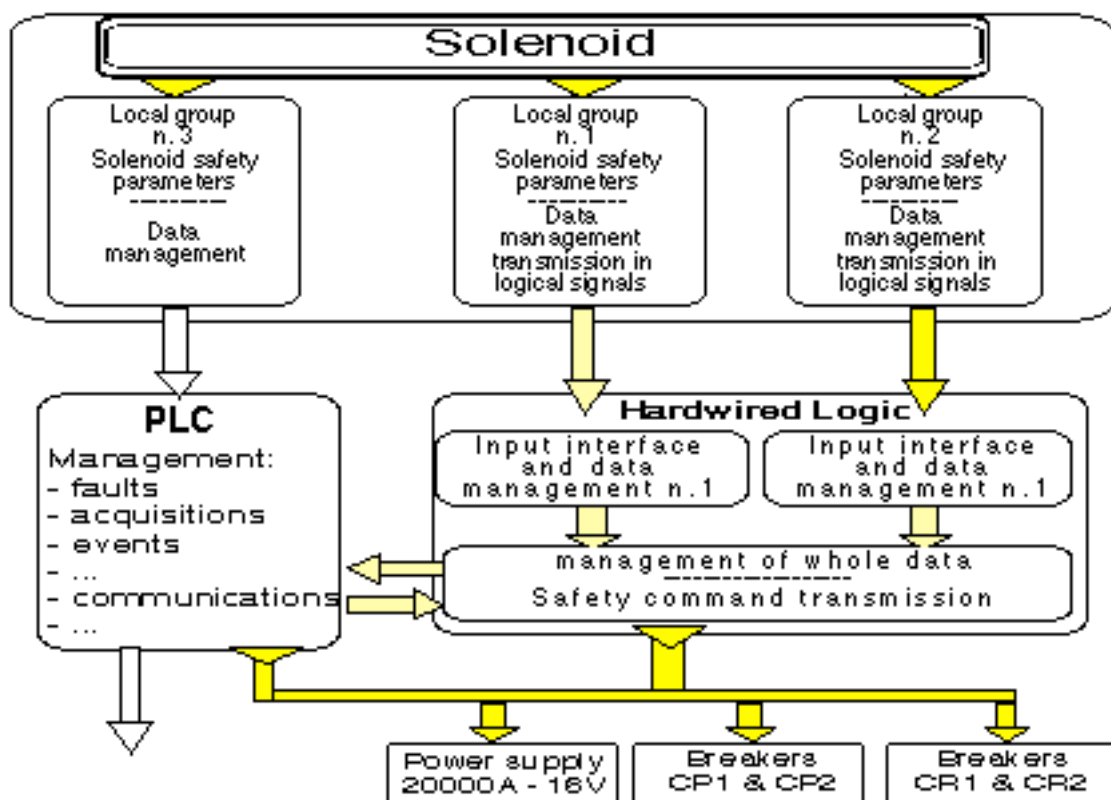


Fig. 22.4: Magnet safety interlocks.

22.5 INTERFACES

A conceptual diagram is shown in Fig. 22.5 summarising the list of interfaces between the systems given in parag. 22.1.

Since XMS is a DCS component, interfacing through DCS is provided with all components of DCS and all control systems interfaced to it. This is achieved via experiment and/or CERN networks.

In some cases, direct links are necessary at the PLC fieldbus level or at the signal level for reliability and/or safety reasons. This is in particular the case for the links with the refrigeration plant which will have to exist at all levels:

- DCS level for general status exchange,
- PLC's level via fieldbus at process control level (warming up or cool down sequences for example in which the external cryogenics takes full control over the proximity cryogenics and the magnet),
- limited direct hardware links for the exchange of vital signals (needed for example in case of fast discharge).

Interfacing through fieldbus requires that External Cryogenic Control System and MCS use compatible PLC and fieldbus systems. This will be achieved by selecting the relevant equipment of MCS within the range of products acceptable to the External Cryogenic Control System.

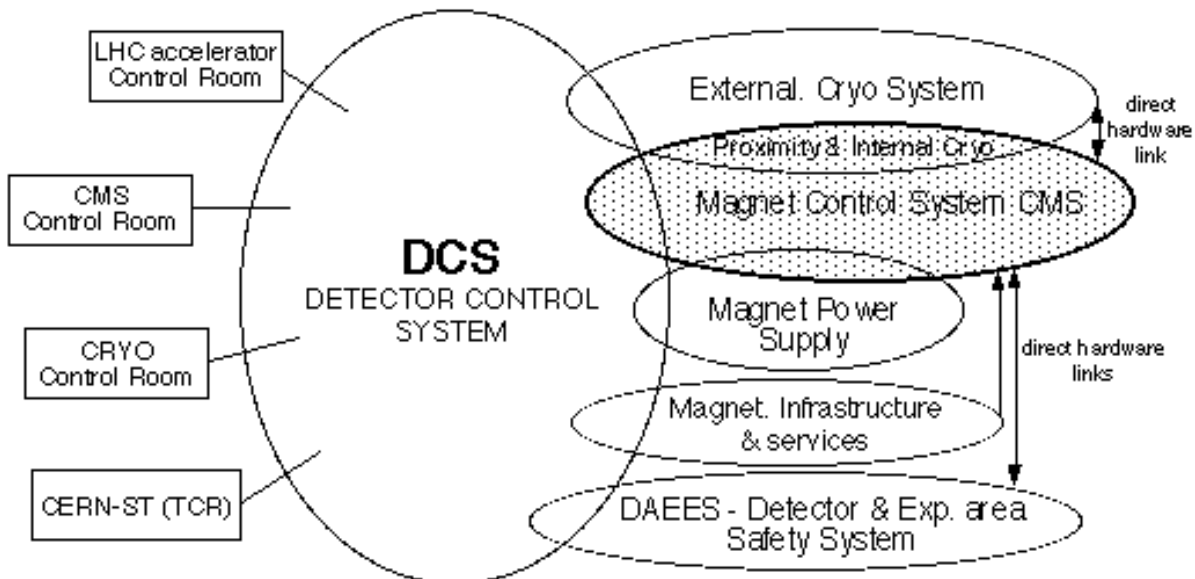


Fig. 22.5: Conceptual Interface Diagram.

23. CONDUCTOR CHARACTERISATION AND PRE-INDUSTRIALISATION

23.1 INTRODUCTION

The interest of the international collaboration for the CMS detector is not only focused to the development of the detector system and subsystems (calorimeter, muon detector, tracking,...) but also to the huge superconducting solenoid, which constitutes the core of the detector itself.

The CMS solenoid project can be considered as going beyond the actual limits of available detector magnet technology. As an example one of the most advanced magnets of this kind is the solenoid constructed more than 10 years ago for the ALEPH experiment at LEP [11-2]. Compared to ALEPH, the CMS solenoid has a field 2.5 times higher, 20% larger bore, 80% longer length and 20 times the stored energy.

To meet this challenging goal and carry out a safe and reliable design, a better knowledge of material properties, cable technology and winding techniques are needed, together with more information on developments of superconducting wires, cable technology and winding techniques. This know-how should be developed at industrial level.

Therefore, intensive R&D programmes were set up in 1993 by the participating institutes, CERN, CEA Saclay, INFN Genova and ETH Zürich.

23.2 MANUFACTURING SAMPLES

As explained in Chapt. 12, in order to build the reinforced conductor from an extruded insert two alternative solutions are considered: the first one using the electron beam welding technique and the second, as a back-up, the soft soldering technique.

Manufacturing lengths of 200 to 300 meters by either method requires the use of an industrial production chain. This chain consists of three play-off drums for the extruded insert and the two reinforcing profiles. Before assembly, each profile has to be straightened, unwarped, and cleaned, then after soldering or EB welding the final conductor must be machined. In both cases large equipment is needed both to pull the conductor and take up the finished lengths. This is shown in Fig. 23.1.

A sample length, 250 m long, with an insert of 70 mm x 10 mm and a 32 strand Rutherford type cable has recently been produced. This enables tooling and production techniques for the pre-industrialisation phase to be developed.

The goal of these activities should be the continuous industrial production of a 200 m long prototype conductor before the end of 1998.

For the prototype lengths a 36 strand Rutherford type cable will be used. Then the high purity aluminium will be extruded around the flat cable by a continuous extrusion process. Two industrial processes are envisaged for this activity: the so-called Conform method, or an aluminium press which is used for the sheathing of electrical power cables and fibre optical cables. Both allow for a continuous process over the full length of the cable. In the Conform process the aluminium is fed into the machine in wire form, while in the Press process ingots of aluminium are used. In both cases the aluminium is fed in from the top of the machine and the Rutherford cable inserted horizontally along a straight line [23-6].

To define the extrusion tools, on-line tests are necessary. These tests will be carried out using superconducting cable, because the mechanical behaviour of superconducting flat cable

is essentially different from flat cable made of hard copper wires. For these trials we will use low purity aluminium (Al-99.7%) for cost reasons. The final extrusion tests will be done with high purity aluminium Al-99.998% and with the Rutherford type cable.

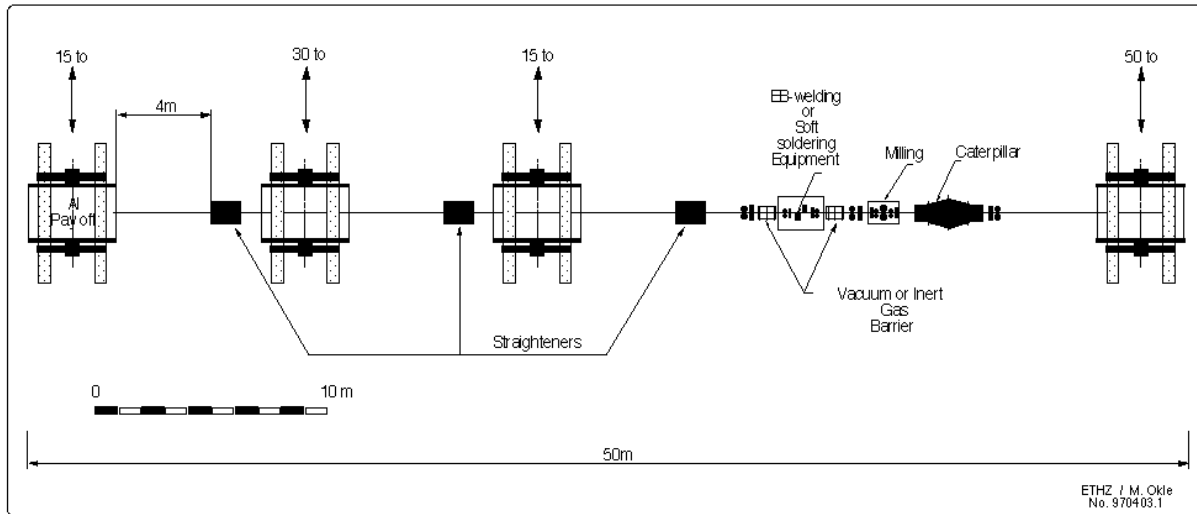


Fig. 23.1: Process line for the final CMS conductor manufacturing.

23.3 TESTS AND MEASUREMENTS TO ENSURE CONDUCTOR QUALITY

These tests are to enable us to understand and qualify all of the conductor production steps in order to optimise the manufacturing process. Some of these tests will be used later, during the manufacturing process to check that the production conforms to the specification.

23.3.1 SC strands

Controls and tests will be in accordance with the Quality Assurance Plan of the companies and they will include chemical analysis of source materials, eddy current measurements on the whole length of the finished wire, continuous checks of the strand diameter, spot checks of Cu/SC ratio, and measurement of the RRR of the copper matrix, and of the critical current.

23.3.2 Rutherford type cable

Manufacturing a cable with 36 strands of 1.28 mm diameter and a length of up to 12 km is a challenging task. Three main problems are seen:

- the critical current degradation at the cable edges,
- the conductor dimensional stability,
- the wearing of the cabling tools.

It is important that during the pre-industrialisation phase a specific R&D programme is planned in order to understand how to optimise the manufacturing process. For example, the compacting of the cable must be made as tight as possible in order to reduce voids inside the cable, but on the other hand it must not induce a critical current degradation exceeding 5%.

To control the cable quality, checks on broken filaments will be carried out on short samples taken from the beginning and the end of the cable. Critical current measurements on single strands extracted from the beginning and the end of the cable will ascertain that the degradation is within the tolerances. During the manufacturing process on-line dimensional measurements will be performed.

23.3.3 Mechanical bonding at the SC cable/Al interface

After extrusion, 250 mm long short samples destined for tensile tests will be cut from the extruded conductor to measure the bond quality. To prepare the samples, the aluminium is first removed from the flat cable for a length of 25 mm and then the conductor is cut using the wire erosion technique. One elongation sensor is attached to the superconducting cable and the second one to the aluminium surface. The distance of the two heads is 20 mm, i.e. an elongation of 0.2 mm under load is equivalent to a 1% strain. The tooling for bond measurements is shown in Fig. 23.2. According to the results of the mechanical analysis, and applying a safety factor of 1.5, the measured bonding strength must always be higher than 30 MPa.

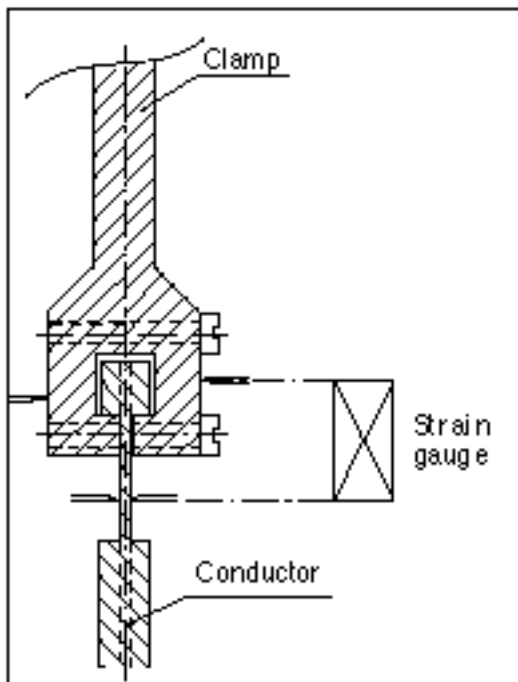


Fig. 23.2: Tooling for mechanical bond measurements.

23.3.4 Bending tests

Bending tests will simulate the winding process used to manufacture the coil or the technique used after the extrusion process to collect the conductor on the take-up spool. Therefore, short samples, taken from the beginning and from the end of each conductor production length, will be bent under a press to the proper radii. After straightening, the samples will be tested both by ultrasonic testing and by the mechanical bond test as described above in paragraph 23.3.3.

23.3.5 Macro and micro photography, electrons micro probe analysis

Samples taken out of the extruded cable will be cut and polished for electron micro probe testing. If a diffusion area of 1 to 3 μm thickness can be observed, like the one seen on Fig. 23.3, then the bonding between the aluminium and the copper matrix is of sufficiently high quality.

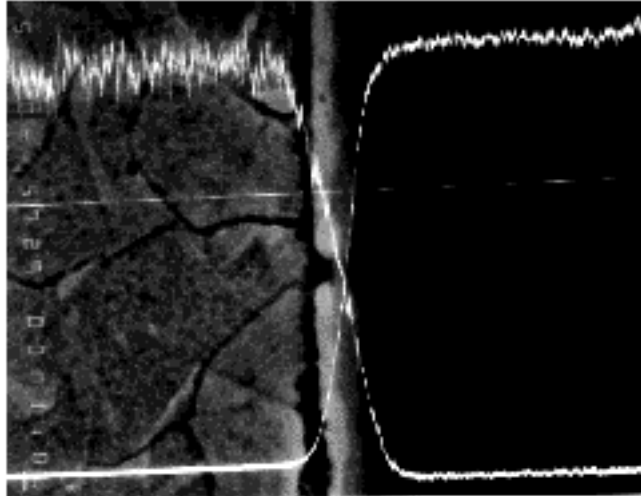


Fig. 23.3: Microphotograph of the conductor cross section. Between the etched copper matrix of the superconductor strands and the aluminium surface of the stabiliser, a diffusion layer of 3 µm thickness can be seen.

23.3.6 Ultrasonic testing

Short samples will be taken from the beginning and end of each production length and prepared for ultrasonic testing. For these tests the pulse-echo ultrasonic method is used. In this method the sensor constitutes the ultrasonic transmitter and receiver. During a short time interval the sensor head transmits US pulses, then during the next interval it receives the echo together with any reflected error echoes.

For the on-line bond measurement a new method, the Phase Array US testing, is proposed. However, before using this method, further R&D work is needed, as described in paragraph 23.4.2.

23.3.7 Measurement of the residual resistivity ratio (RRR)

The residual resistivity ratio (RRR) allows an easy check of the purity of a metal. In general, the RRR is influenced by all the effects that pertain to the electrical resistivity (impurities, defects, mechanical deformations, magnetic fields, etc.). The RRR is defined as the ratio between the room temperature electrical resistivity (or resistance) divided by the 4.2 K electrical resistivity (or resistance). Obviously in superconductors the latter temperature must be increased above the critical temperature.

$$\text{RRR} = \frac{\rho(300\text{K})}{\rho(4.2\text{K})} = \frac{R(300\text{K})}{R(4.2\text{K})}.$$

It is interesting to note that in the case of aluminium and its diluted alloys the temperature coefficient of the resistivity $\frac{d\rho}{dT}$ is constant between 77 K and room temperature [23-1]. This allows an easy correction of the reference temperature which may be also at 273 K instead of 300 K.

Particular precautions are required for RRR measurements of pure aluminium. As an example any heat treatment (soldering) may remove defects and the RRR is changed [23-3]. Mainly for this reason the current contacts are made by screwing the copper blocks to both ends of the sample. Typical dimensions of an Al sample are 4x4x40 mm or 3x3x40 mm.

Voltage taps are fixed with the help of silver paint. Since strain can considerably influence the RRR and its field dependence [23-2], care was taken to ensure a strain free mounting. Only one current contact is fixed to the sample holder while the other one can move freely. The aluminium sample is mounted to ensure that there is no bending strain due to Lorentz forces.

The next step is to measure the electrical resistance at room temperature and zero applied field by ramping the current up to 20 A. The sample is then cooled to 4.2 K and the same measurements carried out with a perpendicularly applied magnetic field between zero and 6 T. After warming up to room temperature the sample resistance is rechecked and compared to the value before cooling.

Typical measurement errors of this method are below $\pm 2\%$. In Fig. 23.4 and Fig. 23.5 RRR measurements of selected 4N8 aluminium samples are shown. The RRR vs. field of the Al stabiliser from two different ATLAS conductors (GEC-ALSTHOM and Europa Metalli) are compared.

23.3.8 Ic measurements on single strands after extrusion

After extrusion, short 2.5 m long samples will be prepared, for critical current measurements. The aluminium around the Rutherford type cable will be removed by etching and single wires extracted out of the flat cable.

The samples will be arranged in one of the allowed configurations for critical current measurement, the critical current being defined according to the resistive criterion (10^{-14} Wm for the NbTi component).

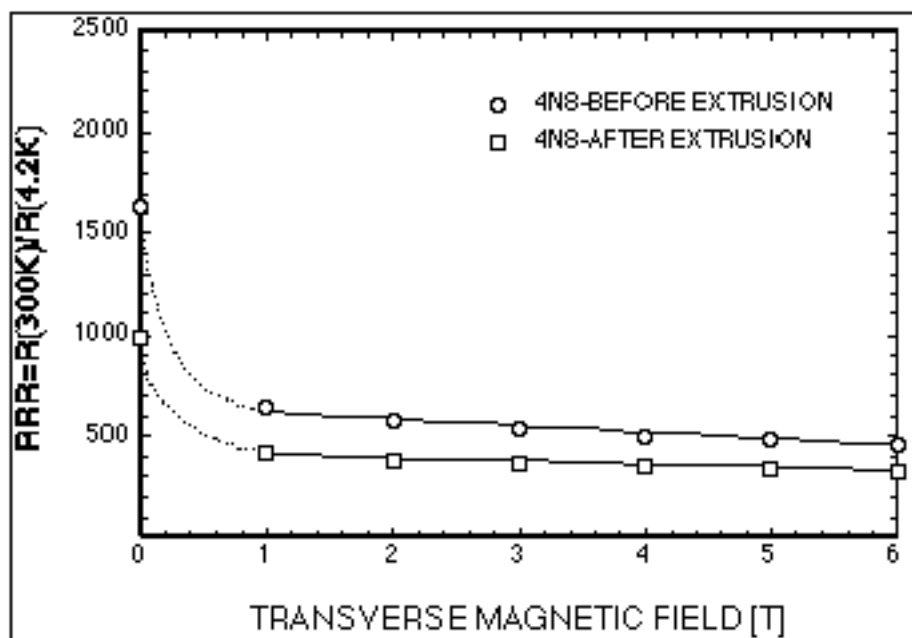


Fig. 23.4: The residual resistivity ratio of 4N8 (99.998%) aluminium vs. transverse applied magnetic field before and after extrusion.

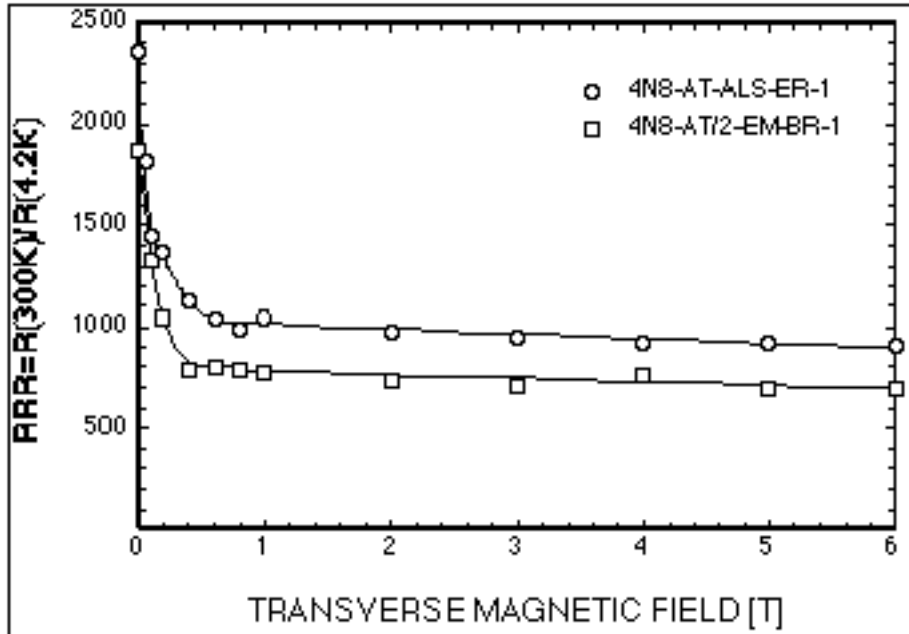


Fig. 23.5: The residual resistivity ratio of 4N8 (99.998%) aluminium stabiliser vs. transverse applied magnetic field from the ATLAS conductor delivered by GEC-ALSTHOM (ALS-ER-1) and Europa Metalli (EM-BR-1).

23.3.9 Ic and MQE measurements on the full conductor

The critical current and the MQE of the conductor will be measured at INFN-Genova using the MA.R.I.S.A. test facility. The critical current measurements will be performed either on the Rutherford cables extracted from the stabilised conductors by alkaline etching, or directly on the stabilised conductor (without reinforcement).

The measurement set-up is schematised in the Fig. 23.6. It is composed of a superconducting solenoid and cryostat with a double wall insert to separate the magnet helium bath and the experimental zone. The measurements are performed on samples arranged in single turns. The Rutherford type cables are soft soldered to copper rings while the aluminium stabilised conductors are placed into an aluminium alloy cylinder and clamped by conical rings. Due to the solenoidal configuration the stabilised conductors can only be measured with the field applied parallel to its wide face.

The main features of the MA.R.I.S.A. facility are the following:

- Maximum background field (at the sample) 6.5 T
- Free bore 420 mm
- Maximum transport current
- Power supply 10 kA
- Transformer method 70 kA
- Length of sample 1.3 m
- Sample temperature range 2 to 300K

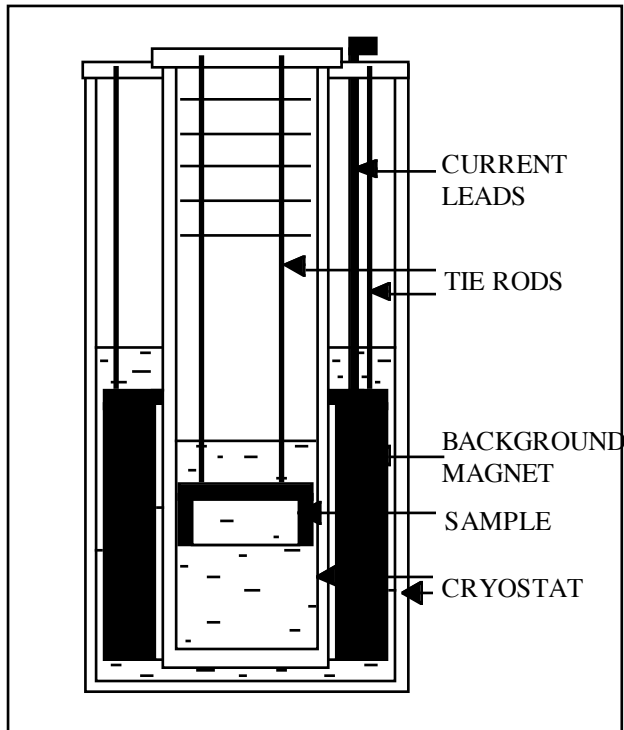


Fig. 23.6: Schematic view of the MA.RI.S.A. test facility.

I_c measurements

The critical current is defined by the resistive criteria $r_c = 10^{-14}$ Wm. The critical magnetic field is defined by the peak field criteria, i.e. the external field plus the maximum value of the self field in the cable. The critical current will be measured at $T = 4.2$ K as a function of the critical magnetic field.

The critical current measurements will be performed using the direct transformer method: the sample is the secondary winding of a transformer, the primary is the background magnet. The sample is arranged in a loop with a low resistance joint ($R < 2 \cdot 10^{-9}$ W) obtained by soft soldering, and is directly cooled by the helium bath. The transport current is measured via the self field using Hall probes, while the voltage is measured at two voltage taps placed diametrically opposite one another and equidistant from the joint.

The current is induced in the sample by decreasing the background field. When the critical current is reached, the magnet ramp is stopped so that the sample current decays allowing the voltage-current to be measured at a constant background field.

The transformer method can also determine the joint resistance by measuring the current decay when the sample is in the superconducting state.

MQE measurements

The minimum quench energy is measured on a short sample of the insert (Rutherford and pure aluminium) arranged in a single turn loop, with the field applied parallel to the wide face. In this case the sample is indirectly cooled in order to simulate the actual situation inside the magnet. The current is induced as in the critical current measurement. When the nominal current is reached the magnet ramp is stopped so that the measurement is performed at constant field. During the measurement, the sample current decays slowly ($t \gg 500\text{-}1500$ s), because of the joint resistance. A pulse disturbance is given using a heater glued onto the

conductor. The pulse energy is increased step by step until the conductor quenches. The MQE is the minimum energy required to produce the transition of the conductor [23-4].

23.3.10 Final conductor characterisation in the SULTAN test facility

The high field, large bore test facility SULTAN, which was built by EPFL/CRPP/ Switzerland and ENEA/Italy, is primarily devoted to qualification tests of full-size cable-in-conduit conductors. However, the existing capabilities are well adapted to the characterisation of the full-size conductor of the CMS solenoid.

The split coil magnet system SULTAN allows radial access of samples to the 12 Tesla centre region. It is equipped for this purpose with a vertically installed insertion unit permitting sample insertion and removal without warming up the background field coils. This unit also comprises a 100 kA superconducting transformer for supplying current to the sample. In the high field zone a pair of pulsed field coils provide additional AC testing capabilities. The pulsed field is applied perpendicular to the conductor and to the background field. Both the sample and the joints can be tested, in the second case the sample is installed in a higher position to ensure that the joint is in the middle of the high field region.

The main features of the SULTAN facility are listed below:

- Maximum background field	12 T
- Maximum transport current	100 kA
- Length of high field zone	0.6 m
- Critical current criterion	0.1 μ V/cm
- Range of conductor temperature	4.5 - 10 K
- Helium inlet pressure	10 bar
- Range of mass flow rate	0 - 10 g/sec

The cross sectional dimensions of the clamped sample must be smaller than 92 mm x 142 mm.

23.3.11 Further facilities for conductor characterisation in NHMFL

Another possibility to characterise the complete conductor is to use the facilities of NHMFL, in Tallahassee. The high field, high current test facility at NHMFL was developed as part of a joint research effort with Oxford Instruments. The facility is primarily devoted to the qualification tests of full-size cable-in-conduit conductors. It consists of a 13 T, 150 mm bore, split solenoid magnet that is integrated with a structural cryostat and a 250 kN capacity hydraulic test machine. The system has access to the main power supply of the laboratory and is currently configured for transport currents of up to 12 kA in the sample, this is imposed by the size of the vapour-cooled current leads. The main power supplies can be configured for currents up to 80 kA. Critical current as a function of magnetic field and/or strain can be measured in monolithic, cabled and cable-in-conduit conductors. The magnet has a horizontal bore and samples are inserted through a 30 mm by 70 mm radial access slot. The facility is currently being used to verify performance of full scale cable-in-conduit-conductors for the 45 T hybrid magnet that is currently under construction at NHMFL. Some of the test facilities important specifications are given below.

For the 13 T Split Solenoid Superconducting Magnet: the field can be increased to 15 T with insertion of Holium pole pieces. The main characteristics are as follows:

- 150 mm bore,
- 30 x 70 mm fixed gap,

- 4 K operation temperature,
- magnet bore orientation can be varied.

The Structural Cryostat which allows a pulling force to be applied to the conductor has the following characteristics:

- 250 kN capacity hydraulic test machine,
- Sample insertion without warm-up of magnet or cryostat,
- Digital test control and data acquisition.

Although, only 12 kA current leads are presently available, power supplies are available with up to 80 kA and a 10^{-5} ripple.

23.4 RUNNING AND PLANNED R&D ACTIVITIES FOR CONTROL METHODS

23.4.1 RRR measurements under cyclic strain

High purity aluminium used for the stabilisation of superconducting cable achieves very low electrical resistivity at 4.2 K even at high magnetic fields. However, the resistivity is strain dependent, especially with cyclic strain. In aluminium stabilised superconducting magnets a strain induced increase of the resistivity can be observed after only a few charging cycles of the magnet. Measurements on both of the most favoured aluminium purities, 4N and 4N8, are foreseen in collaboration with GAP/University of Geneva and EMPA. In the meantime the low temperature equipment at the University of Geneva is being re-built and improved. Two sets of samples are prepared and ready for measuring [23-5].

23.4.2

Ultrasonic Testing of Aluminium Stabilised High-Current Superconducting Cables

Single Probe Ultrasonic Testing

Modern ultrasonic testing is a well-known non-destructive technique to detect regions of delamination. EMPA's laboratories are involved in projects in Europe (CERN: CMS, ATLAS), in USA (Fermilab D0) and Japan (KEK), and a large variety of aluminium stabilised superconducting cables, in different development and production stages, have been tested.

Short samples were analysed with ultrasonic C-scan imaging applying the pulse-echo immersion technique. Focused ultrasonic probes with nominal frequencies up to 50 MHz were used in conjunction with a high-precision mechanical scanner. The quality of the bonding is controlled by measuring the echo amplitude caused by the interface between the extruded high-purity aluminium and the flat-band-cable or between the aluminium alloy and the high-purity aluminium. Any delaminations are indicated by an enhanced echo amplitude.

Figure 23.16, p. C-49, shows 20 MHz C-scans of two different samples of the Fermilab D0 cable. In the upper sample we perceive the regular structure of the flat-band-cable. The echo amplitude is relatively low: the bonding is homogeneously good. The lower sample, however, reveals enhanced echo amplitudes: the high-purity aluminium is debonded from the flat-band-cable. For comparison, a test-block with flat bottom holes has been imaged.

Electron beam welding has been successfully used to join strips of high-strength aluminium alloy to high-purity aluminium as explained in paragraph 23.5.1. Test samples with different production speeds have been imaged with ultrasound (see Fig. 23.15, p. C-49).

At 1.8 m/mn practically the whole width (40 mm) is welded. At the higher production speed of 6.0 m/mn only half of the profile is joined.

For quality control it is desirable to continuously monitor the bond-quality along the whole cable length (up to 80 km). Mechanical (x-y) scanning of the complete bond-area, however, takes too much time. As a first step we performed a partial bond-test with two fixed 10 MHz point-focused probes. The echo amplitude of 1 mm bond-width was recorded as a function of the position. In this way we have continuously tested 5 km Fermilab D0 cable on both sides. The major part of the cable showed no indications (Fig. 23.7, upper part), however, one section revealed a 0.5 m long delamination (Fig. 23.7, lower part).

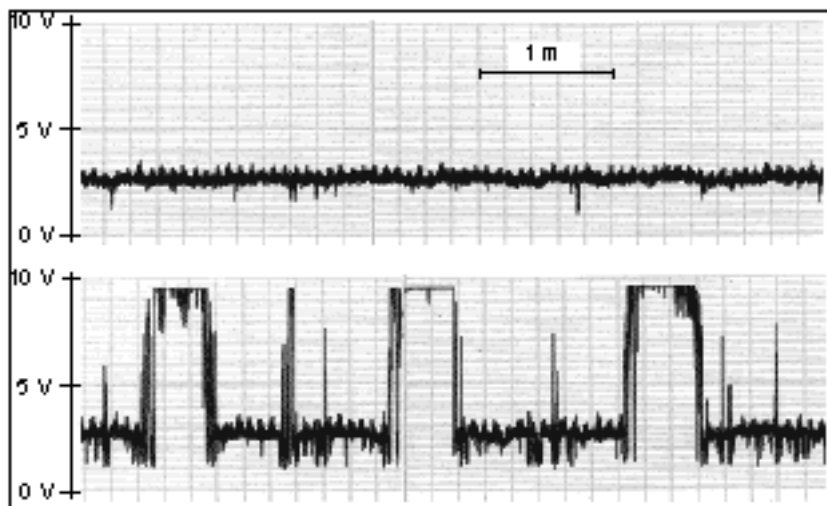


Fig. 23.7: Continuous ultrasonic testing of bond-quality of the Fermilab D0 cable.

Phased Array Ultrasonic Testing System

In May 1996, in collaboration with EMPA, a feasibility study was initiated to design a phased array probe to evaluate the detection of artificial defects in superconducting cables. This ongoing R&D work should enable the quality of the bond between the aluminium and the copper surface of the superconducting strands to be controlled over the whole width and length of the conductor during its manufacture.

In this technique, the sound beam will electronically scan the cable perpendicular to the direction of production. This explains why this method is fast enough to allow a continuous analysis of the complete bond. First phased array results are encouraging.

The phased array technique requires multi-element transducers and sophisticated electronics. Electronic scanning is achieved by successively firing groups of elements. The sound beam moves along the array probe. Since no mechanical motion is involved, very high scanning frequencies are possible (kHz). This should allow a 100% testing of the bond area.

ETH and EMPA in co-operation with the French enterprise NDT Systems S.A., are currently performing a feasibility study. A new 10 MHz linear array probe with 128 elements was designed and manufactured. A large number of test samples are to be investigated with the new probe in conjunction with the appropriate electronics and software. First results on Fermilab D0 samples are encouraging (Fig. 23.17, p. C-49). The flat bottom holes ($\varnothing = 1, 3$ and 5 mm) in the upper sample are easily visible. In the lower, Fermilab D0 test sample disbonded areas (yellow/green/blue) are clearly distinct from the correctly bonded areas (red)

[23-8, 23-9].

23.4.3 Eddy current testing

The eddy current testing is a dry process which would require a shorter time to scan the surface, as the speed could reach 60 m/mn, but it has to be validated on aluminium stabilised superconductors by performing preliminary modelisation tests to determine the limits of the method, and to optimise the sensors. Several sensors must be connected in parallel and perpendicular to the conductor axis. Inner defects influence the mutual inductances and can be detected. A diagnostic of each component of the CMS conductor requires a multi-frequency acquisition. An electromagnetic map of the specimen can be obtained. An example is provided on Fig. 23.18, p. C-50, corresponding to a hole drilled in a ferritic stainless steel sheet. The detection is theoretically easier with aluminium than with steel.

23.5 DEVELOPMENTS FOR FIXING THE REINFORCEMENT

23.5.1 EB welding

The high performance superconducting magnets used in the large detectors for High Energy Physics, such as the CMS detector at LHC and the magnets of magnetic storage devices (SMES) have mechanical stresses on the conductor which go beyond the yield stress level of the high purity matrix stabiliser, especially when aluminium is used and mechanical reinforcement must be added to the conductor, as explained in Chapt. 11. A novel method has been studied to join high strength aluminium strips to a high purity aluminium stabiliser by using electron beam (EB) welding. EB welding, combined with roll-pressing under vacuum, provides minimum heat input on the conductor in comparison with other welding techniques. For example a temperature of 160°C has been measured at a distance of 5 mm from the weld. This method allows very long conductor lengths to be produced and repaired without loosing expensive material.

As this process has to be adapted to the high purity aluminium on the one side and to the high strength material on the other we did tests on the improved EB welding machine at CERN, in collaboration with CERN and with PTR Präzisionstechnik GmbH, the EB welding machine manufacturer.

Within this R&D programme the following aluminium alloys have been tested: AA-5083, AA-6082, AA-7020. The next step will be to test the high strength material AA-2219 together with the insert, recently produced for the CMS pre-industrialisation programme. The schematic view of the EB welding system is shown in Fig. 23.8, [23-7, 23-10].

As was shown by finite element computations (see Chapt. 14), the reinforcement has to be attached to the stabiliser by a metallic bond. To control the quality of the EB weld, cylinders of 10 mm diameter were prepared using the wire erosion technique. Test samples, to measure the shear strength, were taken at the root area, from the beam inlet, and half way down. Two samples extracted from a similar area were always tested together using an adequate shear stress measuring device. These tests have shown that the average value for two comparable samples lies between 63 and 86 MPa. This is quite high for aluminium for which some porosity of the weldment has always to be considered. On-line control of the EB welding can be carried out using the phased array technique as described in paragraph 23.4.2.

An other task to be undertaken is the adaptation of industrially used vacuum gates to the cross section of the CMS conductor. Because the electron beam requires a vacuum higher

than 10^{-4} mb, the atmospheric air pressure has to be reduced step by step to this level. For the continuous welding process it is foreseen to provide graded vacuum gates at the inlet and at the outlet of the vacuum chamber. The main problems to be solved are the form and the wearing out of the sealing of the gates during the continuous manufacturing process.

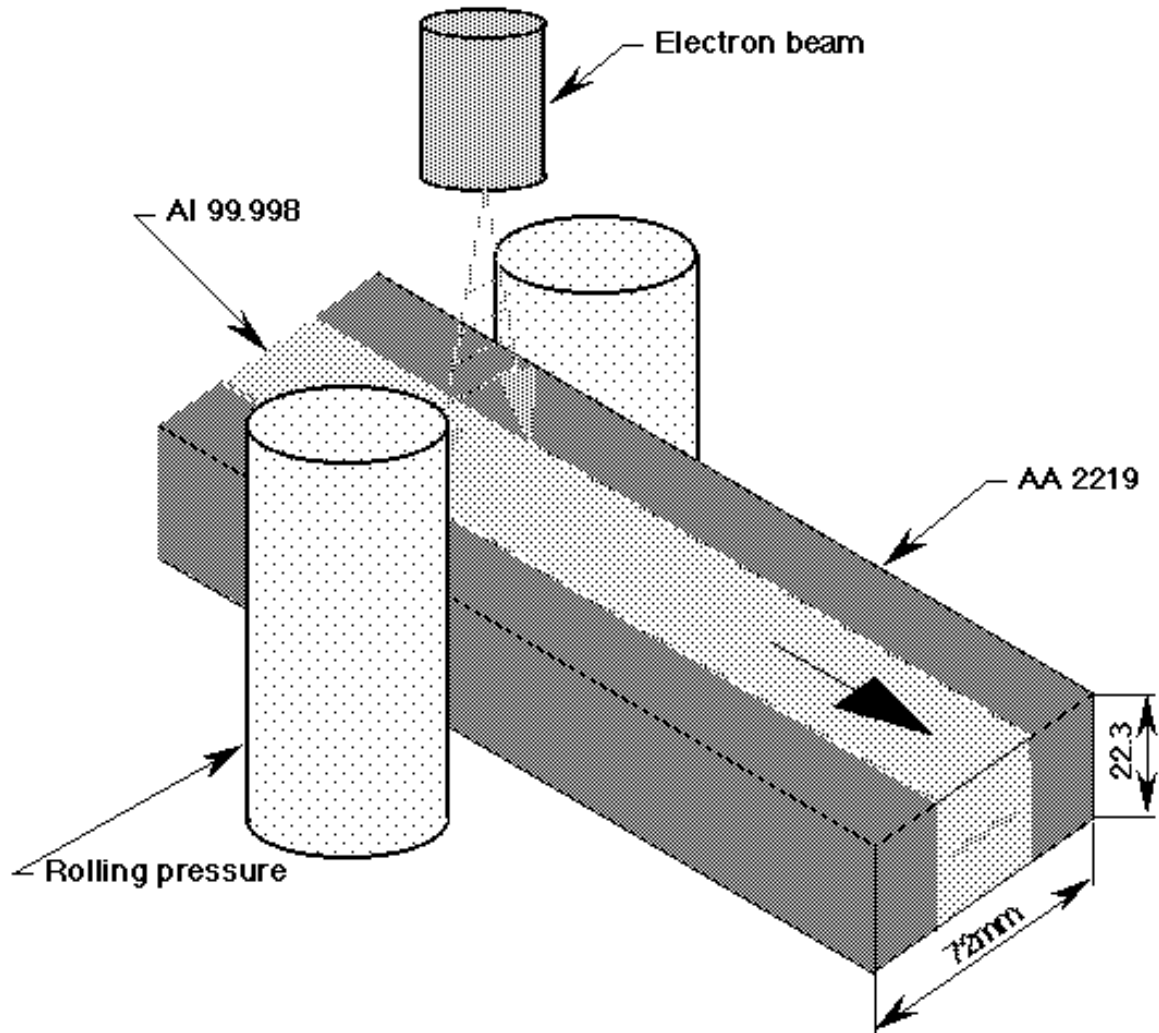


Fig. 23.8: Scheme of the Electron Beam Welding System.

23.5.2 Continuous soft soldering of aluminium

The continuous soft soldering process is an alternative method, providing a back-up for the EB welding solution as described in the Chapt. 23.5.1. In addition, as this technique is readily available for low speed production, it can be used early on with a minimum of investment to produce the 200 m long lengths of conductor which will allow us to start the winding tests with a mechanically representative conductor.

Soft soldering tests have been carried out using cream solder or soldering sheets with flux at Saclay, the bonding tests on aluminium alloy have shown good mechanical properties, in particular shear stress > 45 MPa at 77 K [23-18, 23-19, 23-20]. These characteristics could be improved by soldering in a bath which would limit the amount of bubbles due to the flux being trapped when pressing the components together.

Conductor test assemblies will be undertaken to check the improvement [23-21]. The continuous soldering principle is shown on the Fig. 23.9: the method retained is based on the assembly of the components in the vertical position to ease evacuation of the bubbles trapped between the components.

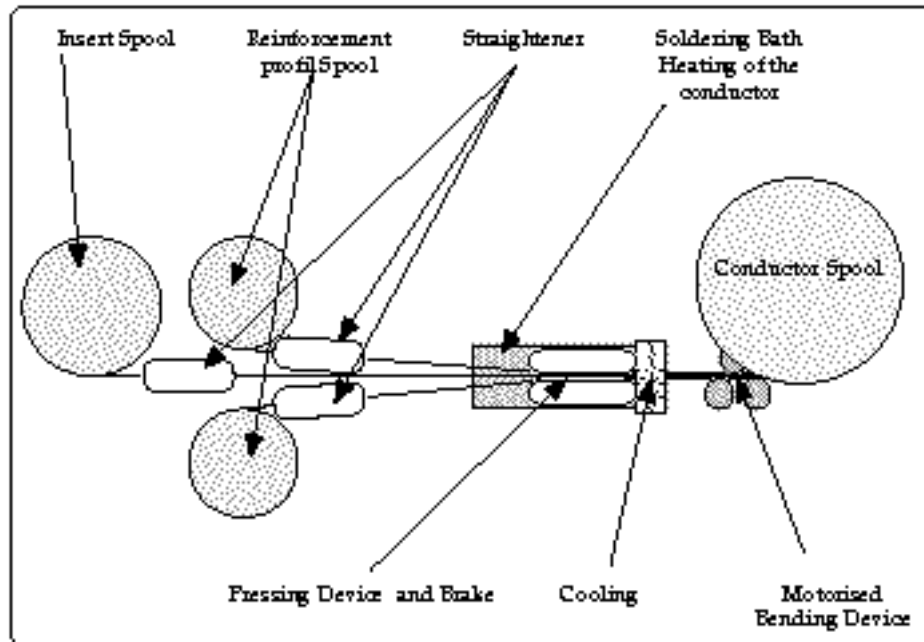


Fig. 23.9: Continuous soldering principle.

The conductor components are inserted inside a gutter, closed on one side by a slotted flange allowing the components to pass with a flow of solder between them. The other side is closed by a one slot flange permitting the conductor to exit. A pump compensates the leaks by transferring solder from a lower tank where it is maintained at the melting temperature by an oil heating system.

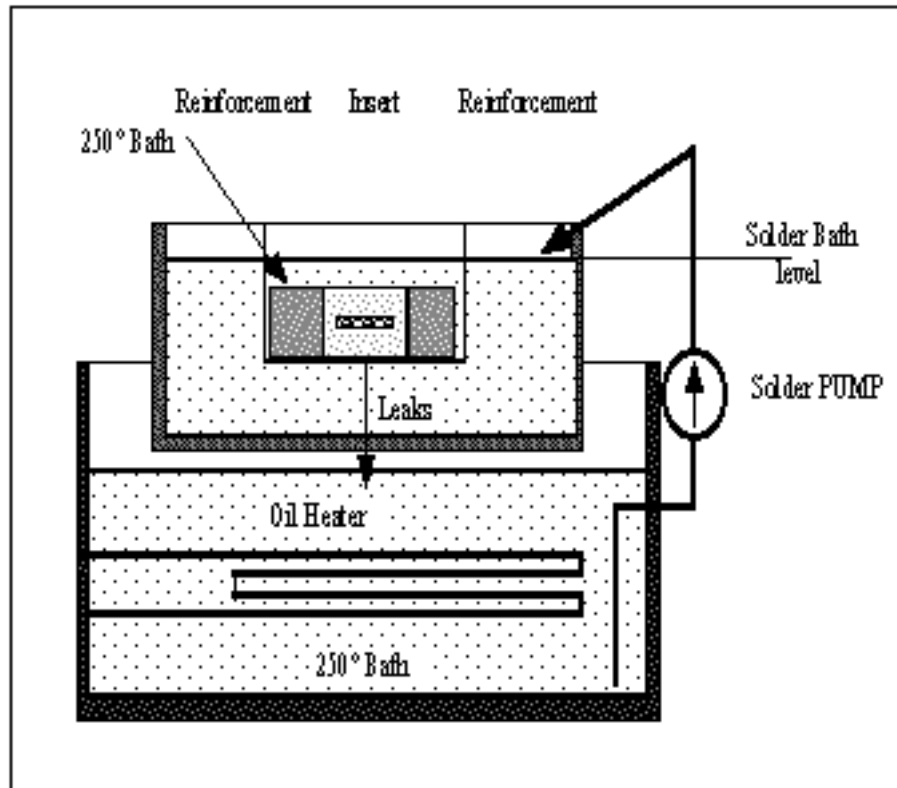


Fig. 23.10: Bath principle component side.

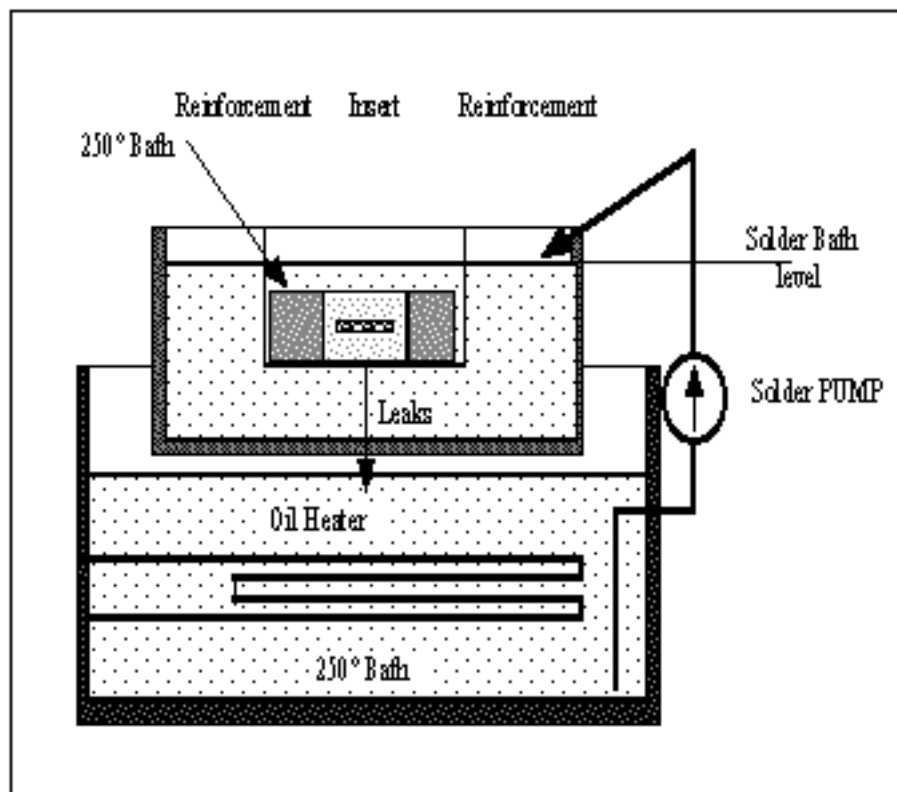


Fig. 23.11: Bath principle assembled conductor side.

The components are heated in the gutter by the solder to the proper soldering

temperature. Then the components are pressed together in the bath and cooled down after leaving the gutter.

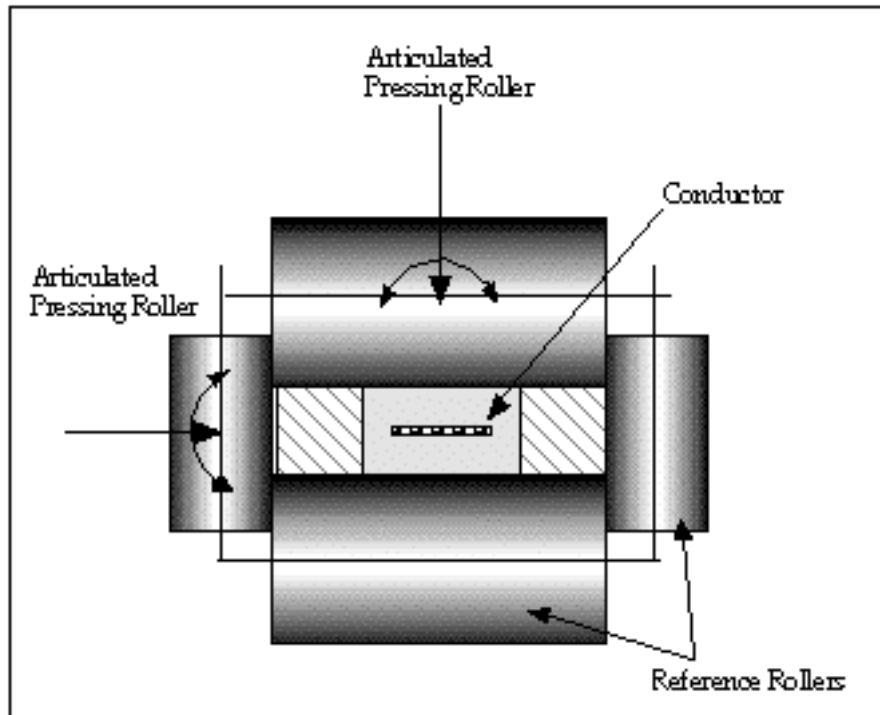


Fig. 23.12: Pressing system in the soldering Bath.

For the final production, the vertical roller system described above can be replaced by a caterpillar equipped with a brake.

The conductor is then spooled and the machining of the final cross section is carried out in another manufacturing line.

23.6 JOINTS

23.6.1 Joining the insert

As said in chapter 12, the extrusion process will be carried out, starting from a 12 km Rutherford cable, until the extrusion process must be interrupted for any reason. If long enough, say more than 2 km, this length will be accepted as a production length. The lengths of insert will be joined together on the CERN site to provide the 12 km long insert required to wind one layer, before adding the reinforcement. Thus CMS requires long unit lengths of insert, to limit the number of joints inside a layer, however, no strict value will be imposed for the definition of a unit length, but the permissible number of joints will be limited.

Clearly these joints cannot be cooled locally by a liquid helium heat exchanger. The joining process must thus be fully qualified in order to produce reliable joints of high quality, especially offering an electrical resistance lower than 10^{-9} W.

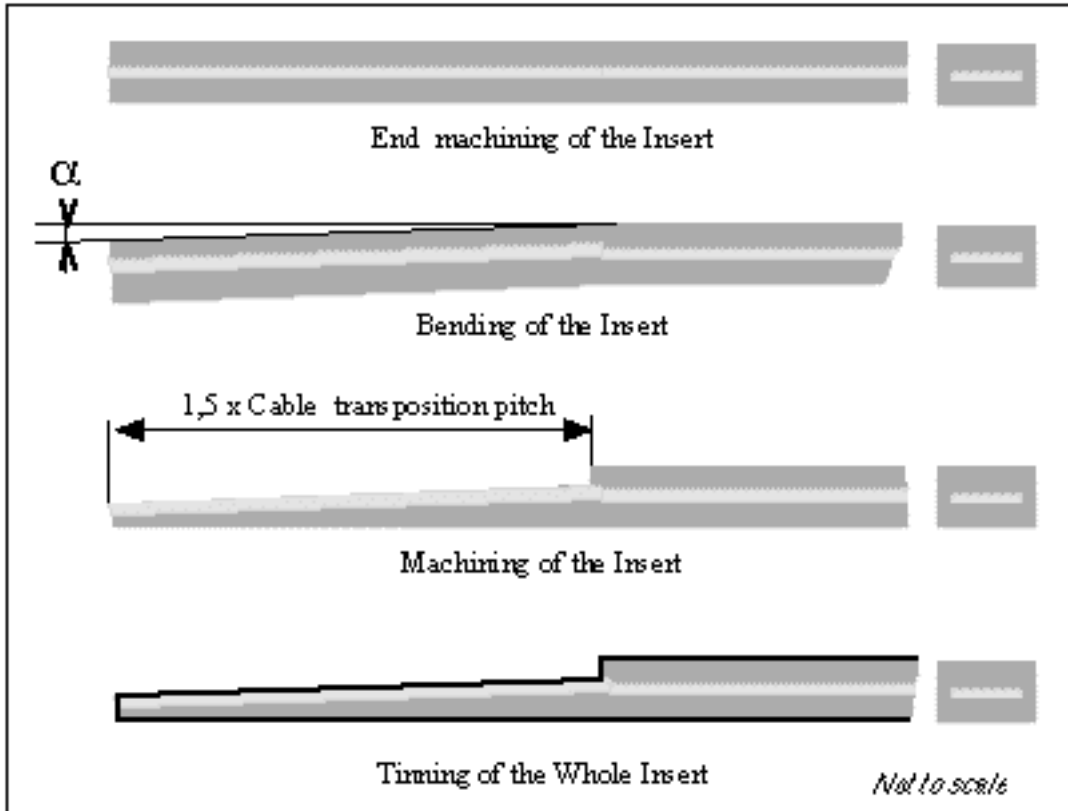


Fig. 23.13: Machining and tinning of an insert end to prepare for a joint. An alternative way is to leave 5 mm of pure aluminium over the insert and use EB welding.

The two insert ends will be prepared by bending and machining like shown in Fig. 23.13 to expose the two Rutherford cable which can then be tinned and soft soldered together in a conventional way. Although first temperature measurements are encouraging, a soft solder with a sufficiently high melting point must be used to support later the addition of the reinforcement by EB welding (see Fig. 23.14).

One will take advantage of the large width of the aluminium insert, i.e. 22.3 mm, and of the presence on site of a dedicated EB welding equipment, to develop a joining method using the EB technique. In this case, after bending, the machining will leave 5 mm of pure aluminium over the Rutherford cable and the joint will be done by EB welding the two inserts through the pure aluminium. First temperature measurements indicate that a distance of 5 mm from the weld is sufficient to protect the superconductor against overheating during EB welding. This method would provide a metallic joint which could be tested by non destructive methods to ascertain the joint quality.

A development program will follow the first production of real insert to fully qualify the joints, and the joining process. Both methods will be developed in parallel.

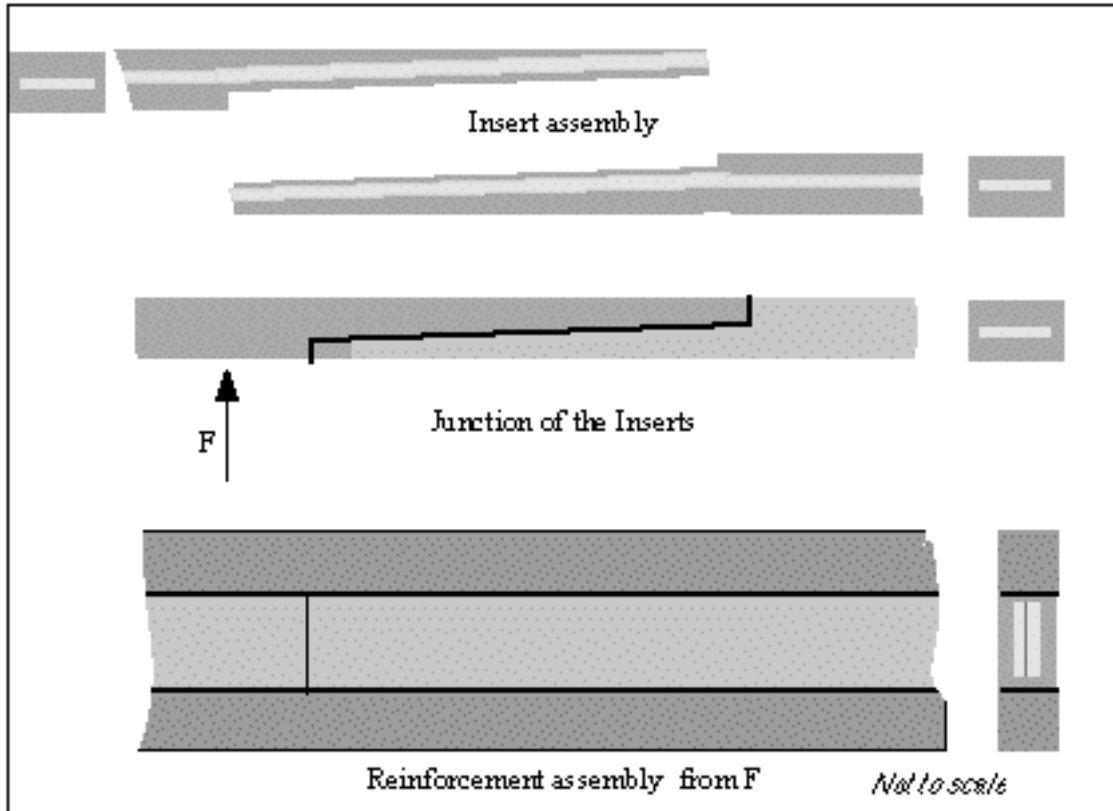


Fig. 23.14: Position of the joint with respect to the reinforcement.

23.6.2 Joining the reinforced conductor

This case must also be developed in order to repair lengths of reinforced conductor which may be damaged by accident.

Due to the presence of the reinforcement, joints on the finished conductor are more complex for the CMS conductor than for other aluminium stabilised conductor.

One possible method to join the conductor consists of welding the aluminium alloy reinforcement, and soft-soldering the insert. As the insert cannot support the welding temperature, if a welding method like TIG is used, it will be locally removed on a sufficient length, and be re-introduced as a segment, between the butt welded external sections. As a consequence, each conductor joint would actually include two electrical joints.

However, here again, advantage can be taken of the presence of an EB welding equipment on site, to develop a joining method for the reinforced conductor based entirely on the use of EB welding.

23.7 PRE-INDUSTRIALISATION

The pre-industrialisation program can be divided into 3 main stages:

- 1) Production of laboratory short samples to show the feasibility of the “block” conductor and prepare the tooling (activity 1).
- 2) Proceed toward continuous process engineering (before mid ‘98) and have all the elements to confirm the final choice (EBW or SS reinforcement fixation) and make the call for tender (activity 2, 3, 4).
- 3) Industrial production phase (end ‘98 beginning ‘99). At this stage the required

investment is not negligible so that any tooling has to be foreseen in the optics of the final production (from activity 5 onward).

Table 23.1 resumes the main activities of the pre-industrialisation program [23-22].

To have a complete view of the pre-industrialisation activities for the coil, this table must be interfaced with Table 24.1, which concerns the winding test, as all the produced lengths of conductor will be used, in the best possible way, to perform winding tests.

Table 23.1

Synthetic table of the pre-industrialisation activities foreseen for the conductor.

	Activity	Time Scheduled	Institut e	Goal	Actions to be taken
1	Produce 200 m of Rutherford type cable with 36 strands for the “block” insert	July 97	ETH	To make 200 m of block type extruded insert	ETH/CERN
2	Extrude all the available cable in the form of “block” type insert	August 97	ETH	Have a real insert to perform short length samples of conductor	ETH
3	Make different short length samples of conductor with Soft Soldering and EBW	End of August 97	ETH/ Saclay	Qualify the fixation process at “laboratory” level	ETH SACLAY CERN
4	Organise, if needed, the extrusion of the block insert with the final Rutherford	End 97	ETH	Have an up to date insert to perform tests (winding and conductor)	ETH CERN SACLAY

5	Produce 250 m (or more) of final conductor with laboratory Soft Soldering line	June '98	Saclay	Prepare a significant length to feed the first set of "winding" test	Organise tendering and delivery of straightening devices, spooling, caterpillar etc. (CERN)
6	Design and construction of vacuum gates for continuous EBW Engineering of the continuous EBW line	Feb. '98	ETH	Qualify the continuous EBW process and continuous testing	Procurement of vacuum gates and design of the EBW line (ETH)
7	Engineering of the continuous industrial Soft Soldering line	July '98	Saclay	Qualify the continuous Soft Soldering process and continuous testing	Design the final continuous Soft Soldering tooling (Saclay)

Choose the fixing technology					
8	Produce 1 (or 2) km of extruded insert with final cable	Sept. 98	ETH/ Saclay	Have an insert for the final assembly technique Have a final conductor for representative winding test	Buy the cable and tooling (ETH) Organise extrusion (ETH)

At this stage the call for tender can be launched (autumn '98 by ETH).

9	Produce 2 km of final conductor (first stage after tender)	April '99	ETH	Test the final industrial production process and go towards a significant winding test	Define final tooling (ETH/Saclay) Call for tender (around Oct. 98) (ETH)
---	--	-----------	-----	--	---

24.**PRE-INDUSTRIALISATION OF THE WINDING AND POLYMERISATION TECHNIQUES****24.1 INTRODUCTION**

This chapter discusses the tests which are foreseen to ascertain both the winding and the curing techniques.

These tests will be performed in collaboration with competent industrial firms who are familiar with the retained winding process. This should allow us to profit of an industrial assessment, allowing to adjust at an early stage, the final definition of the winding process.

The program is divided into different activities each one aiming to verify a particular aspect of the winding operation, such as; bending, insulation behaviour, curing, etc.

An important aspect of these winding tests is that they need to be carried out using significant lengths of the final conductor. These lengths will be manufactured following the conductor pre-industrialisation program as described in Chapt. 23 [23-22]. However, in order to allow an early start to the winding tests, “dummy conductors” made on a case by case basis will be used at first.

24.2 MAIN ACTIVITIES

The whole program is organised around five lines of development.

- Bending and stacking tests on bare conductor;
to test the different winding techniques, determine the cross section deformation of the conductor and the forces to be applied during the winding process.
- Bending and stacking tests on insulated conductor;
to understand the problems related to the insulation, (i.e. maximum pressure to be applied without damaging the insulation), the flow of the impregnation under pressure before curing, and to produce test stacks to measure moduli.
- Characterisation of the insulation;
to characterise the properties of the insulation using the test stacks obtained from the previous activities, and to perform mechanical, electrical and thermal tests.
- Quench back cylinder, winding and welding tests;
to qualify the assembly process of the quench back cylinder and check that the maximum welding temperature behind this cylinder corresponds to the computed estimations.
- Winding a short length model of the solenoid;
to validate the winding and curing process in order to finalise the specification of the winding machine.

Table 24.1 resumes the main activities of the pre-industrialisation program [24-1].

24.3 BENDING

These tests will be done to evaluate and to compare three different bending methods. By measuring the required forces and the cross section deformation the most simple and reliable bending process can be chosen.

The three techniques to be explored are the following:

- 1) bending by directly pulling the conductor while winding it over a mandrel,
- 2) bending using the same method as above, but in addition applying a radial force,
- 3) pre-bending the conductor by passing it through a roller box and then winding it over a mandrel under slight traction.

The preliminary tests will use a simple dummy conductor composed of a pure aluminium insert surrounded by two aluminium alloy sections.

All these tests will be carried out by bending short lengths of the dummy conductor to a radius of 3000 mm and a sector of between 30° and 45°.

The main implication coming from these three choices is the sequencing of the conductor insulation. In the first two cases the insulating tape must be wrapped over the conductor before bending, consequently it has to withstand the forces generated by the bending process. In the third case the conductor is bent before being insulated therefore allowing the cross section to be corrected to the final shape before applying the insulation.

The third method is preferred because it imposes less stringent requirements on the insulation, however it is important to determine if sufficient space can be made available for the installation of the insulation unit which must sit between the bending device and the mandrel.

Stacking of the bare conductors

The first study to be performed, will be to check that the spooling, de-spooling and straightening operations have no adverse effects on the cross section of the conductor. Then short lengths of conductor will be prepared and machined.

The lengths will be cut into short segments and stacked to measure the overall Young's modulus at several points. These measurement will be used to estimate what axial pressure has to be maintained on the conductor during the winding process in order to ensure the correct parallelism of the turns, and therefore the proper filling factor for the final coil. They will also provide a reference for the next series of tests destined to estimate the final thickness of the insulation after curing.

Bending and stacking tests of the insulated conductor

The object here is to test the inter turn and inter layer insulation behaviour during the winding operation. The principle of the test is shown on Fig. 24.1.

These tests will be performed on a stack of bent segments of insulated conductor to determine the volume contraction of the insulation under pressure, both before and during curing. The bending will be done using the third method mentioned above, as it is the simplest method to bend the required length of conductor without a mandrel.

Two models will be built using different insulating materials. They will consist of a stack of ten conductor segments, one meter long, obtained from the bending tests mentioned above. As the final insulation will not be available at this time, the insulation material will be simulated by a B-stage material and semi-wet insulation using glass cloth obtained from DELPHI [24-2], or by using glass cloth over Upilex® or Kapton® material as is currently used at KEK [24-3].

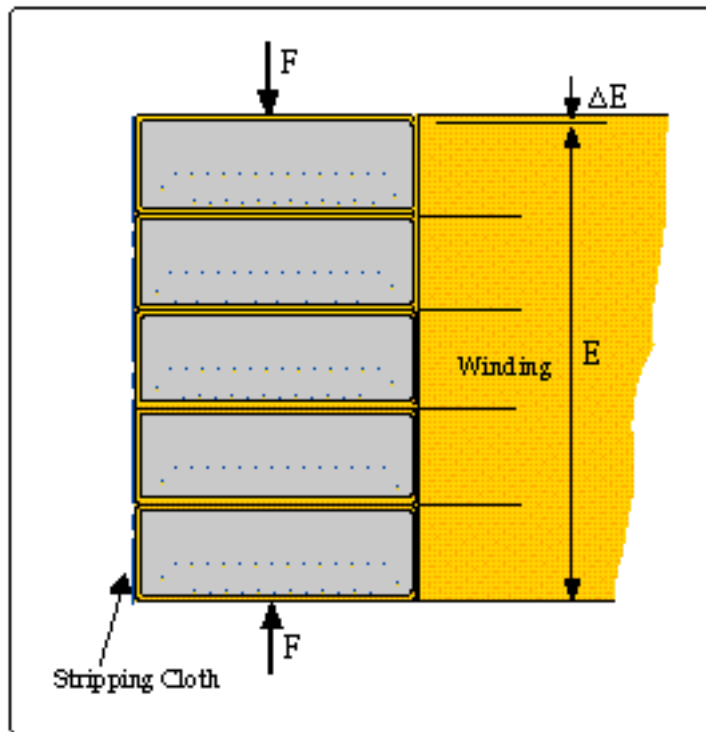


Fig. 24.1: Stacking measurement on insulated conductor.

After completing the test stacks, an axial pressure will be applied during the curing process with the aim of getting a uniform inter-turn insulation thickness.

Measurements will be done on each model, before and after curing to estimate:

- the release of resin from the semi wet prepreg insulation,
- the flow curves of the insulation under constant pressure,
- the filling factor.

Understanding how the resin is released from the insulation is very important for the winding process, as this will determine how the last turns will creep and settle. The insulation thickness can then be measured to determine its accuracy.

During all the tests extensive measurements will also be performed to understand :

- the residual conductor twist deformation,
- the conductor cross section deformation,
- the straightness and influence of spooling and de-spooling,
- the forces required to straighten the conductor,
- the spring back effect, if any.

24.4 CHARACTERISATION OF THE INSULATION

The filling factor of the winding will be estimated after the curing of these layers. The axial elastic modulus will then be measured.

The outer surface of the cured layer will be verified in terms of adherence to the next layer.

The inter-layer insulation will be placed on the outside of the stack. Then, in order to obtain a good contact with the turns, the pulling force or pressure to be applied to the

insulation will be measured. The release of resin from the inter-layer insulation will be checked to verify if any extra resin must be added during this process. The stripping cloth material will then be placed on the outside of the inter-layer insulation.

To obtain a complete knowledge of the insulation behaviour, different curing techniques will be tested on several samples. The curing operation will always be carried out with the axial pressure applied and the dimensional changes will be recorded during the whole process.

The insulation will be fully analysed by cutting the stacks after curing. The mechanical, electrical and thermal characteristics will be measured at room and cryogenic temperatures.

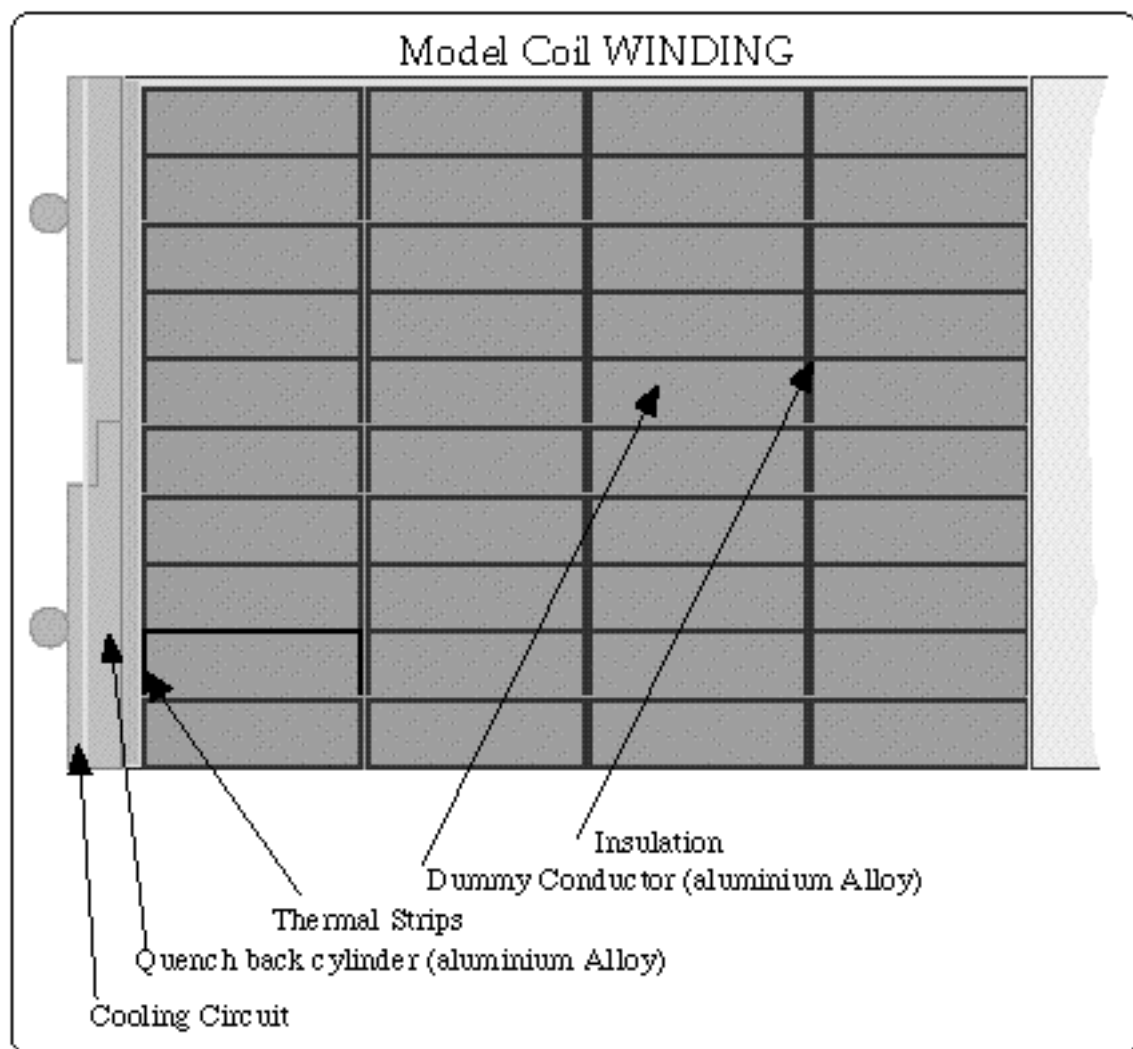


Fig. 24.2: Full diameter short model coil

24.5 QUENCH BACK CYLINDER WINDING AND WELDING TESTS

To qualify the techniques selected for constructing the quench back cylinder, a half scale model will be made on a 2 m long wooden support. This model will contain instruments to verify the maximum temperature reached during the assembly process. Mechanical tests will then be performed to measure the effectiveness of the welding process.

24.6 FULL DIAMETER SHORT WINDING MODEL

When the conclusions of the previous tests have been made and the winding technique finalised, a short length solenoid (10 turns and 4 layers) will be wound. No joints or inter-layer connections will be simulated but the final insulation material and the selected curing process will be used. All the components of the solenoid will be assembled: the four layers, the inter layer insulation, the thermal strips, the quench back cylinder, and the cooling circuits. Each layer will be cured upon completion, and the final curing will be performed after the installation of the heat exchangers, as shown in Fig. 24.2.

The following tests will be undertaken on sections cut from the short model:

- electrical, mechanical and thermal tests,
- estimation of the filling factor,
- bonding tests before and after cooling down,
- destructive testing.

24.7 SOLENOID WINDING PROTOTYPE

At the end of the pre-industrialisation program, the technical specification of the winding machine will be finalised and the call for tender launched. This machine will then be used to build a short length (1.5 m) winding prototype of the solenoid, complete with electrical connections between the layers and conductor joints inside the layer.

This prototype will be used to control the manufacturing process step by step in order to qualify the complete construction process of the coil, and to commission the winding machine and the solenoid components. The prototype will then be examined and tested but not energised. Destructive tests will be performed to measure the bonding quality and the mechanical properties of the structural material. Only after all these tests, have been successfully performed, will the winding of the CMS solenoid proceed.

Table 24.1
 Synthetic table of the pre-industrialisation activities foreseen for the winding
 and polymerisation technique.

	Test	Goals	Implication	Schedule
1	Winding technique assessment 1. Winding by pulling the conductor around the mandrel 2. Same as above + radial force 3. Pre-bending and winding	Define winding tension Assess: <ul style="list-style-type: none"> • twisting • spring back effect • deformation of the cross section • superconducting performance degradation • elastic energy stored in the winding and, if, how to minimise it. 	Define winding procedure and implement spec. for winding machine For technique 3: <ul style="list-style-type: none"> • define pre-bending radius • assess shear forces between layers due to layer shrinking after removal of the mandrel. 	Sept. '97
2	Stacking test <ul style="list-style-type: none"> • using short (2.5 m) length of straight, bare, dummy conductor • using short (2.5 m) length of insulated dummy or real conductor. 	Understand the behaviour of the conductor in the stacking operation. Begin to evaluate part of the axial mechanical characteristics of the winding.	Have stacking references Define first winding instructions and specs for axial pressure jigs	Oct. '97
3	Straightening test of separate components and assembled conductor with dummy profile or short (2.5 m) samples.	Quantify cold work in the different operations Check bonding behaviour at interfaces	Definition of the straightening jigs	Nov. '97 Depending on the tooling available from industry
4	Machining of conductor <ul style="list-style-type: none"> - before bending - after bending - both with dummy and real conductor. 	Define appropriate cross section Optimise the way of machining the profile	Define the tooling to rectify the cross section	End '97
5	Insulation/Curing on short samples	Understand the behaviour of the insulation and how the resin flows out.	Qualification of the process	End '97

6	Cool down using the insulated short samples of 2.5 m	Assess possible problems during cooling down and steady state at 4.2K		March '98
7	Welding technique of the quench back cylinder Short samples welded with TIG, EB, Laser	<ul style="list-style-type: none"> To find the technique which needs the lowest heat input Measure the maximum temperature reached behind the aluminium profile 	Qualify the quench back welding process	End '98
8	Short model at full diameter 4 layers, 10 turns <ul style="list-style-type: none"> with 100/200 m of insulated final conductor with the selected bending technique with the qualified insulating process with the qualified curing process 	Assessment of: <ul style="list-style-type: none"> friction wear behaviour of glass before curing measure filling factor before and after curing 	Finalise and qualify the whole winding technique	June' 98
Writing of winding and winding machine specification and launch the call for tender: End '98				
9	Winding prototype 1 m long, full diameter winding	Global winding assessment	Commissioning of the winding machine	First half 2000

25. EXPERIMENTAL AREA

25.1 INTRODUCTION

When considering the experimental area for the CMS detector, the main constraints are given by the construction and the installation of the magnet and the necessity of providing adequate and safe working conditions during the fabrication, assembly and installation periods. Great effort has been made to balance the necessity and the convenience of a large experimental hall with the overall cost and with the basic limitations set by the LHC machine elements as well as the already existing LEP installations.

The design of CMS is based on a large superconducting solenoid surrounded by an iron muon spectrometer. The 4 T field of the solenoid acts directly on the steel disks, which form the forward part of the iron yoke, thus creating a large magnetic pressure. To resist this force, only assembly based on 600 mm thick plates has been found to provide a satisfactory solution. The design of the barrel yoke consists of three layers built up of steel plates. The thickness of the inner layer is 295 mm, the middle and the outer layers being 630 mm thick each, weighing up to 40 ton per unit piece, which must be assembled to create the five rings of the muon spectrometer barrel. The coil, which will be built as a single unit weighing 250 t, has to be inserted in the horizontal position into the central barrel ring of the yoke YB0. The vacuum tank is then welded around the coil (see Chapt. 26).

Carrying out this heavy assembly work in the underground cavern is excluded for the following reasons. It would require a very large cavern with one additional large access pit and two 80 t cranes, one at each end of the cavern, since large pieces cannot be transferred over the detector unless the height of the cavern is substantially increased. Even if these requirements were met, the detector construction work would have to proceed in series, because of the limited length of the cavern along the beam line, and the fact that most of this work is not compatible with the cleanliness required for the assembly of the superconducting coil. The duration of the construction of the magnet in the underground area is estimated to take at least 45 months (compared to 34 months for assembly at the surface). Furthermore, the duration of this activity would have to be counted from the finishing date of the underground area, i.e. minimum thirty months after the scheduled stop of LEP. An additional 24 months would be required for the assembly and completion of the sub-detectors. Thus a complete assembly of the detector in the underground cavern would imply a shut-down of more than eight years between LEP and LHC, which would be unacceptable. Finally, the safety risk for personnel and equipment would inevitable be greater.

The alternative is to carry out, to the possible extent, all the detector assembly work on the surface, in parallel with LEP operation and with the construction of the underground cavern after the stop of LEP. Several sub-detectors, such as the barrel muon chambers, can be installed in the yoke at the surface, saving additional time in the underground area. In this way, the shut-down period between LEP and LHC can be reduced to less than five years. However, temporarily a larger surface hall is required temporarily, together with the hiring of heavy lifting equipment at some point in time.

25.2 SURFACE BUILDINGS

25.2.1 Building Dimensions

The surface building requirements of CMS are dominated by the need to carry out a

complete assembly and test of the magnet on the surface, which requires a minimum height of 18.3 m under the crane hook. This implies a 23.5 m high building. The construction of the magnet sub-assemblies, too large to transport by road, requires a 100 m long, 23.5 m wide assembly hall (SX5), which will be linked to the main access shaft (PX56) for installation underground after testing (see Fig. 26.3). In order to allow changing the relative position of the large sub-assemblies inside the hall, two alcoves have been added, which locally increase the effective width of the hall. The hall is equipped with two 80 t overhead cranes and a heating and ventilation system, but has no general temperature stabilisation. Further more, the main assembly hall is complemented by a temporary appendix (SXL5) needed for the 'in situ' reinforcement of the conductor for the superconducting coil. Fig. 25.1 shows the general layout of surface buildings at Point 5. The proposed layout extends outside the present Point 5 border and one of the existing buildings (SU5) must be moved.

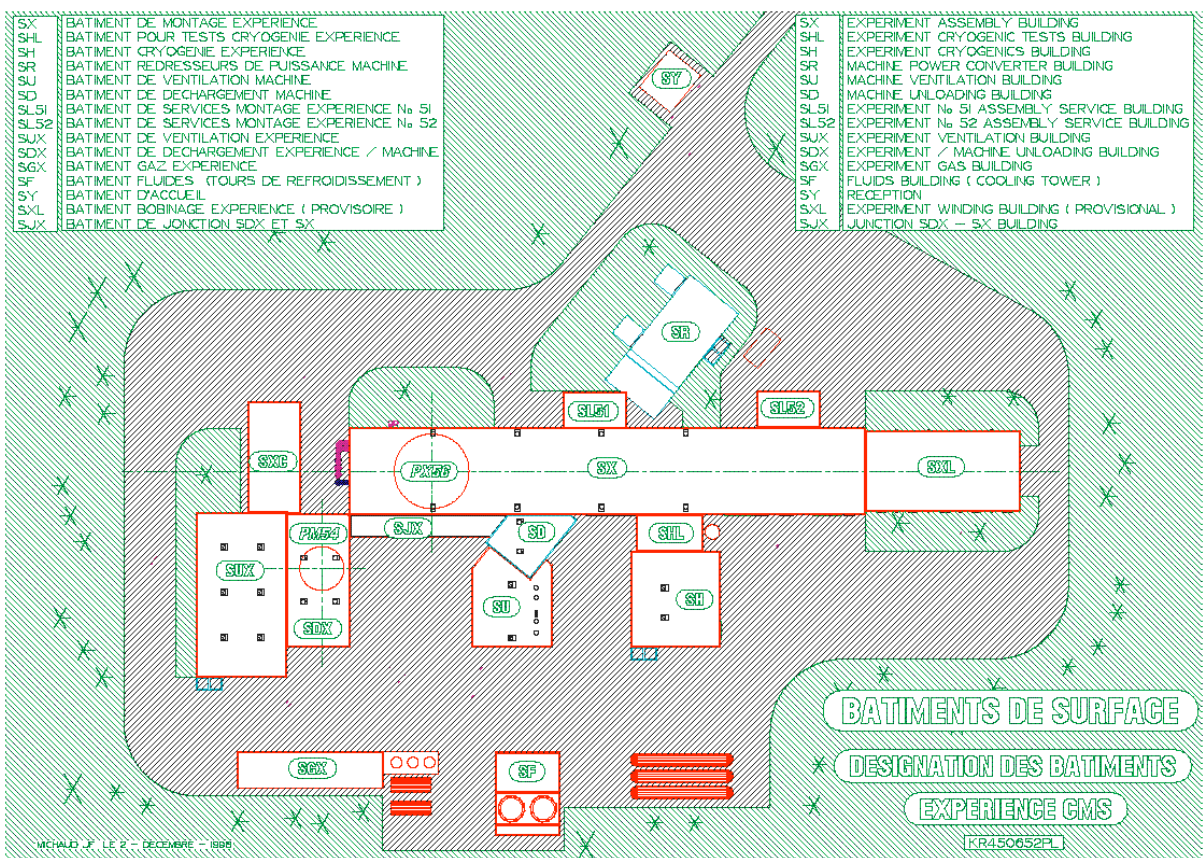


Fig. 25.1: General view of the surface building layout at Point 5

25.2.2 Environmental Impact

The CMS collaboration together with CERN are concerned about the environmental impact of the proposed assembly hall. The preparation of several of the sub-detector units could be made in existing CERN assembly halls, and if more time were to be available for the installation there would be a possibility of constructing even relatively large and heavy sub-assemblies outside the experimental area of CMS. However, road transport sets a strict limit to the size and weight of objects that can be transported. However, after the completion of the manufacturing, assembly and testing of detector components on the surface and their lowering to the cavern, the alcoves and the appendix SXL5 will be demolished, and the height

and the length of the assembly hall will be reduced to 16 m and 100 m respectively from its most extended dimensions of 23.5 m and 141m.

25.3 UNDERGROUND AREAS

25.3.1 General Considerations

The basic design criteria for the integration of the CMS experimental cavern at Point 5, where the beam level is situated at a depth of 90 m, are:

- longitudinally oriented cavern (UXC5) providing space for the withdrawal of the endcap sections,
- one access shafts (PX56), centred on the beam line, permitting successive installation of the large detector pieces from one side of the cavern,
- separate cavern (USC5), placed parallel to the main cavern and integrated with the LHC machine by-pass tunnel, housing the counting room (at a radiation-safe distance, allowing shortest possible routing of the cables), and the technical services (cryogenics, gas, power supplies, cooling and ventilation),
- one personnel access shaft (PM54) serving both caverns USC5 and UXC5, thus avoiding a dead end in the latter,
- preserve and use the existing LEP installations, as far as possible.

The absence of existing major underground structures at Point 5 gives a certain freedom in the design of the overall layout of the experimental cavern. However, the unfavourable underground geological rock structure (compared to Point 1) and the location of the deep underground water layers have been carefully examined prior to the final design. In particular, this has resulted in a 7 m thick separation wall between the two caverns (as compared to the minimum 3 m required for the radiation shielding), hence, the service cavern will be permanently accessible.

Additional reduction of radiation doses will be provided by the intrinsic shielding offered by heavy objects such as the calorimeters and the magnet yoke and the use of mobile shielding around the beam line. The main access shaft is centred on the LHC beam line and must, therefore, have a mobile shielding plug of 2 m thick concrete, which will be situated at the surface level flush with the floor of the assembly hall. A 3 m thick shielding door will separate the access from the bottom the shaft PM54 to the floor of the main cavern.

It is essential that the design of the experimental area also includes facilities to provide for safe and efficient working conditions during the installation and maintenance. The proposed scheme in which all detector units and the magnet are fully assembled and tested on the surface and brought down into the experimental cavern with a minimum of further assembly work, has resulted in reduced dimensions of the underground cavern. An additional demountable platform to separate ventilation systems and to provide mechanical protection from falling objects is incorporated in the main access shaft at the level of the ceiling of the cavern. A three level gangway system fixed to the cavern walls provides for unobstructed circulation and easy access to the two independent exits from the underground caverns.

25.3.2 Layout of the Underground Caverns

Following the general constraints and the installation scenario for the magnet and the

detector units, indicated above (see also Chapt. 26), the overall layout of the underground structures for the CMS experiment has been defined for Point 5 (see Fig. 25.2 and 25.3). The existing underground structures at Point 5, the access shaft PM56 and the junction UJ57 serving the LHC machine proper, do not have to be modified, since they are placed outside the boundaries of the new structures.

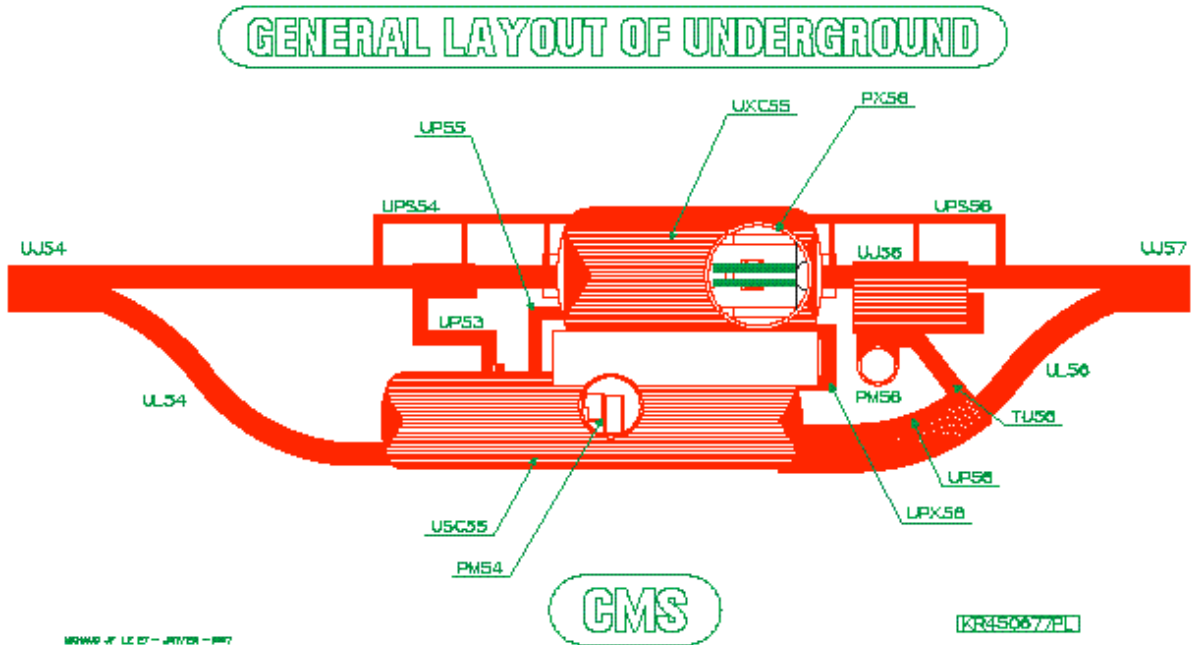


Fig. 25.2: General layout of underground structures at Point 5.

The main cavern UXC5, 26.5 m in diameter and 53 m long, is comparable in size and volume to the present LEP cavern at Point 2. The auxiliary cavern housing the counting room and the technical services as well as the LHC machine by-pass tunnel has an overall diameter of 18 m and a total length of 85 m. It is aligned parallel with the main cavern and separated by a 7 m thick wall. The thickness is primarily dictated by the required civil engineering structures and it largely offers appropriate radiation shielding. Two access tunnels, one from the auxiliary cavern (UP56) and one from the bottom of the shaft PM54 (UP55), join the main cavern at different levels. In addition, at the height of the beam, two smaller survey galleries interconnect the main cavern with the machine tunnel.

The more detailed features of the CMS experimental cavern are shown in Fig. 25.4. The main access shaft PX56, 20.4 m in diameter, provides a net 14 m \times 19.5 m opening for the installation of the magnet and the detector units. A second access shaft PM54, 9 m in diameter, provides lateral installation access at the floor level to the other end of the detector. This is necessary, since the limited crane clearance over the detector does not allow large objects to be transported between the two endcap regions. Metal plates are embedded in the concrete floor inclined by 1.23% and thus running parallel to the slope of the beam line. In the central part of the cavern the floor level is lowered by 3 m in order to provide access under the detector for services. This volume is also connected to the counting room in the auxiliary cavern via 3 labyrinth tunnels to run cables and services.

The low b quadrupoles, which penetrate into the experimental hall, are placed on a solid

concrete platform (see Fig. 25.4) in order to provide a stable foundation for the intersection elements. This concrete structure also serves as a radiation shielded alcove for the HF detectors, when the main endcap sections are withdrawn for access.

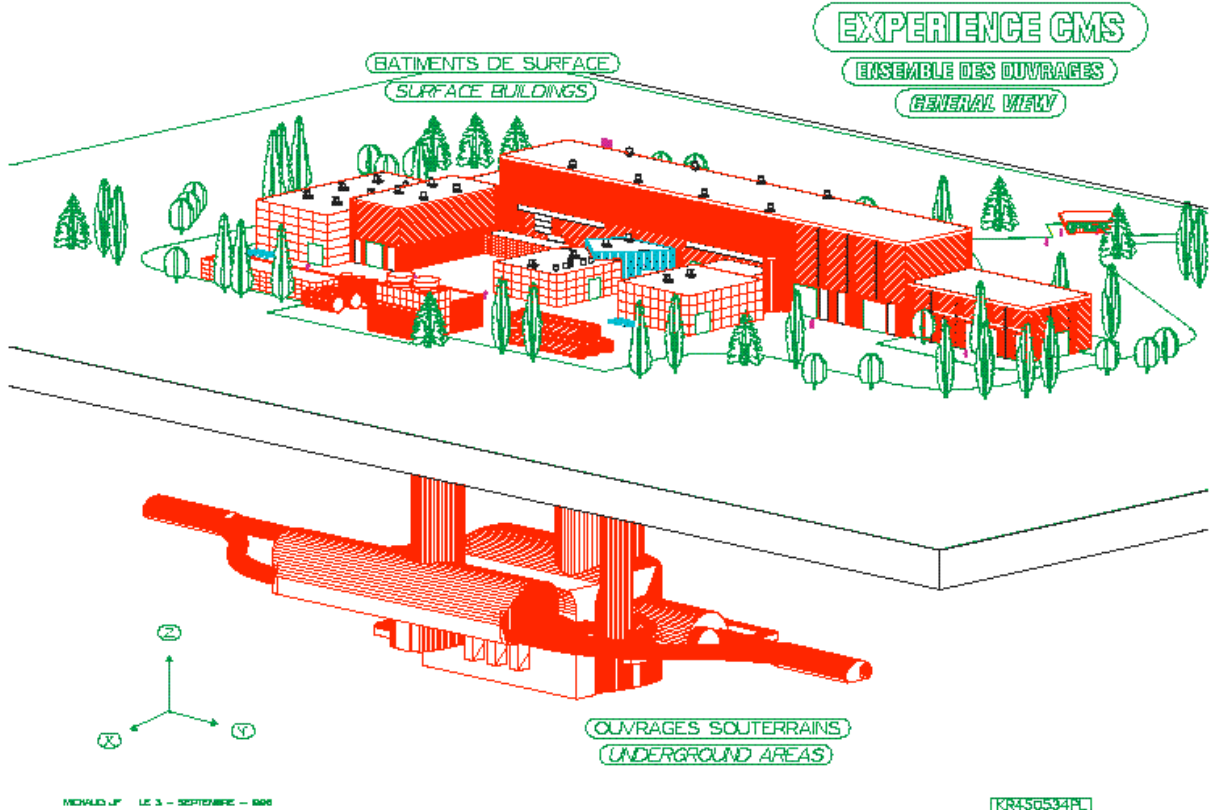


Fig. 25.3: General design of the CMS experimental area.

25.3.3 Main Cavern Infrastructure

Although the bulk of the heat load produced by the detector units will be removed by dedicated cooling arrangements, the environment in the experimental hall will play an important role in the long term stability of the detector. The ambient air in the cavern must be kept at a low humidity level (dew point $9^{\circ}\text{C} \pm 1$) and with a high degree of temperature stability ($18^{\circ}\text{C} \pm 1$). In order to achieve this, a system of distributed ducts for the injection of air into the cavern has been designed to fit the walls behind the gangways.

The gangways are arranged on three levels and aligned with the rack platforms attached to the detector. A series of stairs makes it possible to access the protection platform in the main shaft PX54, (see Fig. 25.5).

The cavern is equipped with a 20 t crane having an effective hook-span of 17 m.

25.3.4 Auxiliary Cavern

The auxiliary cavern USC5, which is horizontal (hence, not aligned with the slope of the main cavern), is essentially divided into two sections, one for the counting room and the gas distribution system, and one for the general detector services. In addition, the latter section will house the power supplies for the low β LHC machine quadrupoles. The two sections, which are nearly identical in size, will be separated by the common access shaft

PM54 and the personnel safe room.

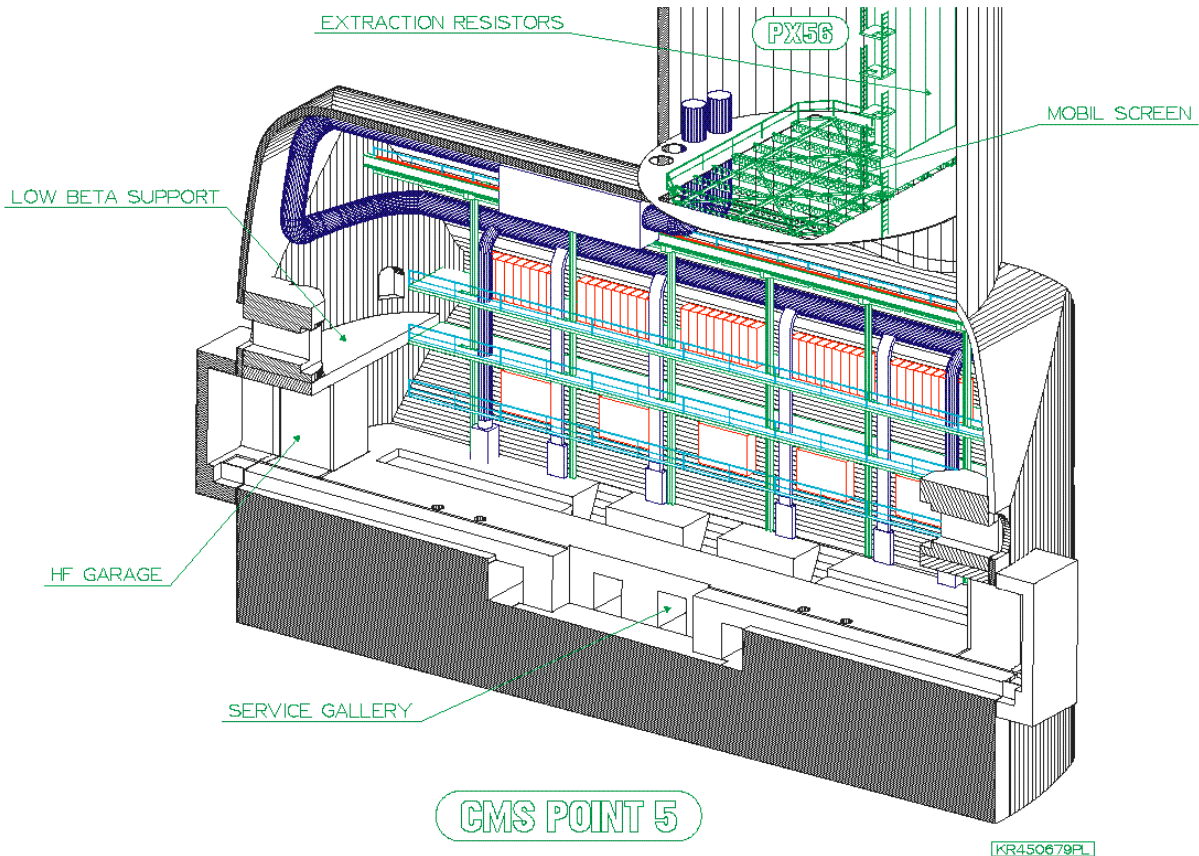


Fig. 25.4: Detailed view of experiment cavern showing the protection platform in the access shaft, the low β concrete platform and the 'garage' for the HF detectors.

The counting room, which is longitudinally centred with respect to the detector in the main cavern, has been designed to house approximately 250 electronics racks installed on a two-floor structure with separation walls. This cavern section also houses the gas distribution system. The 9 m diameter shaft (PM54) will give access to the two floors of the counting room, as well as to the floor level of the main cavern via a dedicated large shielding door in the separation wall. The access shaft will be equipped with a fire protected 3 t lift and staircase system, which will ease the installation of all counting room equipment and provide direct installation access to the main cavern floor level. The limited size of the access shaft will not allow installation of large prefabricated counting room modules. This is, however, not regarded as necessary since the cavern itself will constitute the 'housing structure' and will also allow the centralisation of the cooling, ventilation and power arrangements (see Fig. 26.7).

The other half of the auxiliary cavern will house the power supply and the cryogenic system for the magnet, part of the magnet quench protection system, the cooling and ventilation distribution systems as well as a few racks for the low β LHC machine power supplies.

25.4 construction planning

The construction planning for the civil engineering work at Point 5, is summarised in Fig. 25.6 [3]. CMS activities could start in the assembly hall SX5 and its appendix SXL5 during the last quarter of 1999. Installation in the underground areas could start as from the

middle of 2003. The control building SCX5 would be delivered ready for installation by the middle of 2004.

25.5 safety

The design of experimental area has incorporated several specific safety aspects in addition to those described in Chapt. 28, such as:

- fixed gangways and staircases for easy access at all levels in the underground caverns,
- emergency escape routes at each end of the main cavern,
- smoke extraction, in case of fire,
- fixed and mobile radiation shielding surrounding the low b quadrupoles and absorbers,
- hard cover (demountable platform), providing protection beneath the main access shaft.

The large capital investment and the unique nature of the CMS detector do imply that a first class fire fighting system must be installed in the CMS experimental area. The global fire prevention of the experimental area has not yet been decided on, but in discussions with CERN/TIS experts, general foam generators or more locally placed water fog systems have been considered

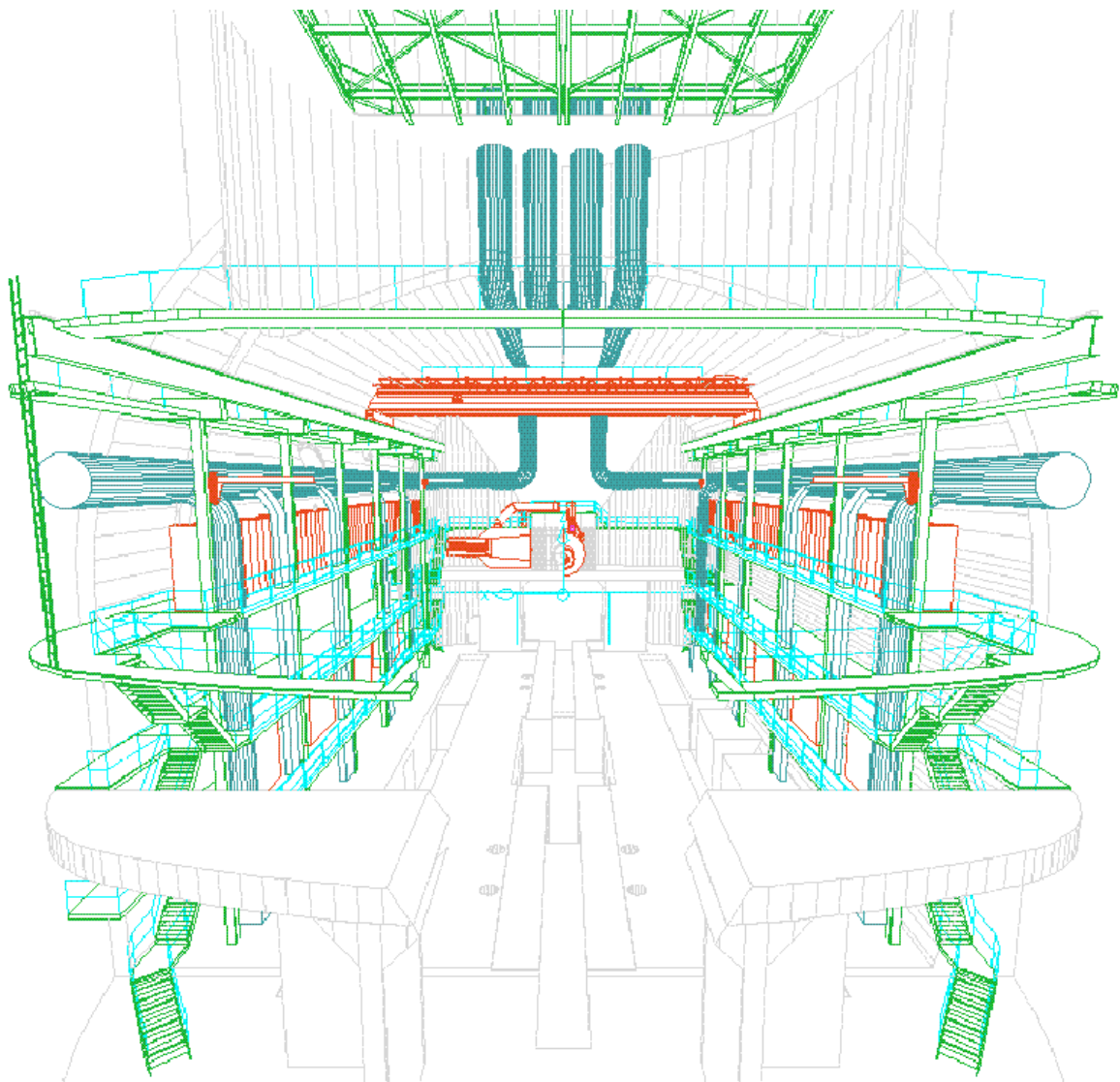


Fig. 25.5: General view of cavern infrastructure.

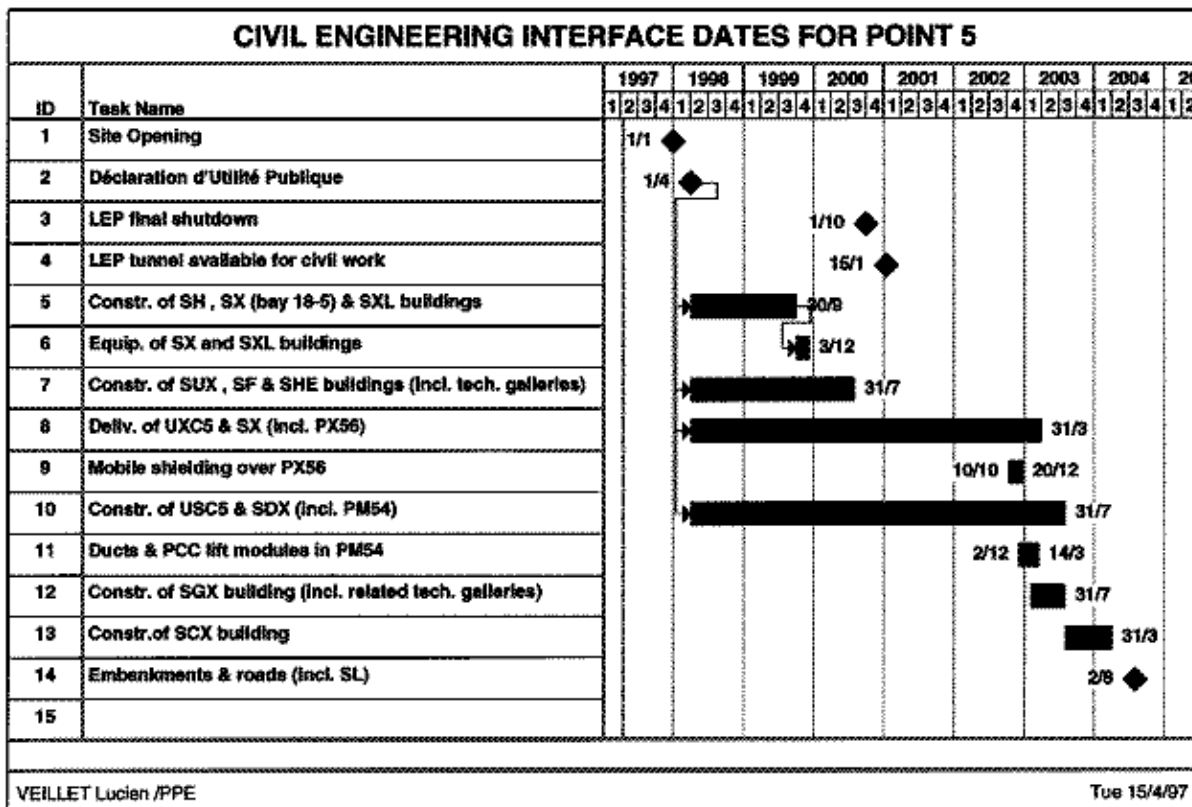


Fig. 25.6: Construction planning for the experimental hall.

25.6 Other surface facilities

During the construction phase of the magnet, and during the assembly phase in the surface hall, other hall surfaces will be required, on a temporary basis elsewhere on the CERN site, for the storage, preassembly, and testing of the sub-detectors. Some of these sub-detectors will require clean (e.g. ECAL and HF) or very clean areas (e.g. central tracker). Table 26.1 summarises the needs, as they are understood today.

25.7 CONCLUSIONS

The design of the experimental area for CMS can be integrated in the LHC machine layout in Point 5 without perturbing the latter. The construction of this experimental area does not present any major difficulty and the experience gained from the construction of the LEP experimental areas can be fully exploited. A large assembly hall, situated at the head of the main access shaft PX 56, will be needed during the construction and assembly phase of the magnet, as well as temporary hall space for the storage and assembly of the sub-detectors.

Table 25.1
Other surface facilities required on a temporary basis.

Sub-detector	Crane capacity [t]	Area [m^2]
Central Tracker;		
- Si and pixels	1	500
- MSGCs	1	1500
ECAL (EB and EF);		
- regional centre	2.5	200
- supermodul assembly	20	1000
- storage area	20	1000
HCAL (HB, HF, VF)	60	600
Muons;		
- barrel	5	1500
- endcap	2	1000
RPOs	1	700
Alignment System	5	740
Integration	10	1000

26. ASSEMBLY AND PLANNING

26.1 EXPERIMENTAL AREA REQUIREMENTS

The assembly of CMS is a demanding task because of the very large size and mass of the various elements. This assembly cannot be done directly in the underground area (UXC5), which has been designed to the minimum size to minimise cost. As explained in Chapt. 25.1, if the assembly was done underground then the required size of the underground area would have to be at least 90 m long with a large cross section allowing for the installation of two 80 tonne travelling cranes.

26.1.1 Requirement for Surface Buildings

Point 5, which has been allocated to CMS is too far from the main site of CERN to allow a meaningful use of existing halls, and, in addition, the transport of large pieces (say more than 15 m in diameter and more than 1000 tonne in weight) is not possible in the region. Thus CMS requires, during the assembly period, a large assembly hall on the surface (SX5), the required occupancy date for the first phase of SX5 being 1/10/1999.

This hall cannot be positioned directly over the main shaft because this area has to be left free for the civil engineering to complete USC5 and UXC5 after the stop of LEP, and then to allow UXC5 to be equipped, (Fig. 26.1).

The cross section of the surface hall SX5, during the assembly period, is determined by the size of the experiment and allows for the installation of two 80 tonne travelling cranes. This determines the outside dimensions of the building as 23.5 m wide and 23.5 m high, (Fig. 26.2).

The assembly of the solenoid which is a 13 m long heavy object inside a 13 m long cryostat, can only be done horizontally. As this operation has to take place when all other large pieces are already present, it is in fact this operation which determines the length of the surface building for the assembly period, (Fig. 26.3). The required length is 92 m.

The decision to wind on site requires only a small additional building (SXL5) to complete and reinforce the conductor and spool it on site, as spools of reinforced conductor are not transportable. This additional building is considered a part of the magnet project and its cost has been taken into account inside the magnet budget.

After the surface test of the magnet, the assembly building will be connected to the part of the SX5 building covering the main shaft, which will have been completed in the mean time, allowing for the transfer of the heavy pieces to the underground area.

After the transfer of the CMS magnet to the underground area has been completed, the surface building SX5 will be reduced in height to 16 m, and in length to 100 m, a size sufficient for the normal running of CMS and which also satisfies environmental requirements, (Fig. 26.4).

26.1.2 Requirement for Underground Area

The main cavern (UXC5), 26.5 m in diameter and 53 m long at a depth of 97 m ground to ground, is very similar in shape, size and volume to the present LEP cavern at point 2, and the CMS detector fills it nearly completely (Fig 26.5). The service cavern (USC5) has a diameter of 18 m and a length of 85 m, and is aligned parallel to the main cavern, but offset to

provide a minimum distance of 7 m between them, (Fig. 26.6), for structural but also shielding reasons as explained in Chapt. 25.3.

The main access shaft to UXC5 is PX56 which has a 20.4 m diameter, providing a 14 m x 19.5 m free opening for the installation of the magnet. A second shaft, PM54, 12 m diameter provides access to USC5, and at the same time gives access to the other end of the detector (from the main access shaft) through a short transfer tunnel TX54, as explained in Chapt. 25.

The part of the service cavern directly facing the experiment is used to house the counting rooms. The other part of the service cavern, farther away behind PM54, is used to house all services, (Fig 26.7). In particular the services for the magnet, mainly the cold box and the power supply will be installed in USC5. In order to maintain the shielding efficiency of the wall between USC5 and UXC5, the transfer lines and the bus bars will pass through the shielding wall at an angle, (Fig 26.8). It is presently planned to installed the dump resistor in the lowest portion of the main shaft PX56, above the demountable platform closing the main shaft.

26.2 ASSEMBLY ON THE SURFACE

The assembly of the magnet in the surface hall SX5 will start with the assembly of the first End-Cap, as described in Chapt. 8. In parallel, the welding of the two end sections of the outer vacuum tank will be finished to form complete shells, and these will be stored inside the side alcove destined to receive, at a later stage, the cold box for the surface test of the magnet, (Fig 26.9, phase 4).

Then assembly of the barrel iron rings will proceed using a Ferris-Wheel arrangement, as described in Chapt. 7. The two rings YB-2 and YB-1 will first be assembled, in this order, using a dedicated jig (Fig. 26.13-A), then the central iron ring YB0 will be assembled using the central shell of the outer vacuum tank, properly reinforced, as the assembly jig (Fig. 26.13-B). The assembly of the two rings YB2 and YB1 can then proceed, in this order, using the same assembly jig as the first two rings (Fig. 26.9, phase 10).

Then the second end-cap will be assembled, as described in Chapt. 8, and the outer shell of the vacuum tank completed by welding the two end sections, previously stored inside the side alcove, to the central part of the vacuum tank, (Fig 26.9, phase 12).

The reinforcement of the conductor on site by Electron Beam welding will proceed in the hall SXL and the conductor for the first layer will be spooled inside SX5, (Fig 26.10, phase 13). The winding machine will then be installed and winding of the first layer may proceed, (Fig 26.10, phase 15).

Winding of the following layers of the coil, and curing, will proceed in parallel with the preparation of the conductor length for the subsequent layers, (Fig 26.10, phase 17) as it is explained in Chapt. 19.

When the coil is finished (see Chapt. 19), including the quench-back cylinder, the outer cold screen and associated superinsulation layers, it will be rotated to the horizontal position, (Fig 26.11, phase 22). To ease the passage of the centre of gravity, from one side to the other of the rotation axis, a removable water counterweight is integrated in the device. The water tank is first filled with water. Then, using a rented gantry crane, the solenoid is tilted to bring the projection of the centre of gravity close to the rotation axis. The system is secured in this

position. Then the water is drained out, and the centre of gravity will slowly change side with respect to the rotation axis. From this point, the securing system will be slowly elongated, bringing the coil axis to the horizontal position. The central barrel ring will then be slid over the coil assembly, (Fig 26.11, phase 23 and Fig. 26.14) using high pressure air pads.

The shell of the inner vacuum tank will be prepared on the same turning system previously used to rotate the coil to the horizontal position. In parallel the cold mass will be completed, (Fig 26.11, phase 25), in particular the layer to layer connections. Then the inner shell of the vacuum tank, equipped with its cold screen and associated superinsulation layers, will be rotated to the horizontal position, and the central barrel ring (now including the coil) will be slid over it, (Fig 26.12, phase 26), using high pressure air pads.

The vacuum tank will then be completed by welding the end flanges, as explained in Chapt. 9. In parallel all connections from the coil to the outside world through the chimneys will be completed.

Cooling down of the coil may then proceed, (Fig 26.12, phase 28). The two halves of the Hadronic Calorimeter will be inserted inside the inner vacuum tank to stress the vacuum tank to its definitive shape in order to have the final position of the coil during the magnetic test at the surface.

The yoke will be closed to allow the magnetic test at full current, (Fig 26.12, phase 32). This test will proceed in steps. The decentering forces will be measured and the position of the coil will be adjusted, acting on the suspension system, to minimise the forces due to decentering and misalignment, as explained in Chapt. 9 and 18. After the magnetic test, the two HB will be removed from the vacuum tank and the magnet will be ready for installation in the underground area.

Then, when the underground hall will be available towards end of October 2003, all heavy elements will be slid over the floor of the surface assembly hall using high pressure air pads, on top of the shielding plug. This plug (2 m thick for protection against radiation) has been designed to support the 2000 tonne weight of the central section of the magnet, (Fig 26.15).

A rented gantry crane (of 2500 tonnes capacity) will be erected over the building SX5 to lift and transfer the heavy pieces to the underground area, (Fig 26.16).

26.3 PLANNING

The general planning of the experiment (version 23) has been reviewed taking into account all known facts:

- i) Surface building SX5 first phase ready by 1/10/99,
- ii) Reinforcement of conductor on site in SXL5,
- iii) Winding of the coil on site (see coil planning in Chapt. 19),
- iv) All known activities in SX5,
- v) The target date for the start up of the LHC Machine of 1/07/05.

Activities in SX5 provide in fact the backbone of CMS master planning, defining when sub-detectors are needed.

This planning (Fig. 26.17) shows the completion of the surface test of the magnet to be the end of October 2003. This is just compatible with the occupancy date of UXC5 given by the present Civil Engineering planning. The critical path starts from the authorisation to

break ground at point 5, then goes through the time needed for the construction of the first phase of the surface building SX5, assembly of the first end cap, assembly of the barrel rings, conductor reinforcement, assembly of the second end cap, coil winding and final assembly of the coil leading to the test of the magnet on the surface.

27. QUALITY ASSURANCE

27.1 INTRODUCTION

The high-tech nature of the CMS Magnet, its size and complexity, and the huge number of partners involved from all over the world call for a Total Quality Management system. This is based on defect prevention and continuous process improvement and relies on a Quality Assurance Plan as foreseen for the whole of the LHC Project, including the Experiments.

Total Quality Management means an approach based on quality, beginning at the design stage and continuing through the complete project. This includes all the manufacturing, handling, delivery, testing, commissioning, operation and maintenance together with the necessary documentation for the above mentioned phases and the associated planning and scheduling programmes.

The essence of quality assurance is: describing what must be done and doing what has been described. The purpose of the Quality Assurance Plan is to provide a framework, as well as guidelines, to make collaboration possible and successful. This eases the work and enables the numerous CMS Magnet Project partners to work to the same standards therefore making communications and understanding easier.

The Quality Assurance Plan for the CMS Magnet project is being completed in parallel with the finalisation of the magnet design. Concerning the Coil Project, the Saclay team has written a draft standard QA plan which is being integrated in the general CMS QA Plan.

Nevertheless it has been recognised that the high dedication of each person involved in the project is a key element to insure quality.

Training will be provided whenever judged appropriate for the success of the implementation of the CMS Magnet QAP.

27.2 THE QUALITY ASSURANCE PLAN (QAP)

The final CMS Magnet Quality Assurance Plan will be based on the recommendations stated in the “ISO 9001 Quality system”. This plan presents a written description of the procedures and structures that are being implemented for CMS. The CMS Quality Assurance Plan presents the following four-level structure:

- level A: Introductory information,
- level B: Quality Assurance Management,
- level C: Quality Process Management,
- level D: Quality Result Management.

27.3 LEVEL A - INTRODUCTORY INFORMATION

This section covers all the basic procedures of product naming and identification, document writing standards and the identification system, and the various codes to ease communication throughout the project.

The purpose of this section is to efficiently identify documents for the Magnet Project and to be able to efficiently identify and locate any item (products and components) in its final position, as long as it is included in the PBS (Product Breakdown Structure).

In addition this section outlines the Quality Assurance Categories (QAC) and provides

guidelines for determining the QAC for each item.

The objective of the document numbering system is to ensure the document traceability during the whole life of the project.

27.4 LEVEL B - QUALITY ASSURANCE MANAGEMENT

This section covers the organisational matters necessary for the co-ordination and management of the Magnet Project: this means, Management Plan, Breakdown Structures, Scheduling Process and Standards, Configuration Management and Change Control.

The first tasks in a large project are to define a planning system and the Product, Assembly, Work and Organisational Breakdown structures.

In the planning phase the work activities are viewed against the project time scale: every activity gets its starting and ending dates and any relationship with other activities. It is crucial, for the detailed project follow-up, to integrate the planning system with all the relevant technical, human resource, material management and financial data.

27.4.1 Breakdown structures

The breakdown structures are the basis for the overall project organisation and the definition of the relationship between systems; they describe the whole project in a structured way, by providing an *organised part list* (PBS), an *assembly sequence list* (ABS) and a *work packages list* (WBS); with these three tools it is then possible to find the right resources and structures people to perform all the defined tasks (OBS) and finally outline a general plan (Management Plan).

The Product Breakdown Structure (PBS) includes the following information:

- product tree structure describing the configuration of the project,
- technical description of the elementary parts of the project,
- instructions on manufacturing, machining, quality control for each level and each branch of the structure.

The Assembly Breakdown Structure complements the PBS and provides the WBS and the planning phase with the relevant constraints. It displays the assembly sequence and contains the following information:

- a description of the time sequence of the different activities,
- all information about the site, the installation tasks and the movement of the items during the processes and finally to the experimental area at P5.

The Work Breakdown Structure (WBS) provides the framework for defining the work to be accomplished.

Its main aims are to:

- insure that all the work required, and only the work required to complete the project, has been identified planned and put under the responsibility of someone,
- inform everyone involved in the collaboration of the possible interfaces and interferences,
- start up the CMS Project planning, scheduling and budgeting process,
- report project control information (physical progress) to the Project Management.

The Organisational Breakdown Structure (OBS) provides a detailed framework for people and their organisational relationship.

27.4.2 Configuration Management and Change Control

The aim of this section is to:

- insure that all technical requirements are clearly defined, documented and controlled throughout the whole project life cycle,
- provide a scheme for a systematic review of all changes,
- assure that the impact of proposed changes in performance, cost and schedule are identified, evaluated and appropriately approved prior to incorporation and implementation,
- maintain the integrity between the project progress and the original project baseline (the Technical Design Report) in regard to performance, cost and schedules,
- to get every project partner working at any given time to the same configuration parameters and objectives of the CMS detector.

27.5 LEVEL C - QUALITY DURING PROCESSES

This section deals with the definition of the Quality Assurance implementation strategy of the processes during the whole product life cycle, from the design phase to the delivery phase; it takes into account the design, the contract, the purchasing, the entire fabrication and the various logistics (handling, storage, packing, delivery).

With respect to the call for tender, a procedure has been established for the call and placing of orders (Chapt. 31). CERN or another CMS Collaborating Institute will be responsible for issuing the price enquiry, placing the order and assuring the financial monitoring.

27.6 LEVEL D - QUALITY RESULT MANUAL

This section covers all matters concerning the quality control procedures to be defined and implemented by the various CMS sub-systems. The quality results are expressed in terms of:

- inspection and acceptance testing,
- control of measuring and test equipment,
- control and quality records,
- internal quality audit.

With respect to the *reception procedure*, a series of tests is defined for every product. In case of non-conformity, a report will be made to decide what should be done

With respect to the *manufacture control*, the supplier will be asked to comply with National Quality Standard or ISO 9000 (the certification will be appreciated but not mandatory). Check points will be defined and the magnet team members will be authorised to visit the manufacturing company.

27.7 QUALITY CONTROL

In order to give the reader a feeling for what happens in a real case, we have listed below the control tests which are foreseen to ensure the final quality of a crucial item during the industrial production of the coil conductor.

Superconducting Strand

- chemical analysis of source materials,
- eddy current measurements of all the final conductor,
- continuous strand diameter check, spot measurements of Cu/SC ratio,
- RRR of the copper matrix,
- critical current of the strands before cabling, after cabling, after extrusion of the insert.

Rutherford type cabling

To control the cable quality and its current degradation, checks on filaments will be carried out on samples taken from the beginning and from the end of the cable.

- measurements on single strands have to show that the degradation is within the tolerances,
- during the manufacturing process, on-line dimensional measurements and the control of the pulling force are foreseen, to make sure that the cable is not damaged.

Extrusion

During the extrusion process of the conductor the following tests are due to be performed:

- temperature control of the billet pre-heating,
- extrusion temperature,
- stop duration time,
- pressure applied,
- speed.

Bonding at the Rutherford-pure aluminium interface

After extrusion, short 250 mm samples will be prepared for tensile tests from the extruded conductor and ultrasonic tests will be carried out on short samples prepared from both ends of the insert. For these tests the pulse-echo ultrasonic method will be used, however, for the on-line bond measurement a new method is proposed.

Off line the following tests will be performed:

- Bending tests.
- Macro and micro photography, electron micro probe analysis for bond quality.
- Measurement of the residual resistivity ratio (RRR).
- Ic measurements on single strand.
- Ic and MQE on full conductor.
- RRR measurements under cyclic strain.

All these tests will have to be organised, followed and recorded in the framework of the Quality Assurance Plan.

28. SAFETY OF THE MAGNET

This chapter provides a safety overview of the magnet project in terms of the safe design of its components at the conceptual and pre-industrialisation stage. This will obviously include hazard evaluation and passive protection systems, also the manner in which the personnel will be invited to react to any potentially dangerous situation. For all other safety aspects related with construction and exploitation a detailed safety plan will be issued.

28.1 GENERAL PRINCIPLES

Reference is made to European directives, CERN safety codes and rules, CERN safety policy document SAPOCO/42, European and/or international construction codes for pressure vessels (CODAP; ASME), structural engineering (Eurocode 3; AISC), cryogenics, and lifting equipment (FEM: Fédération Européenne de Manutention).

Special attention will be given to the correct functioning of any safety device that may be subjected to the fringe field (e. g. all detection and alarm systems, relays in the elevators, solenoid valves in cryogenic equipment, safety valves, and circuit breakers, etc.).

The retained technical solutions aiming to get the high safety standard for each system are described in the corresponding chapters.

28.2 DESIGN PROBLEMS RELATED TO SAFETY

Intrinsic hazards related to large superconducting magnets, and the CMS magnet is exceptional on account of its dimensions, are coming from: coil axial forces (147 MN), magnetic radial pressure (64 MPa), stored energy (2.7 GJ) and magnetic field (4 T in the centre). These hazards are:

- i) dynamic and static structural stress effects;
- ii) magnetic field, fringe field and the induced current, all of which affect equipment, materials and personnel (e.g. pace-makers, metallo-plastic prothesis, etc.);
- iii) high DC currents on bus-bars and terminal connections during normal operation, and on dump resistors in case of coil discharge;
- iv) thermal effects (e.g. loss of vacuum in the coil cryostat, leak of liquid helium, temperature rise on dump resistors);
- v) quench effects.

In addition, the large size and weight of the magnet requires specific attention during assembly, transport and handling of its constitutive elements.

Therefore it is essential that safety is taken into consideration at each phase of the project, from the conceptual design of all the magnet components up to their final assembly on the CERN site, and to the subsequent working test of the complete magnet at its nominal operating conditions.

Gravitational forces have been analysed, especially for the central barrel ring (see Chapt. 7) which is by far the heaviest element due to the sum of, its own weight plus the weight of the vacuum vessel, the coil and the inner detectors. This amounts in total to about 2800 tonnes compared to only 1200 tonnes for the four outer rings. Consideration has also been paid to the situation in the experimental cavern where the floor has a slope of 1.23%; different means of displacing the heavy loads and blocking them in place have been studied (see Chapt. 10).

The magnetic forces acting on the barrel rings and on the endcap disks have been computed (see Chapt. 6) and are used for the design of the barrel yoke (see Chapt. 7) and endcap disks (see Chapt. 8).

The return yoke is almost saturated and because of gaps for the passage of cables and services between the barrel rings and the endcap disks, a strong fringe field is present. This field is somehow reinforced by the ferro-metallic structure which surrounds the whole detector and supports the electronic racks. The stray field is expected to reach 0.12 T (see Chapt. 6), consequently only authorised personnel will be permitted to access the area while the magnet is operational. Safety requirements stipulated in CERN Safety Instruction IS 36 will be strictly followed.

Further away from the magnet, the stray field will still be of the order of 100 - 200 G, so special attention must be paid to insure that any safety system within the area will function correctly (e.g. solenoid valves and cryogenic equipment relays, fail-safe valves and circuit breakers, including relays and/or safety protection for the nearby elevators). Value of the stray field, especially in the counting room area, can be inferred from Fig. 6.11, p C-9.

Live conductors will be protected from accidental contact (human, loose metallic objects, etc.).

In case of a quench, the stored energy of the coil must be rapidly discharged, approximately 1000 V will be generated between the electrical terminals and cause the temperature of the dump resistors to rise to about 350°C, (Chapt. 20). This will generate heat inside the coil which in turn will produce a rapid increase of helium pressure inside the cooling circuits and may be followed by a loss of vacuum due to leakage. The cooling circuits are protected against overpressure by a safety valve which opens to vent the cold helium gas into atmosphere.

28.3 MECHANICAL SAFETY AND DESIGN STANDARDS

Generally the criteria for safe stress levels will follow the European Eurocode 3 and/or American Institute of Steel Construction (AISC). These codes are not directly applicable to the design of large magnets with very thick sections – no such construction codes exist – they are mostly applicable to conventional steel constructions, but we intend to follow their instructions [28-1; 28-2].

Different FEA's have been carried out to demonstrate the safety of the iron structure using the above mentioned codes (see Chapt. 7 and 8).

The vacuum tank supporting the inner detectors is sufficiently strong to maintain its stability and to counter the internal stresses caused by the vacuum. However since it has to support the barrel calorimeters (see Chapt. 9) it has been calculated as a structural element. The vacuum tank will be protected against accidental overpressure by safety valves adjusted to 1 bar absolute pressure. As a potential pressure vessel it will be designed according to the French CODAP and/or ASME codes [28-3; 28-4].

For aluminium structures TIS (Technical Inspection and Safety division) recommends to refer to the technical report ISO TR 11069, and refer for the safety factors to the standard for steel construction ISO 10721.1.

The coil has been extensively analysed (see Chapt. 14, 15, and 16) in all its aspects.

On account of possible asymmetric positioning of the coil in the iron yoke the forces exerted on the suspension and tie-rod retaining system have been found to be quite substantial (Chapt. 6). Therefore the possibility of correcting the cold mass position by adjusting its suspension, after an initial measurement performed at low current, has been adopted to counteract these forces (see Chapt. 18).

28.4 SAFETY SYSTEM FOR EXPLOITATION

The general safety system will be based on the Magnet Safety System, MSS, (see Chapt. 22.4) and the Detector Control System, DCS, [28-5]. In addition to the Magnet Safety Interlocks (Chapt. 22.4.4), a high level hard wired interlock system, based on the BBL3 alarm matrix originally developed for the L3 experiment [28-6], will ensure the safety of equipment and personnel on or near the magnet under any circumstances. In the case of a fault occurring, all equipment will be brought to a stand-by position in an organised and controlled way.

29. RADIATION ENVIRONMENT AND SHIELDING

The radiation environment at the LHC is known to be very hostile for almost all subdetectors envisaged [29-1]. Most of this intense background radiation is due to the beam-beam collision. At the nominal peak luminosity of $10^{34} \text{ cm}^{-2} \text{ s}^{-1}$, we expect 8×10^8 inelastic proton-proton collisions per second. A significantly smaller contribution arises from the expected level of beam losses in the straight section of the LHC ring [29-2]. It must be noted that the maximum luminosity will be reached only at the beginning of a fill. The day-averaged luminosity will depend on the number of fills per day, but is expected to be about half of the peak value. The CMS physics program foresees the accumulation of $5 \times 10^5 \text{ pb}^{-1}$. This corresponds to 5×10^7 seconds at the peak luminosity. Unless explicitly otherwise stated all radiation level values will be given for the total integrated luminosity of $5 \times 10^5 \text{ pb}^{-1}$.

The solution, adopted by CMS, to have the whole calorimetry inside of the superconducting coil provides efficient shielding against the intense radiation emerging from the interaction point.

The radiation levels in the experimental hall are dominated by cascade development in the collimator region. This radiation needs to be considered for installation and estimation of maintenance needs of any radiation sensitive equipment in the experimental hall. The coil itself, however, is protected against this background component by the massive flux return yoke.

For the radiation environment simulations primary proton-proton collisions have been generated with the DPMJET-II event generator [29-3], which is optimised for the generation of minimum bias events. About 15 % of the generated events are single diffractive, so that one of the participating protons suffers only a small deflection and does not add to the radiation background in the experimental area. Because DPMJET-II includes heavy flavours only up to charm, events containing b-quarks were obtained separately from PYTHIA and added to the DPMJET-II events. The cross section estimated for b-production was 0.35 mb, to be compared with the 80 mb estimated for the total inelastic cross section. In order to sample enough of the potentially important b-events a weighted sampling scheme was used, favouring the selection of b-events.

The cascades were followed through the CMS geometry with the FLUKA code [29-4]. Neutrons were transported to thermal energies, other hadrons below the interaction threshold were ranged to zero energy. Electromagnetic energy cuts were adjusted according to the region. In the experimental hall they were 100 keV for e^\pm and 30 keV for photons. In the coil and its surroundings 300 keV for e^\pm and 100 keV for photons. A relatively rough geometry description was used for the CMS detector and the experimental area. In particular no civil engineering installations, except for the dedicated shielding, were taken into account. Cylindrical symmetry was assumed everywhere. The hall was taken to have flat end walls and a half-length of 26 m. The radius of the hall was taken to be 12 m. It has been shown that the radiation field is not significantly changed if a more detailed geometry of the hall is used [29-5].

The iron yoke provides significant shielding, not only to the inner muon stations and the coil, but also to the central parts of the experimental hall. The massive detector sits like a plug in the centre of the hall and results in relatively low radiation levels in the region $|z| < 7$ m.

Figure 29.1 shows the estimated neutron fluence and total radiation dose close to the

lateral wall of the CMS experimental hall in the region $R = 8 - 12$ m. Since the main concern lies in radiation hardness of electronics, only neutrons with kinetic energy in excess of the 'silicon damage threshold' of 100 keV have been considered. The neutron fluence shows a weak radial dependence but is typically of the order of 10^{10} cm^{-2} in the centre of the hall and increases to almost 10^{11} cm^{-2} at $z = \pm 20$ m. Charged hadrons cause similar displacement damage as energetic neutrons, but their fluence outside of the detector is 1-2 orders of magnitude below the neutron fluence.

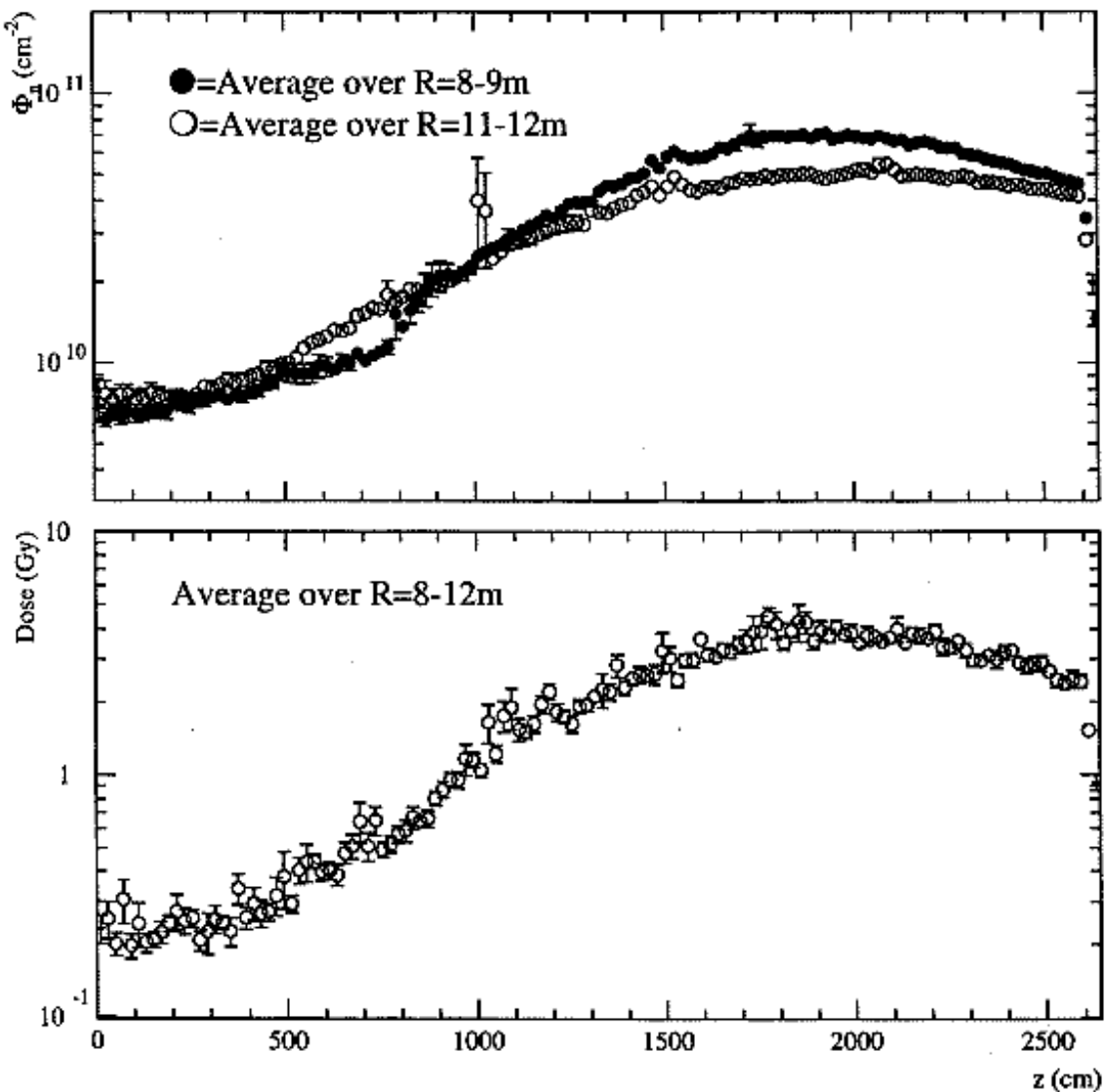


Fig. 29.1: Neutron fluence and radiation dose close to the lateral wall of the CMS experimental hall. Values are for $5 \times 10^5 \text{ pb}^{-1}$. The error bars indicate only the statistics of the simulations.

The radial dependence of the dose is negligible in the region $R = 8 - 12$ m, and only the average is shown. Also the dose varies by roughly one order of magnitude as a function of the z -co-ordinate. The values range from the minimum of 0.3 Gy to about 4 Gy. Two-dimensional maps of the neutron (>100 keV) fluence and the radiation dose in the experimental area are shown in Fig. 29-3, p. C-69, and Fig. 29.4, p. C-70.

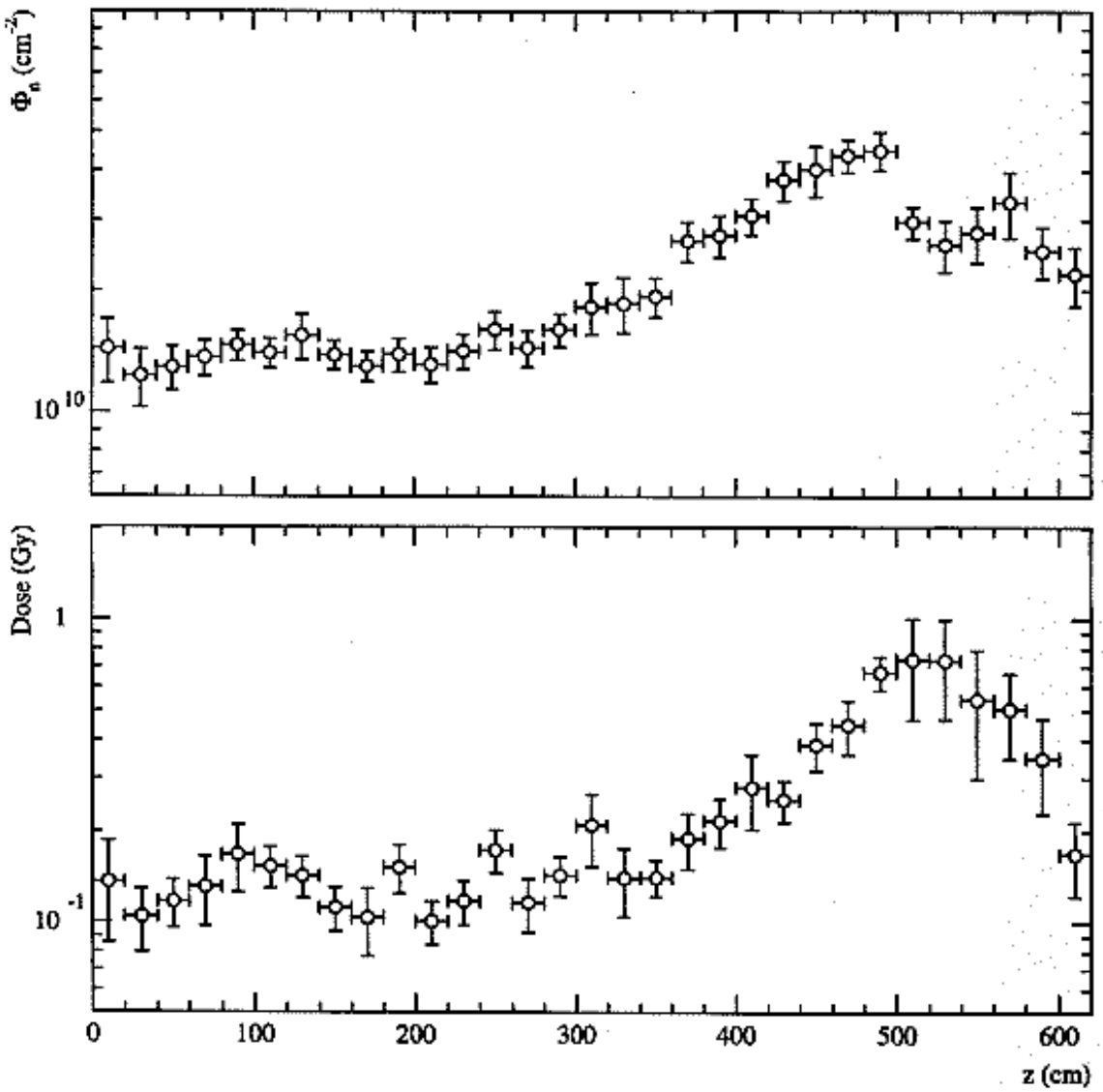


Fig. 29.2: Neutron fluence and radiation dose in the superconducting coil. Values are for $5 \times 10^5 \text{ pb}^{-1}$. The error bars indicate only the statistics of the simulations.

The coil is exposed to neutrons leaking out of the hadron calorimeter. It can be seen from Fig. 29.2, that the neutron fluence is of the order of 10^{10} cm^{-2} in the central parts of the coil. At the ends of the coil we observe a notable increase of the neutron fluence. A pronounced peak comes from the crack between the HB and the HE and reaches a maximum of about $5 \times 10^{10} \text{ cm}^{-2}$. A smaller peak appears due to the channel provided by the slot for the muon chamber ME1.

The radiation dose at the coil remains at very moderate values, not exceeding 1 Gy even in the region of the HB/HE crack.

Especially concerning the neutron fluence in the coil, it should be taken into account that final service and cable layout might affect the neutrons. The simulation set-up has been constructed to be pessimistic by underestimating the amount of material in the cracks. So the

values shown should represent upper estimates.

The fluences and radiation doses for the coil and the experimental hall set bounds for the radiation to be expected in the cryogenics and service line which is located between the barrel wheels YB0 and YB1. The similarity of the values in the hall and at the coil indicate a maximum neutron fluence of $3 \times 10^{10} \text{ cm}^{-2}$ and a radiation dose of no more than 0.5 Gy for this region.

Error estimates, except those from the run statistics which are indicated in the figures, are difficult to obtain by any direct and well defined method. The neutron fluence and radiation dose are affected by uncertainties in the physics models, in the cross section data used by the simulation code and by the approximation done when describing the geometry of CMS for the simulation code. Based on published benchmarks of the FLUKA code [29-6] and on intercomparison of results with different independent geometries, simulation codes (MARS95 and GCALOR) and cross section data sets, the overall error for the neutron fluences and doses presented here can be estimated to be about a factor of three.

The high hadron fluences at LHC imply severe activation of several subdetectors. Again the magnet coil itself is so well protected that its activation is negligible. On average 1.4 high energy hadronic interactions, 'stars', are produced in the coil per cubic centimetre per second at LHC peak luminosity. This star production rate is slightly higher close to the HB/HE crack, reaching up to 5 per second per cubic centimetre. Even if we use a very pessimistic value of $10^{-8} (\text{Sv}/\text{h}) / (\text{star}/\text{cm}^3/\text{s})$ for the w-factor [29-7], the dose rate in contact with the coil is only about 10 nSv/h. For access to the coil, the activation of the endcap calorimeters might be more significant than the activation of the coil itself. Their proper shielding will be discussed in the relevant Technical Design Reports.

29.1 SHIELDING AND RADIATION PROTECTION IN THE UNDERGROUND AREA

The radiological danger to humans is usually expressed as dose equivalent and measured in Sievert (Sv). It is related to the dose (measured in Gy) by a quality factor, which depends on the radiation type but is always greater than unity. The dose equivalent rate in the CMS area during machine operation is shown in Fig. 29.5, p. C-71, it reaches an average of about 1 mSv/h when the LHC operates at its peak luminosity. The design limit for occupied areas is 10 $\mu\text{Sv}/\text{h}$ [29-8]. Therefore the whole experimental cavern will be a radiation exclusion area and no access to it will be permitted during LHC operation.

The counting room area (Fig. 26.7, p. C-57) is separated from the experimental hall by a 7 m thick concrete wall, which provides by far sufficient protection and access will be normally granted to the experimental teams, while the LHC and the magnet are on, under the restrictions applicable to controlled radiation areas.

The cavern itself will be shielded at the bottom of Personnel shaft PM 54 by a moveable 300-tonne concrete door which will slide aside using air pads suspension. The bypass for personnel access to the cavern from the bottom of the Personnel shaft and from the technical gallery will be permanently under control from the MCR using the LHC key-access system.

There will be several small penetrations and bypasses leading from the experiment to the counting room. The radiological impact of all these has been discussed in [29-9], and they have been shown to provide sufficient safety margin. The two 1-meter diameter ducts

provided for the cryogenic and the pumping lines, and for the electrical busbars from the technical gallery to the magnet through the shielding wall, will not necessitate any special shielding but only a safe fence prohibiting any human passage.

The attenuation of dose equivalent in the large cable ducts which have been designed as long labyrinths starting below the CMS endcap is shown in Fig. 29.6, p. C-72. It can be seen, that the $10 \mu\text{Sv/h}$ limit allows access to part of the cable duct even when the machine operates at peak luminosity.

29.2 THE MAIN SHIELDING PLUG ON TOP OF PX 56

To shield the outside world, the top of the experiment shaft PX 56 is closed by a 2000-tonne reinforced concrete plug which will slide onto rollers in the surface assembly hall.

As this reinforced concrete plug will serve as a static transit member during the operation of lowering down all of the constitutive magnet and detector elements (see Chapt. 26 and Fig. 26.15, p. C-65), it will be tested under 110% overload calculated on the heaviest element which is the central ring with coil and vacuum tank, i.e. about 1900 tonnes. Thus the overload of 2100 tonnes will be provided by some 1000 tonnes of iron blocks already available for the test of the air pads system and platform (see Chapt. 10), plus some 1100 tonnes of steel coming from the decommissioning of the Omega magnet. In addition to this test, the 2000 tonne overload mentioned above plus the 2000 tonne weight of the plug itself will be used as dead-weight to test the rented 4000-tonne gantry (see Chapt. 26) as well as the foundations it requires on both sides of the access shaft and very close to it by anchoring the lifting cables through the plug.

30. MANAGEMENT OF THE PROJECT

30.1 INTRODUCTION

The construction of the Magnet is a Common Project of the CMS collaboration. It is financed by all participating institutes with contributions that are proportional to their financial contribution to the experiment as a whole (see Chapt. 31). The guidelines for the contributions to the Magnet Project will be set in the Memorandum of Understanding and are laid down in the document entitled “Guidelines on CMS Common Project Contributions” [31-1].

The CMS Magnet Project is organised under the technical responsibility of the Magnet Project Manager who is nominated by the CMS Spokesperson and endorsed by the CMS Management Board and the CMS Collaboration Board. The Magnet Project Manager is assisted by the Coil Co-ordinator, the Yoke Co-ordinator and a CERN based Project Office.

The financial aspects are monitored by the CMS Budget Co-ordinator and the CMS Resource Manager and ultimately by the CMS Finance Board.

The technical aspects are monitored by the CMS Technical Co-ordinator and ultimately by the CMS Technical Board.

Major issues and changes will be referred to the CMS Management Board for approval.

30.2 ORGANISATION

30.2.1 The Magnet Technical Board

The Magnet Project Manager takes advice from the Magnet Technical Board (MTB), which regularly regroups experts from participating institutes together with experts from institutions that are not members of CMS. The MTB meets every four to six weeks.

Figure 30.1 shows the present organisation of the MTB including the names of the current members.

30.2.2 Technical Working Group

The Technical Working Group (TWG) meets regularly to discuss technical matters concerning mainly the coil. Current members of the working group are:

E. Baynham / Rutherford Appleton Laboratory	D. Campi / CERN-PPE
P. Fabbricatore / INFN-Genova	J.P. Grillet / CERN-PPE
A. Hervé / CERN-PPE	S. Horvath / ETH Zürich
J.C. Lottin / CEA-Saclay	C. Lyraud / CEA-Saclay
W. Maurer / Forschungszentrum Karlsruhe	R. Musenich / INFN-Genova
L. Veillet / CERN-PPE	

30.2.3 Co-operation Protocol with CEA-Saclay

CEA-Saclay has been at the origin of the project for the superconducting coil and has worked on its design since 1991. They have helped the collaboration ascertain that a 4 T coil, with the given parameters, was possible and affordable. CEA-Saclay developed the conceptual design for the Letter of Intent and for the Technical Proposal (end of 1994) which finally led to the approval of CMS by the LHCC and the CERN Research Board. A Protocol of Co-operation was negotiated in 1995 between CERN, acting on behalf of the CMS

Collaboration, and CEA-Saclay.

This Protocol of Co-operation covers the design, manufacture follow-up and commissioning of the superconducting coil. The Magnet Project Manager(*) is responsible for the design and the technical specifications which shall be provided by CEA-Saclay and the participating institutes (see also Chapt. 31).

* Assisted by the Magnet Technical Board.

30.3 PARTICIPATING LABORATORIES

Several institutes have participated in the studies, design, and pre-industrialisation effort for the magnet project. These institutes, which are listed below, are and will continue to be technically involved in the development and procurement of large items. Below we outline the current plans under which the Magnet Project will be carried out. To guarantee the necessary coherence of the project, and satisfy the Quality Assurance Plan, it has been agreed that the work done by an institute participating in the CMS magnet project, must satisfy the following conditions:

- (a) The work will be carried out under the authority of the Magnet Project Manager, with the advice of the Magnet Technical Board, in full accordance with the approved Work-Plans and Schedules of the CMS Magnet Project;
- (b) The participating institute will nominate a Project Engineer who shall be a member of the CMS Collaboration and of the MTB;
- (c) The firm (and subcontractors) selected by a participating institute shall be agreed by the CMS Magnet Project Manager (*) on the basis of technical considerations;
- (d) For the coil project, work shall be carried out according to technical specifications provided by CEA-Saclay and the participating institutes under the control of the CMS Magnet Project Manager (*). The regular follow-up of the contracts will be organised by the Project Engineer. Regular status meetings will be called by the Project Engineer with the participation of representatives of CEA-Saclay and/or of the Project Office, with full access to companies involved. These status meetings may also be called, upon request, by the CMS Magnet Project Manager;
- (e) For the yoke project, work will be carried out under the control the CMS Magnet Project Manager (*). The regular follow-up of the contracts will be organised by the Project Engineer. Regular status meetings will be called by the Project Engineer with the participation of representatives of the Project Office, with full access to companies involved. These status meetings may also be called, upon request, by the CMS Magnet Project Manager;
- (f) Proposals for technical changes, including Work-Plans and Schedules, shall be referred by the Project Engineer to the Magnet Project Manager (*);
- (g) Proposals for changes having potentially significant cost implications shall be jointly presented by the Magnet Project Manager and the Project Engineer to the proper financial authority;
- (h) Provisional and final technical acceptance will be given by the Project Engineer of the participating Institute in accordance with the technical specification, after approval by the CMS Magnet Project Manager (*).

* Assisted by the Magnet Technical Board.

30.3.1 Collaboration with the University of Wisconsin

The University of Wisconsin, with the help of Physical Sciences Laboratory, is designing the endcap section of the magnet. They will prepare the tender documents and organise the main procurements, (see also Chapt. 31).

30.3.2 Collaboration with ITEP Moscow

ITEP Moscow currently provides the necessary connections with the Russian industry which could manufacture the barrel yoke. If the manufacture is in Russia ITEP could take part in the manufacturing follow-up, including quality checks like permeability measurements and ascertain that the manufacture is progressing in accordance with the Quality Assurance Plan.

30.3.3 Collaboration with Fermi National Accelerator Laboratory (FNAL)

FNAL has a major responsibility for the construction of the Hadron Calorimeter and has shown an interest in the vacuum tank, as this is the supporting structure of the barrel part of this detector system. They have participated in the mechanical analysis of the vacuum tank and provided an independent analysis of the barrel yoke. FNAL will participate in the financing of these items, (see also Chapt. 31). FNAL will organise the field mapping strategy taking into account requirements arising from physics.

30.3.4 Collaboration with ETH Zürich and EMPA

From the beginning and with the help of EMPA (Eidgenössisches Material Prüfungs Anstalt) ETH Zürich has been involved in the design of the CMS conductor and has supported the project.

In particular, ETH Zürich, with the help of EMPA, will be in charge of carrying out the work concerning the conductor for the superconducting coil. It also intends to organise the commercial aspects of this procurement (see also Chapt. 31).

30.3.5 Collaboration with INFN Genoa

From the beginning, the INFN Genoa group has been involved in the design of the CMS coil, with full support from INFN. They have participated in the FEA and stability analysis of the coil. In particular they will be in charge of the conductor characterisation.

In addition INFN proposes to provide the complete CMS coil winding. In this context INFN intends to participate technically and to assume the contractual and financial responsibility for the full winding operation (see also Chapt. 31).

30.3.6 Collaboration with NHMFL

NHMFL (National High Magnetic Field Laboratory in Tallahassee) has large testing facilities particularly relevant for magnets the size of CMS, and they will be of great help for the conductor characterisation.

Discussions are going on to define exactly the framework of this collaboration.

Magnet Project

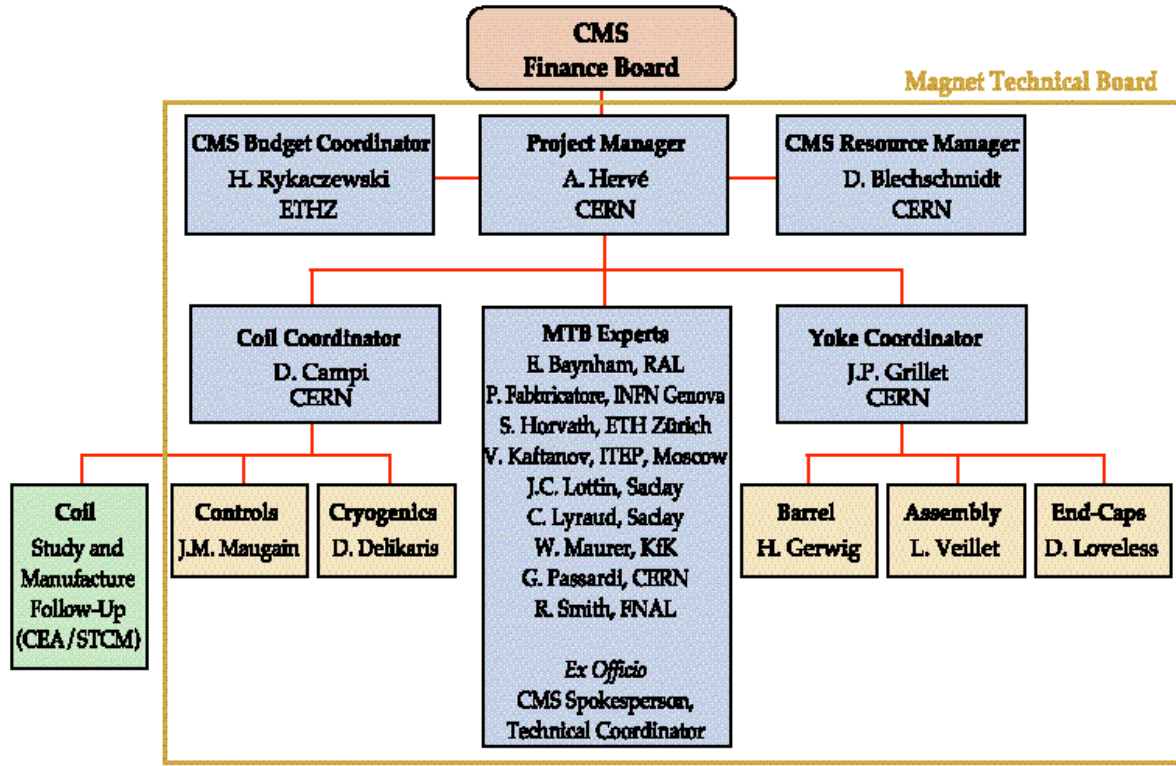


Fig. 30.1: Present organisation of the Magnet Technical Board.

31. COST ESTIMATE AND PROCUREMENTS

31.1 COST ESTIMATE

Ever since the initial studies of the CMS magnet the cost of the entire system has always been a major concern. Throughout the entire design phase, which has led to the submission of this Technical Design Report, the cost estimates have been constantly reviewed by various groups of independent, international experts. In particular, the Magnet Advisory Group MAG and the LHC Cost Review Committee (CORE) have critically reviewed the cost estimates at various stages during the design phase and their findings and recommendations have been taken into account in order to refine and optimise the cost estimate.

The most recent cost estimate of the CMS experiment was released on February 3, 1997 and details of the CMS Magnet can be found there. The cost estimate of the four major components of the Magnet are summarised in Table 31.1.

Table 31.1
Cost Estimate of the CMS Magnet

	Estimated Cost [MCHF]
Barrel Yoke	24.3
Endcap Yoke	19.5
Coil	71.2
Magnet Installation	6.0
Total	121.0

31.2 PROCUREMENT

The guidelines for the contributions to the Magnet Project will be outlined in the Memorandum of Understanding and are laid down in the document entitled “Guidelines on CMS Common Project Contributions” [31-1].

31.2.1 Procedures

Article 5 of the Interim Memorandum of Understanding, signed between CERN and the funding agencies supporting the CMS Collaboration for the initial phase of the experiment up to the end of 1997, defines the procurement policy for the CMS Magnet.

“The total construction work for the detector is divided into:

- sub-detector construction proper, ..., and
- Common Projects which involve construction, transport, assembly, and installation at the common expenses of the Collaboration. The “Magnet” and the “Off-line” have been agreed upon as Common Projects.”

“All Parties must contribute to these Common Projects in proportion to their funding of the CMS detector construction, unless otherwise agreed in exceptional cases by the CMS Finance Board ... The Finance Board may also update the Common Projects contribution level, for example due to a major change in the level of participation of an Institute, or due to a new institute joining the Collaboration. Such updates are subject to approval by the CMS Resource Review Board.”

“Contracts for Common Projects will be placed either by CERN in accordance with document “Financial Guidelines for LHC Collaborations” (CERN/FC/3796), or by other Institutes, in accordance with their own purchasing rules and regulations.”

Based on the CMS Interim Memorandum of Understanding and upon the strategies developed over the last few years, the CMS Collaboration is currently discussing the terms of the CMS Memorandum of Understanding to cover the entire CMS construction phase. As decided by the CMS Finance Board contributions to the Common Projects can be made in three ways:

- a) by taking responsibility for an entire Common Project or parts of it, in agreement with the CMS Finance Board. This option is referred to as an “in-kind contribution”.
- b) by payment of invoices for procurement contracts for Common Project items which were placed by one or more Institutes or Funding Agencies following agreement by the CMS Finance Board. This option is referred to as “payments to contracts”.
- c) by cash payments to a dedicated Common Fund which will be established for the Common Projects through CERN Team Account. The Common Fund will be managed and operated by the CMS Resource Manager, taking advice from the CMS Finance Board, and is monitored by the CERN Finance Division and the CMS Resources Review Board.

The technical responsibility remains with the CMS Magnet Project Manager in all the three cases mentioned above. In case of direct payments or in kind contributions to the procurement of parts for the magnet, the institutes involved will delegate contractually defined technical responsibility to the Magnet Project Manager. The institutes shall closely collaborate with the Project Manager and keep him / her informed of all technical commercial aspects.

31.2.2 Initial Large Procurements

The current plans for large procurements are outlined below.

- a) In the preparatory phase of the CMS Magnet construction an important co-operation agreement between CERN and CEA-Saclay has been reached on the design, studies, testing and supervision of work concerning the superconducting coil. Expenses for this project are and will be covered by the CMS Common Fund.
- b) The CMS Collaboration is preparing a call for tender for elements needed for the barrel part of the magnet. These elements include about 6000 tonnes of steel, the vacuum tank housing the superconducting coil, support structures, tooling, manufacture follow - up, trial assembly and transport to CERN. The Collaboration has mandated ETH Zürich to lead a consortium of CMS institutes to take care of these procurements. The consortium will include institutes from Cyprus, Russia, Switzerland, United States of America, and possibly other countries. The market survey has been conducted by CERN in 1996, and the call for tender is scheduled to be released in June 1997. The contract for these elements, which are on the critical path, is expected to be signed immediately after approval of the magnet project so that construction can start at the end of

1997 or, at the latest, in the beginning of 1998. Expenses for this part of the magnet are direct payments.

- c) The University of Wisconsin has been requested to work on developing the design of the magnet endcap system and consequently the CMS Collaboration has agreed to the procurement of the endcaps by the US - CMS Collaboration through competitive international tendering. The University of Wisconsin has accepted to take care of all commercial aspects of this procurement. A market survey for these elements is in preparation at CERN, to be followed by a call for tender in autumn 1997. It is expected to place one or several contracts for the project by mid 1998. Ongoing discussions with the Institute of High Energy Physics Beijing will be continued to explore whether China could make an in kind contribution to the endcap supports. All contributions from the United States for this project are direct payments, whereas eventual Chinese contributions would be in kind.
- d) Following the recommendation by the CMS Magnet Technical Board, the CMS Finance Board has agreed to an offer from Pakistan to provide eight support feet for the barrel part of the magnet. This contribution will be an in kind contribution and its value will be assessed by the CMS Finance Board.
- e) ETH Zürich has expressed technical interest in the work concerning the conductor for the superconducting coil and intends to also organise the commercial aspects of the procurement. Expenses for this part of the magnet are direct payments.
- f) INFN Italy has submitted a preliminary proposal to provide the CMS coil winding, including tools and the winding operation. Most procurements will be made through competitive international tendering. The organisation of the responsibilities are subject of discussions between INFN and the CMS Collaboration.

Procurements of other major components for the CMS magnet will be arranged according to the progress of construction in due time. We note that the six procurements mentioned above represent about two-thirds of the total estimated cost of the magnet construction.

32. REFERENCES

CHAPTER 1

- [1-1] The Compact Muon Solenoid Technical Proposal, CERN/LHC 94-38.
- [1-2] Report on the CMS Magnet Review held at CERN on October 7th-8th 1996, Preliminary Design Review Committee. Chairman, T. Taylor, CERN. Members: E. Baynham, Rutherford Appleton Laboratory, L. Bottura, CERN, H. Desportes, CEA-Saclay, M. Huguet, ITER, P. Komarek, Forschungszentrum, Karlsruhe, D. Leroy, CERN, W. Maurer, Forschungszentrum, Karlsruhe, R. Parodi, INFN-Genova, H. Schneider-Muntau, National High Magnetic Field Laboratory, Tallahassee, H. ten Kate, CERN, B. Turk, CEA-Cadarache, A. Yamamoto, KEK.

CHAPTER 6

- [6-1] R. Loveless, F. Feyzi, Magnetic and Structural Analysis of the CMS Endcaps, CMS TN 94-293, 1 Dec., 1994.
- [6-2] C. Pes, Magnetic forces on the CMS coil due to misalignment, Internal Report CEA/DAPNIA 5C2100T M-1000 013 97.
- [6-3] C. Pes, Efforts sur la bobine en position excentrée, Internal Report CEA/DAPNIA 5C2100T M-0000 042 94.
- [6-4] S. Farinon, P. Fabbricatore, Preliminary magnetic analysis of CMS magnet , INFN Genova, Group report N.INFN-GE-SC97-02.

CHAPTER 7

- [7-1] H. Gerwig / CERN, Structural Analysis of CMS Central Barrel Yoke and Vacuum Tank, Preliminary Design Report 1996, Part 1.
- [7-2] AISC, Manual of Steel Construction, Allowable Stress Design, Ninth Edition.
- [7-3] CASTEM 2000, Commissariat à l'Energie Atomique (CEA), Finite element program.
- [7-4] B. Wands / FNAL, Finite Element Analysis of the CMS Central Barrel Yoke and Vacuum Tank, Preliminary Design Report 1996, Part 1.
- [7-5] F. Sanchez, H. Gerwig, Mechanical behaviour of the Ferris wheel, CMS Internal Note, IN - 1997/008.
- [7-6] F. Sanchez, H. Gerwig, Universidad de Vigo, Escuela Tecnica Superior de Ingenieros Industriales / CERN, Final project of studies: Comportamiento estructural de la rueda Ferris, Geneva 1997.
- [7-7] Firma Nagel GmbH & KoKG, Eichtal Germany.
- [7-8] Feyzi et al., Barrel yoke central section finite element analysis report, CMS TN 94-277, 1994.

CHAPTER 8

- [8-1] R. Loveless, F. Feyzi, Magnetic and Structural Analysis of the CMS Endcaps, CMS TN 94-293, 1 Dec., 1994.
- [8-2] American Institute of Steel Construction, Manual of Steel Construction, Allowable Stress Design, 9th ed. Dec., 1995.
- [8-3] R.J. Roark, W.C. Young, Formulas for Stress and Strain, 5th ed. McGraw-Hill Book Company, 1975, Table 17, case 7.

- [8-4] Ditto [8-3], Table 16, case 1.
- [8-5] Ditto [8-3], Table 37, case 7a.
- [8-6] L. Greenler, F. Feyzi, R. Loveless, Structural analysis of the YE1 endcap disk, CMS TN 95-117, 1 Dec., 1995.

CHAPTER 9

- [9-1] H. Gerwig / CERN, Structural Analysis of the CMS Central Barrel Yoke and the vacuum tank, Preliminary Design Report 1996, Part 1.
- [9-2] Engineering Analysis Report, EAR-171, FNAL, Bob Wands 1996.
- [9-3] B. Wands / FNAL, Finite Element Analysis of the CMS Central Barrel Yoke and Vacuum Tank, Preliminary Design Report 1996, Part 1.
- [9-4] B. Levesy, Dimensionnement général solénoïde et enceinte à vide, Internal Report DAPNIA/STCM, 5C2100TM-096.
- [9-5] B. Levesy, Loads due to the solenoid suspension on the vacuum tank, Internal Report CEA/DAPNIA 5C2100TM-3000 002 SB.

CHAPTER 10

- [10-1] Agreement No K 292/PPE with ESAB (S) and TTS (N), Studies and realisation of an electroslag welding test and Endcap production for the CMS experiment.
- [10-2] Dr. M. Harzenmoser, A. Sutter, Electroschlacke-Schweissungen für das CMS-Experiment am CERN, EMPA report, Prufbericht nr 165'885/1.
- [10-3] Dr. M. Harzenmoser, A. Sutter, Electroschlacke-Schweissungen für das CMS-Experiment am CERN, EMPA report, Prufbericht nr 165'885/2.
- [10-4] Electroslag Welding Tests for the Endcap of the CMS Magnet, M. Harzenmoser, EMPA; T. de Visser, J.P. Grillet and G. Waurick, CERN; F. Feyzi, University of Wisconsin, Physical Sciences Laboratory; S. Carlson, ESAB AB, Göteborg, Sweden; I. Keim, TTS, Drøbak, Norway; submitted to Eurojoin 3.

CHAPTER 11

- [11-1] J.M. Baze, H. Desportes, R. Duthil, C. Lesmond, J.C. Lottin, Y. Pabot, Conceptual Design of the CMS 4 T Solenoid, DAPNIA/STCM/92-01.
- [11-2] H. Desportes et al., Design, Construction and Test of the Large Superconducting Solenoid ALEPH, MT-10 Boston/USA 1987.
- [11-3] K.T. Hartwig, Strength and Resistivity Changes caused by Cyclic Strain at 4.2 K in pure aluminium, (and all attached references), ICEC Shenyang, China.
- [11-4] J.P. Egan and R.W. Boom, Measurement of the electrical resistivity and thermal conductivity of high purity aluminium in magnetic fields, Advances in Cryogenic Engineering (Material) 1990, Vol. 36.
- [11-5] K.T. Hartwig, Cyclic Strain Resistivity in pure aluminium at 20 K, Advances in Cryogenic Engineering (Material) 1990, Vol. 36, p. 725.
- [11-6] J.C. Lottin, Conception du bobinage, CMS Internal Report DAPNIA/STCM, 5C2100T--1000 001 91.
- [11-7] J.C. Lottin, Permissible stress on the CMS Coil, Internal Report DAPNIA/STCM, 5C2100TT-091.
- [11-8] J.C. Lottin, Mechanical computation on ribbon and block conductor, Internal Report DAPNIA/STCM, 5C2100TM-110097.

- [11-9] S. Waeffler, Essais: Mesures de résistance sur le solénoïde d'ALEPH, Internal Report DAPNIA/STCM, C-2100TF-1000 009 96.

CHAPTER 12

- [12-1] I.L. Horvath, Aluminium Stabilised Cables for Very Large Superconducting Magnets, 14th Int. Conf. on Magnet Technology, Tampere, June 1995.
- [12-2] I.L. Horvath, ATLAS 200 m SC Conductor Test Report, CERN Contract No. CA1064658, June 1996.
- [12-3] R.P. Smith et al., The Aluminium Stabilised Conductor for the Fermilab D0 Solenoid, 16th Int. Cryogenic Eng. Conf. May 1996 Kitakyushu, Japan.
- [12-4] H. Eriksson (Edit.), The Aluminium Stabilised Conductor for KEK, Test Report, Outokumpu Copper Superconductors February 1997.
- [12-5] P. Fabbricatore et al., The Superconducting Magnet for the BABAR Detector of the PEP-II B Factory at SLAC, IEEE Trans. on Magnetics Vol. 32. No.4 July 1996, p. 2210.
- [12-6] B. Curé, Strand critical current of the insert extruded on 14/01/97 at Cortaillod, Internal Report DAPNIA/STCM, 5C2100TF-110097.

CHAPTER 13

- [13-1] E. Baynham and D. Evans, Adhesive Properties at Low Temperatures of Epoxy Resin, Resin Pre-Impregnated Tape, Nonmetallic Materials and Composites at Low Temperatures 3, Hartwig and Evans (Editors) Plenum Publishing Corp. 1986.
- [13-2] J.M. Rey, Mesures d'évolution de la viscosité des résines pendant la polymérisation, Internal Report DAPNIA/STCM, 5C2130TM-1200 007 95.
- [13-3] J.M. Rey, Mesures de contraction de polymérisation en phase solide, Internal Report DAPNIA/STCM 5C2130TM-1200 008 95.
- [13-4] J.M. Rey, Mesures de densité des résines solides, Internal Report DAPNIA/STCM 5C2130TM-1200 009 95.
- [13-5] J.M. Rey, Mesures mécaniques de cisaillement des joints collés utilisant des résines d'imprégnation, Internal Report DAPNIA/STCM.
- [13-6] J.M. Rey, Caractérisation de l'évolution de la viscosité de résines d'imprégnation lors des paliers isothermes, Internal Report DAPNIA/STCM 5C2130TM-1200 011 95.
- [13-7] J.M. Rey, Estimation des propriétés mécaniques d'un composite réalisé à partir de ruban de fibre de verre, Internal Report, DAPNIA/STCM 5C2130TM-1200 016 96.
- [13-8] J.M. Rey, Mesure de la contrainte de cisaillement sur des joints collés: caractérisation du pré-imprégné DELPHI, Internal Report DAPNIA/STCM, 5C2130TM-1200 01797.
- [13-9] J.M. Rey, Mesure de la contrainte de cisaillement sur des joints collés: caractérisation du préimprégné IVA, Internal Report DAPNIA/STCM, 5C2130TM-1200 018 97.

CHAPTER 14

- [14-1] A. Desirelli, Status of the CMS coil mechanical FEA, CMS NOTE, 1997, 035.
- [14-2] S. Farinon and P. Fabbricatore, Impact of winding configuration on stresses of CMS conductor, INFN Genova–Group Report No. INFN-GE-SC97-05.

- [14-3] C. Pes, Mechanical stress analysis on the CMS coil: Block conductor, Internal Report DAPNIA/STCM, 5C2100TM-1000 017 97.
- [14-4] A. Desirelli, Analysis procedures and criteria for the mechanical FEA of the CMS coil at CERN, CEA and INFN, CMS NOTE, 1997, 034.
- [14-5] S. Farinon and C. Pes, Coil Mechanical Analysis - Single unit configuration, Internal Report DAPNIA/STCM, 5C2100TM-1000 008 96.
- [14-6] P. Fabbricatore, S. Farinon and R. Musenich, Study on the possible use of high strength pure Al for the conductor of CMS coil, INFN Genova–Group Report No. INFN-GE-SC97-01.
- [14-7] S. Farinon and P. Fabbricatore, Preliminary magnetic analysis of CMS magnet, INFN Genova–Group Report No. INFN-GE-SC97-02.
- [14-8] S. Farinon, Revised mechanical FEA calculations, INFN Genova–Group Report N°INFN-GE-SC97-03.
- [14-9] P. Fabbricatore and S. Farinon, Mechanical analysis on CMS winding, INFN Genova–Group Report N°INFN-GE-SC97-04.
- [14-10] C. Pes and S. Farinon, Coil Mechanical Analysis - Single unit configuration, 5C2100TM-100096.
- [14-11] C. Pes, Analyse mécanique du solénoïde CMS, 5C2100TM-095 - Mécanique 276TC56.
- [14-12] B. Gallet, Essais mécaniques sur l'aluminium du conducteur ALEPH-VAC, CEA Report No. DSM DAPNIA STCM 276TC02.
- [14-13] A. Desirelli, B. Gallet, F. Kircher, J.M. Rey, Failure criterion of glass/epoxy composites as electrical insulation for large SC magnets, ICMC, Portland, Oregon, USA 28 July - 1 August 1997.
- [14-14] D.E. Baynham, D. Evans, S.J. Gamage, R.J.S. Greenhalgh, D. Morrow and S.J. Robertson, Transverse mechanical properties of glass reinforced composites, Report CLRC: AECT/70/96 Nov. 1996.
- [14-15] A. Desirelli, S. Horvath, S. Sgobba, Experimental assessment of the CMS conductor, CMS NOTE 1997, 033.

CHAPTER 15

- [15-1] F.P. Juster, P. Fabbricatore et al., IEEE TRANS. APPL. SUPERC, 5 (2) p.377-380, 1995.
- [15-2] M.N. Wilson, Superconducting Magnets, Clarendon Press, Oxford 1983.
- [15-3] D.C. Elrod, G.E. Giles and W.D. Turner, ORNL/NUREG/CSD 2/V2, Union Carbide Corp., Nuclear Div., Oak Ridge National Laboratory, 1981.
- [15-4] R. Fast et al., Design report for an indirectly cooled 3-m diameter superconducting solenoid for the FermiLab collider detector facility, FermiLab, TM-1135, 1982.
- [15-5] P. Fabbricatore and R. Musenich, Superconducting magnets for detectors of large colliders, Nuclear Physics B, 44, p 667-671, 1995.
- [15-6] R. De Lorenzi, P. Fabbricatore, S. Farinon, G. Gemme, R. Musenich, R. Parodi, S. Pepe, B. Zhang, Status report of the INFN R&D activities for Al-stabilised conductors of large magnets for LHC detectors, INFN/TC-94/05 22 Aprile 1994.
- [15-7] P. Fabbricatore, L. Boldi, R. Musenich, R. Parodi and G. Gemme, Stability of Al-stabilised Conductors for High Energy Physics Application, contributed paper to

ASC 1996.

CHAPTER 16

- [16-1] B. Curé, Quench-back protection studies and modelisation, Internal Report CEA/DAPNIA 5C2100T T-1000 005 SC.
- [16-2] B. Curé, Synthesis of quench-back protection studies, Internal Report CEA/DAPNIA 5C2100T T-1000 012 SA.
- [16-3] C. Lesmond, B. Curé, Quench protection studies, Internal Report CEA/DAPNIA 5C2100T T-1000 006 SA.
- [16-4] C. Lesmond, CMS electrical circuit, Internal Report CEA/DAPNIA 5C2100T F-1000 007 SA.
- [16-5] S. Farinon, Current diffusion effect, Internal Report INFN/Genoa I-2100T--1100 012 96.
- [16-6] B. Curé, Voltages during quench, Internal Report CEA/DAPNIA 5C2100T F-4000 005 SA.
- [16-7] J.C. Lottin, Gradation du conducteur, Internal Report CEA/DAPNIA 5C2100T--1100 011 96.
- [16-8] B. Curé, Quench propagation analytical calculations, Internal Report CEA/DAPNIA 5C2100T T-1000 014 SA.
- [16-9] B. Curé, Calcul de la pression magnétique dans la frette, Internal Report CEA/DAPNIA 5C2100T F-1300 001 96.
- [16-10] B. Curé, Induced forces in the quench-back cylinder, Internal Report CEA/DAPNIA 5C2100T F-1300 004 SA.

CHAPTER 17

- [17-1] J.P. Lottin., Pressure drop in the CMS coil helium circuits, Internal Report CEA-STCM, 5C2100T--5000 003 SA.
- [17-2] J.C. Lottin, R. Duthil, ALEPH Solenoid Cryogenic System, ICEC-12, Southampton, 1988, p.117.
- [17-3] B. Curé, Calcul des pertes en régime variable, Internal Report CEA-STCM, 5C2100T--5000 004 SA.
- [17-4] J.P. Lottin., Séquences cryogéniques, Internal Report CEA-STCM, 5C2100T-5000 002 SA.

CHAPTER 18

- [18-1] B. Levesy, Solenoid suspension dimensioning, Internal Report CEA-STCM 5C2100TF-1400 001SC, and Loads due to the solenoid suspension on the vacuum tank, Internal Report CEA-STCM 5C2100TM-3000 002 SC.
- [18-2] B. Wands / FNAL, Finite Element Analysis of the supporting system of the CMS coil, in reference to the vacuum tank.

CHAPTER 20

- [20-1] C. Lesmond, Disposition et encombrement de la résistance de protection, CEA/STCM Internal Report, 5C2100T-4000 001 96.
- [20-2] C. Lesmond Implantation générale externe, Puissances électriques et débits d'eau du circuit électrique du solénoïde, CEA/ STCM Internal Report, 5C2100N--0020 001

96.

CHAPTER 22

- [22-1] R. Barrillère, F. Perriollat CMS DCS: User Requirements Document, 01 February 1996.
- [22-2] J. Feyt, E. Sbrissa, S. Waeffler, XMS: User Requirements Document in preparation.

CHAPTER 23

- [23-1] A.F. Clark, G.E. Childs and G.H. Wallace, Electrical resistivity of some engineering alloys at low temperatures, *Cryogenics* 10, 295, 1970.
- [23-2] S.H. Kim and S.T. Wang, Measurements of mechanical and electrical properties of high purity aluminium, *Adv. Cryog. Eng.* 24, 485, 1978.
- [23-3] R.P. Reed, Aluminium 2, A review of deformation properties of high purity aluminium and dilute aluminium alloys, *Cryogenics* 12, 259, 1972.
- [23-4] P. Fabbricatore, G. Gemme, R. Musenich, R. Parodi, Critical current measurements on the cables for LHC detectors magnet, 14th International Conference on Magnet Technology, Tampere, 1995.
- [23-5] V. Esslinger, R. Flükiger, I.L. Horvath, B. Seeber, Measurements on the residual resistivity ratio (RRR) of high purity aluminium under cyclic mechanical stresses, 14th Int. Conf. on Magnet Technology, Tampere, June 1995.
- [23-6] I.L. Horvath, Aluminium stabilised superconducting cable development for high energy physics detector magnets, Applied Superconductivity Conference, Oct. 16.-21, 1994, Boston, USA.
- [23-7] D. Fritz, I.L. Horvath, M. Harzenmoser, J. Neuenschwander, F. Wittgenstein, Development of an aluminium stabilised reinforced superconducting conductor, 14th International Conference on Magnet Technology, June 11-16, 1995, Tampere, Finland.
- [23-8] I.L. Horvath, T. Lüthi, J. Neuenschwander, High-current superconducting cables: application of ultrasonic testing during development and production, DACH Annual Conference on Nondestructive Testing of Materials, May 13-15, 1996, D-Lindau / Germany DGZfP Vol. 52.1, p. 251.
- [23-9] I.L. Horvath, R. Huwiler, Th. Lüthi, W.J. Muster, J. Neuenschwander, Qualification of advanced cryogenic components: Mechanical integrity of high current superconducting cables, *Recent Res. Devel. in Cryogen.*, Vol. 1, 1996, p. 7.
- [23-10] D. Fritz, I.L. Horvath, M. Harzenmoser, J. Neuenschwander, F. Wittgenstein, Development of an aluminium stabilised reinforced superconducting conductor, 14th Int. Conf. on Magnet Technology, Tampere, June 1995.
- [23-11] I.L. Horvath (Edit.), Electron beam welding on CMS conductor reinforcement, CERN Contract No. CA 1067563, March 1996.
- [23-12] B. Curé, Strand critical current measurements, Internal Report CEA/DAPNIA 5C2100T F-1100 031 96.
- [23-13] F. Kircher, Mesure des courants critiques de brins, Internal Report CEA/DAPNIA 5C2100T F-0000 049 94.
- [23-14] B. Gallet, Conducteur ALEPH, Caractérisation de l'interface câble supraconducteur aluminium, Internal Report CEA/DAPNIA 5C2100T F-0000 044 94.
- [23-15] F. Kircher, Mesure du RRR de l'aluminium, Internal Report CEA/DAPNIA

- 5C2100T F-0000 047 94.
- [23-16] J.M. Rey, Regnier, Synthèse des résultats de l'étude de la diffusion Cu/Al sur le conducteur ALEPH, Internal Report CEA/DAPNIA 5C2100T F-1100 001 95.
 - [23-17] B. Curé, FE modelisation of Aluminium/Rutherford-cable electrical contact, Internal Report CEA/DAPNIA 5C2100TF-1100 026 96.
 - [23-18] B. Curé, Micrographical analysis of soldered conductor, Internal Report CEA/DAPNIA 5C2100TM-1100 044 97.
 - [23-19] B. Gallet, Essais de cisaillement sur éprouvettes en alliage 6060T5 soudées par brasures tendres (crèmes de brasage), Internal Report CEA/DAPNIA 5C2100TM-1100 027 96.
 - [23-20] B. Levesy, Mesure de cisaillement sur éprouvettes soudées avec ruban, Internal Report CEA/DAPNIA 5C2100T-1100 036 97.
 - [23-21] B. Levesy, Tests de la brasure ZnAl, Internal Report CEA/DAPNIA 5C2100T--1100 049 97.
 - [23-22] D. Campi, Guidelines for the pre-industrialisation program for the CMS conductor, CMS Internal note, 1997, 018.

CHAPTER 24

- [24-1] D. Campi, Guidelines for the pre-industrialisation program for the CMS winding, CMS Internal note, 1997, 017.
- [24-2] E. Baynham and D. Evans, RAL, private communication.
- [24-3] A. Yamamoto, KEK, private communication.

CHAPTER 25

- [25-1] Technical Proposal CMS, CERN/LHC 94-38. LHCC/P1, 15 December 1994.
- [25-2] Minutes of the CERN Research Board, Meeting on 8 February 1996, CERN/DG/Research Board 96-237, Minutes 125, 26 February, 1996.
- [25-3] Ongoing contractual preparation of tendering documents with civil engineering consortium GIBB-SGI-GEOCONSULT, CERN ST-CE, schedule No. LHC/CE G023 rev.0.5.

CHAPTER 27

- [27-1] T. Meyer, CMS-GE-CERN-QAP-0100.00 (on progress) QAP Contents and Status
- [27-2] CMS Magnet QAP (on progress, as part of the General CMS QAP)
- [27.3] G. Bachy, Ari Pekka Hameri, What to be implemented at the early stage of a large scale project. CERN-MT/95-02 (DI) LHC Note 315
- [27.4] Saclay Technical Team, Plan d'assurance qualité 5C2100Q - - 000 001 PA

CHAPTER 28

- [28-1] Eurocode 3, Design of steel structures (ENV 1993-1-1 edited by Comité Européen de Normalisation).
- [28-2] American Institute of Steel Construction, Manual of Steel Construction, Allowable Stress Design, 9th ed, Dec. 1995.
- [28-3] CODAP 95, (French Code for Unfired Pressure Vessels) edited by Syndicat National de la Chaudronnerie, de la Tôlerie et de la Tuyauterie Industrielle, Paris, 30 June 1995.

- [28-4] 1992 ASME Boiler and Pressure Vessel Code - Section VIII, Rules for Construction of Pressure Vessels, American Society of Mechanical Engineers, New York, 1992.
- [28-5] R. Barrillère, F. Perriollat, CMS DCS, User Requirements Document 01 February 1996.
- [28-6] J. Pothier, BBL3, Nouveau Concept en Sécurité Câblée, 1992.

CHAPTER 29

- [29-1] M. Huhtinen, Radiation environment simulations for the CMS detector, CERN CMS TN/95-198, 1995, Presented at SARE2 workshop, CERN, 9-11 October, 1995, Proceedings: CERN/TIS-RP/97-05 (1997).
- [29-2] A.I. Drozhdin, M. Huhtinen and N.V. Mokhov, Accelerator related background in the CMS detector at LHC, Nucl. Instr. and Meth. A381, 1996, 531.
Azhgirey, V. Talanov, A. Uzunian, Background muons generated in the CMS detector area by the beam losses in the LHC, CERN CMS TN/95-202, 1995.
- [29-3] J. Ranft, Phys. Rev. D51 (1995) 64. J. Ranft, DPMJET-II, a Dual Parton Model event generator for hadron-hadron, hadron-nucleus and nucleus-nucleus collisions, Presented at SARE2 workshop, CERN, 9-11 October, 1995, Proceedings: CERN/TIS-RP/97-05, 1997.
- [29-4] P.A. Aarnio et al., CERN TIS-RP/168 (1986) and CERN TIS-RP/190 (1987).
A. Fassò et al., Proc IV Int. Conf. on Calorimetry in High Energy Physics, La Biodola, Sept. 20-25, 1993, Ed. A. Menzione and A. Scribano, World Scientific, p. 493, 1993.
- [29-5] M. Huhtinen and G. R. Stevenson, Shielding requirements in the CMS experimental area, CERN CMS TN/95-056, 1995.
- [29-6] A. Fassò et al, Nucl. Instr. and Meth. A332 (1993) 459. G. Stevenson, Adv. Space Res. 17 (1995) 2. C. Birattari et al., Nucl. Instr. and Meth. A338, 1994, 534.
- [29-7] M. Huhtinen, Method for Estimating Dose rates from Induced Radioactivity in Complicated Hadron Accelerator Geometries, to be published as CERN TIS Divisional Report, 1997.
- [29-8] M. Hoefert, K. Potter and G.R. Stevenson, Summary of Design Values, Dose Limits, Interaction Rates etc. for use in estimating Radiological Quantities associated with LHC Operation, CERN/TIS-RP/IR/95-19.1, 1995.
- [29-9] M. Huhtinen and G.R. Stevenson, Radiological Impact of Access Ways and other Shield Penetrations in the CMS Experimental Area, CERN/TIS-RP/IR/96-24, 1996.

CHAPTER 31

- [31-1] Guidelines on CMS Common Project Contributions, CMS-M/97-013.
- [31.2] Financial guidelines for LHC collaboration (CERN/FC/3797).